



The  
University  
Of  
Sheffield.

# **Novel techniques in the scanning electron microscope for characterising polymer-based photovoltaic materials**

**By:**  
Robert Masters

A thesis submitted in partial fulfilment of the requirements for the  
degree of Doctor of Philosophy

The University of Sheffield  
Faculty of Engineering  
Department of Materials Science and Engineering

**Alternative format thesis**

Submitted July 2017  
Corrected January 2018

## **Acknowledgements**

Writing a few words of acknowledgement for my thesis gives me cause to reflect on the past four years, and doing so makes me feel truly fortunate and extremely grateful for the guidance, friendship and support I've received during this time from friends, family and colleagues.

Most obviously, to Conny – thank you for making the whole thing possible; for giving me the chance to study with you in the first place, for providing me with a wealth of fantastic opportunities during my PhD, and for being such a committed and dedicated supervisor throughout. Your guidance and encouragement has been the main driver for everything I have achieved in my work for the past few years.

It has been a pleasure to watch Conny's research group grow from being just me four years ago, to today being a fantastic, varied group of researchers performing genuinely exciting research. Quan, Alaa, Sameer, Vikas, Kerry, Nicola, Kostas – thanks for the friendship, the support in helping me out of a few holes, and the stimulating conversation that has sparked new ideas. I should also thank the staff at the Sorby Centre, who have provided for all of my experimental needs throughout. I look forward to continuing working with you all over the next year!

To David Lidzey – thank you for your support and advice in all things solar, for generously providing me access to the fantastic EPMM labs, and for offering new perspectives on my research. Thanks also to the various postdocs and PhD students in David's EPMM group – especially Andrew, Chris, Yiwei and Ben – for being always willing to offer time and assistance.

To the various collaborators I've been fortunate enough to work with – especially Hongzhou and Yangbo in Dublin; Tom, Andrew and Athene in Cambridge; and Adrian, Letian and Fabian from FEI – thanks for providing me access to a range of fantastic facilities and equipment, and for offering the time and support that has enabled us together to get some brilliant results. I hope I get the chance to work with some of you again in the future.

To my friends – thanks for keeping me smiling regardless of how well the work was going. I’ve had the privilege of sharing a house with some of my best mates at Springvale Road for the past four years. Dave, Jonny, Tom, Martin, Ben – it’s been absolutely brilliant and I’m really going to miss living with you all. I’ve also been fortunate to share an office with good friends – Friday night pub after work has been the perfect tonic at the end of many a long week! Thanks as well to my bandmates at the Music Players’ Society for keeping it funky.

To Rita – thanks for being there through everything in the past couple of years, bringing joy and love to every situation. For keeping my spirits up through my low points in recent months, and for making the good times so much fun. Posso?

And finally, all of my love to my family – Mum, Dad and Rick – to whose unwavering love and support I owe everything.

## Abstract

In this thesis, a range of new techniques are developed in the scanning electron microscope (SEM) for investigating and imaging the nanoscale morphology of polymer:fullerene blends with organic photovoltaic (OPV) applications. The primary focus of these techniques is energy-selective detection of secondary electrons (SE) emitted in the SEM, applied both to measure the energy spectrum of a sample's SE emissions, and for high-resolution energy-filtered SEM (EFSEM) imaging with improved material contrast. The SE energy-filtering performance of a FEI Sirion SEM is evaluated, and the SE spectrum of P3HT, a popular polymer for OPV, is measured and found to demonstrate a range of spectral features. These features are believed to reflect molecular ordering in the polymer. It is also found that degradation of the P3HT film under air and light alters the SE spectrum of the sample. Based upon SE spectroscopy methods, energy-filtered SE images are then applied to image the phase-separated morphology of a P3HT:PC<sub>60</sub>BM film with increased material contrast. EFSEM images of the blend film surface are found capable of mapping the blend morphology with a lateral resolution of  $(0.8 \pm 0.1)$  nm, and demonstrate approximately double the material contrast in conventional SEM images. This improved contrast allows for the direct identification of mixed phase material in the image data, a first for this particular blend system. In P3HT:PC<sub>60</sub>BM films processed for optimal performance,  $(25 \pm 5)$  % of the imaged phase area is classified as mixed phase by the technique. A further imaging technique is developed using low-energy backscattered electrons (BSE) in the SEM to probe the 3-dimensional morphology of the polymer:fullerene film as well as the surface. The technique is used to compare reference P3HT:PC<sub>60</sub>BM blends with a modern, high-performance PffBT4T-2OD:PC<sub>70</sub>BM blend film. At the surface, correlation between the phase size of fullerene domains in both blend systems is found, with both films showing a most probable domain radius of 6 nm. Further, by carefully tuning the primary beam energy, BSE images are used to probe for 'columnlike' phases that penetrate a large fraction of the film's thickness; a characteristic feature of optimised OPV blend morphologies. The subsurface characterisation of the two blend systems reveals the highly optimised morphology of the modern, high-performance system.

## Publications:

- [1] R.C. Masters, A.J. Pearson, T.S. Glen, F.-C. Sasam, L. Li, M. Dapor, A.M. Donald, D.G. Lidzey, C. Rodenburg, Sub-nanometre resolution imaging of polymer–fullerene photovoltaic blends using energy-filtered scanning electron microscopy, *Nat. Commun.* 6 (2015) 6928. doi:10.1038/ncomms7928.
- [2] R.C. Masters, Q. Wan, Y. Zhou, A.M. Sandu, M. Dapor, H. Zhang, D.G. Lidzey, C. Rodenburg, Application of low-voltage backscattered electron imaging to the mapping of organic photovoltaic blend morphologies, *J. Phys. Conf. Ser.* 644 (2015) 12017. doi:10.1088/1742-6596/644/1/012017.
- [3] C. Bracher, H. Yi, N.W. Scarratt, R.C. Masters, A.J. Pearson, C. Rodenburg, A. Iraqi, D.G. Lidzey, The effect of residual palladium catalyst on the performance and stability of PCDTBT: PC70BM organic solar cells, *Org. Electron.* 27 (2015) 266–273. doi:10.1016/j.orgel.2015.10.001.
- [4] A.T. Barrows, R.C. Masters, A.J. Pearson, C. Rodenburg, D.G. Lidzey, Indium-free multilayer semi-transparent electrodes for polymer solar cells, *Sol. Energy Mater. Sol. Cells.* 144 (2016) 600–607. doi:10.1016/j.solmat.2015.10.010.
- [5] Y. Zhou, D.S. Fox, P. Maguire, R. O’Connell, R.C. Masters, C. Rodenburg, H. Wu, M. Dapor, Y. Chen, H. Zhang, Quantitative secondary electron imaging for work function extraction at atomic level and layer identification of graphene, *Sci. Rep.* 6 (2016) 21045. doi:10.1038/srep21045.
- [6] Q. Wan, R.C. Masters, D.G. Lidzey, K.J. Abrams, M. Dapor, R.A. Plenderleith, S. Rimmer, F. Claeysens, C. Rodenburg, Angle selective backscattered electron contrast in the low-voltage scanning electron microscope: Simulation and experiment for polymers, *Ultramicroscopy.* 171 (2016) 126–138. doi:10.1016/j.ultramic.2016.09.006.
- [7] D.K. Mohamad, B. Freestone, R.C. Masters, M. Reinhardt, S.L. Canning, C. Rodenburg, D.G. Lidzey, Optimized organometal halide perovskite solar cell fabrication through control of nanoparticle crystal patterning, *J. Mater. Chem. C.* (2017). doi:10.1039/C6TC05189H.
- [8] R.C. Masters, Q. Wan, Y. Zhang, M. Dapor, A.M. Sandu, C. Jiao, Y. Zhou, H. Zhang, D.G. Lidzey, C. Rodenburg, Novel organic photovoltaic polymer blends: A rapid, 3-dimensional morphology analysis using backscattered electron imaging in the scanning electron microscope, *Sol. Energy Mater. Sol. Cells.* 160 (2017) 182–192. doi:10.1016/j.solmat.2016.10.029.
- [9] V. Kumar, W.L. Schmidt, G. Schileo, R.C. Masters, M. Wong-Stringer, D.C. Sinclair, I.M. Reaney, D. Lidzey, C. Rodenburg, Nanoscale Mapping of Bromide Segregation on the Cross Sections of Complex Hybrid Perovskite Photovoltaic Films Using Secondary Electron Hyperspectral Imaging in a Scanning Electron Microscope, *ACS Omega.* 2 (2017) 2126–2133. doi:10.1021/acsomega.7b00265.
- [10] M. Dapor, R.C. Masters, I. Ross, D.G. Lidzey, A. Pearson, I. Abril, R. Garcia-Molina, J. Sharp, M. Uncovsky, T. Vystavel, F. Mika, C. Rodenburg, “Secondary electron spectra of semi-crystalline polymers – A novel polymer characterisation tool?”, *J. Electron Spectros. Relat. Phenomena.* 222 (2018) 95-105. doi: 10.1016/j.elspec.2017.08.001

## **Conference Presentations:**

### **Microscience Microscopy Congress (MMC), Manchester, UK, July 2014.**

Identification of organic photovoltaic films and related impurities using secondary electron spectra in the scanning electron microscope (**Poster presentation**)

### **International Microscopy Congress (IMC), Prague, Czech Republic, September 2014.**

Characterization of nanoscale morphology in photovoltaic polymer blends using energy-filtered scanning electron microscopy (**Oral presentation**)

### **Microscience Microscopy Congress (MMC), Manchester, UK, July 2015.**

Application of low-voltage backscattered electron imaging to the mapping of organic photovoltaic blend morphologies (**Poster presentation**)

### **European Materials Research Society (E-MRS) Spring Meeting, Lille, France, May 2016.**

Through-thickness characterisation of novel organic photovoltaic blend morphology with low-energy backscattered electron imaging (**Extended oral presentation**)

### **Microscience Microscopy Congress (MMC), Manchester, UK, July 2017.**

Revealing the cross-sectional morphology of organic photovoltaic blends in 2-dimensions with a Helium-ion Microscope (**Poster presentation**)

## Table of Contents

Acknowledgements .....	ii
Abstract .....	iv
Publications .....	v
Conference Presentations .....	vi
<b>Chapter 1: Introduction.....</b>	<b>1</b>
Section 1.1: References .....	8
<b>Chapter 2: Background .....</b>	<b>11</b>
Section 2.1: Introduction.....	11
Section 2.2: The photovoltaic effect: generating current from solar photons .....	12
Section 2.3: Conjugated polymers .....	13
Section 2.4: Organic photovoltaics .....	22
Section 2.5: Morphology characterisation .....	31
Section 2.6: Scanning electron microscope.....	45
Section 2.7: Secondary electron spectroscopy in the SEM .....	65
Section 2.8: Conclusions .....	73
Section 2.9: References .....	74
<b>Chapter 3: Methods .....</b>	<b>84</b>
Section 3.1: Sample preparation.....	84
Section 3.2: SE Spectroscopy.....	86
Section 3.3: High-resolution energy-filtered SEM imaging .....	88
Section 3.4: Backscattered electron imaging .....	89
Section 3.5: Helium ion microscopy of cross-sections .....	90
Section 3.6: Image processing and analysis .....	90
Section 3.7: UV-Visible absorption spectroscopy .....	94
Section 3.8: References .....	94
<b>Chapter 4: Secondary electron spectroscopy of P3HT in SEM conditions.....</b>	<b>96</b>
Section 4.1: Introduction.....	96
Section 4.2: Calibration of FEI Sirion through-lens detector.....	98
Section 4.3: SE spectroscopy of P3HT, results.....	103
Section 4.4: Energy-filtered imaging of ‘fresh’ and air-exposed P3HT films, results .....	113
Section 4.5: Discussion of P3HT spectra and energy-filtered imaging.....	116

Section 4.6: SE Spectrum of PCBM .....	126
Section 4.7: Comparison with modelled SE spectrum, determination of detector effects ....	128
Section 4.8: Conclusions .....	137
Section 4.9: References .....	139
<b>Chapter 5: Published paper: Sub-nanometre resolution imaging of polymer:fullerene photovoltaic blends using energy-filtered scanning electron microscopy .....</b>	<b>143</b>
Section 5.1: Introduction .....	144
Section 5.2: Results .....	147
Section 5.3: Discussion .....	158
Section 5.4: Methods .....	160
Section 5.5: Supplementary Information .....	164
Section 5.6: Supplementary Notes .....	170
Section 5.7: References .....	173
<b>Chapter 6: Published paper: Novel organic photovoltaic polymer blends: A rapid, 3-dimensional morphology analysis using backscattered electron imaging in the scanning electron microscope.....</b>	<b>178</b>
Section 6.1: Introduction .....	181
Section 6.2: Experimental Methods .....	186
Section 6.3: Results .....	189
Section 6.4: Discussion .....	198
Section 6.5: Conclusion .....	205
Section 6.6: Supporting Information .....	207
Section 6.7: References .....	214
<b>Chapter 7: Conclusions.....</b>	<b>218</b>
Section 7.1: Future work .....	225
Section 7.2: References .....	228

## Chapter 1: Introduction

Photovoltaics, which convert light energy from the sun directly into an electrical current, are an increasingly important factor in the global energy landscape[1]. Mounting concerns over the ever more imminent threat of anthropogenic global warming have forced the international community to work towards ending its reliance on the burning of fossil fuels for energy[2], [3]. Perhaps the most obvious source of alternative energy is the sun, given the abundance of solar energy on earth [4]. Further, the low land-use of solar energy makes photovoltaic technology an attractive proposition in comparison to other renewable sources ( $\sim 10 \text{ m}^2 \text{ MWh}^{-1} \text{ yr}^{-1}$  compared to  $\sim 80$  and  $\sim 120 \text{ m}^2 \text{ MWh}^{-1} \text{ yr}^{-1}$  for wind and hydroelectric power, respectively) [5]. A range of technologies has been developed to harvest solar energy for electricity, with silicon solar cells by far the most dominant at present[1]. A number of competing technologies are under development at present however, with one of the most promising using semiconducting polymer to harvest light – a field of research known as organic photovoltaics (OPV)[6]–[8].

Generally consisting of a polymeric active layer sandwiched between contact layers (Section 2.4), organic solar cells have a number of important benefits that make them an attractive proposition for solar power generation [4], [6], [9]. The active layers can be processed rapidly and efficiently on a large scale, with minimal waste and energy input in comparison to conventional inorganic photovoltaic cells[9], [10]. Furthermore, the basic components are non-toxic and relatively abundant, reducing environmental concerns surrounding potential large-scale manufacturing of OPV devices[1]. Consisting of device structures that rarely exceed a few microns in thickness, organic solar cells are lightweight and mechanically flexible, allowing for a large array of potential applications, ranging from grid-level implementation[9] to building-integrated solutions[11], [12].

The earliest polymer solar cells were some of the first organic semiconductor devices ever built[13], however developing a commercially-viable OPV device has to date proven extremely challenging. The main barriers to commercial uptake revolve around 2 key issues. Firstly, the efficiency with which solar energy is converted to electrical power (power conversion efficiency;

PCE) is comparatively low for OPV devices in comparison to even the most basic silicon-based devices. The highest published efficiencies for small lab-based organic solar cells in recent years have consistently reached around ~10% [14], [15], but have struggled to improve far beyond this point. The performance of real-world devices is generally significantly worse[4], while in contrast, commercial silicon-based solar cells frequently reach PCEs of up to 20% [1], [4]. Whilst this uncompetitive efficiency is somewhat offset by low production costs[1], [9] it is often felt that greater efficiency in real-world devices is required[1], [16]. Secondly, the useful operating lifetimes of OPV are limited by numerous degradation pathways; most notably the active layers readily reacting with water or oxygen[17], [18]. Whilst lifetimes have improved considerably in recent years, even well-encapsulated modern OPV devices tend to show a performance degradation of at least 20% after 2 years of operation[16], [18].

It should be noted that despite these difficulties, intensive research in to the improvement of OPV materials and processes continues apace. Small spin-out companies, such as InfinityPV (Denmark) or Heliatek (Germany) already sell small commercial OPV systems, although at present their market share is negligible in comparison to established technologies. The development of promising large-scale manufacturing techniques, such as roll-to-roll printing[19] or spray-casting[20] have strengthened a general optimism that the underlying issues restraining the progress of OPV can be overcome. New development pathways are consistently being explored in an effort to push OPV towards mainstream adoption.

The PCE of a given OPV active layer in particular is greatly reliant on the nanoscale material properties of the system[21]. In the case of the most common OPV design variant, a semiconducting conjugated polymer is blended with an electron acceptor material (usually a fullerene derivative) to aid charge extraction[22]. The ‘bulk-heterojunction’ blend film demonstrates nanoscale phase separation, where the 3-dimensional size, shape, distribution, interconnectivity, nanostructure and purity of the material phases must be optimised in order to generate maximum efficiency[23]. These properties are altered by using different methods to process the OPV device, however the optimal processing parameters differ somewhat between

material systems. The processes involved in the formation of OPV active layers are however highly complex, and as such rational design of OPV active layers with the required properties is extremely difficult[23]. Most advances made in the realm of device processing therefore tend to be made as a result of systematic testing and optimisation of a vast range of processing parameters. These include but not limited to the choice of acceptor material, solvent and solution concentrations, blend ratios, film thicknesses and casting technique, as well as post-processing methods such as thermal or solvent annealing (which present their own process optimisation challenges). It has been suggested [23] that due to this complexity, a general lack of understanding surrounding OPV morphology and the range of processing factors that can influence it has resulted in a major process optimisation bottleneck hindering the development of new OPV solutions. To overcome this bottleneck, better information on OPV morphology from advanced characterisation methods is required [24].

Obtaining a full, detailed material characterisation of an OPV polymer blend system in 3 dimensions is challenging[21], [24]–[26]. Spatial resolution of the order of nanometres is a minimum requirement, and the similar organic nature of the blend components means that it is often difficult to distinguish one component from the other using a range of conventional techniques[25]. Furthermore, polymer films tend to be fragile and extremely susceptible to radiation damage, especially when subject to the high localised doses necessary to probe at the required spatial resolution[25]. In attempts to tackle these issues, a vast array of techniques has been employed to study the morphology of OPV blend films. No one technique is sufficiently successful at this task to be considered dominant however.

An overview of the currently available characterisation methods for OPV morphology is given in Section 2.5 of this thesis. Importantly, many of the more advanced techniques require specialist skills or equipment that have limited availability to the average OPV research group. Some, such as neutron or x-ray scattering from synchrotron light sources, often require researchers to obtain access to large national facilities such as the UK's ISIS or Diamond light sources (Section 2.5.2). Furthermore, the techniques offering the most detailed analysis are often slow; with single

samples sometimes taking hours to process and analyse (especially true of some imaging methods such as transmission electron microscopy).

Naturally, the optimum morphology for a given blend system can only truly be proven by real-world solar cell performance, however whole multi-layered devices including evaporated metal electrodes must be made rather than simply studying the single layer of interest. This makes a complete optimisation of process parameters and techniques based solely on the parameters giving the solar cell with best PCE a slow, arduous process. However, the available morphology characterisation techniques are frequently inadequate to provide an effective alternative. As such, it has been suggested that the most popular and best-performing OPV material systems known today are simply those whereby process parameters giving good results were found quickly by chance[23]. Many ‘discarded champion’ materials have offered great promise but have never had their potential unlocked by optimised processing, simply due to the time investment required to complete a full morphology optimisation.

It is clear therefore that in order to inform a more focussed, efficient, and ultimately successful process optimisation procedure for new OPV material systems, better and faster morphology characterisation techniques are needed. Offering competitive spatial resolution and rapid data acquisition, and requiring little sample preparation, the scanning electron microscope (SEM) appears a promising alternative. The SEM has been used in many OPV studies to date, however its use has been limited to imaging the layered structures of OPV devices in cross-section and larger-scale morphology features. With conventional SEM imaging (using secondary electrons, SE – Section 2.6), image contrast is primarily a result of sample topography[27], although material variations can result in image features[28]. In the case of an OPV active layer, however, the material differences between the blend components, both organic materials of similar density, are not sufficient to generate adequate contrast for high-resolution SE imaging. Backscattered electron (BSE) imaging techniques in the SEM produce images containing stronger material contrast, but standard BSE imaging methods lack the imaging resolution (both depthwise and

lateral) to effectively probe OPV blend morphology[29]. As such, attempts to image nanoscale OPV blend morphology using conventional SEM techniques have often been unsuccessful.

However, recent developments in SEM technology have the potential to resolve these issues. Most obviously, significant steps have been made towards improving the resolution available from state-of-the-art SEM tools. These have made sub-nanometre resolution attainable on high-end instruments, with even atomic-level resolution imaging using secondary electrons demonstrated in some extreme cases[30]. As a result, the imaging power of the SEM is now considered by many to be competitive with the TEM[31]. In addition, recent years have seen a gradual revival of secondary electron energy spectroscopy techniques in the SEM. The conventional SEM does not consider the energies of the SEs it detects; only the total SE count (integrated over all SE energies) is used to build an image. Numerous works have however shown that the energy spectrum of a sample's SE emissions can reflect material properties, or act as 'fingerprints' for a given material[32]. Imaging using only SE falling within a selected energy window (energy-filtered SEM) can exploit the unique SE energy spectra emitted by different materials to give high-resolution maps of material variation. The concept of studying the energy of the SEs emitted from the sample dates back to the very earliest days of the SEM itself[33], however only in recent years has the concept of performing SE spectroscopy and energy-filtered SEM imaging been combined with the imaging resolution offered by modern SEM equipment[34]. Finally, the introduction of solid-state backscattered electron detectors, in conjunction with beam-decelerated imaging modes, have resulted in the availability of low-energy backscattered electron imaging techniques[35], [36]. By reducing the energy of the primary electron beam incident on the sample, the imaging resolution (both depthwise and lateral) is improved dramatically. Three-dimensional material variation in thin samples (such as OPV active layers) can thus be probed much more effectively with BSE than was previously possible.

The combination of high-resolution imaging with material-specific contrast in the SEM is an excellent proposition as a tool for mapping OPV active layer morphology. The sample throughput of the SEM is very high in comparison to competing methods[25], and high-quality SEM

equipment is widely available at many research facilities worldwide. Empowering researchers in the field of OPV with high quality, easily- and rapidly-accessible morphology data should help boost the rate of uptake for new OPV materials by helping researchers to efficiently identify processing methods that result in promising morphologies.

Whilst promising, these advanced SEM-based techniques are all in their relative infancy. None have been applied to analyse the morphology of an OPV blend film. SE spectroscopy and energy-filtered SE imaging in the SEM have only been demonstrated previously on inorganic samples. Furthermore, the models that currently explain the nature of SE energy spectra and the relationship with material properties are rudimentary at best. The complex nature of OPV materials results in SE spectra that are harder to understand and employ. Furthermore, as previously mentioned, polymer samples damage easily when exposed to electron beam irradiation, which generates a degree of uncertainty in the results obtained. In the case of low-energy backscattered electron imaging whilst using beam deceleration techniques, numerous theoretical considerations must be made to ensure the images generated are unambiguous backscattered electron images.

The goal of this PhD project is to address and overcome these challenges, and in doing so help to introduce, develop and demonstrate advanced techniques in the SEM for OPV blend morphology analysis. Specifically, this thesis aims to explore the potential of three new SEM-based methods for OPV characterisation: SE spectroscopy, energy-filtered SEM and low-energy backscattered electron imaging. These methods are developed to enable the high quality characterisation of OPV blend morphology in a significantly faster, more accessible manner than is currently possible.

In this work, SE spectroscopy and energy-filtered SEM are extensively tested on OPV materials, and the potential new insights available, as well as limits of their applicability in this context are explored. The capabilities of energy-filtered SEM for imaging OPV morphology are then demonstrated on P3HT:PCBM OPV blends. Finally, low-voltage backscattered electron imaging is used to probe the morphology of both P3HT:PCBM and the state-of-the-art PffBT4T-2OD:PC70BM blend. It is hoped that this work will help to introduce a range of useful

morphology analysis tools to the wider OPV research community. It should not be ignored however that whilst this project is primarily focussed on OPV materials, the challenge of mapping material variation at the nanoscale is a common one. Researchers in many fields are increasingly probing the nanostructure of materials and attempting to link these to macroscale behaviour. It is highly likely therefore that the techniques addressed and advanced in this work will be highly applicable to researchers in the wider academic community.

The main body of results contained in this thesis consists of two journal articles as well as one original chapter. The primary focus of Chapters 4 and 5 is to develop and apply the concepts of SE spectroscopy and energy-filtered SE imaging to the characterisation of organic photovoltaic blends and materials. In Chapter 6, low-energy backscattered imaging is developed and presented as an alternative OPV imaging technique that complements the findings in earlier chapters. A statement of contributions is included prior to both journal articles, detailing the extent of my contributions to that article.

In Chapter 4, the SE spectrum of P3HT is explored experimentally, after the SE spectroscopy function of a FEI Sirion SEM is first briefly calibrated and tested on a copper sample. The SE spectrum of P3HT is then tested under a range of conditions, both by altering microscope parameters and by measuring the spectra of samples with different process history. Energy-filtered SE images of pure P3HT samples are also investigated, with the relationship between contrast in energy-filtered images and localised molecular ordering explored. Finally, the experimentally measured SE spectrum of P3HT is compared with a computer-modelled spectrum. Through this, the impact of the SE detector performance on the shape of the measured spectrum is considered, including the selective filtering of SEs based upon their angle of emission.

In Chapter 5 ('Sub-nanometre resolution imaging of polymer– fullerene photovoltaic blends using energy-filtered scanning electron microscopy'; Nature Communications **6**, 6928, 2015), the SE spectroscopy techniques developed and demonstrated in Chapters 4 and 5 are applied with energy-filtered SEM to map the nanoscale morphology of a P3HT:PCBM blend. Using a state-of-the-art FEI Helios SEM, the technique is demonstrated capable of mapping polymer blend morphology

with unprecedented resolution, and offers a detailed morphology analysis including the first directly imaged identification of mixed-phase regions in a P3HT:PCBM system.

In Chapter 6 ('Novel organic photovoltaic polymer blends: A rapid, 3-dimensional morphology analysis using backscattered electron imaging in the scanning electron microscope'; *Solar Energy Materials and Solar Cells* **160**, pp. 182-192, 2017), a different approach polymer:fullerene morphology imaging in the SEM, completely independent of SE spectroscopy, is presented. Unlike the SE-based methods in Chapters 4 and 5, blend morphology is probed in three dimensions as well as two using BSE imaging. This requires the development and application of novel low-voltage BSE imaging techniques. By careful optimisation of the imaging parameters, BSE images enable identification of 'stacked' or 'columnar' phases that penetrate a large fraction of the film thickness. As such phases are ideal for optimal device performance, this BSE technique is demonstrated to be a highly useful tool for rapid polymer:fullerene morphology analysis. The technique is used to probe the highly optimised PffBT4T-2OD:PC70BM blend and the morphological origin of its impressive photovoltaic performance.

In Chapter 7, the principal findings of this thesis are summarised, and the results placed in context with the overall goals of this PhD project. A brief insight is offered in to work ongoing as an extension to these results, and some suggestions for future work to build upon this thesis are given.

## Section 1.1: References

- [1] A. Polman, M. Knight, E. C. Garnett, B. Ehrler, and W. C. Sinke, "Photovoltaic materials: Present efficiencies and future challenges," *Science* (80-. ), vol. 352, no. 6283, p. aad4424-aad4424, Apr. 2016.
- [2] United Nations/Framework Convention on Climate Change, "Paris Agreement," p. 3, 2015.
- [3] IPCC, "Climate Change 2014 Synthesis Report Summary Chapter for Policymakers," p. 31, 2014.
- [4] S. B. Darling and F. You, "The case for organic photovoltaics," *RSC Adv.*, vol. 3, no. 39, pp. 17633–17648, 2013.
- [5] National Academy of Sciences, *Electricity from Renewable Resources*. Washington, D.C.: National Academies Press, 2010.

- [6] B. Kippelen, J.-L. Brédas, and J.-L. Br Edas, “Organic photovoltaics,” *Energy Environ. Sci.*, vol. 2, no. 3, p. 251, 2009.
- [7] L. Dou *et al.*, “25th anniversary article: A decade of organic/polymeric photovoltaic research,” *Adv. Mater.*, vol. 25, no. 46, pp. 6642–6671, 2013.
- [8] J. Halls and R. H. Friend, “Organic photovoltaic devices,” in *Clean electricity from photovoltaics*, M. D. Archer and R. Hill, Eds. 2001, pp. 377–445.
- [9] F. C. Krebs, N. Espinosa, M. Hösel, R. R. Søndergaard, and M. Jørgensen, “25th Anniversary Article: Rise to Power - OPV-Based Solar Parks,” *Adv. Mater.*, vol. 26, no. 1, pp. 29–39, Jan. 2014.
- [10] R. Søndergaard, M. Hösel, D. Angmo, T. T. Larsen-Olsen, and F. C. Krebs, “Roll-to-roll fabrication of polymer solar cells,” *Mater. Today*, vol. 15, no. 1–2, pp. 36–49, Jan. 2012.
- [11] J. Kettle *et al.*, “Three dimensional corrugated organic photovoltaics for building integration; improving the efficiency, oblique angle and diffuse performance of solar cells,” *Energy Environ. Sci.*, vol. 8, no. 11, pp. 3266–3273, 2015.
- [12] K.-S. Chen, J.-F. Salinas, H.-L. Yip, L. Huo, J. Hou, and A. K.-Y. Jen, “Semi-transparent polymer solar cells with 6% PCE, 25% average visible transmittance and a color rendering index close to 100 for power generating window applications,” *Energy Environ. Sci.*, vol. 5, no. 11, p. 9551, 2012.
- [13] G. A. Chamberlain, “Organic solar cells: A review,” *Sol. Cells*, vol. 8, no. 1, pp. 47–83, 1983.
- [14] Y. Liu *et al.*, “Multiple Cases of High-Efficiency Polymer Solar Cells,” *Nat. Commun.*, vol. 5, p. 5923, 2014.
- [15] S. Zhang, L. Ye, W. Zhao, D. Liu, H. Yao, and J. Hou, “Side chain selection for designing highly efficient photovoltaic polymers with 2D-conjugated structure,” *Macromolecules*, vol. 47, no. 14, pp. 4653–4659, 2014.
- [16] Y. Zhang *et al.*, “PCDTBT based solar cells: one year of operation under real-world conditions,” *Sci. Rep.*, vol. 6, p. 21632, 2016.
- [17] A. J. Parnell *et al.*, “Physical mechanisms responsible for the water-induced degradation of PC<sub>61</sub>BM/P3HT photovoltaic thin films,” *J. Polym. Sci. Part B Polym. Phys.*, p. n/a-n/a, 2015.
- [18] S. A. Gevorgyan *et al.*, “Lifetime of organic photovoltaics: Status and predictions,” *Adv. Energy Mater.*, vol. 6, no. 2, pp. 1–17, 2016.
- [19] F. C. Krebs, “Fabrication and processing of polymer solar cells: A review of printing and coating techniques,” *Sol. Energy Mater. Sol. Cells*, vol. 93, no. 4, pp. 394–412, 2009.
- [20] T. Wang *et al.*, “Fabricating High Performance, Donor-Acceptor Copolymer Solar Cells by Spray-Coating in Air,” *Adv. Energy Mater.*, vol. 3, no. 4, pp. 505–512, Apr. 2013.
- [21] W. Chen, M. P. Nikiforov, and S. B. Darling, “Morphology characterization in organic and hybrid solar cells,” *Energy Environ. Sci.*, vol. 5, no. 8, p. 8045, 2012.
- [22] J. Nelson, “Polymer:fullerene bulk heterojunction solar cells,” *Mater. Today*, vol. 14, no. 10, pp. 462–470, Oct. 2011.
- [23] N. E. Jackson, B. M. Savoie, T. J. Marks, L. X. Chen, and M. A. Ratner, “The Next Breakthrough for Organic Photovoltaics?,” *J. Phys. Chem. Lett.*, vol. 6, pp. 77–84, 2015.
- [24] P. G. Nicholson and F. A. Castro, “Organic photovoltaics: principles and techniques for nanometre scale characterization,” *Nanotechnology*, vol. 21, no. 49, p. 492001, Dec. 2010.
- [25] M. Pfannmöller, W. Kowalsky, and R. R. Schröder, “Visualizing physical, electronic, and

- optical properties of organic photovoltaic cells,” *Energy Environ. Sci.*, vol. 6, no. 10, pp. 2871–2891, 2013.
- [26] F. Liu, Y. Gu, X. Shen, S. Ferdous, H.-W. Wang, and T. P. Russell, “Characterization of the morphology of solution-processed bulk heterojunction organic photovoltaics,” *Prog. Polym. Sci.*, vol. 38, no. 12, pp. 1990–2052, Dec. 2013.
- [27] H. Seiler, “Secondary electron emission in the scanning electron microscope,” *J. Appl. Phys.*, vol. 54, no. 11, pp. R1–R18, 1983.
- [28] M. Dapor, B. J. Inkson, C. Rodenburg, and J. M. Rodenburg, “A comprehensive Monte Carlo calculation of dopant contrast in secondary-electron imaging,” *EPL (Europhysics Lett.)*, vol. 82, no. 3, p. 30006, 2008.
- [29] G. Bar, E. Tocha, E. Garcia-Meitin, C. Todd, and J. Blackson, “New Routes to High Resolution and Automated Polymer Morphology Microscopy via Scanning Electron Microscopy,” *Macromol. Symp.*, vol. 282, no. 1, pp. 128–135, Aug. 2009.
- [30] Y. Zhu, H. Inada, K. Nakamura, and J. Wall, “Imaging single atoms using secondary electrons with an aberration-corrected electron microscope,” *Nat. Mater.*, vol. 8, no. 10, pp. 808–812, Oct. 2009.
- [31] D. C. Joy, “Scanning electron microscopy: Second best no more,” *Nat. Mater.*, vol. 8, no. 10, pp. 776–777, Oct. 2009.
- [32] D. C. Joy, M. S. Prasad, and H. M. Meyer, “Experimental secondary electron spectra under SEM conditions,” *J. Microsc.*, vol. 215, no. Pt 1, pp. 77–85, Jul. 2004.
- [33] O. C. Wells and C. G. Bremer, “Voltage measurement in the scanning electron microscope,” *J. Phys. E.*, vol. 1, no. 9, pp. 902–906, Sep. 1968.
- [34] C. Rodenburg, M. A. E. Jepson, E. G. T. Bosch, and M. Dapor, “Energy selective scanning electron microscopy to reduce the effect of contamination layers on scanning electron microscope dopant mapping,” *Ultramicroscopy*, vol. 110, no. 9, pp. 1185–1191, Aug. 2010.
- [35] D. Phifer, L. Tuma, T. Vystavel, P. Wandrol, and R. J. Young, “Improving SEM Imaging Performance Using Beam Deceleration,” *Micros. Today*, vol. 17, no. 4, pp. 40–49, Jun. 2009.
- [36] Q. Wan *et al.*, “Angle selective backscattered electron contrast in the low-voltage scanning electron microscope: Simulation and experiment for polymers,” *Ultramicroscopy*, vol. 171, pp. 126–138, 2016.

## **Chapter 2: Background**

### **Section 2.1: Introduction**

In this chapter, the state of research around the materials and techniques applied in this thesis is considered. As discussed in Chapter 1, photovoltaics are likely to be crucial to the planet's future energy supply, and OPV is a highly promising technology developing in the photovoltaic sector. However, a more complete understanding of OPV blend nanomorphology is required in order to accelerate this technology towards commercial viability, and novel techniques in the SEM have potential to provide this understanding.

In order to adequately describe the context in which the research contained in this thesis takes place, and provide a sound basis on which this research can build, many topics must be considered in this Background chapter. Briefly, this includes the nature of photovoltaics, the materials and methods used to make effective OPV blend films, the present state of OPV blend morphology characterisation, and detailed aspects of SEM operation that enable the novel techniques addressed in this thesis.

In Section 2.2, the basic concept of the photovoltaic effect is described. In Section 2.3, the origin and nature of electronic properties in conjugated polymers is discussed, followed by the considerations required to produce an efficient OPV blend film morphology from these polymers in Section 2.4. In Section 2.5, an overview of the leading, relevant OPV morphology characterisation techniques is given. Section 2.6 addresses the basic operation of the SEM as well as various technical aspects that must be addressed when imaging polymeric samples in the SEM. Finally, in Section 2.7, the background of secondary electron spectroscopy in the SEM, crucial to Chapters 4 and 5 in this thesis, is discussed briefly.

## Section 2.2: The photovoltaic effect: generating current from solar photons

At the simplest level, solar cells require a semiconducting material to harvest light for electricity generation[1]–[3]. Semiconductors demonstrate an electronic band structure consisting of a filled valence band and empty conduction band separated by a band energy gap,  $E_g$ , from ~0.5 to a few eV. An electron can absorb the energy of a photon with energy  $h\nu > E_g$  and be excited across the band gap into the conduction band. Once in the conduction band, an abundance of free neighbouring states in the material means that transport of that electron is permitted, allowing a current to flow. The excitation of an electron from a valence to a conduction band leaves a ‘hole’ in the valence band, and this ‘hole’ state can be conducted like a positive charge carrier through the valence band[3]. An effective solar cell will absorb a large fraction of the solar energy incident on it and efficiently harvest this absorbed energy to generate free electrons and holes. These photogenerated electrons and holes must then be transferred to the external electric circuit with minimal losses.

### Section 2.2.1: Maximising efficiency

The choice of a suitable material or material system for a solar cell is naturally based on a wide range of factors, however one particularly important factor to consider is clearly its power conversion efficiency (PCE) – defined as the ratio of solar power incident on the solar cell to its electrical power output:

$$\text{PCE}(\%) = \frac{P_{\text{Elec}}}{P_{\text{Incident}}} \times 100\% \quad (2.1)$$

Where  $P_{\text{Elec}}$  is the electrical power output by the solar cell, and  $P_{\text{Incident}}$  is the solar photon power incident on the cell. Theoretically, an absolute limit of ~33% can be placed on the PCE available from a single (non-tandem) solar cell as a function of  $E_g$ , known as the Shockley-Queisser (S-Q) limit[4]. This limit stems from a number of intrinsic losses, which are present even in a hypothetical ‘perfect’ solar cell architecture. These relate to the use of a single band-gap semiconductor to absorb a wide-band solar spectrum, and the occurrence of ‘recombination’ events, whereby photogenerated free electrons and holes meet and recombine to emit a photon.

Most solar cell concepts (and organic solar cells in particular) do not demonstrate real-world PCEs that approach the S-Q limit however. For example, the PCE of ‘champion’ OPV devices is around 12% at present, a long distance from the limit derived from applying S-Q principles to OPV systems[5], [6].

It is clear, therefore, that scope for significant improvement in the performance of polymeric solar cells remains. This low PCE is a result of two key issues: 1) Poor efficiency of light harvesting (i.e. the process of generating free electrons and holes from incident photons[7]), and concurrently, 2) Significant losses in the process of extracting these photogenerated charges[8]. Crucially, both the generation and extraction of free charges can be strongly linked to the nanomorphology of a polymer solar cell’s active layer[9] – and as such significant improvements in terms of morphology are required in order to improve the PCE of OPV devices. To explain how this can be improved however, the origin and nature of semiconducting behaviour and charge transport in conjugated polymers must first be understood.

### **Section 2.3: Conjugated polymers**

The most common base material for a polymer solar cell is a conjugated polymer, defined by the presence of ‘conjugated’ segments containing delocalised electron structures. These form as a consequence of the nature of carbon-carbon bonding in some polymer chains[1]. Carbon atoms have the electronic structure  $1s^2, 2s^2, 2p^2$ , having four outer-shell valence electrons available for bonding. When forming a bond with another carbon atom, it is energetically favourable[10] for a 2s electron to be promoted in to a 2p orbital, resulting in the valence electrons occupying 2s, 2p<sub>x</sub>, 2p<sub>y</sub>, and 2p<sub>z</sub> orbitals. Bonds are formed between carbon atoms from linear combinations of these four orbitals in a process known as sp-hybridisation[2], [10]. Different ‘degrees’ of hybridisation in a given polymer molecule determine the conductivity or insulating properties of that polymer. In the case of insulating polymers, sp<sup>3</sup> hybridisation is present, whereby all four valence electrons in each C atom form hybridised orbitals and form strong, localised covalent bonds, defined as  $\sigma$ -bonds. In this arrangement, no delocalised electrons remain to allow for conducting or

semiconducting properties. Conjugated polymers, with conductive properties, demonstrate  $sp^2$  hybridisation in the carbon valence electrons, whereby 3 valence electrons ( $2s$ ,  $2p_x$  and  $2p_y$ ) enter  $sp$ -hybridised orbitals and form 3 strong covalent  $\sigma$ -bonds in the  $xy$  plane. These form the strong ‘backbone’ of the polymer. The remaining  $2p_z$  electron orbits out of the plane of the molecule, and forms weaker, more delocalised  $\pi$ -bonds with neighbouring carbon atoms in the molecule. The combination of a  $\sigma$ - and  $\pi$ -bond between two carbon atoms being the origin of a  $C=C$  double bond. Long-chain carbon molecules in which  $sp^2$  hybridisation is present exhibit alternating carbon-carbon double and single bonds, with this effect most obviously demonstrated by polyacetylene, though benzene is another well-known example (See Figure 2.1). The  $\pi$ -electrons in these systems can in fact be delocalised over many carbon atoms in a  $sp^2$ -hybridised polymer chain, and this delocalisation (known as conjugation) is the fundamental basis for the electronic and optical properties of a semiconducting polymer.

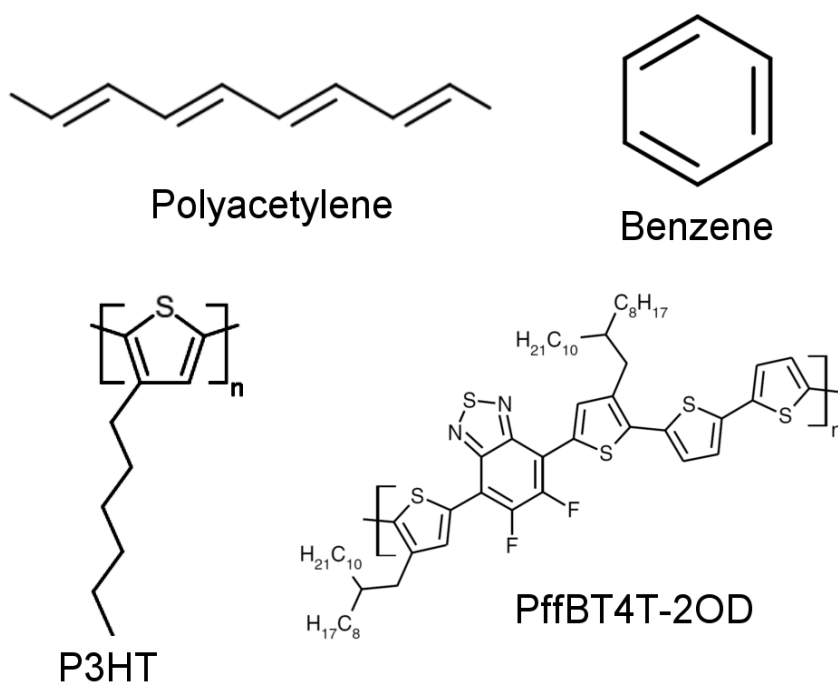


**Figure 2.1:** Structure of a benzene ring and example polymers demonstrating delocalised electronic properties. PffBT4T-2OD schematic adapted from [11] on a CC BY 4.0 license.

The band structure of a semiconducting polymer can be described in analogy with a conventional inorganic semiconductor, however the origin of this structure results from a consideration of the possible arrangements for electrons occupying  $\pi$ -orbitals[1]. When in the ground state, the  $\pi$ -

bonding electrons occupy the highest-occupied molecular orbital (HOMO), which is analogous to the top of the valence band in an inorganic, crystalline semiconductor. The next available electron orbital is a  $\pi^*$ -antibonding orbital, with an energy gap between it and the HOMO[3]. This  $\pi^*$ -orbital is defined as the lowest unoccupied molecular orbital, or LUMO, which acts analogously to the bottom of the conduction band in an inorganic semiconductor. With longer conjugated chains in a polymer molecule, the number of possible arrangements for  $\pi$ -electrons in the molecule increases, with the result in longer polymer molecules being that many  $\pi$ - and  $\pi^*$  molecular bonding orbitals of similar energy are present[1]. With a long enough polymer chain, the large number of similar energy levels available for  $\pi$ -electrons forms a band structure, in analogy to the tight-binding model of band theory for inorganic semiconductors. The energy gap between the HOMO and LUMO level is explained as a result of the Peierls instability[1]. Conjugated regions, as defined by  $sp^2$ -hybridisation, consist of alternating C-C single and C=C double bonds. These have different bond lengths associated with them. The movement of a  $\pi$ -electron from one carbon atom to another along the polymer chain has the effect of converting C-C bonds to C=C and *vice versa*. As the different bond types have different lengths, the movement of electrons along a conjugated polymer segment therefore results in a distortion of the molecular structure, which has an associated energy cost. This energy cost of swapping a C-C bond for C=C, or *vice versa* is the band gap of the semiconducting polymer. A detailed treatment of this effect is given by the classic Su-Schrieffer-Heeger work[12], which describes a semiconducting band structure arising from the energy considerations of electron transport in a polymer chain where the movement of an electron is coupled with a related lattice distortion. This band gap plays an important role in the nature of SE emissions from a polymer sample, addressed in Section 2.7.1.

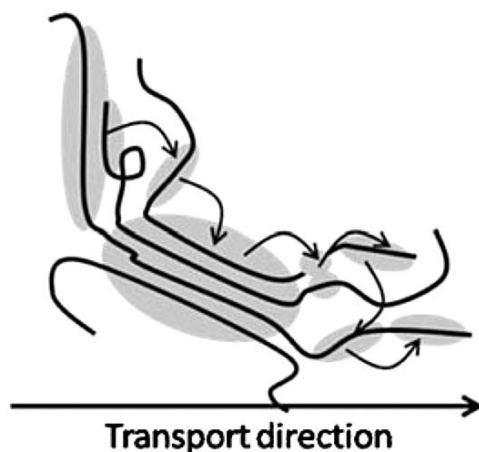


**Figure 2.2:** Schematic of electron transport in a bulk conjugated polymer. Electrons travel along polymer chains with ‘band-type’ transport, with the majority of transport occurring within ordered regions of the polymer (shaded grey). Electrons ‘hop’ between neighbouring chains or even non-continuous regions of the same chain, as depicted by arrows. Reproduced in part from [13] with permission from The Royal Society of Chemistry.

Whilst this band-type transport along a polymer chain is the fundamental origin of charge conduction in a conjugated polymer, it is limited by its localisation to a single conjugated segment. Effective conjugation can be broken by defects or kinks within the chain, and of course the finite length of a single polymer molecule. Bulk charge conduction is therefore highly reliant on ‘hopping’ transport between monomers (see Figure 2.2), whereby free charges move from one conjugated polymer segment to an available state in another by way of quantum-mechanical tunnelling. Hopping transport can occur between different segments of the same polymer, or between different polymer chains when two chains are close enough to one another. However, the probability of these tunnelling events limits the efficiency of charge hopping, dependent on the both the distance between two polymer sites, and the energy difference between an electron’s original and new state[1], [3]. Charge mobilities through a bulk sample are therefore strongly reliant on hopping transport, which can be improved by optimising the morphology of the polymer film. This is addressed in detail in Section 2.3.2.

### **Section 2.3.1: Typical organic photovoltaic materials**

**1) Poly(3-hexylthiophene):** More commonly known as P3HT, this undoubtedly the most studied polymer in an OPV context[14], although in the context of solar cell applications its performance

(offering PCEs of 4-5%[15]) has long since been surpassed by newer polymer designs[1]. Its relative stability and tendency to form polymer crystallites that demonstrate good electronic properties has historically made it a popular choice for a vast range of studies in to the inner workings of OPV devices [14]. Typically, it forms semicrystalline films (containing both crystalline and amorphous regions[16]), although the extent of crystallinity is influenced by processing and the nature of polymerisation (Sections 2.3.2). The base monomer (Figure 2.1) is simple in comparison to current state-of-the-art polymer designs, consisting of a thiophene ring structure that generates delocalised electronic properties, with a hexyl chain attached to offer a greater degree of solubility.

In this thesis, P3HT-based films are used for two purposes. Firstly, the huge body of literature regarding the morphology of P3HT-based OPV devices makes them excellent reference samples, for verifying the morphology characterisations obtained with new techniques (Chapters 5 and 6)[17], [18]. Secondly, for the development of new materials characterisation techniques in the SEM, testing for variation in the crystallinity of P3HT is an ideal challenge for testing and demonstrating the effectiveness of these techniques (Chapter 4).

**2) PffBT4T-2OD:** Developed recently[19] as a state-of-the-art, high-efficiency polymer for OPV applications, PffBT4T-2OD has demonstrated impressive PCEs of around 11% when used in organic solar cells. The monomer is clearly far more complex than P3HT (Figure 2.1), containing numerous ‘ring’ structures that offer large-scale electron conjugation, and alkyl side-chains that have been optimised in length to enable controlled crystallisation of the polymer in OPV films[19]. PffBT4T-2OD demonstrates high levels of crystallinity in general, which further boosts its electronic characteristics (see next Section).

However, as a newly-developed polymer, few attempts at understanding the nature and behaviour of PffBT4T-2OD in OPV applications have been made[19], [20]. Particularly, only rudimentary efforts have been made to image the morphology of OPV films that use this polymer[20]. Therefore, in this thesis, particularly Chapter 6, new insights have been gained in to PffBT4T-2OD and its related OPV systems using the developed SEM techniques.

### Section 2.3.2: Crystallinity and charge transport through a bulk polymer semiconductor

Conjugated polymers often crystallise easily due to higher stiffness in comparison to saturated polymer molecules, a result of the C=C double bonds present in their structure[1]. As a polymer film is cast from solution, crystalline regions can form as molecules arrange themselves in an energetically favourable configuration. The generally inherent stiffness of a conjugated molecule helps regular molecular packing to develop as crystalline regions nucleate out of an amorphous matrix[1]. Highly impressive crystalline formations [21], [22] of P3HT have been observed as a result of this tendency to form crystals, however these tend to result from expensive and highly specialised techniques such as epitaxy. In practical applications, conjugated polymer films are generally semi-crystalline, combining crystalline and amorphous phases in a complex morphology. This is because the speed of polymer diffusion and crystal formation is very slow, and practical film casting techniques are simply too fast to enable high quality or large crystallites to form. Subjecting a film to a heating process (thermal anneal) can help improve crystallisation by raising the temperature of the film above its glass transition temperature and allowing further diffusion and crystallisation of polymer chains, however the extent of this effect is limited as the rate of diffusion remains slow[23].

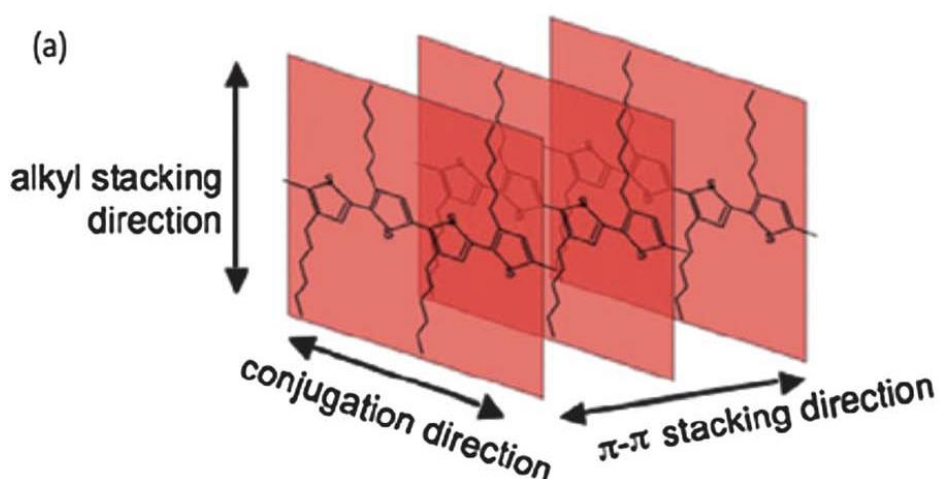


**Figure 2.3:** Crystalline  $\pi$ -stacking in P3HT. Thiophene rings align in the  $\pi$ - $\pi$  stacking direction when crystallites form, increasing the level of electron conjugation in ordered P3HT. Reproduced in part from [24] with permission from The Royal Society of Chemistry.

A higher level of crystalline ordering will contribute to improved charge transport through a polymer film in various ways. Band-type transport along a polymer chain is aided by greater coherency and ordering (reducing the number of conjugation-breaking kinks and chain defects), and the proximity of neighbouring atoms in a crystal greatly improves the efficiency of hopping transport. Some polymers with aromatic groups form crystals that enable ‘ $\pi$ -stacking’, whereby the delocalised electrons in neighbouring polymer chains interact and form stable, ordered stacks of aromatic rings. P3HT is a notable example of this (see Figure 2.3)

It is therefore unsurprising that many conjugated polymers are designed to encourage crystal formation. This is demonstrated with P3HT, where the monomer consists of a thiophene ring with a hexyl chain attached to aid the solubility of the polymer. If 3HT monomers polymerise in a disordered way, the hexyl groups in the resulting polymer can be oriented in different directions and in different planes, hindering crystallisation. So-called regio-random (RRa) P3HT (Figure 2.4a), where the location of the hexyl group in each monomer is randomly assigned, will therefore form amorphous films[1]. However, steps[1] can be taken in the polymer synthesis to ensure that the monomers combine such that the large majority of hexyl chains originate at the same point on the thiophene unit in the resulting polymer. In the case of regio-regular (RR) P3HT (Figure 2.4b), the hexyl groups along the polymer chain take an ordered formation in the same plane, aiding crystallisation. RR-P3HT can be easily processed in to a film with ~50% crystallinity[16].

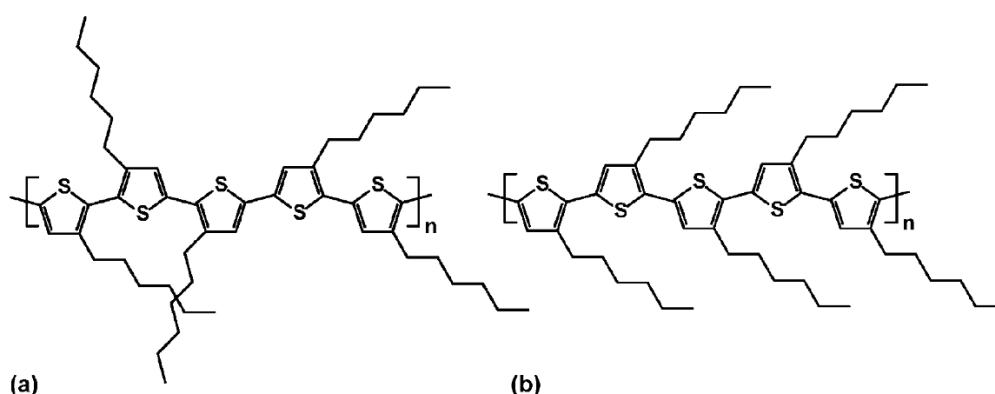


**Figure 2.4:** Comparison of a) regiorandom and b) regioregular P3HT. Disorder in the location and orientation of the hexyl sidechains in a) hinders crystallisation in regiorandom P3HT. Reproduced from [25] with permission from The Royal Society of Chemistry

Even in the case of higher order polymers however, large amorphous phases will remain. Conjugated chains in amorphous domains will of course still conduct charge, however due to poor connectivity with neighbouring polymer chains and a higher likelihood of kinks or chain defects, amorphous phases have poor charge transport properties in comparison to crystalline ones. Amorphous regions demonstrate little direct overlap in electronic structure with crystalline regions as a result[26]. As such, charges must overcome an energy barrier to cross phase boundaries from crystalline to amorphous domains, and it has been demonstrated that the large majority of charge transport in a bulk polymer film occurs only through the crystalline domains[16], [27].

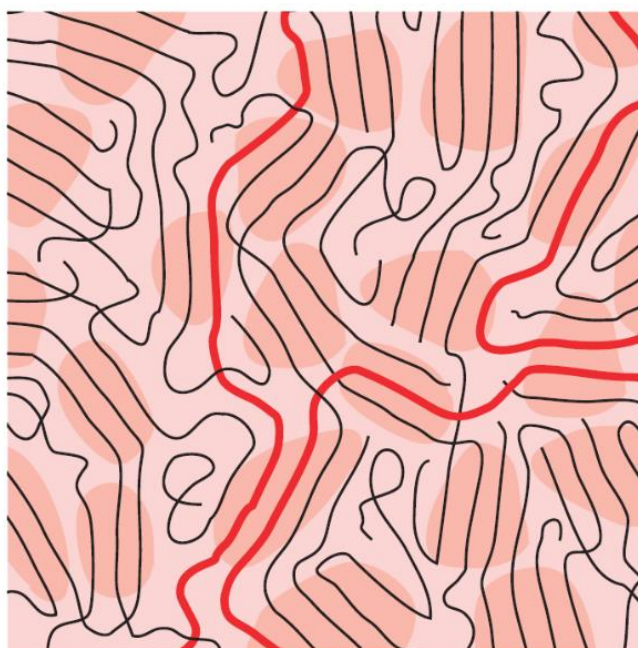


**Figure 2.5:** Polymer chain structure of semicrystalline polymers. The majority of charge transport occurs within ordered regions (darker-shaded areas). Long polymer chains (in red) act as ‘tie chains’ providing electron transport between ordered regions. Adapted by permission from Macmillan Publishers Ltd: Nature Communications [16] Copyright 2013.

However, the complex nature of charge transport through a bulk polymer film means that crystallinity is not the sole defining factor in the electronic performance of a polymer film. The assumption that greater crystallinity results in improved transport was challenged by several recent works that demonstrated improvements in charge mobility resulting from increased polymer molecular weight ( $M_w$ )[28], [29]. These findings were problematic as it has long been known that an increased  $M_w$  inhibits crystalline formation, with longer chains becoming more

entangled and difficult to assemble into crystals. A breakthrough work by Noriega *et al.*[16] provides an explanation for this effect and perhaps the best model to date of the nature of charge transport in a conjugated polymer film. It was demonstrated that although a large  $M_w$  does indeed inhibit the formation of large crystalline phases, the majority of charge transport is limited to the smaller crystalline phases that are formed. The benefit of a large  $M_w$  polymer is that long, conjugated polymer segments are present in the film, and act effectively as ‘wires’, or ‘tie chains’[30], to connect the crystalline regions within the bulk film (see Figure 2.5). In lower  $M_w$  films, a greater number of larger crystalline regions may be formed, however these are separated by regions of poorly-conducting amorphous phases, with individual polymer chains not being long enough to connect the different regions of crystalline material.

The strong link between polymer morphology and charge transport means that tools capable of mapping this morphology in high resolution are paramount to enable a greater understanding of charge transport. For this reason, energy-filtered SEM techniques are developed in Chapter 4 to investigate localised molecular ordering in P3HT.

### ***Section 2.3.3: Electron and hole transport***

It is common for semiconductors to demonstrate unipolar behaviour; that is, to have a significantly higher charge mobility for one type of carrier (i.e. electron or hole). For example, crystalline silicon demonstrates an electron mobility  $\sim 3$  times larger than its hole mobility[31]. Organic semiconductors tend to show pronounced unipolarity [1], with most stable and higher-mobility polymers (including P3HT) being predominantly hole conductors. This is thought to result from the ease with which free electrons can be trapped, especially by highly electronegative oxygen impurities within the polymer[1]. However, this effect (like many of the details of polymer charge transport) is poorly understood, and indeed there are an increasing number of high electron-mobility polymers being engineered[32]. These are thought to enable good electron transport by having a ‘deep-lying’ LUMO (or high electron affinity), whereby electrons are transported with energies greater than the depth of most electron trap states. The semiconducting polymers considered in this work are all unipolar hole conductors.

## **Section 2.4: Organic photovoltaics**

Making an effective solar cell from a semiconducting polymer is unsurprisingly a difficult task, requiring consideration of a vast array of variables in order to make an effective device. A growing understanding of the processes that convert absorbed light into an electric current is making optimal device design easier however[7].

### ***Section 2.4.1: Excitons***

A photon with sufficient energy will be absorbed by an electron in the HOMO of the conjugated polymer, scattering the electron into the LUMO. As previously discussed, in principle, an abundance of available neighbouring states allows an electron in the LUMO to move freely along a conjugated polymer segment. However, in practice the excited electron experiences a Coulombic attraction from the hole it leaves in the LUMO, and forms a bound electron-hole quasi-particle known as an exciton[33]. Similar excitons are formed in all semiconductors, however excitons formed in conjugated polymers are much more tightly bound than in inorganic materials. This is a result of 1) the confinement of the exciton to the polymer chain, meaning electron-hole separation in an organic exciton is never more than a few monomers, and 2) the comparatively low dielectric constant of organic semiconductors, which results in a stronger Coulombic attraction between electron and hole in polymers[9]. As a result, whereas the loosely-bound ‘Mott-Wannier’ excitons in inorganic semiconductors have a binding energy less than  $kT$  and as such spontaneously dissociate at room temperature[9], the closely-bound ‘Frenkel’ excitons formed in conjugated polymers are difficult to separate into free charges[34].

In a polymer, an exciton will decay within a few ns, most commonly by the radiative recombination of the electron and hole[1], [35]. Prior to decay, however, excitons can diffuse through an organic semiconductor, either along conjugated chains or hopping between molecules[36]. Typically, this exciton ‘diffusion length’ is of the order  $\sim 10$  nm[37]–[39] (recent studies suggest that a greater degree of polymer crystallinity will improve exciton mobility however, doubling this value[38]). This is crucial to the operation of PffBT4T-2OD based OPV

films, where crystalline phases enable longer exciton diffusion lengths. This effect is discussed in Chapter 6.

**Section 2.4.2: Generating free charges from an exciton, bulk-heterojunction morphology**

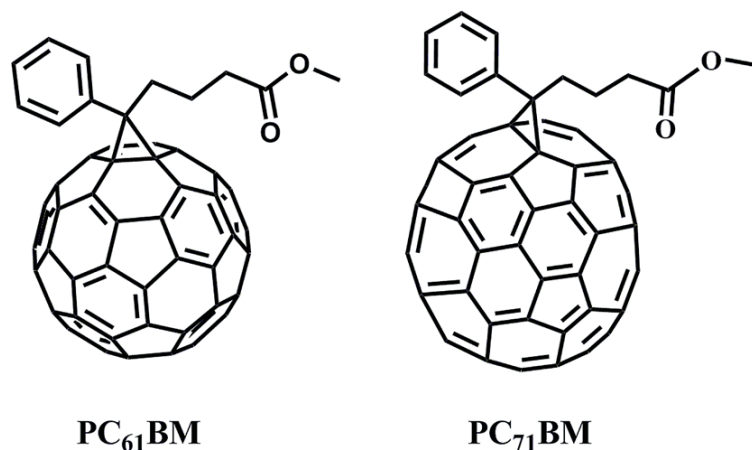


**Figure 2.6:** Chemical structure of PC<sub>60</sub>BM and PC<sub>70</sub>BM fullerene derivatives. Adapted from [15] with permission from Wiley.

To generate a useful current from a polymer solar cell, this exciton must of course be dissociated in to a free electron and hole before it decays. As such, in modern OPV device architectures, the semiconducting polymer is combined with an electron acceptor material (most commonly a fullerene, derivative of the C<sub>60</sub> ‘buckminsterfullerene’ structure or the elongated C<sub>70</sub> structure – Figure 2.6). This material is selected with energy levels offset relative to the polymer, such that a localised electric field is present at the interface between polymer (acting as an electron donor) and acceptor. The dynamics of exciton dissociation are complex and of little relevance to the work in this thesis, however on a simple level, this localised field is strong enough to separate the exciton in to a free electron in the acceptor material, and a free hole in the conjugated polymer (see Figure 2.7)[40]. This use of an electron acceptor material here is also particularly useful due to the generally poor electron mobility of many semiconducting polymers (Section 2.3.3) – in this instance the electron is transferred to a higher electron-mobility material for transport, with free holes remaining in the more ‘hole-friendly’ polymer.

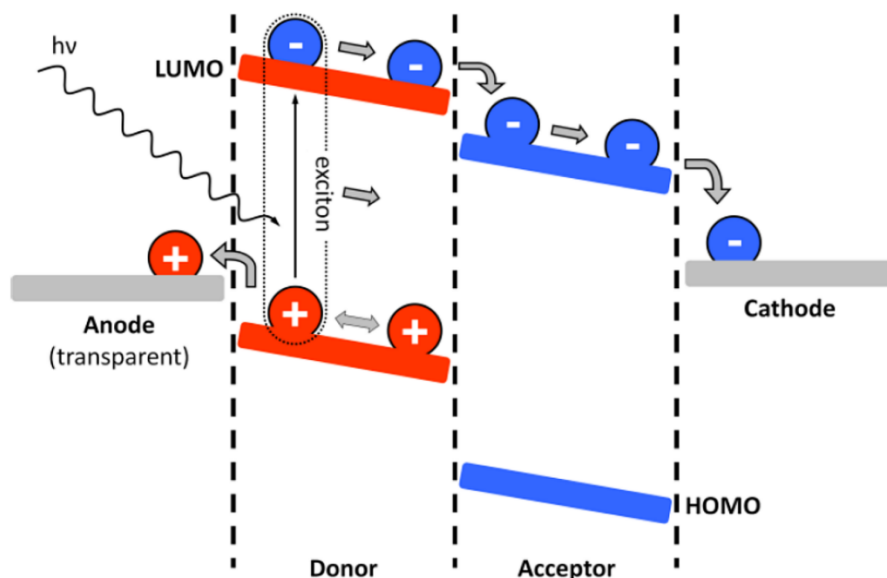


**Figure 2.7:** Schematic of exciton dissociation at a donor-acceptor boundary. An exciton is formed in the donor polymer and diffuses to the boundary with the acceptor, where localised fields due differences in electronic energy level extract the electron in to the acceptor (fullerene) phase. The now free electron and hole can be extracted through the cathode and anode respectively. Reproduced from [41] with permission from The Royal Society of Chemistry.

The simplest donor-acceptor ‘heterojunction’ device structure is the bilayer[42] (see Figure 2.8a), whereby the donor and acceptor are layered on top of each other. Due to the  $\sim 10$  nm exciton diffusion length before decay, only excitons generated within this distance of the donor-acceptor interface are efficiently separated. However, a functioning solar cell in this design remains feasible due to the ultra-thin nature of organic solar cells, made possible by the strong absorbance of semiconducting polymers ( $\sim 90\%$  of light incident on an organic solar cell can be absorbed by a  $\sim 100$  nm thick active layer once reflection off the back metal contact is taken in to account[7]). Nonetheless, even in a  $\sim 100$  nm thick polymer layer, the large majority of photo-generated excitons will clearly be generated further than 10 nm from the interface, resulting in most of the incident solar energy being wasted as the electron and hole decay back to their ground state.

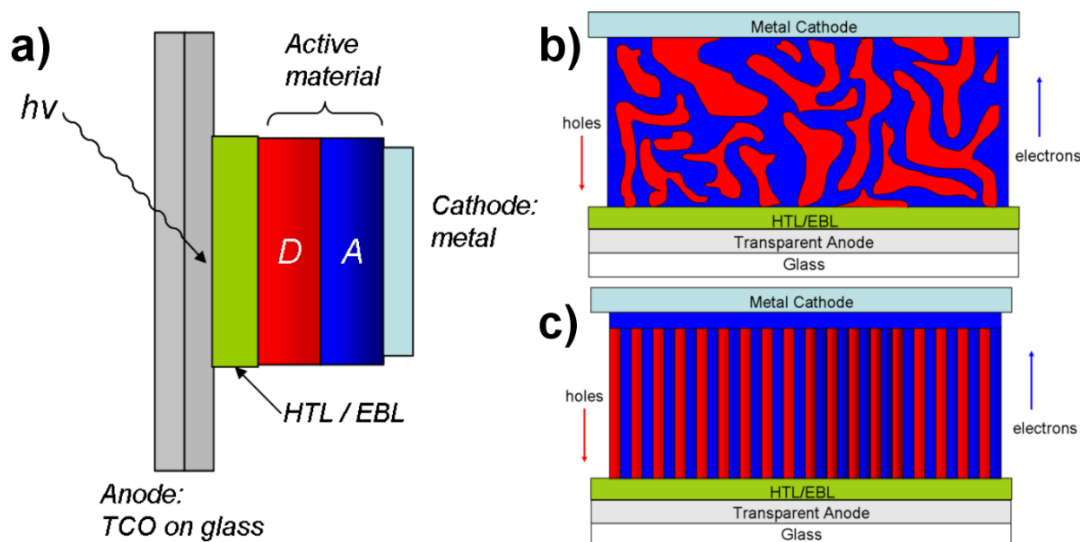


**Figure 2.8:** Evolution of OPV active layer architectures. *a)* depicts a bilayer of donor polymer (D, red) and acceptor fullerene (A, blue) sandwiched between electrodes. A combined hole transport and electron blocking layer (HTL/EBL) improves PCE by reducing contact resistance for hole extraction whilst also reducing the electron leakage current through the anode. *b)* depicts a bulk heterojunction architecture, where donor and acceptor are intimately mixed to aid exciton dissociation. *c)* depicts an idealised ‘columnar’ blend morphology, where intimate lateral mixing of donor and acceptor aids exciton dissociation, but direct pathways to the electrodes within a single phase exist to aid extraction of free charges. A layer of acceptor material ‘caps’ the blend film neighbouring cathode to limit hole leakage to the cathode.

Adapted from [40] under a CC BY 3.0 license.

The bulk-heterojunction solar cell architecture (Figure 2.8b) is a natural progression from the bilayer design, and today is the dominant concept for organic solar cell active layers. Here, the acceptor material is blended with the polymer in solution, and this solution is cast as a single-layer blend film[9]. The polymer and acceptor in an OPV blend are not miscible, that is, spinodal decomposition will occur during the casting of blend film to produce a phase-separated morphology [30], [43], [44]. More recent studies suggest that further phase-separating effects, such as the formation of polymer crystallites and the aggregation of fullerene molecules, as well as the formation of mixed-phase domains, combine to produce a highly-complex, hierarchical blend film morphology with nanometre-scale phases of both blend materials in close proximity to each other[30], [45]. The exact nature of this bulk-heterojunction film is crucial to the performance of the OPV device.

Clearly, the primary benefit of the bulk-heterojunction architecture is that when optimised, phase sizes are of the order of 10 nm, such that a donor-acceptor interface can easily be reached by

excitons produced anywhere in the blend film. As such, the efficiency of exciton dissociation is greatly improved in comparison to a bilayer architecture[9]. Using optimised bulk-heterojunctions, modern organic solar cells often claim close to 100% internal quantum efficiency; that is, every absorbed photon is successfully converted in to an electron-hole pair[39].

The nature and importance of intermixing of polymer and fullerene phases is a question that has been raised and addressed in more recent works. For example, in the popular well-studied P3HT:PCBM OPV blend, it is has been shown that a significant fraction (up to ~30%) of the supposedly ‘phase-separated’ morphology in fact consists of mixed phase[17], [46], with PCBM nucleated in regions of amorphous P3HT. The role of these regions in the generation of a photocurrent is a matter of some debate, although it has been postulated [30], [47] to have important (although not entirely quantified) effects. It should however be noted that some state-of-the-art OPV material systems, most notably the PffBT4T-2OD:PC70BM blend addressed in Chapter 6 of this thesis, have been designed to minimise intermixing of the blend components as a result of highly-crystalline blend phases[19]. This mixed-phase should therefore not be considered crucial to OPV morphology design for all materials systems. The key differences between the P3HT:PCBM and PffBT4T-2OD:PCBM morphologies are described in Chapter 6.

### ***Section 2.4.3: Extracting free charges from a bulk-heterojunction***

Once the dissociation of an exciton is completed in a bulk-heterojunction blend morphology, a free electron is present in the acceptor phase and a free hole in the donor phase. These charges must be successfully extracted from the blend film to generate useful current from an organic solar cell device. Again here, the nature of the film morphology is crucial.

Most importantly, once electrons or holes have been separated in to their respective phases (holes in the donor phase, electrons in the acceptor phase), there exists an energy barrier to injection in to the other material phase. This is inherent to the donor-acceptor design; the energy level offset between the two blend components exists to create localised fields that encourage exciton dissociation. These same localised electric fields at the donor-acceptor interface result in an energy barrier that inhibits the injection of holes in to the acceptor phase, or electrons in to the

donor phase. As such, once a carrier is generated at the donor-acceptor interface, a continuous pathway to the electrodes should exist within its native phase. Otherwise, the presence of isolated phases that do not offer such a continuous pathway can result in the trapping of carriers at the phase boundary of the isolated phase, as carriers cannot easily cross this boundary. An often-cited ‘ideal’ OPV blend morphology is a ‘columnar’ morphology (Figure 2.8c), where intimate lateral phase separation enables efficient exciton dissociation, but a direct unobstructed pathway exists to facilitate the extraction of free charges once generated. In Chapter 6, an imaging method is developed that is devoted to assessing the extent and properties of potential charge-extraction pathways in a blend film.

The nature of this inter-phase morphology is crucial to solar cell performance, however two further considerations are also relevant[7], [48]. Firstly, the fine, percolated ideal morphology of an active layer blend ‘sandwiched’ between two electrodes should be ‘capped’ above and below by layers of pure material – such that only the electron-transporting material contacts the cathode and only the hole-transporting material contacts the anode. This prevents the ‘leakage’ of generated charge – i.e. recombination of holes at an electron-rich electrode, or *vice versa*. Further, it should be noted that intra-phase morphology is important – as already noted in Section 2.3.2, better ordering in conjugated polymers can give improved charge transport. Better mobility results in improved collection of current, and thus better current generation efficiency. For these aspects of morphology to be assessed by imaging techniques, effective methods for accessing the cross-sectional morphology of the film are required. One novel technique in the Helium ion microscope for this purpose is proposed in Chapter 7.

#### Section 2.4.4: Morphology formation and optimisation

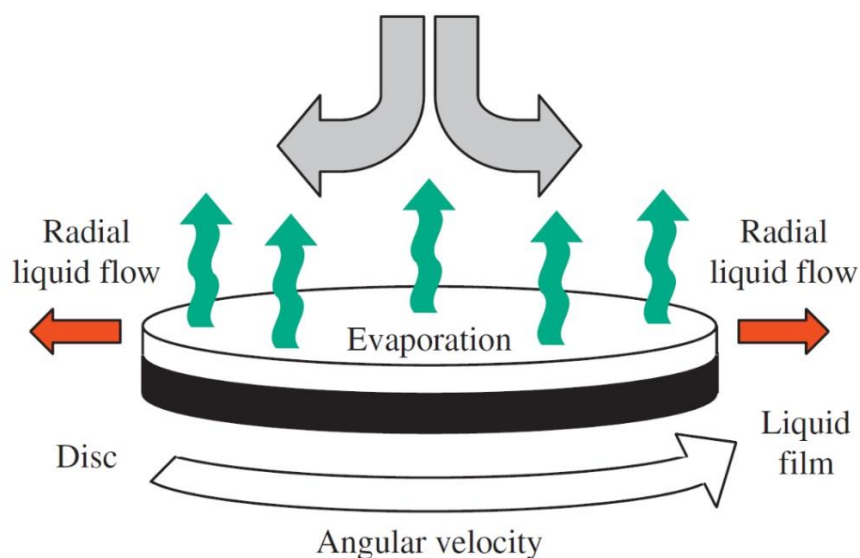


**Figure 2.9:** Schematic of spin-coating process. Reproduced from [49] with permission from Elsevier.

Despite the obvious benefits afforded by a properly optimised bulk-heterojunction morphology, it is a major challenge to obtain this morphology type for a given polymer-acceptor blend[50]. The morphology of a blend film forms in a complex, multi-step procedure, the specifics of which depend on the method of casting a polymer film from solution. A wide range of casting methods exist[49], for example: spray-coating a film from solution; ink-jet or screen printing; drop-casting (dropping a small amount of solution on to a substrate and allowing it to dry); or doctor-blading (passing a sharp blade a fixed distance over a solution-wetted substrate). Many more techniques exist with their own strengths and weaknesses, however for the work in this thesis only spin-casting is used (Figure 2.9); this is the most popular casting method for OPV at present. Here, a polymer solution is prepared by dissolving the polymer in a relatively low boiling-point solvent, which should evaporate quickly at room temperature (the exact choice of solvent is an important consideration, as discussed below). A small amount ( $\sim 50 \mu\text{l}$  for a  $3 \text{ cm}^2$  film) of solution is dropped on to a substrate and rotated at speeds of  $\sim 1000\text{-}5000 \text{ rpm}$ [51]. Excess solution slides off the substrate due to the large centrifugal forces, leaving a thin layer of solution wetting the substrate, which gradually dries as the solvent evaporates. As the viscosity of the wet film

increases, the phase-separated morphology of the film forms as a result of polymer crystallisation and fullerene aggregation[52] before being 'locked' in place once enough solvent has evaporated. However, a wide range of variables in this processing step affects the kinetics and specifics of this process, and as such the resulting blend film morphology. Naturally, different variables influence the morphology and properties of the film in different ways and to varying extents. Some example processing variables (those most relevant to the work in this thesis) follow, with a brief discussion of their effect on the resulting film morphology:

**1) Choice of solvent:** Modern polymers for organic photovoltaics are designed with easy processing in mind; a good level of solubility is therefore important. Halogenated solvents are a popular choice as they offer a high level of solubility for most conjugated polymers[53]. However, many possible halogenated solvents exist, offering different properties. For example, in the case of the popular conjugated polymer P3HT, and its common OPV blend with the fullerene PCBM, it is common to use chloroform (CF) as the main processing solvent. CF has a relatively low boiling point, and as such dries quickly during spin-casting. As a result, P3HT or P3HT:PCBM films spin-cast from CF have less time to form P3HT crystallites or PCBM aggregates, producing a morphology that is more amorphous, with smaller P3HT crystallite sizes and poor levels of  $\pi$ -stacking (see Section 2.3.2:)[52], [54]. Poor charge mobilities and smaller phase sizes are therefore observed. Using higher boiling point alternative solvents, such as dichlorobenzene or trichlorobenzene[52], [54], or the addition of high boiling point solvent additives[55] results in a film that dries and forms a phase-separated morphology much more slowly. As a result, phases in the resulting film are larger and more crystalline, offering improved charge mobilities and better PCEs. However, this is simply the specific case for P3HT:PCBM; other polymer-fullerene combinations may give improved performance from faster-drying solvents[56].

**2) Blend ratio:** The exact ratio in which the polymer and fullerene should be blended for optimal performance varies drastically between individual materials. Here the key goal is to use a fullerene concentration that is large enough that the fullerene phases in the blend film connect with each other and form interconnected charge extraction pathways through the film[57]. Naturally

however, if the fullerene concentration is too high, the resulting large fullerene phases will interfere with the interconnectivity of polymer phases, limiting the hole extraction efficiency. The polymer:fullerene ratio giving optimal solar cell morphology has been shown to vary from 1:0.8 (P3HT:PCBM) to 1:4 (PCDTBT:PCBM), and needs to be optimised for each new set of materials.

**3) Thermal anneal:** After the film has dried, an anneal step can be used to further evolve the blend morphology towards a desired state. Solvent annealing, whereby the dried film is exposed to a solvent vapour, is a popular annealing method[58], however in this thesis only thermal annealing is used. Here, the dried, spin-cast film is heated above its glass transition temperature, allowing the polymer and fullerene in the dried film to diffuse and self-organise. As a result, some crystalline aggregation of both the polymer and fullerene phase occurs, as well as diffusion of the fullerene in to amorphous polymer regions. As a result, crystalline regions of polymer and fullerene can increase in size[23], [30], whereas initially amorphous polymer phases become intimately mixed with the fullerene[59], [60]. This step is used if the initial spin-casting process forms films that are poorly optimised for OPV performance[61]. The thermal annealing temperature is an important variable to consider – if too low the anneal is ineffectual in terms of morphology and OPV device performance, and if too high the domain sizes can be too large for efficient photocurrent generation[23]. The optimal annealing temperature for a given material system is highly dependent on the blend ratio of polymer to fullerene in the blend film[23], [61]. A greater fraction of fullerene in the film means that the annealing temperature must be reduced to prevent the aggregation of fullerene phases that are too large for good photovoltaic performance. It should be noted, however, that a thermal anneal does not always improve the photocurrent generation characteristics of a given polymer-fullerene blend. An obvious example is the PCDTBT:PC70BM blend, where a thermal anneal was shown to reduce the PCE of a solar cell[39].

**4) Spin speed:** The speed at which the substrate is rotated when spin-coating a film strongly influences the rate of solvent evaporation, with films spun at faster speeds drying more quickly[62]. The effect of a larger spin speed is therefore similar to that of a higher boiling point

solvent, in that the film dries faster and less time is available for the formation of crystalline order or large phases. It should also be noted that a faster spin speed results in thinner films; a result of the greater centrifugal force forcing a larger amount of solution off from the substrate in the initial phase of the spin-casting process[57].

The above is simply a small cross-section of the processing variables available to researchers when attempting to optimise the morphology of a polymer:fullerene blend for OPV application[57]. Simultaneous optimisation of this range of parameters is required in order to produce an optimised organic solar cell from a given set of materials. This is a formidable challenge, and strategies for the rational selection of processing techniques based on the properties of the blend materials are lacking at present[50]. Furthermore, the complex relationship between blend morphology and solar cell performance is, perhaps unsurprisingly given the complexity of the materials involved, still not completely understood[7]. A significant research effort has therefore been applied to the task of characterising OPV blend morphologies, to understand better the exact defining features of an optimal morphology as well as the processing methods that give rise to desirable features. The development of a high-throughput, accessible and high-resolution morphology characterisation method has been described as a ‘holy grail’ of organic photovoltaics research[63].

## Section 2.5: Morphology characterisation

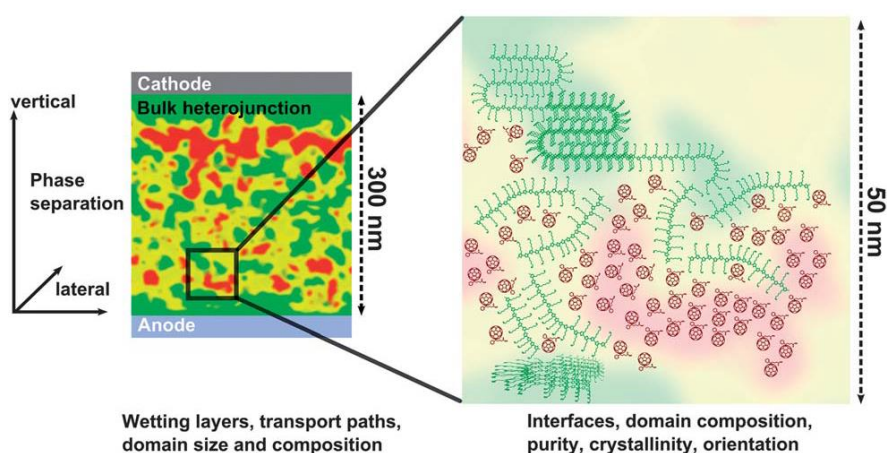


**Figure 2.10:** Schematic depicting challenges of morphology characterisation, with multifaceted information on a range of different length-scales required for a full understanding. Adapted from [64] with permission from The Royal Society of Chemistry.

Accurately characterising the morphology of an OPV blend, like many aspects in the development of a competitive organic solar cell, is a complex problem. The notoriously fragile and easily-damaged nature of polymer materials[64] compound the already challenging task of probing the intricate, nanoscale morphological features inherent to an OPV blend film. Further issues arise due to the chemical similarity between many of the blend components used in OPV active layers – most consist primarily of carbon, oxygen and hydrogen, with only small quantities of additional elements present in some conjugated polymers. The need for material, crystallinity, and phase purity information at high spatial resolution, as well as probing for features such as phase size, shape and percolation on a larger scale through the whole film morphology (Figure 2.10), means that a wide range of complimentary techniques is required at present for a full characterisation [64], [65]. It is unsurprising therefore that a wide range of techniques have been applied in attempts to meet this challenge, with varying degrees of success. These techniques can be divided in to two broad groups: 1) those using real-space ‘imaging’ techniques to visualise the morphological properties of a blend, and 2) those using the scattering pattern of radiation (usually neutrons or x-rays) incident on the film to probe average film properties.

### ***Section 2.5.1: Real-space imaging techniques***

The high spatial resolution required to image nanoscale features mean that simple techniques such as optical microscopy are inadequate for probing OPV morphologies. The most popular and highest-resolution imaging techniques use either high-energy electron beams or scanning probes to map morphological features.

**Scanning probe techniques:** Due to their highly ubiquitous nature and ease-of-use requiring little specialist training, atomic force microscopes (AFMs) are almost certainly the most widely-used tools for probing blend morphology[64], [65]. Here, an ultra-fine tip mounted to a cantilever is passed over the surface of the film. In the case of OPV, this tip can be used to perform a range of different measurements on the topographical and electrical properties of a blend film, using various innovative techniques. By far the most popular technique however is the simplest; that of mapping the surface topography of the film by scanning the tip over the film surface, generally

in ‘tapping mode’, whereby the tip is oscillated at a driven frequency above the surface, periodically contacting it [1]. Topographical images of blend films surfaces are commonly used to demonstrate the effects of different processing steps, for example the use of a thermal anneal, on sample morphology[19], [66] (Figure 2.11). However, sample topography images, whilst arguably a rough approximation of the nature of morphology at the surface[51], cannot be used to probe morphology in any great detail. The origin of topographical features at the surface of a blend film is highly convoluted, and difficult to draw conclusions from regarding the blend morphology[65]. As such, phase-contrast AFM is more commonly used, whereby changes in the oscillation of the tip are used to infer the properties of the surface beneath. Here, when the tip contacts the sample, the localised surface properties of the sample (eg. viscoelasticity, surface adhesion[67]) result in dissipation of the tip’s energy, damping its oscillation out of phase[68]. The phases in a OPV blend result demonstrate different energy dissipation properties (P3HT crystallites demonstrate higher energy dissipation than PCBM phases, for example), and as such an AFM phase map reflects the localised chemical properties of the blend with a resolution of ~10 nm[68]. However, AFM phase data cannot be used for a quantitative analysis of the blend morphology without a detailed understanding of the tip-damping effect of the blend components, which is difficult to obtain for individual material systems[67], [68].

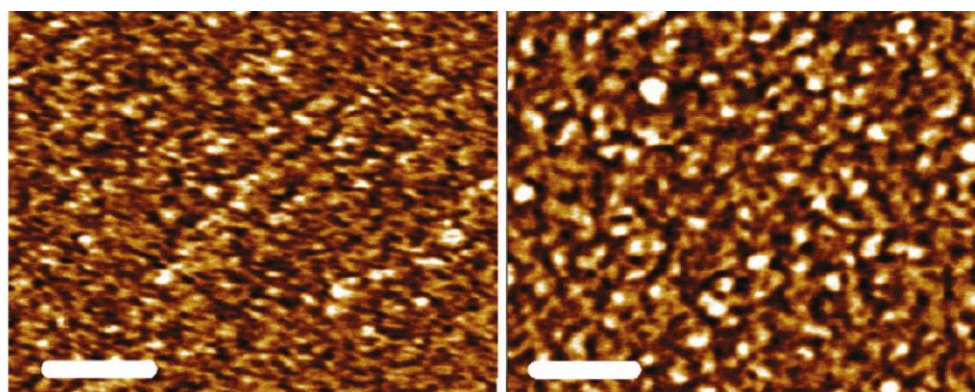


**Figure 2.11:** AFM phase contrast images depicting the topography of the P3HT:PCBM surface. Part a) shows a film annealed at 150°C for 15 minutes, b) shows a film annealed at 190°C for 15 minutes. Scale bars represent 200 nm. Adapted with permission from [69]. Copyright 2011, American Chemical Society.

More detailed morphology information can be obtained by using the AFM tip to perform high-resolution electrical measurements on the blend film, such as mapping localised charge mobility. These studies give a unique and direct insight in to regions of the film morphology that most efficiently generate or transport photocurrent, however their spatial resolution is somewhat lower than competing imaging techniques[64].

The simplest electrical measurements apply conductive AFM (c-AFM). Here, the AFM tip acts as a localised electrode, contacting the blend film surface, whilst a metal electrode acts as the film's substrate. As the tip passes along the surface, a map of localised charge mobility is generated by measuring the (dark, not photogenerated) current flowing through the tip at a constant bias[70]. The technique has been improved upon with localised laser illumination, such that the AFM tip maps only localised photo-generated currents in the sample[71]. These electrical measurements usefully demonstrate the best-performing features of the morphology regarding the most important aspect – the actual photogeneration of charge under illumination. By understanding the morphological features that produce good photogeneration characteristics, a conductivity or charge-generation map can be used to infer the presence of desirable features, such as 'columnar' or highly crystalline phases.

Arguably the most effective scanning probe technique is Kelvin probe force microscopy (KPFM), notable for its impressive imaging resolution of ~2 nm, and material identification capability[68], [72]. Here, the AFM tip is used to map the spatially resolved surface electronic potential of the sample. As different blend components have different surface potentials, the resulting map is analogous to a high-resolution surface morphology image. By comparing KPFM maps taken in the dark and under illumination, the localised carrier generation properties of the blend can also be inferred[68]. KPFM produces results that are undoubtedly powerful and revealing, however it should be noted that the practical applicability of the technique is severely limited by its 7-10 hr/image acquisition time[68], making sample throughput extremely slow.

**Transmission electron microscopy:** Although the equipment and expertise is not as widespread as that for basic scanning probe techniques, the transmission electron microscope (TEM) is

perhaps the most complete, high quality imaging tool for OPV characterisation at present[64]. State-of-the-art methods allow for 3-dimensional mapping of blend morphology at nanometre resolution with strong material identification capabilities. However, suitable and representative electron transparent blend film specimens are first required.

All TEM-based techniques are based upon the same fundamental concept of projecting a high-energy (~100 keV) electron beam through an electron-transparent sample (either a whole blend film, or a pre-prepared cross-section of the film), and forming an image using the transmitted electrons. The simplest technique is bright-field TEM (BF-TEM), whereby an image is collected along the optical axis of the electron beam after being transmitted through the sample[73]. In the brightest regions of a BF-TEM image, the beam has been scattered the least by the sample and in the darkest regions, the beam has been more strongly scattered away from its initial angle of incidence. When imaging an OPV blend film in this way, the different blend components scatter the transmitted electron beam to different extents, generating contrast in the resulting image. This variation in scattering strength is thought to originate from the different densities of polymer and fullerene[74] (for example, depending on crystallinity P3HT has a density of 1.09-1.13 g.cm<sup>3</sup>, compared to 1.5 g.cm<sup>3</sup> for PCBM), however these are often small due to the blend components being predominantly carbon-based [7]. Large, crystalline features such as polymer ‘fibrils’ can therefore be often discerned fairly easily, however distinguishing these from amorphous regions of polymer or fullerene, or even regions of mixed phase is extremely difficult using a BF-TEM image[46]. Defocusing the incident beam can enhance image contrast on certain length scales to produce clearer BF-TEM images[75], however this comes with a cost of reduced resolution, and it is difficult to conclude that any new features observed in a defocused image are indeed a result of morphological features[74].

Interpretation of the contrast a BF-TEM image is challenging. Localised variations in sample thickness can also result in the generation of easily misinterpreted contrast[64], as thicker regions scatter the transmitted beam to a greater extent than thinner ones. Further, as TEM images are formed from electrons that have been transmitted through the whole sample, any contrast

observed at a specific point on the sample is a result of sample properties averaged through the whole sample thickness at that point[74]. This is a significant issue in the case of OPV, as phases sizes and blend features often have length scales significantly smaller than the film thickness. As such, contrast is averaged out and lost when the beam signal projects through different material phases or features, making the unambiguous identification of these features (especially smaller ones) difficult.

These effects can be mitigated by using tomography techniques[76], whereby a series of exposures from the same sample area are taken at different tilt angles (taking exposures at  $4^\circ$  steps in the  $\pm 90^\circ$  tilt range – 45 exposures total – in one recent study[77]), and combined to generate a 3-dimensional reconstruction of the sample volume. Whilst the resulting morphology characterisation is a definite improvement on single TEM exposures, issues with low contrast between blend components remain low and as a result, conventional TEM images are not clear enough to generate a convincing morphology characterisation.

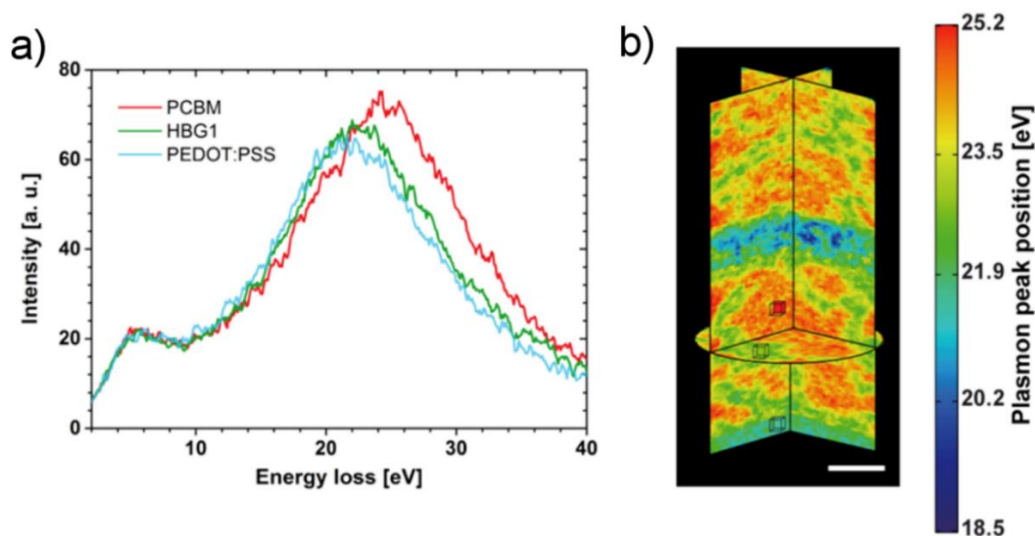


**Figure 2.12:** Analytical TEM applied to an OPV tandem cell consisting of two separate OPV blend systems separated by a ZnO layer. The two blend layers are clearly observed in part b), separated by a blue/green band of ZnO and PEDOT:PSS. The upper blend film is blend is PDPP5T:PC<sub>70</sub>BM, and lower film is HBG1:PC<sub>60</sub>BM. In part a) the EELS spectra of the blend components in the lower film is presented: the dominant feature in these spectra is the peak resulting from plasmon excitation around 22-25 eV, with PCBM having a higher-energy peak than the polymer. The peak energy of the EELS plasmon excitation is the basis for colour contrast in the ‘spectrum image’ of the whole tandem cell in part b), shown in 3-dimensions after applying tomography methods. In this image, PCBM phases are shown in red due to the higher energy plasmon peak, with polymer phases shown in green. Scale bar represents 50 nm. Adapted with permission from [77]. Copyright 2015, American Chemical Society.

More recently, a powerful solution was demonstrated for improving OPV imaging contrast in the TEM, with the development of analytical techniques and application of energy-filtered TEM (EFTEM). Here, the electron energy loss spectrum (EELS) of the electron beam transmitted through the sample is used as a way to confidently differentiate between the blend components[46]. The EELS of the individual blend components is first measured, and demonstrated to be different for each component. A ‘spectrum image’ of the blend morphology is then taken, whereby for each pixel in the image, the EELS spectrum is measured. By analysing the spectrum of each pixel, and comparing it to the reference spectra measured from the individual blend components using machine learning algorithms[46], each pixel in the image can be assigned to a particular blend component, or even mixed phase. More recently, analytical TEM has been combined with full tilt-range tomography to give a truly impressive, 3-dimensional reconstruction of blend morphology with phase identification from EELS[77] (Figure 2.12).

However, it should be noted that despite its impressive analytical power, this technique is not without considerable drawbacks. Inherent to all TEM imaging experiments is the small field of view[65], which restricts the researcher’s view of the sample to a small window often  $<1\mu\text{m}$  wide. This prevents an overview of the sample as a whole, and the potential for discrepancies in the film morphology to be misinterpreted as representative of the whole film.

Another key issue is electron beam damage, whereby the energy implanted by a very high energy incident electron beam focussed on an area generally  $<1\mu\text{m}$  across inevitably results in chemical changes to the area being imaged during acquisition[64], [78]. Applying advanced TEM techniques multiplies the beam dose received by the sample; tomography requires multiple exposures of the same area, whereas EELS acquisition from every pixel in an image greatly increases the required exposure time. As such, significant effort must be made with every analytical TEM study in order to demonstrate that the imaged features are not merely artefacts of beam damage.

Further damage issues arise with the preparation of electron transparent samples for imaging in the TEM. Typically, an electron transparent sample needs to be less than a few hundred

nanometres thick, with thinner samples preferred in order to minimise the negative effect of contrast projection[79]. In order to apply tomography techniques or to image cross-sectional morphology, a ‘lift-out’ of the blend film must be milled and subsequently thinned to an appropriate thickness using a Gallium focussed ion beam (FIB)[77], [80]. The sample heating and ion implantation resulting from ion beam irradiation results in significant localised damage to the sample[81], leaving a damage layer (typically ~10 nm thick in the best case) in which the sample microstructure has been destroyed[46]. This places a lower limit on the thickness of a useful blend morphology lift-out, with this damage layer making up a larger fraction of the bulk of thinner samples.

A more practical issue with TEM lies in its complexity of application, especially in the case of advanced analytical techniques. To date, only a small number of (undoubtedly impressive) studies in to OPV blend morphology using advanced TEM have been published, many authored by researchers with highly specialist expertise in the field[77], [82], [83]. This indicative of a wider trend, whereby the most advanced morphology characterisation tools are simply too complex to obtain large-scale adoption. In the case of TEM analysis, skills such as the preparation of a suitable, high-quality TEM lift-out from a fragile polymer sample are highly specialist, similarly with the acquisition of analytical TEM images and the identification of phases based upon EELS analysis. Unsurprisingly, obtaining a full characterisation of a single blend film takes many hours, and requires expensive modern equipment. As such, characterising a wide range of blend films using high-resolution, state-of-the-art TEM techniques is simply beyond the majority of laboratories. Addressing this issue, and developing higher-throughput characterisation techniques that are easily accessible to a wider range of OPV researchers, is a key theme of this thesis.

**Helium-ion microscope:** Helium ion microscopy (HeIM) has been employed to produce high-resolution images of lateral phase separation in OPV blends using secondary electron imaging[84]. HeIMs are rare and highly specialised tools, but are ideally suited to the task of OPV film characterisation. The operation is highly analogous to the SEM, with a finely focused helium ion beam scanned across the surface of a sample, inducing the emission of secondary electrons

(SE) which are used to image the sample. As with conventional SEM imaging, differences in the electron structures of the blend components can generate contrast[85], although the HeIM produces images with greatly improved contrast. He<sup>+</sup> ions are very efficient at inducing SE emission in comparison to electrons[86], and as such an excellent SE signal can be produced with fairly low beam current. In addition, SE emissions are emitted only from the top few nanometres of the sample (see Section 2.6.2), and as such HeIM images are largely 2-dimensional in nature with none of the projection issues observed with EFTEM images[84]. However, as blend films tend to have a pure-polymer polymer wetting layer [74], [87] which obscures the phase-separated morphology beneath, this layer must be removed prior to imaging by using a brief plasma etch of the sample. Figure 2.13 is an example HeIM image of a P3HT:PCBM blend after a 14-minute low-power plasma etch; where a brighter matrix (P3HT) is interspersed by darker (PCBM) domains. The lateral resolution of this image is a few nanometres[17].

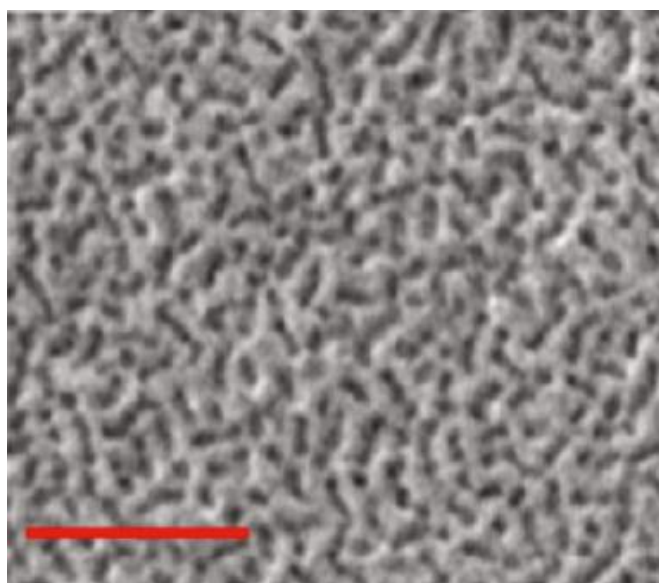


**Figure 2.13.** Helium ion microscope image of a P3HT:PCBM film annealed at 140°C for 10 minutes, and plasma etched at low power for 14 minutes. Scale bar represents 150 nm. Reprinted with permission from [84]. Copyright 2011, American Chemical Society.

### **Section 2.5.2: Reciprocal space techniques**

Reciprocal-space characterisation techniques, based upon analysis of the scattering pattern of high-energy radiation incident on a blend film, have been the subject of considerable interest in recent years. These scattering and reflectivity techniques offer an insight in to the average

properties of a blend film's nanomorphology[65]. A range of different experimental techniques exist, with different types and energies of radiation used to probe different aspects of morphology. A detailed treatment of scattering methods is given in Ref.[88], however a brief overview of the capabilities of some of the most relevant techniques for this thesis is given below.

**1) X-ray scattering techniques:** As they propagate through a blend film, x-rays are scattered most strongly from regions of higher electron density within a sample, for example molecular planes in a polymer crystallite, or on a longer length-scale, material phases with a larger electron density[88]. Periodic features of this type will result in the constructive interference of scattered radiation, resulting in peaks in the distribution of transmitted radiation. The energy and experimental setup can be changed to investigate different aspects of morphology.

To characterise the blend film phase distribution, small-angle x-ray scattering (SAXS) has been employed. Here, the scattering pattern of x-rays scattered at small angles is fitted to a variety of models in order to probe features such as phase separation length-scale, degree of intermixing, or fullerene aggregation[65]. As an example, one notable work by Parnell *et al.* [59] deduced the base length-scale of a P3HT:PCBM blend by fitting model systems to the peak in the SAXS scattering profile. The sample was then thermally annealed, and by observing how this scattering peak changed (alongside results from other characterisation techniques), deductions were made regarding the morphological changes that occur during the anneal process.

Wide-angle x-ray scattering, meanwhile, can be used with high-energy x-rays to probe the degree and orientation of crystallinity in the sample[88], [89]. The regular spacing in polymer crystallites results in scattering peaks that can be linked to crystal spacing, and crystal orientation and alignment can be inferred from the 2-dimensional projection of the scattering pattern[90], [91].

Despite the number of prominent works employing x-ray scattering techniques[88], applications of neutron scattering have grown in popularity in recent years due to the often improved contrast that neutron techniques offer for OPV materials [92].

**2) Neutron scattering techniques:** As opposed to x-rays, neutrons are scattered off nuclei, with the contrast mechanism from neutron scattering techniques being variation in mass density[88]. This tends to give improved polymer-fullerene contrast in comparison to x-ray scattering. Similarly to SAXS, small-angle neutron scattering (SANS) is used to probe the size and purity of phases in the blend morphology. Again here, the scattering profile of the blend film is compared with, for example, a two-phase model system, in order to deduce various morphological features (such as average domain size) of the real film[58].

By changing the experimental arrangement such that neutrons are incident almost normally to the film surface, with scattered neutron intensities measured as a function of the angle of reflection, neutron reflectivity (NR) data can be collected. Using NR, the vertical composition profile of the two blend components through the thickness of the film is probed[87] by extrapolation of the NR function through a model system. This can be used to, for example, probe for layers in the film that are depleted in one component. For example, Parnell *et al.* [87] used NR to demonstrate a 20 nm-thick PCBM deficient layer that is present at the top of an as-cast P3HT:PCBM blend.

**3) Perspective on reciprocal space techniques:** Radiation scattering techniques can be used to provide a compelling insight in to the nature of OPV blend morphology. The length-scale of features that can be resolved is unmatched by any imaging technique, allowing for insights in to crystallinity properties and fine material inter-mixing that would not be available elsewhere. The fact that scattering methods probe bulk properties rather small imaging windows (as with high-resolution imaging methods) can be taken as a significant benefit, whereby localised variations are averaged out to give a ‘whole-sample’ picture of blend morphology.

However, the general applicability of scattering techniques as a high-throughput tool for researchers looking to optimise blend morphology must be questioned. Neutron scattering techniques require highly-specialised, advanced neutron beam sources such as ISIS in the UK[87], [93], and for high-quality x-ray scattering data from an OPV system, the intensity and collimation of a synchrotron source is required[88]. Time available on these facilities is extremely limited, and as such can only be used for very specific experiments on perhaps the most prominent

materials systems. The nature of the OPV field, with new materials and methods being constantly developed and requiring testing, is not particularly compatible with this arrangement[50]. Further, the reliability of scattering results can easily be called in to question, with the findings of these experiments being strongly tied to the relevance and accuracy of a proposed model system to which the scattering profiles are compared. Often assumptions are made which may or may not be valid, and drawing conclusions with regards to the nature of a highly complex, multi-faceted blend system based on a scattering peak or the shape of a scattering profile will always be subject to a degree of speculation, even if the techniques applied are well-proven and understood[88]. It is for this reason that most works that apply scattering methods to OPV systems include verification by another method or by comparison with literature[45], [59], [89]. It should also be noted that the bulk averaging of properties measured by scattering techniques can also be viewed as a drawback, in that fine, localised details of the morphology such as domain shapes or interconnectivity can remain undetected[94].

### ***Section 2.5.3: Perspective on present state of OPV morphology characterisation, potential of the scanning electron microscope***

As summarised in Table 2.1, there is undoubtedly an impressive range of OPV characterisation techniques at present, which combined can give a detailed overview of a polymer blend morphology. Imaging techniques, especially analytical TEM methods, perhaps give the most detailed overview of phase separation by offering accurate material identification and nanometre resolution. By enabling direct visualisation of morphological features (as opposed to obtaining more abstract results from scattering experiments) images reduce ambiguity and give a more intuitive understanding of morphological features (once care has been taken to eliminate causes of misinterpreted image contrast). By combining imaging with spectroscopy techniques, such as EELS, it is possible to be confident of material identification.

On the contrary, inverse space techniques offer a different type of insight into the nature of OPV morphology. Comparing bulk-averaged properties of two different, but related samples (for example, before and after a thermal anneal) can give a powerful insight in to the general effects

of altering a processing technique. Further, the ability to probe bulk-averaged polymer crystallinity and orientation, amongst other molecular-scale properties, demonstrates capability beyond that available from TEM or any other imaging technique.

An overarching drawback runs amongst all of the highest-quality characterisation techniques presented in this section however, in the fact that they rely on techniques requiring specialist expertise and/or equipment with limited access, or have a low throughput. As a result, the availability of high-quality morphology characterisation data is limited to the small minority of researchers that have regular access to either advanced facilities or highly specialist expertise. Given the size of the OPV research field, where, as an example, ~1700 related articles were published in 2013 alone[95], this inevitably results in a large volume of OPV research that is not informed by morphology characterisation techniques that have adequate resolution or phase identification capability. This has resulted in the situation described as a morphology optimisation bottleneck[50], whereby researchers developing new OPV solutions have struggled to optimise the morphology of new blend systems, thus preventing them from getting the most out of new methods or solutions. As noted in the Introduction to this thesis, new characterisation techniques are required to help relieve this bottleneck, that combine high-quality characterisation and adequate spatial resolution with wider accessibility and higher throughput.

<b>Characterisation technique</b>	<b>Strengths</b>	<b>Weaknesses</b>
Phase-contrast AFM	<ul style="list-style-type: none"> <li>• Polymer-fullerene contrast from different energy dissipation properties</li> <li>• Widely available equipment</li> </ul>	<ul style="list-style-type: none"> <li>• Slow, low-throughput</li> <li>• Difficult to interpret data without deep understanding of mechanical properties of materials</li> <li>• 2-dimensional information</li> </ul>
Advanced scanning probe methods	<ul style="list-style-type: none"> <li>• Directly measure electronic properties</li> <li>• Can infer aspects of 3-dimensional morphology</li> </ul>	<ul style="list-style-type: none"> <li>• Very low throughput</li> <li>• Complex to set up</li> <li>• Difficult to interpret data</li> </ul>

*Table 2.1: Continued on next page*

BF-TEM	<ul style="list-style-type: none"> <li>• Infer aspects of 3-dimensional morphology</li> <li>• Excellent lateral resolution</li> </ul>	<ul style="list-style-type: none"> <li>• Difficult to interpret – contrast projection, defocus methods produce contrast of questionable origin</li> <li>• Time consuming sample preparation</li> <li>• Limited field of view</li> </ul>
Analytical TEM	<ul style="list-style-type: none"> <li>• Tomography allows full 3-dimensional reconstruction of morphology</li> <li>• Material identification from EELS – removes ambiguity in data interpretation</li> <li>• Excellent resolution</li> </ul>	<ul style="list-style-type: none"> <li>• Data interpretation requires specialist expertise</li> <li>• Preparation of samples for tomography is time consuming, challenging</li> <li>• Tomography + EELS collection risks electron beam damage</li> </ul>
Helium-ion microscope	<ul style="list-style-type: none"> <li>• High SE yield of He<sup>+</sup> ions gives high quality morphology image</li> <li>• Good resolution</li> <li>• High throughput, little/no sample preparation</li> </ul>	<ul style="list-style-type: none"> <li>• Data is 2-dimensional</li> <li>• HIM equipment is rare, potential uptake of techniques is limited at present</li> </ul>
Reciprocal space techniques	<ul style="list-style-type: none"> <li>• Range of complimentary techniques available to probe different aspects of morphology</li> <li>• Excellent resolution – probe crystallinity, intermixing</li> <li>• Bulk averaging gives whole-sample overview of sample properties</li> </ul>	<ul style="list-style-type: none"> <li>• Highest-quality data requires specialised facilities such as synchrotrons</li> <li>• Reliable interpretation of scattering data is difficult</li> </ul>
Conventional SEM	<ul style="list-style-type: none"> <li>• Modern SEM has lateral resolution competitive with TEM</li> <li>• High throughput, little/no sample preparation</li> </ul>	<ul style="list-style-type: none"> <li>• Low contrast between polymer and fullerene</li> <li>• SE imaging methods only give 2-dimensional data</li> <li>• Data can be difficult to reliably analyse, open to interpretation</li> </ul>

**Table 2.1:** Overview of state-of-the-art in OPV morphology characterisation techniques

In this thesis, it is proposed that novel techniques in the scanning electron microscope (SEM) can offer a viable solution to this problem. As noted in Table 2.1, SEMs are already widely available in universities and research facilities throughout the world. Technological advancements over the

past decade have improved the available spatial resolution from modern tools to a level highly competitive with the TEM[96]. Typically, the SEM is far easier to operate than the TEM and requires little-to-no sample preparation, in stark contrast to the arduous process of generating a high-quality electron-transparent lift-out with a FIB[65]. Further, the energy of the primary electron beam in the SEM is a factor of  $\sim 100\times$  smaller than the TEM, with various forms of beam damage, such as knock-on damage, significantly reduced as a result[17].

However, similarly to basic BF-TEM methods, conventional secondary electron (SE)-based SEM techniques are not well suited for high-resolution OPV blend characterisation (Table 2.1). The material contrast between polymer and fullerene is typically small because of the similarities between the two organic compounds, and sample topography can result in the generation of difficult-to-interpret contrast. Common techniques for material identification in the SEM do exist in the form of energy-dispersive x-ray spectroscopy (EDX), or backscattered electron (BSE) imaging, however both of these methods in their conventional arrangements lack the spatial resolution required to probe the nanometre-scale features of a typical blend morphology. In order to apply the SEM to the task of OPV morphology characterisation, new methods must therefore be found to address the shortcomings of the SEM in this context. This thesis aims to tackle these shortcomings and in doing so, develop the SEM as a viable, competitive morphology characterisation tool.

## **Section 2.6: Scanning electron microscope**

In order to develop and understand new techniques in the scanning electron microscope, a thorough understanding of the SEM must first be obtained. This includes not only the basic workings of the instrument, but also the detailed interactions of the primary electron beam with the sample that result in the emission of backscattered and secondary electrons and the generation of an imaging signal. From this base, we can recognise the opportunities for developing and advancing new techniques in the SEM that can be exploited for high-quality OPV morphology characterisation.

**Section 2.6.1: Fundamental operation of the scanning electron microscope**

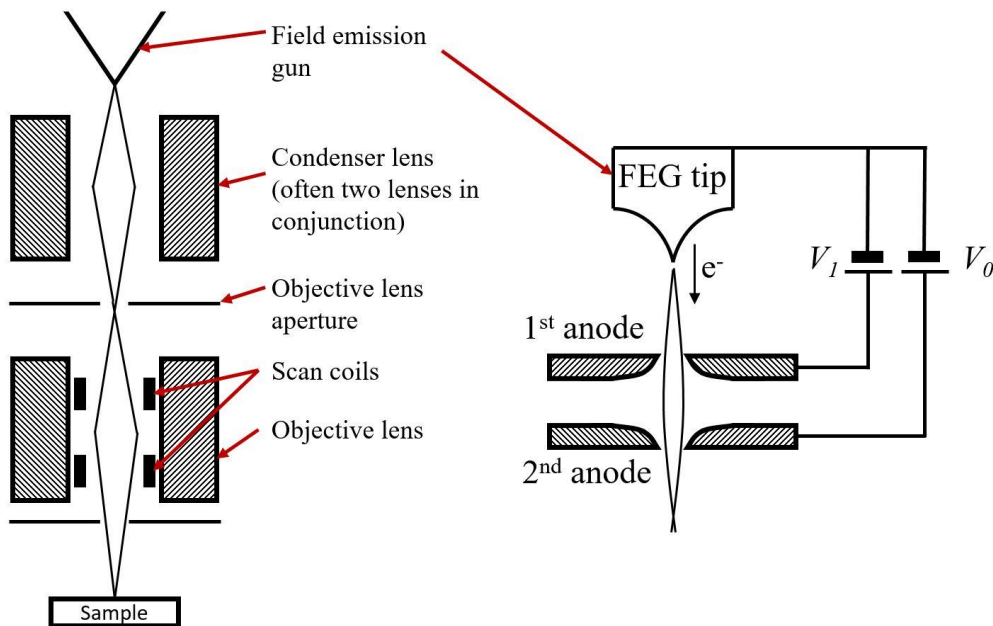


**Figure 2.14:** Basic schematics of SEM and FEG, based on descriptions in [97], [98]. In the FEG, bias  $V_1$  is a few kV, and acts to draw electrons from the tip.  $V_0$  is the primary accelerating voltage.

In the SEM, an accelerated, highly focused electron beam is scanned over a sample under vacuum to excite electrons from a sample, with an image built from measuring the localised electron emission from each point in the image. A schematic of a typical instrument is displayed in Figure 2.14. In the modern-day SEM, a field-emission electron gun (FEG) is used as the electron beam source[99], which incorporates a single-crystal tungsten wire sharpened to a fine point ( $\sim 100$  nm), and often capped with a thin layer of  $ZrO_2$  to lower the surface work function (the ‘Schottky’ field emitter design)[97], [98]. An anode located close to the tip is biased to a few kV in order to generate an electric field that extracts a narrow beam of electrons from this tip, which is subsequently accelerated by a second anode to an energy in the range  $\sim 0.2$ – $30$  keV as selected by the operator (Figure 2.14). This ‘primary’ electron beam from the FEG source is demagnified, or ‘focused’ on to the sample by a series of electromagnetic lenses, which use the current flowing through a coiled wire to generate a magnetic field that acts to focus electrons in a similar manner to the way an optical lens acts on light. Condenser lenses and an objective lens aperture act to control the current reaching the sample, whilst the strength of the final, or ‘objective’ lens is

adjusted (by increasing or decreasing the current flowing through the lens coil) in order to focus the beam to a fine point on to the sample[98]. Modern electron microscopes have demonstrated sub-nanometre probe sizes with the use of extra magnetic coils that act to effectively place the sample *within* the objective lens aperture – an arrangement known as an ‘immersion lens’. This allows for extremely high-resolution imaging with fewer aberrations[96], [98].

The focused beam is ‘scanned’ across the sample in small, discrete steps (each equivalent to a pixel in the SEM image) by electromagnetic deflection coils, with the electron signal emitted from the sample at each step measured by one of a range of possible detectors (Section 2.6.3). This process is repeated over an array of pixels and an image is formed, with the measured electron signal at each pixel being strongly related to its brightness in the resulting image.

### ***Section 2.6.2: Electron-sample interactions, emitted electrons***

The primary electron beam will interact with atoms and electrons in the sample, with various physical interactions, both elastic and inelastic, occurring as a result[98], [99]. Elastic interactions alter the path of the incident electron whilst having a negligible effect on its kinetic energy, whilst inelastic interactions result in a loss of a fraction of this energy. Due to the attenuation effect of inelastic interactions, the electron beam will only interact within a finite interaction volume, with a characteristic ‘teardrop’ shape (see Figure 2.15). The size of this volume can be controlled by the primary beam energy – naturally, higher-energy primary electrons will demonstrate a larger interaction volume. Typical interaction depths for the organic materials and beam energies used in this thesis are in the range 20 - 300 nm for primary beams with energy 0.5 - 3 keV respectively [18].

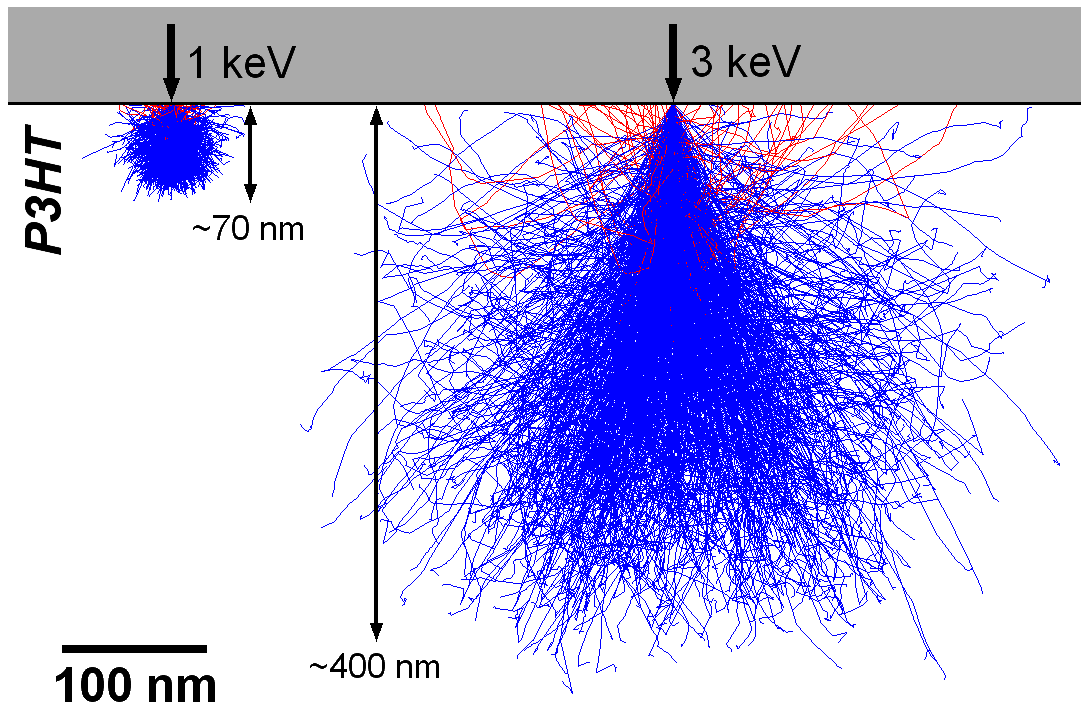


*Figure 2.15: Simulated trajectories of electrons incident on P3HT at 1 keV and 3 keV. Each blue line reflects the trajectory of a single electron that is ultimately stopped by the material, whereas each red line reflects a backscattered electron. Simulations performed in CASINO software.*

The electron-sample interaction for individual primary electrons can vary widely. Crucially to the operation of an SEM, various beam-sample interactions will result in the emission of radiation from the sample, with the type and properties of the emitted radiation often characteristic of the interactions that caused the emission. As such, the different types of emission in the SEM are often detected and considered separately in order to probe different aspects of the sample.

**1) Backscattered electron emission:** Backscattered electrons (BSEs) are primary beam electrons that are ‘reflected’ back out of the sample surface whilst retaining a large fraction of the primary beam’s energy[98]. BSEs are the result of primary beam electrons elastically scattering off atoms in the sample, from interactions that transfer momentum with little loss of energy[99]. Whilst it is possible for an electron to be backscattered out of the sample after a single scattering event, a typical BSE will be elastically scattered multiple times before escaping the sample.

As BSEs are generally result from interactions with atomic charge, the fraction of the incident primary electrons that are backscattered (defined as the backscattering coefficient) demonstrates

a strong dependence on the density[100] or atomic number  $Z$  [97], [98] of the sample. As such, images formed from the BSE signal emitted by the sample demonstrate compositional, or ‘material’ contrast, with brighter regions in a BSE image consisting of denser or higher- $Z$  materials. In this thesis, all of the studied materials are carbon-based, which is an important consideration as carbon demonstrates a relatively low backscatter coefficient[98]. The implications of this are addressed in Section 2.6.4.

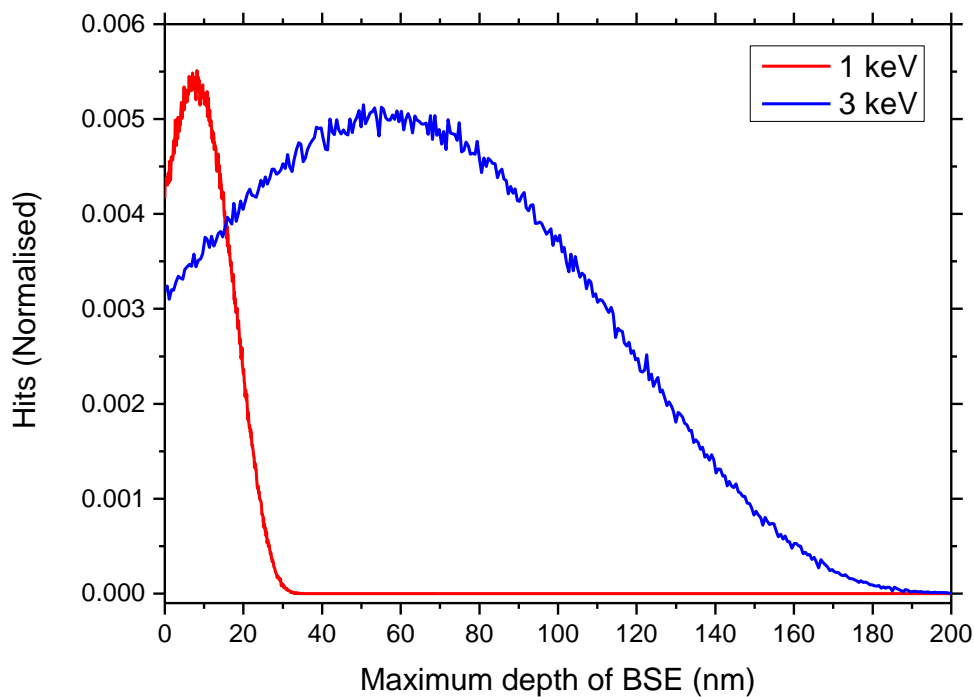


**Figure 2.16:** Maximum depth in to a P3HT film reached by electrons subsequently emitted as BSEs, from incident electrons with 1 keV and 3 keV. Simulated in CASINO software.

As elastically scattered primary beam electrons, BSEs can travel large distances through the sample due to their high energy (especially in comparison to secondary electrons, discussed below). This has important consequences for the sample information contained in a BSE image. Firstly, a typical BSE can escape the sample from depths of up to a few tenths of the primary beam’s whole interaction depth (see Figure 2.16)[98], and as such the BSE imaging signal can contain sample information from well beneath the sample surface. Similarly, these large propagation lengths, combined with the multiple elastic scattering events experienced by most BSE, limit the lateral resolution of a BSE image (see red lines in Figure 2.15 ) [98]. Elastically scattered primary electrons can propagate a significant lateral distance from the beam incidence

point before being backscattered out of the sample; as such the BSE imaging signal can be influenced by features many nanometres away from the beam incidence point.

Of course, the energy, and therefore propagation length, of elastically scattered electrons inside the sample, scales with the primary beam energy. This allows for the sample properties reflected in a BSE image to be tuned to an extent. For example, the sample depth probed by a BSE image can be reduced by decreasing the primary beam energy, in order to give a more surface-sensitive image[101]. Likewise, BSE images taken with a lower-energy primary beam demonstrate better resolution as elastically scattered electrons cannot propagate as far from the beam incidence point[18], [102]. This ‘tuning’ of the BSE signal by altering the primary beam energy is a crucial aspect of Chapter 6 in this thesis, where BSE images are used to probe both the surface and whole-film morphology of polymer:fullerene blends.

**2) Secondary electron emission:** Secondary electrons (SEs) are perhaps the emissions most commonly related with SEM images[103]. Typically defined as electrons emitted from a sample with  $< 50$  eV (a fairly arbitrary threshold), SEs are often the product of ionisation. The inelastic scattering of a primary beam electron can transfer enough kinetic energy (either directly or *via* plasmon or phonon excitation[99]) to valence electrons in the sample for them to be emitted. In a semiconductor, for example, these outer-shell valence electrons (equivalent to electrons in the HOMO for conjugated polymers) will have energies below the vacuum level of no more than a few eV. Primary beam electrons, even in low-energy modes (see Section 2.6.4), have orders of magnitude more energy than a valence electron, phonon or plasmon, and therefore little kinetic energy is transferred to the SE[98]. As such, most SEs that escape the sample have low kinetic energies below 10 eV once emitted [98], [104].

One result of these low energies is that the mean free path,  $\lambda$ , of a secondary electron inside the sample is often small, with inelastic interactions easily attenuating their initial energy. The expected  $\lambda$  of an internal SE is rarely more than a few nm in non-insulating samples[17], [103], [105] (although the presence of a band-gap in the material can have an effect on  $\lambda$ , as discussed in Section 2.7.1). Crucially, this places a limit on the escape depth of SEs generated in the sample;

as an estimate, only SEs generated within a few  $\lambda$  (i.e.  $< \sim 10$  nm) of the sample surface have any chance of emission, with the majority of emitted SE generated at the smaller end of this range[17]. SE images are therefore surface sensitive. This is an important aspect of SE images considered in Chapter 5.

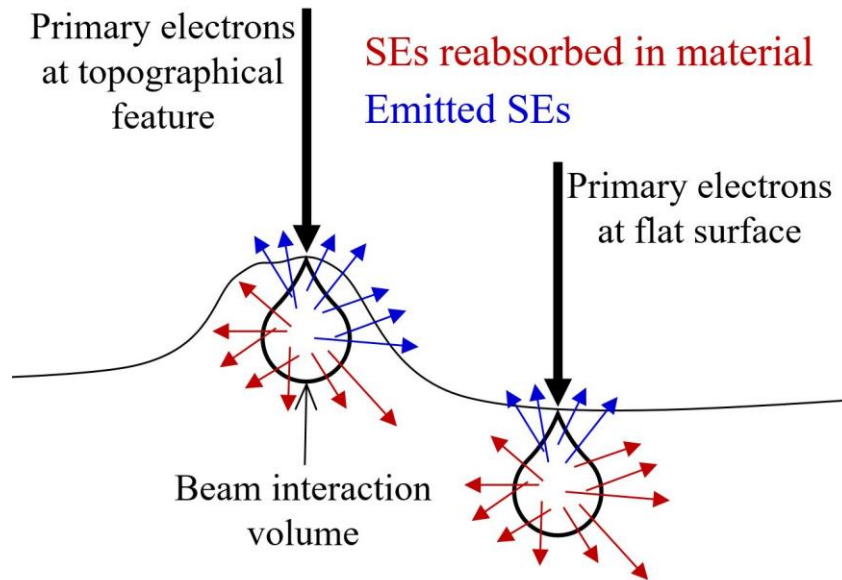


**Figure 2.17:** Schematic depicting the edge effect. At topographical features, SE emission from the sample is enhanced.

Due to this surface sensitivity, the image contrast of a conventional SE image is highly dependent on sample topography. A phenomenon known as the ‘edge effect’, depicted in Figure 2.17, results in the emission of larger numbers of SEs from topographical features, such as areas of the sample that are not flat or planar, or more notably edges or peaks[97]. This contrast is related to the surface area of the sample illuminated by the beam at a given point. As demonstrated in Figure 2.17, at edges or peaks, or other regions where the beam is incident at an angle, more SEs are therefore generated within the required SE escape depth at these regions. As such, whilst the same total number of SEs are generated in all instances, the SE flux escaping the sample is greater for topographical features in comparison to a completely flat region with beam incidence normal to the surface[97], [98].

SEs emitted as a result of direct excitation from the primary electron beam are denoted  $SE_1$ , and can be envisioned as ‘pure’ SE emissions. The  $SE_1$  imaging signal is of high resolution, emitted

from a lateral distance often  $<1$  nm from the incident electron beam ‘spot’[17], and has an intensity dependant only on the strength and nature of the inelastic interactions between the beam and sample that generate SEs[97]. However, BSEs are also capable of generating SE near the surface in significant quantities. The resulting SEs are denoted SE<sub>2</sub>[98]. As they are generated by BSE, the strength and nature of the SE<sub>2</sub> signal shares some properties with the BSE signal – the generated intensity is naturally dependent on the number of BSE emitted by the sample, and the lateral radius of emission is much larger than SE<sub>1</sub>s, similarly to BSE. The ratio of SE<sub>1</sub> to SE<sub>2</sub> is highly sample dependent, and reliant on the backscattering coefficient of the material. For polymers, the low backscatter coefficient of carbon means that the ratio of SE<sub>1</sub> to SE<sub>2</sub> is high, around 5.5 for primary beam energies above  $\sim 1$  keV [98].

### ***Section 2.6.3: Electron detectors***

As SEs and BSEs carry separate information about the sample, modern SEMs use different detectors customised to detect primarily only one type of emission, or at least user-controlled detectors that enable the filtering of either SEs or BSEs from the imaging signal[97], [98]. This prevents the unwanted convolution of different types of imaging contrast, and allows for clearer interpretation of image features. Many designs exist, each specialised for a different purpose[98], [99], [106]–[109]. Three detectors are used for the work in this thesis:

**1) Everhart-Thornley detector (ETD):** As depicted in Figure 2.18, the Everhart-Thornley detector, or ETD, is the most common detector design employed in modern SEMs[109]. Primarily a SE detector (although it can be employed as a BSE detector), the ETD is mounted at an angle to the beam incidence axis, above the sample. In operation, an emitted electron strikes the scintillator material at the front of the detector, causing the emission of a light pulse which is passed down a light guide to the photocathode of the photomultiplier[98]. This generates an electron pulse which is amplified through the multiple electrodes of the photomultiplier, before reaching the final signal collector.

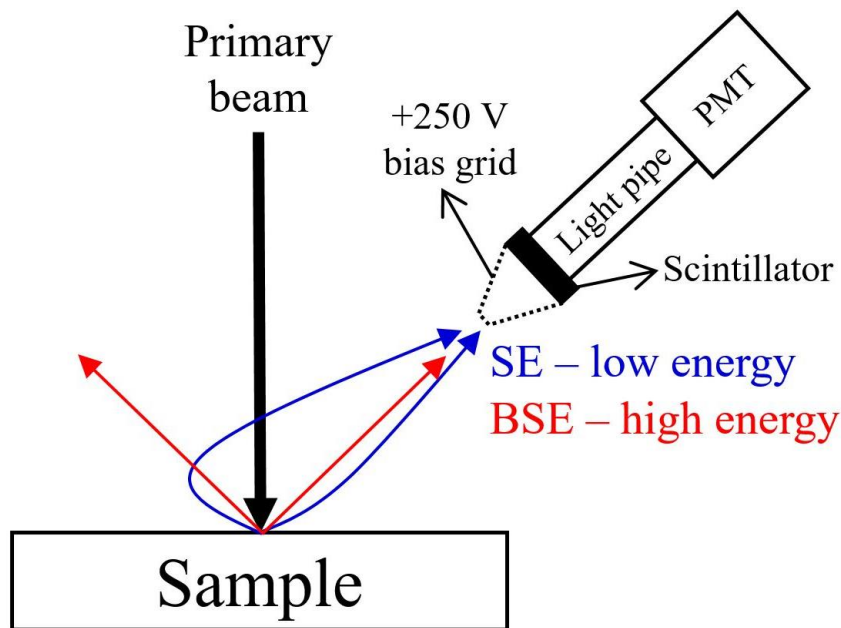


**Figure 2.18:** Schematic of Everhart-Thornley detector (ETD). Lower energy SEs emitted over a wide range of angles attracted towards scintillator by biased grid. Higher energy SEs less affected by electric field. Adapted from [103] with permission from AIP.

A grid surrounding the front scintillator of the ETD can be biased in order to select the nature of the electrons that reach the detector[98]. By applying a positive bias ( $\sim 250$  V) to the grid, low-energy SE emissions can be attracted to the detector largely regardless of their emission angle. In this condition, BSEs can still reach the detector and contribute to the imaging signal, however these are small in number compared to the detected SE signal[102]. Applying a negative bias to the grid will repel SEs due to their low energy, and as such only BSEs will be able to reach the scintillator and contribute to the imaging signal.

**2) Through-lens detector (TLD):** When using the SEM in a high-resolution immersion mode (Section 2.6.1) the magnetic fields acting to place the sample inside the effective objective lens have the effect of trapping the SEs emitted by the sample[98]. As a result, SEs emitted in an immersion mode condition do not reach the ETD, and will instead pass up the pole-piece of the electron column. Therefore, in immersion mode, a different SE detector mounted above the objective lens of the electron column is required to collect these SEs and form an image – the through-lens detector (TLD).

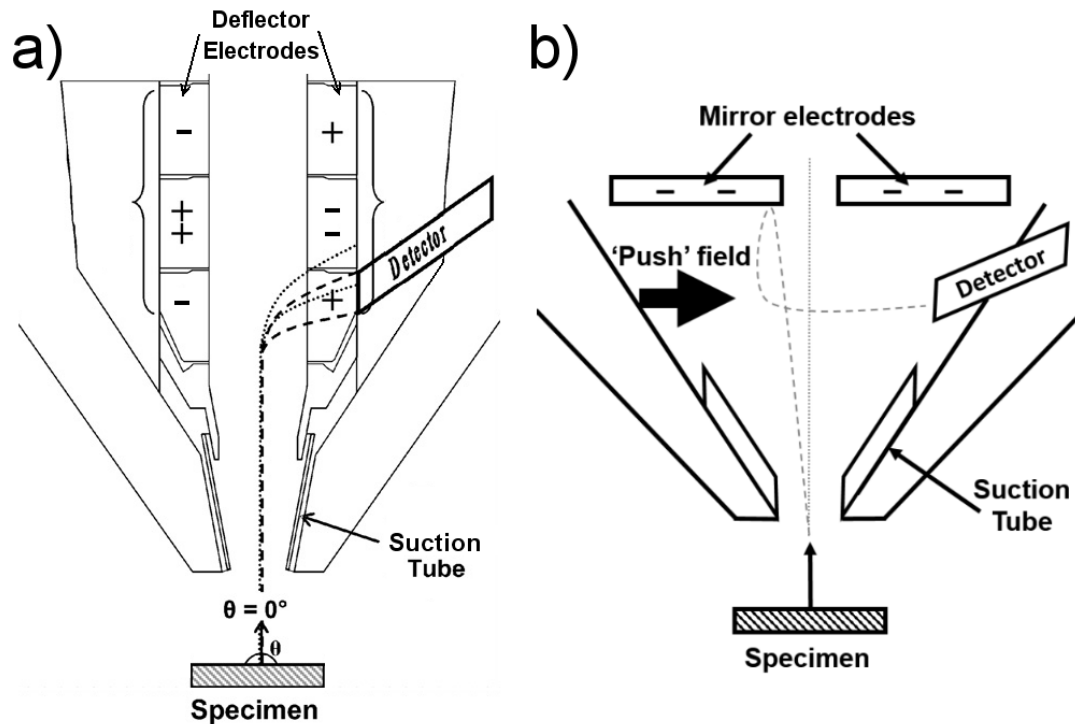


**Figure 2.19:** Schematics of TLD arrangements in two SEMs manufactured by FEI Co. and used in this thesis. a) XL-30 design TLD. Adapted from [110] with permission from Elsevier. b) Elstar design TLD, based upon information available in [111], [112]. The origin and nature of the ‘push’ field deflecting SEs on to the detector has not been made publicly available, and as such the effect depicted here is an estimation.

Specific designs of the TLD vary between microscopes (see Figure 2.19). In this thesis, SEMs with two different TLD arrangements are used – an important consideration as the operation of the TLD is crucial to performing the SE spectroscopy methods featured in Chapters 4 and 5. Figure 2.19a demonstrates an older but more common ‘XL-30’ design[113]. Here, a scintillator detector (similar to that in the ETD) is mounted to the side of the electron column, and a ‘deflector’ electrode biased to -60 V is placed on the opposite side of the column pushes SEs towards the detector as they pass[110]. A positively-biased ‘suction’ electrode is also mounted to the electron column’s pole-piece to attract SEs in the sample chamber towards the column and improve collection efficiency.

A more modern ‘Elstar’ design is depicted in Figure 2.19b. Once more, a scintillator detector is mounted to the side of the electron column, and a suction electrode is used at the end of the pole piece to improve collection efficiency. However, rather than using a single deflector electrode, the Elstar design uses a combination of two negatively biased electrodes to first trap collected

SEs inside the column (using a ‘mirror’ electrode), and then deflect these trapped electrons towards the detector (a ‘push’ electrode). This 3-electrode design gives greater detection efficiency than the XL-30 arrangement[111].

In the context of SE spectroscopy, the bias on the deflector electrode in the XL-30 design, or the bias on the mirror electrode in the Elstar design, is altered in order to control the energy of the SEs that are able to reach the scintillator detector (see Section 2.7.2, Chapters 4 and 5).

**Concentric backscatter detector (CBS):** Optimised to detect only the BSE imaging signal, the CBS detector is mounted to the end of the pole piece and consists of four concentric solid-state detectors arranged in a ring formation (see Figure 2.20)[102]. These detectors have a detection threshold of around ~400 eV, and as such any SEs incident on the detector will not contribute to the imaging signal. Further, the solid state design of the CBS detector allows it a far smaller physical footprint in comparison to scintillator designs, allowing it to be placed in close proximity to the sample and maximise collection efficiency without the need for deflector grids or electrodes[98].

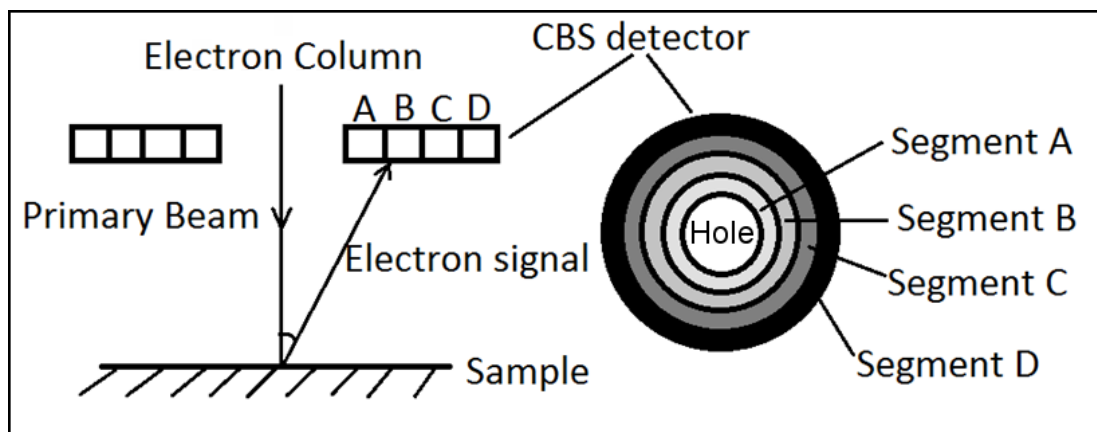


**Figure 2.20:** Schematic of CBS detector. Reproduced from [18] under CC BY 3.0 license. This figure can also be found in Section 6.7 (the Supplementary Information from [18]).

The four detector rings can be used individually or in any combination, and allow for the filtering of BSEs based on their emission angle[18]. This can help to generate optimised images based on the contrast the user wants to highlight. In Wan *et al.*[102] it is demonstrated that BSEs emitted with a high angle relative to the beam incidence tend to carry topographical information (a result of geometry considerations in the beam-sample interaction, discussed in-depth in the referenced

work), and as such imaging with the outer detector rings of the CBS detector gives images containing more topographical information. However, imaging with the inner, lower angle detector rings generates the expected BSE images containing material contrast. This effect is used to boost image quality in Chapter 6.

#### ***Section 2.6.4: Imaging polymers in the SEM***

Whilst SEM imaging of polymeric samples is today a fairly common technique thanks to advancements in SEM technology[98], [114], [115], some of the unique features of polymers, and organic materials in general, can still present challenges to the SEM operator that require careful consideration[114].

**Low-voltage SEM:** The use of a low-voltage primary electron beam is a crucial aspect of these polymer-optimised imaging conditions for multiple reasons explained in this section[114], [116]. Low-voltage SEM (LVSEM), using primary beam energies of ~0.5 – 5 keV, has been considered an ‘advanced’ technique in comparison to more conventional imaging methods at higher energies. This is generally because older SEM technology was unable to generate high-quality images at low energy: early electron sources could not emit a stable beam in the LVSEM energy range, and low-energy beams are more susceptible to lens aberrations which limited the available resolution[117]. The development of the field emission electron gun alongside advanced electron optics has enabled a stable low-voltage beam with nanometre-scale probe size, enabling the use of LVSEM in this thesis[114]. Nonetheless, even today LVSEM demonstrates worse resolution than higher-energy techniques[111], [118], [119].

Beam deceleration techniques, whereby either a few-kV sample bias[101] or a ‘beam booster’ electrode on the objective lens[120], can be used to help bypass this resolution drop at low beam voltages. Using these techniques, a higher-energy beam with fewer aberrations is generated by the electron column, and subsequently decelerated by an electromagnetic field (generated by the sample bias or beam booster) such that the beam is incident on the sample with reduced ‘landing energy’[101]. Thus, the beam is incident on the sample with LVSEM-level energies, but with fewer resolution-limiting aberrations. Beam deceleration methods are used in Chapter 6 to

generate excellent quality images with primary beam energies down to 500 eV[18], however the electromagnetic fields involved interfere with the SE spectroscopy techniques applied in Chapters 4 and 5.

Even without beam deceleration however, low-energy electron beams are considerably more suitable than higher energy ones for imaging polymer samples. This is due to a number of practical benefits addressed below.

Common issues encountered when imaging polymers in the SEM are:

**1) Sample charging:** Perhaps the most obvious issue with imaging most polymers in the SEM is that the majority tend to be electrical insulators. As such primary electrons that are incident on an insulating polymer sample in the SEM are unable to drain away from the imaged area at a faster rate than new ones are added by the electron beam[114]. Localised charge will build up in the electron-irradiated area as a result, which has the effect of repelling the electron beam if it is scanned over the same sample area enough times.

Of course, the materials characterised in this thesis are conjugated polymers or conductive fullerenes developed for use in electronic devices. Charge accumulation under the electron beam is not therefore a major concern for most of the SEM work performed here. However, OPV materials and blends, whilst demonstrating charge mobilities adequate for charge transfer over a few hundred nanometre-thick film in an organic solar cell, still demonstrate relatively poor conductivity compared to materials considered more 'suitable' for SEM imaging (silicon has an electron mobility several orders of magnitude higher than P3HT, for example[31], [54]). Importantly, conjugated polymer films must also be processed correctly to enable optimal charge mobility (see Section 2.3.2). If a non-optimised sample is imaged, bulk conductivity will be poor and localised charge accumulation in the SEM is likely[121]. It is therefore good practice to take steps to minimise sample charging, even with optimised OPV materials.

The simplest way to mitigate charging effects, especially in the case of a partially conductive sample, is to limit the incident current, or to use a fast scan-speed to limit the electron dose

incident on the sample[100]. Naturally, this will not prevent charging, however it can reduce the extent of the accumulated charge to a more manageable level[98]. This has an obvious drawback in that a reduced beam dose per pixel will give a weaker imaging signal, and the resulting images will demonstrate a worse signal-to-noise ratio (SNR)[100]. However, depending on the application, this effect may be tolerable and a low imaging current can be used.

High-quality images can be obtained from partially-conductive samples by employing advanced beam scanning patterns to obtain SEM images, most obviously frame integration[122]. It can be assumed that a point on a charge-accumulating sample works similarly to capacitor, accumulating charge whilst the beam is irradiating that point, and gradually dissipating it whilst the beam is scanned elsewhere on the sample[98]. The rate of dissipation is naturally dependent on the localised charge mobility of that point on the surface. Frame integration works by acquiring a number of sequential frames of the same sample area with short dwell times, and integrating these together to give the final image[100]. The short dwell times in each individual frame reduce the accumulation of charge, which may dissipate (if the localised charge mobility is high enough) before the next frame in the integration series. A single frame has a poor SNR due to the short dwell time, however noise is averaged out in the final, higher-quality integrated image. The SEM operator can select how many images are acquired for this integration series for an optimised result that balances the quality of the final image (more frames results in lower noise) whilst minimising beam exposure. Other advanced scan patterns, such as scan interlacing[123] acquire lines of the image in a non-sequential order (for example acquiring lines in the order 1, 8, 2, 9, 3, 10 etc.). This allows more time for charge to dissipate between scans of localised charging areas. A further common technique to eliminate localised charging is to sputter-coat polymers with a few-nm thick metal layer to help with the dissipation of accumulated charge[98]. This technique is not used in this thesis as metal coatings would interfere with the surface-sensitive BSE techniques and material-specific SE spectra applied.

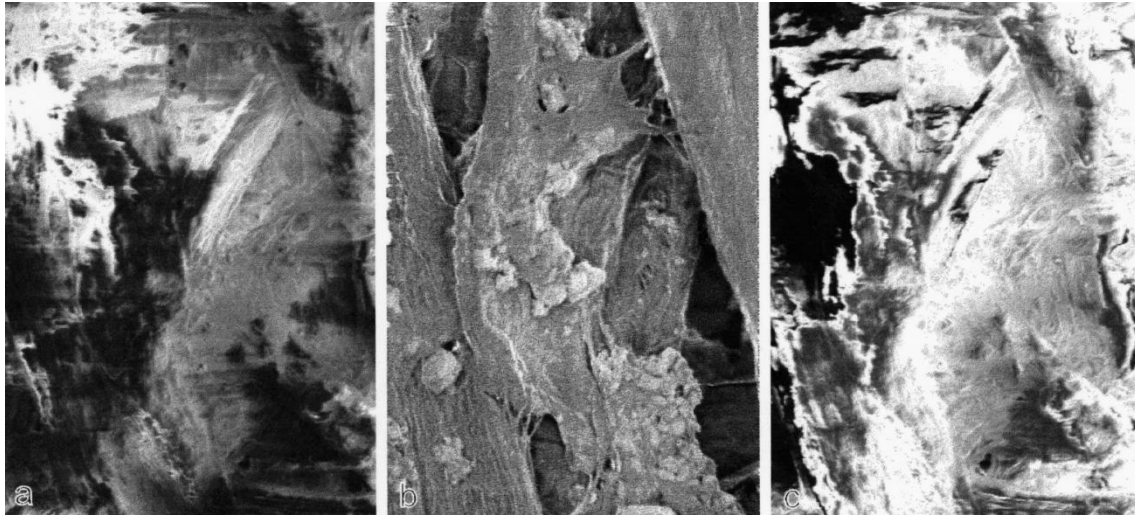


**Figure 2.21:** Demonstration of sample charging in an insulating sample at different primary beam energies, and elimination of charging phenomena at  $E_2$  primary beam energy condition. Common writing paper imaged with a)  $E_0 = 3.65$  keV, b)  $E_0 = 2.65$  keV (the sample's  $E_2$  value) and c)  $E_0 = 1.65$  keV. At the  $E_2$  point, sample features can be observed clearly with no discernible charging. At primary beam energies and below this point, sample charging occurs, producing extreme artificial contrast and image distortion. Image field width is  $40 \mu\text{m}$ .  
 Reprinted from [124] with permission from Wiley.

Furthermore, coating techniques can be rendered unnecessary by the correct application of low-voltage SEM methods (Figure 2.21). As already discussed in Section 2.6.2, the incident electron beam in an SEM excites the emission of further electrons, primarily in the form of BSE and SE. When the SEM is used with a primary beam of more 'conventional' energies (i.e.  $> 5$  keV), the incident beam current is typically far greater than the 'emitted current' of SEs and BSEs[103], [114]. An electrically insulating sample will charge negatively as a result. However, when the beam energy is reduced, the SE yield in particular increases, and can reach a point whereby the incident beam current is in fact equal to the emitted current[114]. At this point (theoretically at least), no charging will occur. For most polymer materials, the primary beam energy at this point, denoted  $E_2$ , is around 1 keV[114]. Even if a sample is not imaged at its precise  $E_2$  value, by imaging at low primary beam energies around 1 keV, charge accumulation is minimised at least to the point where the conductivity of OPV samples may be sufficient to dissipate any residual charge.

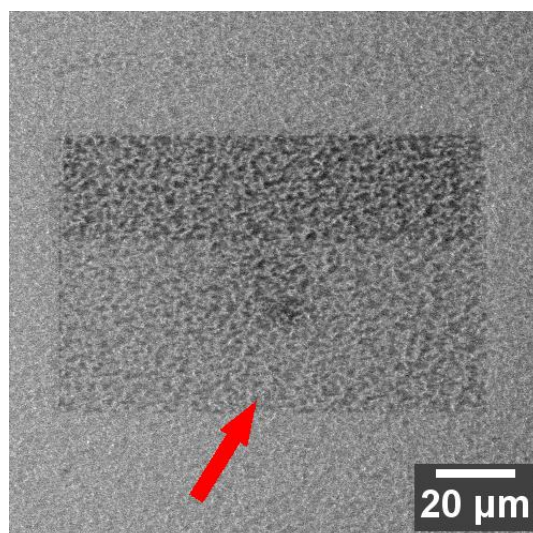


*Figure 2.22: Damage to P3HT sample resulting from prolonged electron beam exposure. The rectangle shape marked in the image is the SEM's field of view during the exposure period. New contrast has formed in the exposed area due to electron beam damage.*

**2) Sample damage:** Polymers are extremely susceptible to localised beam damage when subject to the highly focused, high-energy primary electron beam in an SEM[114] (see Figure 2.22). The energy transferred to the sample in inelastic beam-sample collisions is often considerably larger than the few eV required to break chemical bonds[100] and can cause effects such as chain scission or crosslinking[125]. Localised heating from thermalisation of this incident energy can cause deformation or shrinkage of the polymer. The extent of this damage increases dramatically with image magnification, as the implanted electron beam dosage (incident electrons/unit area) increases.

As an example, an in-depth study into the damage incurred by P3HT during electron irradiation has been performed[126]. This work indicated that when subject to increasing levels of irradiation from electrons with energies in the LVSEM range, the polymer undergoes progressive degradation. The initial observed effect (seen after doses of  $4 \times 10^{17}$  electrons.cm<sup>-2</sup>, roughly equivalent to a high-resolution 1 μm<sup>2</sup> SEM image) is the gradual destruction of delocalised electron structures, including the thiophene ring, as chemical bonds are broken. Hydrogen and short-chain hydrocarbon ions are emitted, or 'desorbed' from the sample as a result of these interactions, although the escape of longer carbon chains is restricted by entanglement with

surrounding molecules[127]. After extended irradiation, hydrogen is expelled from the irradiated region completely and a carbon skeleton remains with graphitic properties.

For the work in this thesis, it should be noted however that whilst sensitive to electron irradiation in comparison to many inorganic materials, conjugated polymers are far more resilient than most organic materials[128]. This is a result of the large delocalised  $\pi$ -electron structures in the materials, which act to rapidly dissipate any absorbed energy from an inelastic beam interaction[85]. For example, the large number of available states in a  $\pi$ -conjugated system (Section 2.3) allows for the loss of an electron to be compensated by the rearrangement of the remaining electrons in the system[127]. This effect helps to slow the rate of radiation damage to conjugated polymer molecules.

Whilst it is perhaps intuitive to expect that the damage incurred by the sample upon electron beam exposure will decrease with the energy of the incident beam, this is not necessarily the case. Certainly some types of irradiation damage are minimised to the point of being negligible with LVSEM, for example ‘knock-on’ damage, whereby electron impact causes displacement of sample atoms[78]. However, the incident energy from even the lowest energy primary beams realistically feasible for high-quality imaging in a SEM (a few hundred eV) is still more than sufficient to cause significant damage effects on polymeric materials[100]. In fact the inelastic collision cross-section is greater at low beam energies, and the smaller interaction volume of lower energy beams means that this energy tends to be deposited closer to the surface[129]. Importantly in the context of SE imaging, this effect also results in the generation of a far stronger SE signal for a given beam current at low beam energies. As such, the electron dose required to generate a high-quality SE image in a LVSEM configuration is smaller than that required at more conventional high energies[100] – this can help to reduce beam damage at low energies.

**3) Contamination:** Whilst an issue affecting practically any sample imaged in the SEM, contamination is a particularly important consideration when imaging polymers, especially using LVSEM[98], [100]. Short-chain hydrocarbons can be present on improperly cleaned samples or on any surface inside the SEM vacuum chamber, which are able to diffuse and migrate over the

sample at room temperature. If contacted by the electron beam, these hydrocarbons can polymerise and form a thin film obscuring the surface of the sample, an effect known as contamination[100], [130]. Thorough sample cleaning, as well as high vacuum levels and regular cleaning of the sample chamber can help to minimise these contamination effects by limiting the presence of these hydrocarbons in the microscope environment. However, when imaging polymers, the electron beam can crack hydrocarbons on the sample surface, resulting in the emission of short chain hydrocarbons (as previously noted in this section)[126]. These will polymerise under the electron beam to form contamination layers regardless of the sample or chamber cleanliness[100].

Imaging contaminated samples is a particular challenge in LVSEM conditions due to the small interaction volume of the beam and surface sensitivity of the resulting images[98], [129]. As such, if a contamination layer is present, the content of SEM images taken with a low-energy primary beam will be significantly more affected than those taken at higher energies. Little can be done to mitigate this effect using ‘conventional’ SEM techniques (although energy-filtered SEM has been shown to enable imaging through a contamination layer[131] – see Section 2.7.2). Again, here the solution is to reduce the electron dose received by the sample, and attempt to limit the initial formation of the layer.

**4) Perspective on polymer imaging in the SEM:** It is clear that polymer materials are highly sensitive to electron beam irradiation. However, it should be noted that by operating the SEM with consideration of these irradiation effects, the worst issues can be mitigated. The typical course of action is to image in LVSEM conditions, and minimise the electron dose incident on the sample (by reducing beam current, dwell time or magnification). As already noted, reducing the incident dose often requires a trade-off with image quality, however a balance that enables a quality image to be acquired with minimal damage, charging or contamination can usually be found. This is evidenced by the wealth of published work that has employed SEM techniques to image polymer, or even biological, samples in high resolution[114], [132]–[134]. For all work in

this thesis, polymer imaging considerations formed a crucial part of the SEM methodologies used, with specific details given in Chapter 3.

### ***Section 2.6.5: Generation of material contrast from polymer:fullerene blends***

Mapping the phase-separated morphology of a polymer:fullerene blend in the SEM is a significant challenge as material contrast between organic materials is inherently low. In the case of SE images, the similar chemical composition and electron density between various polymers results in very similar SE yields, at least for primary beam energies large enough for high-resolution imaging in the SEM[135] (some dramatic yield variation between polymers occurs for primary beam energies <500 V[136]). As a result, creating chemical maps of polymer blends using SE emission is extremely difficult, especially if the sample is not completely flat and topographical contrast is visible[137]. This issue is compounded by the low SE emission coefficient of carbon-based materials[98], which makes the generation of images with good SNR difficult, especially when excessive irradiation can cause sample damage. Further, the high ratio of SE<sub>1</sub> to SE<sub>2</sub> in carbon-based materials (Section 2.6.2) means that the more material-sensitive, BSE-generated SE<sub>2</sub> signal constitutes only a small fraction of the SE signal.

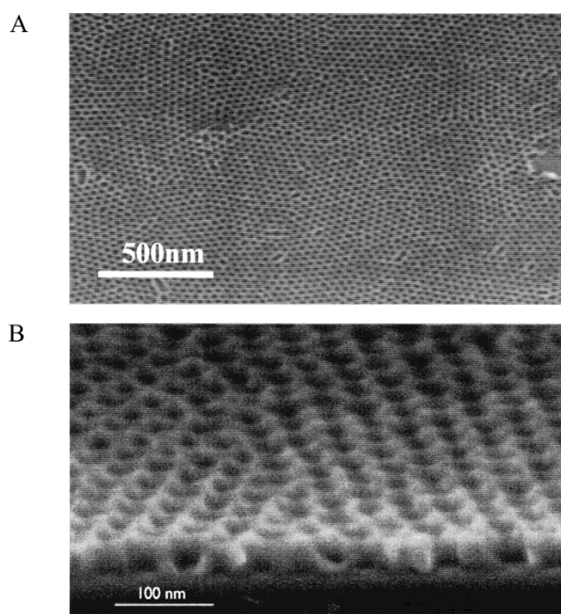


***Figure 2.23: SEM imaging of Polystyrene – Poly(methylmethacrylate) (PMMA) diblock copolymer film morphology by selective dissolution of the PMMA component. Morphology shown in a) plan view and b) cross-section, showing the selective dissolution effect. Reproduced from [138] with permission from Wiley.***

Early attempts at visualising micron-scale phase separation in polymer blend samples using SE images required imaginative sample preparation. Examples include sample staining[132], attempts at the selective dissolution of one phase (Figure 2.23) [137], [138], or the fracturing of a sample at a temperature above the glass transition of one material but below that of the other, allowing for one phase to remain intact during the fracturing process[139]. Almost certainly, these sample preparation techniques generate artefacts that would completely obscure the nanoscale morphology of a polymer:fullerene OPV blend[98]. In the context of OPV, the SEM has never been successfully employed to map nanoscale phase-separation in the active layer, as it is prohibitively difficult to generate the contrast required using conventional imaging techniques[64].

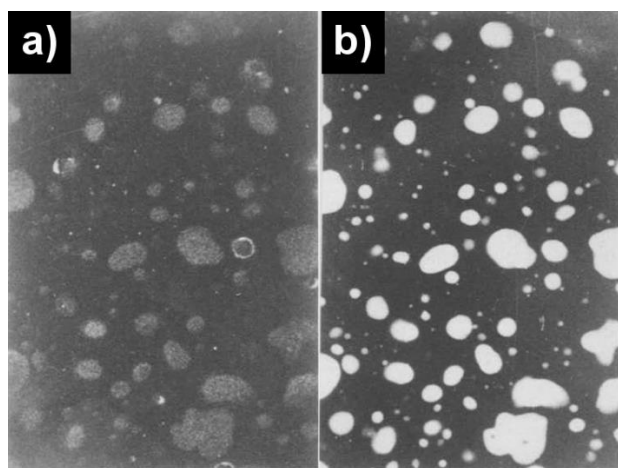


**Figure 2.24:** Polystyrene/Ethylene-propylene-diene rubber (EPDM) blend stained with  $\text{OsO}_4$  vapour, and imaged with a) SEs and b) BSEs. EPDM phases are more heavily stained and appear significantly brighter in the BSE image. Reproduced from [132] with permission from Elsevier.

Similar contrast-generation issues are found when applying conventional BSE imaging techniques to polymer blends. Polymers have a low atomic number (consisting primarily of hydrogen and carbon) and have relatively low density[98]. The backscattering coefficient of polymers and fullerenes is therefore low, and the BSE imaging signal again poor. Similarly to SE imaging, staining techniques have commonly been used to boost the available contrast from BSE images of polymer blends. For BSE images, blend films are exposed to oxidising compounds containing heavy elements, for example  $\text{OsO}_4$ [139], or more recently  $\text{RuO}_4$ [116], [140], [141],

are attached to one phase. In a polymer system where staining is effective, the staining agent will react more readily with one blend component than the other, significantly increasing the average atomic number of that component. As a result, the more heavily stained component generates a significantly stronger BSE signal and appears as bright regions in BSE images. Staining methods with RuO<sub>4</sub> have been used in limited cases to aid attempts to image P3HT:PCBM blends in the TEM[142], however have never reached wide scale adoption in OPV. This is perhaps due to the formation of RuO<sub>2</sub> nanocrystals on the surface of stained samples, which affect image contrast on the scale of a few nm[143] and inhibit high-resolution imaging.

Clearly, conventional SEM techniques, even those developed for optimal polymer imaging, are not adequate for nanoscale polymer:fullerene phase mapping. In this thesis, new and emerging advanced techniques in the SEM are applied to resolve this issue. Recent advancements in low-voltage BSE imaging are adapted and applied to image OPV blends in Chapter 6; the background and novelty of this technique is addressed fully within that chapter. In Chapters 4-5, secondary electron spectroscopy and energy-filtered secondary electron imaging are applied as tools for generating ultra-high-resolution maps of polymer-fullerene blends using SE emissions. Whilst a developing technique in the context of modern SEM, a small body of literature regarding the nature and origin of SE spectra was published in the earlier stages of the SEM's development. Some aspects of this early work most relevant to this thesis are summarised in the next section.

### **Section 2.7: Secondary electron spectroscopy in the SEM**

In theory, secondary electron spectra can easily be used as an empirical tool to enable boosted material contrast in the SEM, assuming the researcher has access to a tool capable of SE spectroscopy. In the context of a polymer:fullerene blend, the SE spectrum of the polymer and fullerene can be measured separately, and used to inform a spectral window in which images of polymer:fullerene blends can be imaged with improved material contrast[17]. This is largely the concept of the paper constituting Chapter 5, where little attempt was made at understanding the nature and origin of the spectra (the nature of SE spectra emitted from P3HT is the subject of

Chapter 4). A similar concept has been used to improve dopant contrast in images of p-n junctions in silicon[144].

Despite this, recent applications of SE spectroscopy are relatively rare. This is a combination of two factors: 1) A lack of modern LVSEMs that are equipped with the capability for SE spectroscopy[17], and 2) The complex nature of SE spectra, which, although demonstrated to be reproducible and unique for a given material in an SEM[104], result from a wide range of complex beam-sample interactions. SE spectra are therefore difficult to interpret as relating to physical properties of the sample[145]. As previously noted, various attempts at developing an understanding of the origin of the SE spectrum emitted by carbon samples under electron beam irradiation have been made.

### ***Section 2.7.1: Physical aspects of a secondary electron spectrum***

Prior to this thesis, very few SE spectra have been measured from polymeric materials[104]. However, highly-ordered pyrolytic graphite (HOPG) has proved a popular reference sample for testing the nature of an SE spectrum[146]–[148]. One particular benefit is that its molecular structure, with 2-dimensional graphene planes loosely bonded together in a layered formation, enables ‘cleaving’, or the removal of the topmost layers before performing spectroscopy experiments[146]. This removes the effects of surface contamination and enables a fresh, reproducible surface to be probed – this is of great importance when studying surface sensitive emissions. For the purpose of this thesis, studies of graphite or allotrope forms of carbon[149] are the most relevant analogues in the literature, with their electronic structures based upon similar  $\pi$  and  $\sigma$  orbital systems already discussed in Section 2.3.

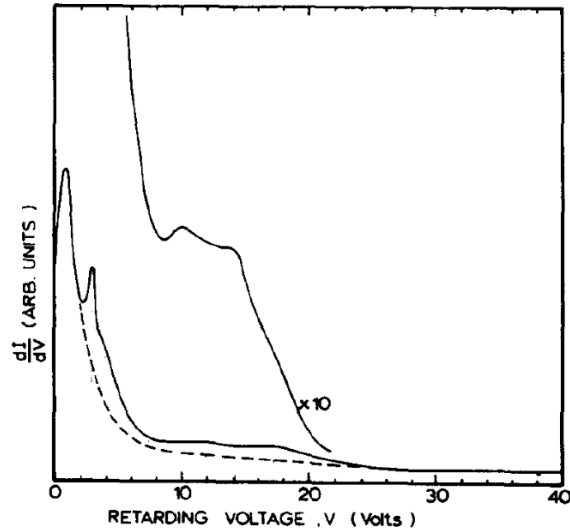


**Figure 2.25:** SE spectrum emitted from HOPG. Dashed line is the estimated shape of the initial onset peak, on to which further features are superimposed. Plot marked '×10' is a 10-factor magnification of the higher energy spectrum range, allowing fine structure in the spectrum at higher energies to be observed more clearly. Reprinted from [146] with permission from Elsevier.

The shape of a typical graphite spectrum is displayed in Figure 2.25. The most notable feature immediately apparent is the large onset peak, known as the 'cascade' peak[150]. Whilst present in all SE spectra and usually the dominant feature, this is perhaps the least informative feature in the spectrum. Primary beam electrons entering the sample collide inelastically with multiple electrons in the sample, exciting them to higher-energy states. As a result, these now-secondary electrons will propagate through the sample (in semiconductors or insulators, excited SEs occupy conduction band states[151], [152]), and will undergo further, random inelastic scattering events that will transfer this energy to more electrons, phonons or plasmons[153]. The random nature of these multiple inelastic collisions dissipates the primary beam energy over a large number of secondary electrons which, by undergoing multiple further inelastic scattering events, will have small and randomly distributed energies. The emission of electrons resulting from this 'cascade' effect forms the major low-energy peak of the typical SE spectrum[146].

As noted by Willis *et al.*[146] and Papagno *et al.*[148], and visible in Figure 2.25, the SE spectrum of graphite has further peaks superimposed on this cascade feature. This suggests that more SE are emitted from certain energy levels within the sample. Willis *et al.* noted that the locations of

these peaks correlate to minima in the various graphite conduction bands[154], and proposed that SEs excited by an inelastic collision will relax (via electron-phonon interactions, for example) to these minima before emission, thus making emission from these energy levels more likely. Based upon this finding, SE spectroscopy has been used to probe the conduction band structure of graphite[147], and to investigate the graphitic nature of carbon fibre surfaces[149].

In the context of polymers, SE energy spectra have never been employed to this end. However, some notable works have investigated the effect of material properties on the SE yield of various polymers, with implications for the findings in this thesis (Chapter 4). In the case of semiconducting polymers, the presence of  $\pi$ -electron orbitals and extended delocalised electron structures in a given polymer material are important to SE emission. In any semiconducting or insulating sample, ground state electrons must be excited across the electronic band gap (between HOMO and LUMO) and into a conduction band in order to be transported to the surface and emitted[85], [155]. SEs excited directly into the LUMO by the primary beam will travel through the material and undergo various inelastic collisions as discussed above. For SEs with energies above a certain threshold level[151], the most likely collision for the SE is for it to transfer energy to a valence-band (HOMO) electron[151]. As an electron cannot have an energy within the band gap, this HOMO electron must be excited across the band gap for this interaction to occur[152]. As such, the band-gap is thought to play an important role in the SE emissions of semiconductors and insulators[151], [152], [156], [157].

Work by Kishimoto *et al.* [85] has suggested that for organic materials, the fraction of  $\pi$ -electrons with respect to  $\sigma$ -electrons within the material plays an important role in the SE mean free path and as such its SE yield. As the band gap of  $\pi$ -electron structures is significantly smaller than for  $\sigma$ -electrons ( $sp^3$ -hybridised polymers containing only  $\sigma$ -bonds are considered insulators[1])  $\pi$ -electrons are more easily excited by inelastic collisions with a propagating SE. It was therefore postulated that SEs transported through materials containing a larger fraction of  $\pi$ -electrons will collide with ground-state electrons more frequently and dissipate their energy faster, reducing the SE yield of the material.

Building upon this concept, it has been suggested that SEs transported through a material with energies below a certain threshold level  $E_t$  above the LUMO do not interact inelastically with HOMO-level electrons[151]. Below  $E_t$ , a SE does not have the energy required to generate an electron-hole pair by scattering a HOMO-level electron in to the LUMO[152]. For SEs transported below  $E_t$ , this reduces the probability of electron-electron collisions and dramatically improves SE transport to the surface.  $E_t$  is highly dependent on  $E_g$  (explaining the effect observed by Kishimoto *et al.* [85]), however the shape of the electron band structure, and any exciton binding energy between the generated electron and hole can also affect its value[151]. Estimates of  $E_t$  range from  $\sim 1.5E_g$ [151] to  $\sim 3E_g$ [152]. In some materials, particularly some insulators which demonstrate electron affinity  $\chi \ll E_g$ , electrons can be emitted to the vacuum level from below  $E_t$  and as such the material's SE yield becomes extremely high[152]. The band gap of the semiconducting polymers investigated in this thesis is not large enough for this effect to occur however[156]. Nonetheless, the presence of even a small ( $<1$  eV) band gap in the electronic structure of the material has been demonstrated to have a significant effect on a material's SE yield, by limiting the number of states in to which a HOMO-level electron can be scattered by a SE[152]. This reduces the frequency of electron-electron interactions for a propagating SE and increases its mean free path. The size of a band gap in a semiconducting polymer material may therefore play an important role in defining the nature of its SE emission and therefore its SE spectrum. It should be noted however that the relevance of this effect on the SE yield of a polymer has been called in to question by the results of more recent SE yield experiments [135]. This is due to the specific, complex nature of electronic transport in a polymer (Section 2.3.2).

The role of electron transport in defining the SE yield of a polymer sample was observed with differently processed, but compositionally identical, samples demonstrating SE yield variation[135], [136]. This is an unsurprising effect related to the discussion of polymer charge transport in Section 2.3.2, whereby polymer samples processed with a greater degree of order show improved charge transport, with fewer traps and longer mean free paths. Simply, a SE generated in a more ordered polymer sample will be more likely to reach the surface and escape,

giving improved SE yield. Once more, it is clear that this can have important implications for the origin of features in SE spectra (Chapter 4); with more ordered polymer samples (or even regions of a single sample) offering different SE transport properties to less ordered ones, with this variation reflected in the emitted SE spectrum.

### ***Section 2.7.2: Secondary electron spectrometers in the SEM***

In order to probe the SE spectrum of a sample, an electron detector capable of selectively detecting emitted electrons based upon their energy is required. Conventional SEM operation regularly employs a degree of energy-selective detection in the process of acquiring BSE images with an ETD, for example[98]. Here, the grid mounted over the aperture of the scintillator detector can be biased with a small negative voltage, which will repel SEs due to their low energy but allow higher energy BSEs to pass through and reach the detector. However, this arrangement constitutes a crude energy filter, with its mounting away from the beam axis resulting in collection efficiency that depends on SE emission angle as well as energy[110]. Improved collection efficiency and fine control over the energy-selectivity of the detector are required for suitable SE spectroscopy characteristics.

The early attempts at SE spectroscopy discussed in Section 2.7.1 were not performed in SEM conditions, rather low-energy electron diffraction systems modified for optimal SE spectroscopy performance[158]. Using such equipment for SE spectroscopy however removes the possibility of applying energy-filtered SE detection for high-resolution imaging[104]. More accurate, high-resolution SE spectroscopy has been applied successfully in SEM conditions, using a wide range of increasingly novel spectrometer designs. A detailed account of the various spectrometer concepts developed over the SEM's history is given in [113].

In Chapters 4 and 5 of this thesis, the operation of the TLD designs discussed in Section 2.6.3 is altered in order to perform SE spectroscopy without the need for specially designed detectors. This ensures that the wider accessibility of the techniques is maximised, and allows for high-quality imaging to be performed concurrently with energy-selective SE detection [17] (Section 2.6.3).

In the case of both the XL-30 and Elstar designs used in the course of Chapters 4 and 5, the bias on the suction electrode is increased when performing energy-selective SE detection[159]. This has two effects[110]: firstly to maximise SE collection efficiency, and secondly to reduce the effect of SE emission angle on detection efficiency. Without a suction bias, SEs emitted at small angles relative to the beam incidence are more likely to pass up the electron column and reach the TLD than those emitted at larger angles (even accounting for the ‘trapping’ effect of the immersion lens fields discussed in Section 2.6.3). This has the potential to skew the nature of the detected SE spectrum[159] (an effect discussed in detail in Chapter 4).

For the XL-30 column, energy selective detection of SEs is performed by reducing the bias on the deflector electrode, which pushes SEs passing up the electron column towards the scintillation detector (see Figure 2.19a)[17]. In normal operation, the bias on this detector should be large enough to deflect all collected SEs on to the detector, in order to generate the strongest possible imaging signal. However, when this bias is reduced, higher energy electrons passing up the column are not deflected through a large enough angle to be incident on the detector[110]. This places a low-pass filter on the electrons reaching the detector and contributing to the imaging signal, with the cut-off energy for SE detection decreasing as the bias is reduced. SE spectra are measured by taking a stack of images from a sample over a range of deflector biases, with the image brightness at each deflector bias taken as an analogue for the number of SEs below the detection cut-off energy at that bias. Details of the specific spectrum acquisition methods are given ref. [110] and Chapter 3.

In the case of the Elstar TLD (Figure 2.19b) the negatively biased ‘Mirror’ electrode at the top of the detector assembly is used to control the energy of the SEs that are ‘trapped’ in the detector assembly and subsequently deflected towards the detector. Electrons pass into the bottom of the assembly with a velocity related to their initial emission energy. By reducing the magnitude of the negative bias on the mirror electrode, or even applying an increasing positive bias, higher-energy electrons are allowed to pass through the TLD assembly and not contact the detector[17]. Once again, this has the effect of placing a low-pass energy filter on the detected electrons. The

method for measuring an SE spectrum is the same as with the XL-30, with image brightness taken as an analogue for the number of SEs emitted with energies below the detection cut-off as set by the Mirror electrode bias.

By employing a conventional TLD as an energy-selective SE detector, energy-filtered SE images can be acquired. This works similarly to energy-filtered TEM (Section 2.5.1), where the EELS spectra of two materials is acquired and used to inform a spectral window in which contrast between those materials is improved over conventional, non-filtered TEM[46]. Likewise, with energy-filtered SEM (EFSEM), the SE energy spectra emitted by two different materials or material phases informs energy window in which high-contrast material mapping with SEs is possible[17].

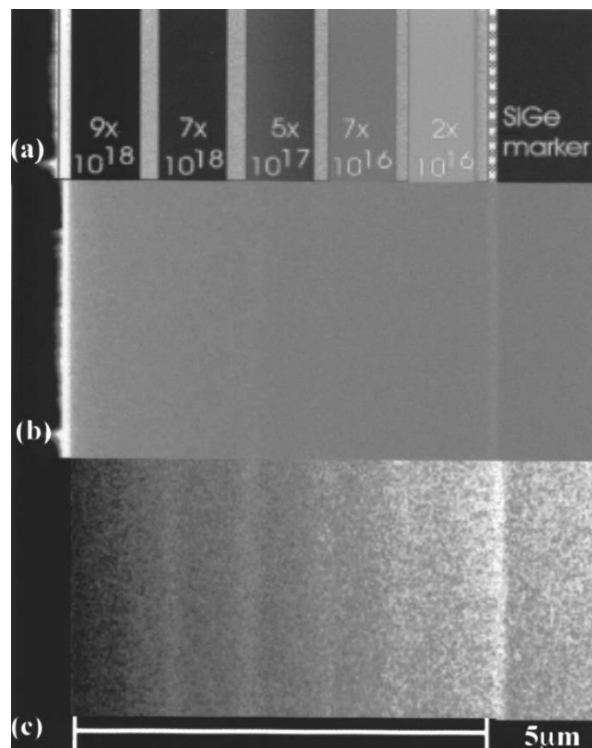


**Figure 2.26:** EFSEM using a XL-30 based TLD used to improve dopant contrast in silicon. Part a) depicts the test structure, with differently n-doped regions separated by regions of intrinsic material. Part b) is a conventional, non-filtered SE image of the test structure, and part c) shows a low-pass energy-filtered SE image of the same region, demonstrating significantly improved dopant contrast. Reprinted from [160] with permission from AIP publishing.

EFSEM imaging techniques using an adapted TLD have been most notably used in recent years for dopant mapping in silicon samples[144], [160]. Here, the SE spectra emitted from differently-

doped regions of silicon were noted to shift in energy relative to each other, enabling an ideal imaging window which the dopant level could be spatially mapped with improved contrast, using a low deflector bias (see Figure 2.26).

Low-pass energy-filtered SE imaging has also been shown to reduce the impact of contamination layers on imaging contrast[131], by imaging using only low-energy SEs. As it travels through the sample, the energy of an individual SE is rapidly attenuated by various inelastic interactions (Section 2.7.1). This rapid attenuation effect is exacerbated by the shorter inelastic mean free path (IMFP) of higher energy SEs (the IMFP of a 50 eV SE in P3HT is  $\sim 1.5$  nm, less than half that of a 10 eV SE)[161]. SEs that are generated by a primary beam interaction near the surface, however, can travel a distance  $\leq 1$  IMFP prior to escaping the sample, and as such will undergo few inelastic collisions before emission. As such, SEs generated near the surface can be emitted with energies significantly higher than those generated deeper beneath the sample surface due to reduced attenuation.

As a result, by imaging only with SEs of lower energies, a significant fraction of SEs generated near the surface are filtered out. For a highly contaminated sample, this is important, as the SE signal generated near the surface will only reflect the properties of the contamination layer. By imaging using only lower energy SEs, more of the imaging signal is generated beneath this layer, and images better reflect the properties of the sample beneath[131].

This effect is particularly important in the context of Chapter 5 of this thesis, whereby low-pass energy-filtered imaging is used to image a polymer:fullerene blend (which, as noted in Section 2.6.4, will contaminate easily). By employing energy-filtered imaging, EFSEM helps to image through contamination layers, probing the nanoscale morphology of the polymer:fullerene blend beneath.

## **Section 2.8: Conclusions**

As this thesis concerns advances at the junction of advanced scanning electron microscopy and organic photovoltaics, it has been necessary to discuss a broad range of topics in this Chapter.

The current state of understanding regarding the origin and nature of charge transport in polymers, and the properties of an efficient organic photovoltaic film constitute the context of the work in the following Chapters. The present state of organic photovoltaic morphology characterisation consists of a large number of competing methods, each with unique strengths as well as weaknesses that, especially in the case of the most powerful characterisation methods, limit the broad applicability of the technique. The need for the advancements presented in this thesis is clear when set against this background – powerful, yet fast, widely available and broadly applicable methods to probe the detailed nature of OPV systems are in short supply at present. Advanced methods in the SEM, specifically energy-filtered SE imaging and low-energy BSE methods have never been applied in the context of polymer blend imaging. However, these have the potential to offer more user-friendly and widely available approach to high-quality OPV morphology characterisation.

## Section 2.9: References

- [1] M. Geoghegan and G. Hadziioannou, *Polymer Electronics*. Oxford University Press, 2013.
- [2] W. Barford, *Electronic and Optical Properties of Conjugated Polymers*. Oxford University Press, 2005.
- [3] A. J. Heeger, N. S. Sariciftci, and E. B. Namdas, *Semiconducting and Metallic Polymers*. 2010.
- [4] W. Shockley and H. J. Queisser, “Detailed Balance Limit of Efficiency of p-n Junction Solar Cells,” *J. Appl. Phys.*, vol. 32, no. 3, pp. 510–519, Mar. 1961.
- [5] J. Zhao *et al.*, “Efficient organic solar cells processed from hydrocarbon solvents,” *Nat. Energy*, vol. 1, no. 2, p. 15027, 2016.
- [6] T. Kirchartz, K. Taretto, U. Rau, V. Ief-photo, and F. Ju, “Efficiency Limits of Organic Bulk Heterojunction Solar Cells,” vol. 1, pp. 17958–17966, 2009.
- [7] G. J. Hedley, A. Ruseckas, and I. D. W. Samuel, “Light Harvesting for Organic Photovoltaics,” *Chem. Rev.*, vol. 117, no. 2, pp. 796–837, Jan. 2017.
- [8] A. Polman, M. Knight, E. C. Garnett, B. Ehrler, and W. C. Sinke, “Photovoltaic materials: Present efficiencies and future challenges,” *Science (80-. )*, vol. 352, no. 6283, p. aad4424-aad4424, Apr. 2016.
- [9] J. Nelson, “Polymer:fullerene bulk heterojunction solar cells,” *Mater. Today*, vol. 14, no. 10, pp. 462–470, Oct. 2011.
- [10] P. W. Atkins and R. S. Friedman, *Molecular Quantum Mechanics*, 5th editio. Oxford University Press, 2010.

- [11] N. Li *et al.*, “Abnormal strong burn-in degradation of highly efficient polymer solar cells caused by spinodal donor-acceptor demixing,” *Nat. Commun.*, vol. 8, no. February, p. 14541, Feb. 2017.
- [12] W. Su, J. Schrieffer, and A. J. Heeger, “Soliton excitations in polyacetylene,” *Phys. Rev. B*, vol. 22, no. 4, pp. 2099–2111, Aug. 1980.
- [13] S. Stafstrom, “Electron localization and the transition from adiabatic to nonadiabatic charge transport in organic conductors,” *Chem. Soc. Rev.*, vol. 39, no. 7, p. 2484, 2010.
- [14] K. Tremel and S. Ludwigs, “Morphology of P3HT in Thin Films in Relation to Optical and Electrical Properties,” in *P3HT Revisited - From Molecular Scale to Solar Cell Devices*, vol. 265, 2014, pp. 39–82.
- [15] L. Dou *et al.*, “25th anniversary article: A decade of organic/polymeric photovoltaic research,” *Adv. Mater.*, vol. 25, no. 46, pp. 6642–6671, 2013.
- [16] R. Noriega *et al.*, “A general relationship between disorder, aggregation and charge transport in conjugated polymers,” *Nat. Mater.*, vol. 12, no. 11, pp. 1038–44, 2013.
- [17] R. C. Masters *et al.*, “Sub-nanometre resolution imaging of polymer–fullerene photovoltaic blends using energy-filtered scanning electron microscopy,” *Nat. Commun.*, vol. 6, p. 6928, 2015.
- [18] R. C. Masters *et al.*, “Novel organic photovoltaic polymer blends: A rapid, 3-dimensional morphology analysis using backscattered electron imaging in the scanning electron microscope,” *Sol. Energy Mater. Sol. Cells*, vol. 160, pp. 182–192, Feb. 2017.
- [19] Y. Liu *et al.*, “Multiple Cases of High-Efficiency Polymer Solar Cells,” *Nat. Commun.*, vol. 5, p. 5923, 2014.
- [20] W. Ma *et al.*, “Influence of Processing Parameters and Molecular Weight on the Morphology and Properties of High-Performance PffBT4T-2OD:PC71BM Organic Solar Cells,” *Adv. Energy Mater.*, vol. 5, no. 23, 2015.
- [21] M. Brinkmann and P. Rannou, “Molecular Weight Dependence of Chain Packing and Semicrystalline Structure in Oriented Films of Regioregular Poly(3-hexylthiophene) Revealed by High-Resolution Transmission Electron Microscopy,” *Macromolecules*, vol. 42, no. 4, pp. 1125–1130, Feb. 2009.
- [22] M. Brinkmann, F. Chandezon, R. B. Pansu, and C. Julien-Rabant, “Epitaxial growth of highly oriented fibers of semiconducting polymers with a shish-kebab-like superstructure,” *Adv. Funct. Mater.*, vol. 19, no. 17, pp. 2759–2766, 2009.
- [23] A. J. Pearson *et al.*, “Rationalizing Phase Transitions with Thermal Annealing Temperatures for P3HT:PCBM Organic Photovoltaic Devices,” *Macromolecules*, vol. 45, no. 3, pp. 1499–1508, Feb. 2012.
- [24] Y. Yao, H. Dong, and W. Hu, “Ordering of conjugated polymer molecules: recent advances and perspectives,” *Polym. Chem.*, vol. 4, no. 20, p. 5197, 2013.
- [25] H. Klauk, “Organic thin-film transistors,” *Chem. Soc. Rev.*, vol. 39, no. 7, p. 2643, 2010.
- [26] K. Kanai, T. Miyazaki, H. Suzuki, M. Inaba, Y. Ouchi, and K. Seki, “Effect of annealing on the electronic structure of poly(3-hexylthiophene) thin film,” *Phys. Chem. Chem. Phys.*, vol. 12, no. 1, pp. 273–282, 2010.
- [27] V. Podzorov, “Conjugated polymers: Long and winding polymeric roads,” *Nat. Mater.*, vol. 12, no. 11, pp. 947–8, 2013.
- [28] A. Facchetti, “ $\pi$ -Conjugated polymers for organic electronics and photovoltaic cell applications,” *Chem. Mater.*, vol. 23, no. 3, pp. 733–758, 2011.

- [29] W. Zhang *et al.*, “Indacenodithiophene Semiconducting Polymers for High-Performance, Air-Stable Transistors,” *J. Am. Chem. Soc.*, vol. 132, no. 33, pp. 11437–11439, Aug. 2010.
- [30] P. Kohn *et al.*, “Crystallization-Induced 10-nm Structure Formation in P3HT/PCBM Blends,” *Macromolecules*, vol. 46, no. 10, pp. 4002–4013, May 2013.
- [31] N. D. Arora, J. R. Hauser, and D. J. Roulston, “Electron and hole mobilities in silicon as a function of concentration and temperature,” *IEEE Trans. Electron Devices*, vol. 29, no. 2, pp. 292–295, 1982.
- [32] D. O’Brien, M. S. Weaver, D. G. Lidzey, and D. D. C. Bradley, “Use of poly(phenyl quinoxaline) as an electron transport material in polymer light-emitting diodes,” *Appl. Phys. Lett.*, vol. 69, no. 7, p. 881, 1996.
- [33] D. Hertel, E. V. Soh, H. Bässler, and L. J. Rothberg, “Electric field dependent generation of geminate electron–hole pairs in a ladder-type  $\pi$ -conjugated polymer probed by fluorescence quenching and delayed field collection of charge carriers,” *Chem. Phys. Lett.*, vol. 361, no. 1–2, pp. 99–105, Jul. 2002.
- [34] B. a. Gregg and M. C. Hanna, “Comparing organic to inorganic photovoltaic cells: Theory, experiment, and simulation,” *J. Appl. Phys.*, vol. 93, no. 6, p. 3605, 2003.
- [35] I. G. Scheblykin, A. Yartsev, T. Pullerits, V. Gulbinas, and V. Sundström, “Excited state and charge photogeneration dynamics in conjugated polymers,” *J. Phys. Chem. B*, vol. 111, no. 23, pp. 6303–6321, 2007.
- [36] A. J. Heeger, “Semiconducting polymers: the Third Generation.,” *Chem. Soc. Rev.*, vol. 39, no. 7, pp. 2354–71, Jul. 2010.
- [37] P. E. Shaw, A. Ruseckas, and I. D. W. Samuel, “Exciton Diffusion Measurements in Poly(3-hexylthiophene),” *Adv. Mater.*, vol. 20, no. 18, pp. 3516–3520, Jul. 2008.
- [38] M. Sim *et al.*, “Dependence of Exciton Diffusion Length on Crystalline Order in Conjugated Polymers,” *J. Phys. Chem. C*, vol. 118, no. 2, pp. 760–766, 2014.
- [39] S. H. Park *et al.*, “Bulk heterojunction solar cells with internal quantum efficiency approaching 100%,” *Nat. Photonics*, vol. 3, no. 5, pp. 297–302, Apr. 2009.
- [40] Y.-C. C. Tseng and S. B. Darling, “Block Copolymer Nanostructures for Technology,” *Polymers (Basel)*, vol. 2, no. 4, pp. 470–489, Oct. 2010.
- [41] S. B. Darling and F. You, “The case for organic photovoltaics,” *RSC Adv.*, vol. 3, no. 39, pp. 17633–17648, 2013.
- [42] C. W. Tang, “Two-layer organic photovoltaic cell,” *Appl. Phys. Lett.*, vol. 48, no. 2, p. 183, 1986.
- [43] R. A. L. Jones, *Soft Condensed Matter*. Oxford University Press, 2002.
- [44] S. Walheim, M. Böltau, J. Mlynek, G. Krausch, and U. Steiner, “Structure Formation via Polymer Demixing in Spin-Cast Films,” *Macromolecules*, vol. 30, no. 17, pp. 4995–5003, Aug. 1997.
- [45] W. Chen *et al.*, “Hierarchical nanomorphologies promote exciton dissociation in polymer/fullerene bulk heterojunction solar cells.,” *Nano Lett.*, vol. 11, no. 9, pp. 3707–13, Sep. 2011.
- [46] M. Pfannmöller *et al.*, “Visualizing a homogeneous blend in bulk heterojunction polymer solar cells by analytical electron microscopy.,” *Nano Lett.*, vol. 11, no. 8, pp. 3099–3107, Aug. 2011.
- [47] M. Campoy-Quiles *et al.*, “Morphology evolution via self-organization and lateral and vertical diffusion in polymer:fullerene solar cell blends.,” *Nat. Mater.*, vol. 7, no. 2, pp. 158–64, Feb. 2008.

- [48] C. J. Brabec, M. Heeney, I. McCulloch, and J. Nelson, "Influence of blend microstructure on bulk heterojunction organic photovoltaic performance.," *Chem. Soc. Rev.*, vol. 40, no. 3, pp. 1185–99, Mar. 2011.
- [49] F. C. Krebs, "Fabrication and processing of polymer solar cells: A review of printing and coating techniques," *Sol. Energy Mater. Sol. Cells*, vol. 93, no. 4, pp. 394–412, 2009.
- [50] N. E. Jackson, B. M. Savoie, T. J. Marks, L. X. Chen, and M. A. Ratner, "The Next Breakthrough for Organic Photovoltaics?," *J. Phys. Chem. Lett.*, vol. 6, pp. 77–84, 2015.
- [51] E. Moons, "Conjugated polymer blends: linking film morphology to performance of light emitting diodes and photodiodes," *J. Phys. Condens. Matter*, vol. 14, no. 47, pp. 12235–12260, Dec. 2002.
- [52] T. Wang *et al.*, "The development of nanoscale morphology in polymer:fullerene photovoltaic blends during solvent casting," *Soft Matter*, vol. 6, no. 17, pp. 4128–4134, 2010.
- [53] Y.-C. Huang, H.-C. Cha, C.-Y. Chen, and C.-S. Tsao, "Morphological control and performance improvement of organic photovoltaic layer of roll-to-roll coated polymer solar cells," *Sol. Energy Mater. Sol. Cells*, vol. 150, pp. 10–18, 2016.
- [54] J. F. Chang *et al.*, "Enhanced Mobility of poly(3-hexylthiophene) transistors by spin-coating from high-boiling-point solvents," *Chem. Mater.*, vol. 16, no. 23, pp. 4772–4776, 2004.
- [55] V. Kumar, H. Wang, and C. Rodenburg, "High-efficiency inverted polymer solar cells via dual effects of introducing the high boiling point solvent and the high conductive PEDOT : PSS layer," *Org. Electron.*, vol. 15, no. 9, pp. 2059–2067, 2014.
- [56] S. Guo *et al.*, "Solvent–Morphology–Property Relationship of PTB7:PC 71 BM Polymer Solar Cells," *ACS Appl. Mater. Interfaces*, vol. 9, no. 4, pp. 3740–3748, Feb. 2017.
- [57] H. Hoppe and N. S. Sariciftci, "Morphology of polymer/fullerene bulk heterojunction solar cells," *J. Mater. Chem.*, no. 16, pp. 45–61, 2006.
- [58] D. Chen, A. Nakahara, D. Wei, D. Nordlund, and T. P. Russell, "P3HT/PCBM bulk heterojunction organic photovoltaics: correlating efficiency and morphology.," *Nano Lett.*, vol. 11, no. 2, pp. 561–7, Mar. 2011.
- [59] A. J. Parnell *et al.*, "Nanoscale Phase Separation of P3HT PCBM Thick Films As Measured by Small-Angle X-ray Scattering," *Macromolecules*, vol. 44, no. 16, pp. 6503–6508, Aug. 2011.
- [60] H. Chen, R. Hegde, J. Browning, and M. D. Dadmun, "The miscibility and depth profile of PCBM in P3HT: thermodynamic information to improve organic photovoltaics," *Phys. Chem. Chem. Phys.*, vol. 14, no. 16, p. 5635, 2012.
- [61] E. Verploegen, R. Mondal, C. J. Bettinger, S. Sok, M. F. Toney, and Z. Bao, "Effects of Thermal Annealing Upon the Morphology of Polymer-Fullerene Blends," *Adv. Funct. Mater.*, vol. 20, no. 20, pp. 3519–3529, Oct. 2010.
- [62] D. M. DeLongchamp *et al.*, "Variations in semiconducting polymer microstructure and hole mobility with spin coating speed," *Chem. Mater.*, vol. 17, no. 23, pp. 5610–5612, 2005.
- [63] P. G. Nicholson and F. A. Castro, "Organic photovoltaics: principles and techniques for nanometre scale characterization.," *Nanotechnology*, vol. 21, no. 49, p. 492001, Dec. 2010.
- [64] M. Pfannmöller, W. Kowalsky, and R. R. Schröder, "Visualizing physical, electronic, and optical properties of organic photovoltaic cells," *Energy Environ. Sci.*, vol. 6, no. 10, pp. 2871–2891, 2013.

- [65] W. Chen, M. P. Nikiforov, and S. B. Darling, "Morphology characterization in organic and hybrid solar cells," *Energy Environ. Sci.*, vol. 5, no. 8, p. 8045, 2012.
- [66] G. Li, V. Shrotriya, Y. Yao, and Y. Yang, "Investigation of annealing effects and film thickness dependence of polymer solar cells based on poly(3-hexylthiophene)," *J. Appl. Phys.*, vol. 98, no. 2005, p. 43704, 2005.
- [67] R. Garcia, C. J. Gómez, N. F. Martínez, S. Patil, C. Dietz, and R. Magerle, "Identification of Nanoscale Dissipation Processes by Dynamic Atomic Force Microscopy," *Phys. Rev. Lett.*, vol. 97, no. 1, p. 16103, Jul. 2006.
- [68] E. J. Spadafora, R. Demadrille, B. Ratier, and B. Grévin, "Imaging the carrier photogeneration in nanoscale phase segregated organic heterojunctions by Kelvin probe force microscopy," *Nano Lett.*, vol. 10, no. 9, pp. 3337–42, Sep. 2010.
- [69] W-R. Wu *et al.*, "Competition between Fullerene Aggregation and Poly(3-hexylthiophene) Crystallization upon Annealing of Bulk Heterojunction Solar Cells," *ACS Nano*, vol. 5, no. 8, pp. 6233–6243, Aug. 2011.
- [70] L. S. C. Pingree, O. G. Reid, and D. S. Ginger, "Electrical Scanning Probe Microscopy on Active Organic Electronic Devices," *Adv. Mater.*, vol. 21, no. 1, pp. 19–28, Jan. 2009.
- [71] D. C. Coffey, O. G. Reid, D. B. Rodovsky, G. P. Bartholomew, and D. S. Ginger, "Mapping local photocurrents in polymer/fullerene solar cells with photoconductive atomic force microscopy," *Nano Lett.*, vol. 7, no. 3, pp. 738–44, Mar. 2007.
- [72] Z. Cui, J. Sun, X. Niu, J. Chen, W. Ma, and L. Chi, "Photo-generated charge behaviors in all-polymer solar cells studied by Kelvin probe force microscopy," *Org. Electron. physics, Mater. Appl.*, vol. 39, pp. 38–42, 2016.
- [73] S. S. van-Bavel, E. Sourty, G. de With, and J. Loos, "Three-dimensional nanoscale organization of bulk heterojunction polymer solar cells," *Nano Lett.*, vol. 9, no. 2, pp. 507–13, Feb. 2009.
- [74] D. M. DeLongchamp, R. J. Kline, and A. A. Herzing, "Nanoscale structure measurements for polymer-fullerene photovoltaics," *Energy Environ. Sci.*, vol. 5, no. 3, pp. 5980–5993, 2012.
- [75] J. S. Moon, C. J. Takacs, Y. Sun, and A. J. Heeger, "Spontaneous formation of bulk heterojunction nanostructures: multiple routes to equivalent morphologies," *Nano Lett.*, vol. 11, no. 3, pp. 1036–9, Mar. 2011.
- [76] P. A. Midgley and R. E. Dunin-Borkowski, "Electron tomography and holography in materials science," *Nat. Mater.*, vol. 8, no. 4, pp. 271–280, 2009.
- [77] M. Pfannmöller *et al.*, "Quantitative Tomography of Organic Photovoltaic Blends at the Nanoscale," *Nano Lett.*, vol. 15, no. 10, pp. 6634–6642, Oct. 2015.
- [78] F. Banhart, "Irradiation effects in carbon nanostructures," *Reports Prog. Phys.*, vol. 62, no. 8, pp. 1181–1221, Aug. 1999.
- [79] J. S. Moon, J. K. Lee, S. Cho, J. Byun, and A. J. Heeger, "'Columnlike' structure of the cross-sectional morphology of bulk heterojunction materials," *Nano Lett.*, vol. 9, no. 1, pp. 230–4, Jan. 2009.
- [80] J. Loos, J. K. J. van Duren, F. Morrissey, and R. A. J. Janssen, "The use of the focused ion beam technique to prepare cross-sectional transmission electron microscopy specimen of polymer solar cells deposited on glass," *Polymer (Guildf.)*, vol. 43, no. 26, pp. 7493–7496, Dec. 2002.
- [81] R. J. Bailey, R. Geurts, D. J. Stokes, F. de Jong, and A. H. Barber, "Evaluating focused ion beam induced damage in soft materials," *Micron*, vol. 50, pp. 51–6, Jul. 2013.

- [82] A. A. Herzing, L. J. Richter, and I. M. Anderson, "3D Nanoscale Characterization of Thin-Film Organic Photovoltaic Device Structures via Spectroscopic Contrast in the TEM," *J. Phys. Chem. C*, vol. 114, no. 41, pp. 17501–17508, Oct. 2010.
- [83] L. F. Drummy, R. J. Davis, D. L. Moore, M. Durstock, R. A. Vaia, and J. W. P. Hsu, "Molecular-Scale and Nanoscale Morphology of P3HT:PCBM Bulk Heterojunctions: Energy-Filtered TEM and Low-Dose HREM," *Chem. Mater.*, vol. 23, no. 3, pp. 907–912, Feb. 2011.
- [84] A. J. Pearson, S. A. Boden, D. M. Bagnall, D. G. Lidzey, and C. Rodenburg, "Imaging the bulk nanoscale morphology of organic solar cell blends using helium ion microscopy," *Nano Lett.*, vol. 11, no. 10, pp. 4275–4281, Oct. 2011.
- [85] Y. Kishimoto, T. Ohshima, M. Hashimoto, and T. Hayashi, "A consideration of secondary electron emission from organic solids," *J. Appl. Polym. Sci.*, vol. 39, no. 10, pp. 2055–2066, May 1990.
- [86] D. Cohen-Tanugi and N. Yao, "Superior imaging resolution in scanning helium-ion microscopy: A look at beam-sample interactions," *J. Appl. Phys.*, vol. 104, no. 6, p. 63504, Sep. 2008.
- [87] A. J. Parnell *et al.*, "Depletion of PCBM at the cathode interface in P3HT/PCBM thin films as quantified via neutron reflectivity measurements," *Adv. Mater.*, vol. 22, no. 22, pp. 2444–7, Jun. 2010.
- [88] J. Rivnay, S. C. B. Mannsfeld, C. E. Miller, A. Salleo, and M. F. Toney, "Quantitative determination of organic semiconductor microstructure from the molecular to device scale," *Chem. Rev.*, vol. 112, no. 10, pp. 5488–519, Oct. 2012.
- [89] J. W. Kiel, B. J. Kirby, C. F. Majkrzak, B. B. Maranville, and M. E. Mackay, "Nanoparticle concentration profile in polymer-based solar cells," *Soft Matter*, vol. 6, no. 3, p. 641, Jan. 2010.
- [90] H. Sirringhaus *et al.*, "Two-Dimensional Charge Transport in Self-Organized, High-Mobility Conjugated Polymers," *Nature*, vol. 401, no. 6754, pp. 685–688, 1999.
- [91] Y. Kim *et al.*, "A strong regioregularity effect in self-organizing conjugated polymer films and high-efficiency polythiophene:fullerene solar cells," *Nat. Mater.*, vol. 5, no. 3, pp. 197–203, 2006.
- [92] W. Yin and M. Dadmun, "A new model for the morphology of P3HT/PCBM organic photovoltaics from small-angle neutron scattering: rivers and streams," *ACS Nano*, vol. 5, no. 6, pp. 4756–68, Jun. 2011.
- [93] P. A. Staniec *et al.*, "The Nanoscale Morphology of a PCDTBT:PCBM Photovoltaic Blend," *Adv. Energy Mater.*, vol. 1, no. 4, pp. 499–504, Jul. 2011.
- [94] M. Rides, "NPL Report MAT 34: Review of Methods for the Characterisation of the Dispersion of Nanoparticles in Polymer Nanocomposites," *National Physical Laboratory*, 2009. [Online]. Available: [http://resource.npl.co.uk/cgi-bin/download.pl?area=npl\\_publications&path\\_name=/npl\\_web/pdf/mat34.pdf](http://resource.npl.co.uk/cgi-bin/download.pl?area=npl_publications&path_name=/npl_web/pdf/mat34.pdf).
- [95] A. J. Moulé, D. Neher, and S. T. Turner, "P3HT-Based Solar Cells: Structural Properties and Photovoltaic Performance," in *P3HT Revisited - From Molecular Scale to Solar Cell Devices*, Springer, 2014, pp. 181–232.
- [96] D. C. Joy, "Scanning electron microscopy: Second best no more," *Nat. Mater.*, vol. 8, no. 10, pp. 776–777, Oct. 2009.
- [97] W. Zhou, R. P. Apkarian, Z. L. Wang, and D. C. Joy, "Fundamentals of Scanning Electron Microscopy," in *Scanning Microscopy for Nanotechnology*, W. Zhou and Z. L. Wang, Eds. New York, NY: Springer New York, 2006, pp. 1–40.

- [98] J. Goldstein *et al.*, *Scanning Electron Microscopy and X-Ray Microanalysis, 3rd Edition*. Springer, 2003.
- [99] P. J. Goodhew, J. Humphreys, and R. Beanland, *Electron Microscopy and Analysis*. 2001.
- [100] J. B. Pawley, “LVSEM for High Resolution Topographic and Density Contrast Imaging,” in *Advances in Electronics and Electron Physics*, 1992, pp. 203–274.
- [101] D. Phifer, L. Tuma, T. Vystavel, P. Wandrol, and R. J. Young, “Improving SEM Imaging Performance Using Beam Deceleration,” *Microsc. Today*, vol. 17, no. 4, pp. 40–49, Jun. 2009.
- [102] Q. Wan *et al.*, “Angle selective backscattered electron contrast in the low-voltage scanning electron microscope: Simulation and experiment for polymers,” *Ultramicroscopy*, vol. 171, pp. 126–138, 2016.
- [103] H. Seiler, “Secondary electron emission in the scanning electron microscope,” *J. Appl. Phys.*, vol. 54, no. 11, pp. R1–R18, 1983.
- [104] D. C. Joy, M. S. Prasad, and H. M. Meyer, “Experimental secondary electron spectra under SEM conditions,” *J. Microsc.*, vol. 215, no. Pt 1, pp. 77–85, Jul. 2004.
- [105] H. Inada *et al.*, “Atomic imaging using secondary electrons in a scanning transmission electron microscope: experimental observations and possible mechanisms,” *Ultramicroscopy*, vol. 111, no. 7, pp. 865–876, Jun. 2011.
- [106] B. J. Griffin, D. C. Joy, and J. R. Michael, “Ollie was Right! A Review of Angular Dependence, Detector Bandwidth and Sample Preparation on Contrast in Secondary and Backscattered Electron Images in the SEM,” *Microsc. Microanal.*, vol. 20, no. S3, pp. 14–15, 2014.
- [107] T. Otsuka *et al.*, “SEM Images Obtained with an Energy and Takeoff Angle Selective Detector,” *e-Journal Surf. Sci. Nanotechnol.*, vol. 12, no. 0, pp. 279–282, 2014.
- [108] R. Rasch, A. Stricher, and R. W. Truss, “Energy filtered low voltage ‘in lens detector’ SEM and XPS of natural fiber surfaces,” *J. Appl. Polym. Sci.*, vol. 131, no. 9, p. 39572, May 2014.
- [109] T. Everhart and R. F. M. Thornley, “Wide-band detector for micro-microampere low-energy electron currents,” *J. Sci. Instrum.*, vol. 37, no. 7, pp. 246–248, 1960.
- [110] P. Kazemian, S. A. M. Mentink, C. Rodenburg, and C. J. Humphreys, “Quantitative secondary electron energy filtering in a scanning electron microscope and its applications,” *Ultramicroscopy*, vol. 107, no. 2–3, pp. 140–150, 2007.
- [111] R. Young *et al.*, “XHR SEM: enabling extreme high resolution scanning electron microscopy,” in *Proceedings of SPIE*, 2009, vol. 7378, p. 737803.
- [112] I. Konvalina, F. Mika, S. Kratky, and I. Mullerova, “Bandpass filter for secondary electrons in SEM - Simulations,” in *Proceedings of Recent Trends in Charged Particle Optics and Surface Physics Instrumentation*, 2016, pp. 28–29.
- [113] A. Khursheed, *Scanning Electron Microscope Optics and Spectrometers*. World Scientific, Singapore, 2011.
- [114] J. Butler, D. C. Joy, G. Bradley, and S. Krause, “Low-voltage scanning electron microscopy of polymers,” *Polymer (Guildf.)*, vol. 36, no. 9, pp. 1781–1790, 1995.
- [115] J. Benawra, A. M. Donald, and M. Shannon, “Developing dual-beam methodologies for the study of heterogeneous polymer-based systems,” *J. Microsc.*, vol. 234, no. 1, pp. 89–94, Apr. 2009.

- [116] G. M. Brown and J. H. Butler, "New method for the characterization of domain morphology of polymer blends using ruthenium tetroxide staining and low voltage scanning electron microscopy (LVSEM)," *Polymer (Guildf.)*, vol. 38, no. 15, pp. 3937–3945, 1997.
- [117] D. L. Vezie, E. L. Thomas, and W. W. Adams, "Low-voltage, high-resolution scanning electron microscopy: a new characterization technique for polymer morphology," *Polymer (Guildf.)*, vol. 36, no. 9, pp. 1761–1779, Apr. 1995.
- [118] T. Ogawa, B. Cho, and S. J. Ahn, "Low-energy scanning electron microscope using a monochromator with double-offset cylindrical lenses," *J. Vac. Sci. Technol. B, Nanotechnol. Microelectron. Mater. Process. Meas. Phenom.*, vol. 33, no. 6, p. 06FJ01, 2015.
- [119] D. C. Joy, "Protons, ions, electrons and the future of the SEM," *J. Phys. Conf. Ser.*, vol. 241, p. 12002, Jul. 2010.
- [120] E. Plies, B. Degel, A. Hayn, G. Knell, J. Neumann, and B. Schiebel, "Experimental results using a 'low-voltage booster' in a conventional SEM," *Nucl. Instruments Methods Phys. Res. Sect. A Accel. Spectrometers, Detect. Assoc. Equip.*, vol. 427, no. 1–2, pp. 126–130, 1999.
- [121] C. Rodenburg, R. C. Masters, D. G. Lidzey, M. Uncovsky, T. Vystavěl, and F. Mika, "SECONDARY ELECTRON SPECTROSCOPY AND ENERGY SELECTIVE IMAGING FOR THE ENGINEERING OF CARBON BASED MATERIALS," in *Proceedings of Recent Trends in Charged Particle Optics and Surface Physics Instrumentation*, 2016, pp. 58–59.
- [122] D. C. Bell and N. Erdman, *Low voltage electron microscopy: Principles and applications*. Wiley, 2013.
- [123] J. L. Riesterer, C. S. López, and E. Barklis, "Extreme High Resolution Imaging of Uncoated Cells in a DualBeamTM," *Microsc. Microanal.*, vol. 19, no. S2, pp. 922–923, 2013.
- [124] I. Müllerová, "Imaging of Specimens at Optimized Low and Very Low Energies in Scanning Electron Microscopes," *Scanning*, vol. 23, pp. 379–394, 2001.
- [125] I. Zailer, J. E. F. Frost, V. Chabasseur-Molyneux, C. J. B. Ford, and M. Pepper, "Crosslinked PMMA as a high-resolution negative resist for electron beam lithography and applications for physics of low-dimensional structures," *Semicond. Sci. Technol.*, vol. 11, no. 8, pp. 1235–1238, 1999.
- [126] H. Ahn, D. W. Oblas, and J. E. Whitten, "Electron Irradiation of Poly(3-hexylthiophene) Films," *Macromolecules*, vol. 37, no. 9, pp. 3381–3387, May 2004.
- [127] A. Charlesby, *Atomic Radiation and Polymers: International Series of Monographs on Radiation Effects in Materials*. Oxford: Pergamon Press, 1960.
- [128] K. E. Bower, Y. A. Barbanel, Y. B. Shreter, and G. W. Bohnert, *Polymers, Phosphors, and Voltaics for Radioisotope Microbatteries*. CRC Press, 2002.
- [129] D. C. Joy and C. Joy, "Low voltage scanning electron microscopy," *Micron*, vol. 27, no. 3, pp. 247–263, 1996.
- [130] M. T. Postek, A. E. Vladár, and K. P. Purushotham, "Does your SEM really tell the truth? How would you know? Part 2," *Scanning*, vol. 36, no. 3, pp. 347–355, 2014.
- [131] C. Rodenburg, M. A. E. Jepson, E. G. T. Bosch, and M. Dapor, "Energy selective scanning electron microscopy to reduce the effect of contamination layers on scanning electron microscope dopant mapping," *Ultramicroscopy*, vol. 110, no. 9, pp. 1185–1191, Aug. 2010.

- [132] G. Goizueta, T. Chiba, and T. Inoue, "Phase morphology of polymer blends: 2. SEM observation by secondary and backscattered electrons from microtomed and stained surface," *Polymer (Guildf.)*, vol. 34, no. 2, pp. 253–256, Jan. 1993.
- [133] C. Harrison, M. Park, P. M. Chaikin, R. A. Register, D. H. Adamson, and N. Yao, "Layer by layer imaging of diblock copolymer films with a scanning electron microscope," *Polymer (Guildf.)*, vol. 39, no. 13, pp. 2733–2744, Jun. 1998.
- [134] M. S. Joens *et al.*, "Helium Ion Microscopy (HIM) for the imaging of biological samples at sub-nanometer resolution.," *Sci. Rep.*, vol. 3, p. 3514, Jan. 2013.
- [135] J. Cazaux, "A new model of dependence of secondary electron emission yield on primary electron energy for application to polymers," *J. Phys. D. Appl. Phys.*, vol. 38, no. 14, pp. 2433–2441, Jul. 2005.
- [136] J. Cazaux, "Secondary electron emission yield: graphite and some aromatic hydrocarbons," *J. Phys. D. Appl. Phys.*, vol. 38, no. 14, pp. 2442–2445, 2005.
- [137] J. Karger-Kocsis, A. Kalló, and V. N. Kuleznev, "Phase structure of impact-modified polypropylene blends," *Polymer (Guildf.)*, vol. 25, no. 2, pp. 279–286, Feb. 1984.
- [138] T. Thurn-Albrecht *et al.*, "Nanosopic Templates from Oriented Block Copolymer Films," *Adv. Mater.*, vol. 12, no. 11, pp. 787–791, Jun. 2000.
- [139] G. Goizueta, T. Chiba, and T. Inoue, "Phase morphology of polymer blends: scanning electron microscope observation by backscattering from a microtomed and stained surface," *Polymer (Guildf.)*, vol. 33, pp. 886–888, 1992.
- [140] J. S. Trent, J. I. Scheinbeim, and P. R. Couchman, "Ruthenium tetroxide staining of polymers for electron microscopy," *Macromolecules*, vol. 16, no. 4, pp. 589–598, Jul. 1983.
- [141] H. . Haubruge, A. . Jonas, and R. Legras, "Staining of poly(ethylene terephthalate) by ruthenium tetroxide," *Polymer (Guildf.)*, vol. 44, no. 11, pp. 3229–3234, May 2003.
- [142] S. Shoaee *et al.*, "Correlating Non-Geminate Recombination with Film Structure: A Comparison of Polythiophene: Fullerene Bilayer and Blend Films," *J. Phys. Chem. Lett.*, vol. 5, no. 21, pp. 3669–3676, Nov. 2014.
- [143] T. M. Chou, P. Prayoonthong, A. Aitouchen, and M. Libera, "Nanoscale artifacts in RuO<sub>4</sub>-stained poly(styrene)," *Polymer (Guildf.)*, vol. 43, pp. 2085–2088, 2002.
- [144] P. Kazemian, S. A. M. Mentink, C. Rodenburg, and C. J. Humphreys, "High resolution quantitative two-dimensional dopant mapping using energy-filtered secondary electron imaging," *J. Appl. Phys.*, vol. 100, no. 5, p. 54901, 2006.
- [145] M. Dapor, B. J. Inkson, C. Rodenburg, and J. M. Rodenburg, "A comprehensive Monte Carlo calculation of dopant contrast in secondary-electron imaging," *EPL (Europhysics Lett.)*, vol. 82, no. 3, p. 30006, 2008.
- [146] R. F. Willis, B. Feuerbacher, and B. Fitton, "Graphite conduction band states from secondary electron emission spectra," *Phys. Lett. A*, vol. 34, no. 4, pp. 231–233, Mar. 1971.
- [147] R. F. Willis, B. Feuerbacher, and B. Fitton, "Experimental investigation of the band structure of graphite," *Phys. Rev. B*, vol. 4, no. 8, pp. 2441–2452, 1971.
- [148] L. Papagno, L. S. Caputi, M. De Crescenzi, and R. Rosei, "Graphite: Electronic and structural properties studied by electron-energy-loss and secondary-electron-emission spectroscopy," *Phys. Rev. B*, vol. 26, no. 4, pp. 2320–2322, Aug. 1982.
- [149] R. F. Willis, B. Fitton, and D. K. Skinner, "Study of carbon-fiber surfaces using Auger and secondary electron emission spectroscopy," *J. Appl. Phys.*, vol. 43, no. 11, pp. 4412–4419, 1972.

- [150] K. Nishimura, J. Kawata, and K. Ohya, “Comparative study of secondary electron emission from solids under positron and electron impacts,” *Nucl. Instruments Methods Phys. Res. Sect. B Beam Interact. with Mater. Atoms*, vol. 164, pp. 903–909, 2000.
- [151] A. Howie, “Threshold energy effects in secondary electron emission,” *Microsc. Microanal.*, vol. 6, no. 4, pp. 291–296, 2000.
- [152] N. E. Nickles, “The Role of Bandgap in the Secondary Electron Emission of Small Bandgap Semiconductors: Studies of Graphitic Carbon,” Utah State University, 2002.
- [153] M. Dapor, “Computer simulation of electron transport in solids with applications to materials analysis and characterization,” 2013.
- [154] G. S. Painter and D. E. Ellis, “Electronic band structure and optical properties of graphite from a variational approach,” *Phys. Rev. B*, vol. 1, no. 12, pp. 4747–4752, 1970.
- [155] G. F. Dionne, “Effects of secondary electron scattering on secondary emission yield curves,” *J. Appl. Phys.*, vol. 44, no. 12, pp. 5361–5364, 1973.
- [156] K. I. Grais and A. M. Bastawros, “A study of secondary electron emission in insulators and semiconductors,” *J. Appl. Phys.*, vol. 53, no. 7, pp. 5239–5242, 1982.
- [157] F. Iwase and Y. Nakamura, “Enhancement of secondary electron emission from heavily Si-implanted and Si-doped GaAs,” *Appl. Phys. Lett.*, vol. 71, no. 15, p. 2142, 1997.
- [158] D. K. Skinner and R. F. Willis, “Refinements to a standard LEED-Auger system for the analysis of electron emission at low primary beam energies,” *Rev. Sci. Instrum.*, vol. 43, no. 5, pp. 731–734, 1972.
- [159] C. Schönjahn, R. F. Broom, C. J. Humphreys, a. Howie, and S. a M. Mentink, “Optimizing and quantifying dopant mapping using a scanning electron microscope with a through-the-lens detector,” *Appl. Phys. Lett.*, vol. 83, no. 2, pp. 293–295, 2003.
- [160] C. Schönjahn, C. J. Humphreys, and M. Glick, “Energy-filtered imaging in a field-emission scanning electron microscope for dopant mapping in semiconductors,” *J. Appl. Phys.*, vol. 92, no. 12, pp. 7667–7671, Dec. 2002.
- [161] M. Dapor *et al.*, ““Secondary electron spectra of semi-crystalline polymers – A novel polymer characterisation tool?,”” *J. Electron Spectros. Relat. Phenomena*, pp. 1–11, 2017.

## Chapter 3: Methods

As this thesis includes published articles, many of the methods discussed in this Chapter are also included in the articles' respective methods sections. Due to space constraints, these methods sections have been limited in scope however. As such, a complete and detailed overview of all the techniques and methods employed in this thesis is offered here.

### Section 3.1: Sample preparation

All polymer and fullerene materials were prepared by spin-casting films from solution in a nitrogen-filled glovebox environment. Solutions for all materials were made in the glovebox by dissolving dry polymer or fullerene in a glass vial, with the vial then heated to 70°C for at least 2 hours to ensure complete dissolution. The solution concentration and solvent varied for each material as discussed below.

For all experiments in the SEM, films were prepared on silicon substrates, and for UV-visible absorption spectroscopy, (Section 4.3.3) commercial quartz-coated glass substrates purchased from Ossila Ltd. were used. Substrates were washed in hot isopropanol and subject to further cleaning in either UV-ozone or oxygen plasma (depending on availability) for ~10 minutes to remove residual substrate contamination.

An Ossila-brand spin coater was used for spin casting. With the substrate fixed to the spin-coater chuck, around 50 µl of solution was pipetted on to the stationary substrate. The substrate was then spun at the desired speed for 40 seconds, or 2 minutes if using dichlorobenzene solvent. If a thermal anneal was required, the coated substrate was then transferred immediately to a hotplate.

For SEM analysis, substrates were attached to an aluminium pin stub using conductive silver DAG paint within the glovebox. To prevent air degradation of the materials occurring, the samples were transferred to a vacuum desiccator within the glovebox, and retained under vacuum until inserted in to the SEM chamber. If degradation under air was desired (see Chapter 4), the samples were stored exposed to light to ensure photo-oxidation of the sample surface occurred[1].

**P3HT** was purchased in two forms: 1) Regiorandom with  $M_w = 65000-90000$  Da from Sigma-Aldrich, and 2) Regioregularity 94.2% and  $M_w = 54200$  Da from Ossila Ltd. Regiorandom films were cast from chlorobenzene solution at  $25 \text{ mg.ml}^{-1}$  and not subject to any anneal step. For different regioregular samples, the polymer was dissolved in 1) chloroform, 2) chlorobenzene or 3) dichlorobenzene at a concentration of  $25 \text{ mg.ml}^{-1}$ . The choice of solvent was varied to influence the drying time of the film, with solvents from 1) to 3) giving sequentially higher drying time, and as such more ordered films.

In solution, nanoribbons or other P3HT crystallites can form over time, which would affect ordering in the spin-cast film[2]. For this reason, solutions were heated to  $80^\circ\text{C}$  immediately prior to spin-casting, in order to remove this ‘thermal history’ break apart any such structures. After cooling the solution back to room temperature, films were spin-cast at 1500 rpm, with the exception of the low-order P3HT sample discussed in Section 4.6, which was cast at 3000 rpm from chlorobenzene at  $70^\circ\text{C}$ . Resulting P3HT films were of the order 100-150 nm thick as measured by an AFM.

By heating P3HT films above their glass transition temperature, further self-organisation of the P3HT chains is promoted. Under a thermal anneal, P3HT films become more crystalline, with an increased packing density of P3HT molecules. This results in a greater degree of electron conjugation within the film, somewhat altering the electronic structure of the bulk film[3]. Further, the orientation of P3HT molecules at the film surface is found to change with increased crystallinity. In this thesis, samples described as annealed were heated to  $170^\circ\text{C}$  for ~30 minutes, this temperature corresponding with that found in ref. [3] to induce significant changes in the film morphology.

**PCBM** was purchased from Ossila Ltd. and cast from chlorobenzene solution at  $25 \text{ mg.ml}^{-1}$ . Films were cast at 1500 rpm and not subjected to any anneal step.

**P3HT:PCBM** solution was formed by blending pure P3HT and pure PCBM solutions (chlorobenzene solvent, both at  $25 \text{ mg.ml}^{-1}$ ) in the ratio 1:0.8 (P3HT:PCBM); these parameters are typical of P3HT:PCBM blends used for OPV[4]. Films were cast at 1500 rpm and some

subject to a range of different annealing processes as desired. In Chapter 5, P3HT:PCBM blends were imaged as-cast, or after a thermal anneal at 150°C for either 10 minutes (to give an optimised blend morphology for OPV)[5], or 60 minutes to increase the degree of phase separation encouraged by the anneal. In Chapter 6, samples were either imaged as-cast or after a thermal anneal of 190°C for 60 minutes, used to encourage a still larger degree of phase separation as well as vertical domain stacking.

**PffBT4T-2OD:PC70BM:** The PffBT4T-2OD:PC70BM blend films were cast from solution in chlorobenzene and o-dichlorobenzene (1:1 volume ratio) with 3% diiodooctane by volume used as a solvent additive. Pure polymer and PC70BM solutions were made with concentrations 9 mg·ml<sup>-1</sup> and 10.8 mg·ml<sup>-1</sup> respectively and subsequently blended in a 1:1 ratio. The blend solution was heated on a hot plate at 110 °C and spin-coated on to pre-heated silicon substrates (110 °C) at 1000 rpm in a nitrogen glove box. The substrates were then moved to a hot plate at 100 °C immediately after spin casting for drying.

### Section 3.2: SE Spectroscopy

Secondary electron spectra were measured in a FEI Sirion SEM, at base pressure in the sample chamber ( $\sim 2 \times 10^{-6}$  mbar) to minimise potential contamination effects. All spectra were measured using the immersion lens TLD of the microscope, with samples held at a 3 mm working distance and TLD suction tube bias (Figure 2.19a) set to 250 V. These parameters matched those used for the detector response simulations used to calibrate the FEI Sirion TLD in Section 4.2 (Figure 4.1). A beam current of around 10-20 pA was used (as measured directly by a beam current probe), although the FEI Sirion only allows selection of a 'spot size' parameter, and no direct control of the beam current. The beam current associated with a given spot size is dependent on the primary beam energy  $E_0$ ; as such, the spot size giving a beam current closest to the 10-20 pA range was selected for a particular  $E_0$ . SE spectra were measured at the lowest magnification available in immersion mode at 3mm working distance, image area 62 x 42  $\mu\text{m}$  (at resolution 712 x 484

pixels). Images were acquired in ‘TV-scan’ mode with dwell time  $\sim 100$  ns, using 4-fold frame integration (Section 2.6.4).

For the work in Chapter 4, a Diener Zepto plasma cleaner was used to subject P3HT films to a plasma etch and alter surface properties of the films. Samples were placed in the vacuum chamber, and etched by a 33 W air or argon plasma at a pressure of  $\sim 0.5$  mbar. Samples were plasma cleaned for 15 minutes before being immediately transferred to the SEM for spectroscopy.

To measure a SE spectrum, a stack of images was acquired of a flat, featureless sample area. For each sequential image in the stack, the bias on the TLD deflector electrode  $V_{def}$  was increased in 0.5 V steps from 0 – 30 V. The  $V_{def}$  value was linked to a cut-off energy for SE detection using the detector calibration discussed in Section 4.2. The grey level in each image was assumed proportional to the intensity of SE emission from the sample with energies below the detection cut-off energy defined by this calibration (Equations 4.1 and 4.2). Therefore, by plotting the average grey level of the images in the stack as a function of  $V_{def}$ , an effective ‘integrated’ SE spectrum can be measured.

### ***Section 3.2.1: Processing of data***

To process a SE spectrum, the acquired spectrum image stack was imported in to ImageJ. The average grey level of each image in the stack was measured, excluding the edges of the images (where stronger beam damage effects and some SE spectrum distortions were found) as well as any defects or film aggregates present in the field of view. This integrated spectrum was transferred to OriginPro 9.0 software, and was differentiated using a 5-point, 2<sup>nd</sup> order Savitzky-Golay smoothing algorithm to reduce the impact of randomised noise in the resulting spectrum. This algorithm fits a 2<sup>nd</sup> order polynomial to a moving 5-point window of data points in the integrated spectrum, and then analytically differentiates and recombines these data windows to produce the final differentiated spectrum.

### **Section 3.3: High-resolution energy-filtered SEM imaging**

High-resolution SE imaging was performed in a FEI Helios SEM (or, for Figure 5.2, a FEI Magellan with identical electron optics to the FEI Helios). These offered significantly improved imaging performance over the older FEI Sirion. All images of P3HT and P3HT:PCBM were acquired with 2800 eV primary beam energy; this was based on rudimentary models that suggested that at this energy, the electron beam penetrates the full thickness of a 100 nm thick film. This limited the accumulation of electronic charge from the polymer film by allowing a significant fraction of the incident electrons to reach the more conductive silicon substrate.

Energy-filtered SE images were acquired using the TLD at 1mm working distance and 1.3 $\mu$ s dwell time, using a 50-pA beam current. 18-fold line integration was also used to obtain better quality images. ‘Conventional’ SE images were collected for comparison using the standard ‘Secondary Electron’ imaging mode on the TLD, using a suction tube bias of 70 V and mirror electrode bias of -15 V.

SE energy filtering was performed with the FEI Helios by altering the bias on the TLD mirror electrode (Section 2.7.2, Figure 4.19b). All EFSEM images were acquired at a SE detection cut-off energy of 8 eV. This was calibrated to mirror electrode bias of -6 V using detector efficiency data acquired from FEI Co. in confidential private communication (although a small part of this data can be found in ref. [6]). A larger suction tube bias of 140 V was used when performing energy filtering to improve SE collection and minimise the angular dependence of SE detection (Section 4.6).

For the work in Chapter 5, P3HT:PCBM films were subject to a 6-minute plasma cleaning process in air prior to EFSEM imaging to remove a P3HT wetting layer on the surface, to reveal the phase separated morphology beneath. This was performed using the in-chamber plasma cleaner in the FEI Helios SEM.

### Section 3.4: Backscattered electron imaging

For backscattered electron imaging in Chapter 6, blend film samples were imaged using a FEI Nova NanoSEM 450 equipped with a segmented concentric backscatter (CBS) electron detector acquired from FEI Co. (described in Section 2.6.3). The CBS detector was optimised for BSE imaging by the enabling only the detector segments (or combination of segments) giving the strongest signal-to-noise ratio. Imaging was performed at 4 mm working distance with immersion lens active, and a -4 kV bias applied to the sample stage.

As detailed in Section 2.6.2, the sample depth probed by BSE imaging is highly dependent on the primary beam energy  $E_0$ . Surface morphology images were therefore acquired using low  $E_0 = 500$  eV, with morphological features penetrating the majority of the film thickness probed by imaging at  $E_0 = 3$  keV (this effect is discussed in detail in Chapter 6). When acquiring surface morphology images, the surface wetting layer discussed in the previous section again obscured the morphology beneath, as at low  $E_0$ , a significant fraction of BSEs are reflected from this wetting layer. As such, this layer was again removed with a plasma etch process. However, the in-chamber plasma cleaning capability of the FEI Nova cannot be used when a CBS detector is mounted to the pole-piece of the electron column as the plasma may damage the detector. Samples were therefore plasma cleaned externally in the Diener Zepto plasma cleaner. Air plasma was used at 0.5 mbar pressure and 33 W power to etch samples for 8 minutes. Samples were then immediately transferred to the SEM chamber for imaging.

Importantly, in instances where higher primary beam energies were used to probe the sub-surface morphology of the various blend films in Chapter 6, films were not subject to a plasma process prior to imaging. This is because the few-nm thick wetting layer has a negligible effect on BSE emissions at higher primary beam energy. It was therefore unnecessary to subject films to a plasma process.

### **Section 3.5: Helium ion microscopy of cross-sections**

A Zeiss Orion Plus helium ion microscope based at Trinity College Dublin was used to image cross-sections of P3HT:PC60BM and PffBT4T-2OD:PC70BM films. Samples on silicon substrates were submerged in liquid nitrogen for ~5 minutes and cleaved with a diamond knife, then immediately transferred to the microscope chamber. To remove cleaving artefacts and reveal morphological features, the samples were then subject to a plasma clean in air for 24 min using the HeIM in-chamber plasma cleaner. The cross-sections were imaged at a 70° tilt, using a 30 kV primary beam and 1 pA beam current at a working distance of 10 mm.

### **Section 3.6: Image processing and analysis**

To analyse OPV blend morphology from the EFSEM and BSE image data in Chapters 5 and 6, different image analysis methods in ImageJ were used to quantify aspects such as phase size and area. The specific method was selected based upon the characteristics of images acquired by the different imaging methods.

As discussed in Chapter 5, the high-resolution EFSEM images of P3HT:PCBM blends demonstrated three phases (P3HT, PCBM and mixed phase) with well-defined image grey levels relative to each other. As such, grey level based thresholding methods were applied to classify the image in to P3HT, PCBM and mixed-phase regions. To improve the quality of the threshold result, all EFSEM images were subject to a polynomial background subtraction. Here, a 2-dimensional, 2<sup>nd</sup> order polynomial was fit to and subtracted from the whole-image grey level to remove the effect of large-scale image features especially shading around the edge of the images (these were likely caused by contamination).

For the highest-quality EFSEM images of P3HT:PCBM films in Chapter 5 (Figure 5.3), the image area of each phase was quantified from both raw, unprocessed image data, as well as images passed through a noise-reduction filter. Whilst acquiring EFSEM images is relatively simple by design, reliably interpreting the image data in a quantitative manner is a challenging process. EFSEM images reveal a nanoscale, intimately-mixed 3-phase system, in which the classification

of certain image features may be open to differing interpretation or bias. It is important to note, however, that the improved contrast between polymer and fullerene in EFSEM images makes the classification process significantly easier than it would be with conventional SEM images. The classification and subsequent quantification process used for EFSEM data was developed as part of this PhD project, specifically for quantifying phase areas in EFSEM images. By segmenting the image based upon on contrast profiles or the grey level histogram in specific areas of the image, it is designed to minimise the impact of user error. Nonetheless, user error undoubtedly still exists in the data –the sizeable errors found in Tables 5.1 and 5.2 are intended to reflect this. To highlight the contrast improvement provided by EFSEM, and enable discussion in terms of image brightness on a normalised scale, pixel grey levels are converted to a contrast value in Chapter 5, using the contrast equation from Seiler[7]:

$$C_{A/B} = \frac{I_A - I_B}{I_A + I_B} \times 100\% \quad (3.1)$$

The conversion was made by measuring ten line profiles across regions clearly demonstrating 3 phases. The ‘zero-point’ of the contrast calculation was taken as the midpoint between the minimum and maximum grey level measured in these line profiles, averaged across all ten. When employing Equation 3.1 to calculate a pixel contrast value, this ‘zero-point’ grey level was taken as  $I_B$ . These line profiles were also used as the basis of raw image thresholds to calculate the relative area of each phase in an image (Figure 3.1). The contrast range equating to the mixed phase was calculated by averaging the contrast range of conspicuous mixed phase regions. Pixel contrast values above and below this contrast range were taken to represent either pure P3HT or pure PCBM respectively. Particle analysis algorithms in ImageJ were used to calculate raw-image phase areas based upon these threshold levels.

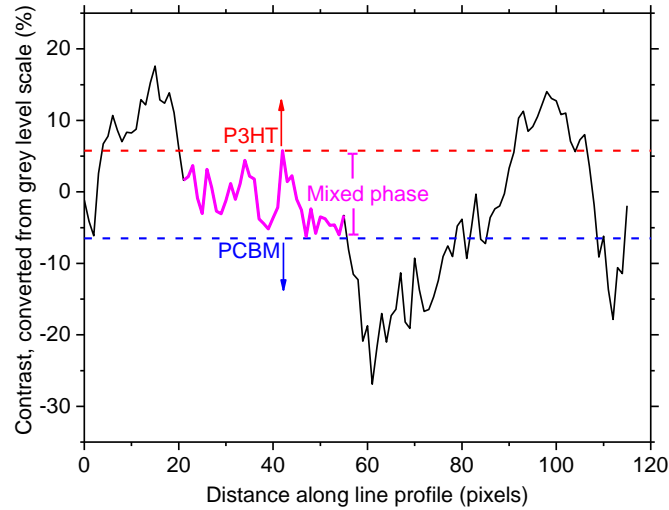


**Figure 3.1:** Example of threshold-level calculations on unprocessed EFSEM images. A line is drawn through clear 3-phase regions, and the grey level profile along this line plotted (after converting to a contrast scale with equation 3.1). The contrast range equating to clear mixed-phase regions is used as the basis for segmenting P3HT, mixed phase, and PCBM regions in analysis of the image. For the final phase area analysis in Table 5.1, the mixed phase contrast range was averaged from ten line profiles of this type from across the EFSEM image.

For improved phase-size analysis with less noise, images were passed through a 3-pixel, fast Fourier transform (FFT) ‘band-pass’ filter in ImageJ to suppress noise. Here, the image is converted to the frequency domain via a 2-dimensional FFT algorithm, and components with spatial frequency smaller than 3 pixels removed from the Fourier-transformed data. This is then inverse-transformed to the real-space domain, with the resulting image having suppressed image features with a length-scale of 3 pixels or fewer.

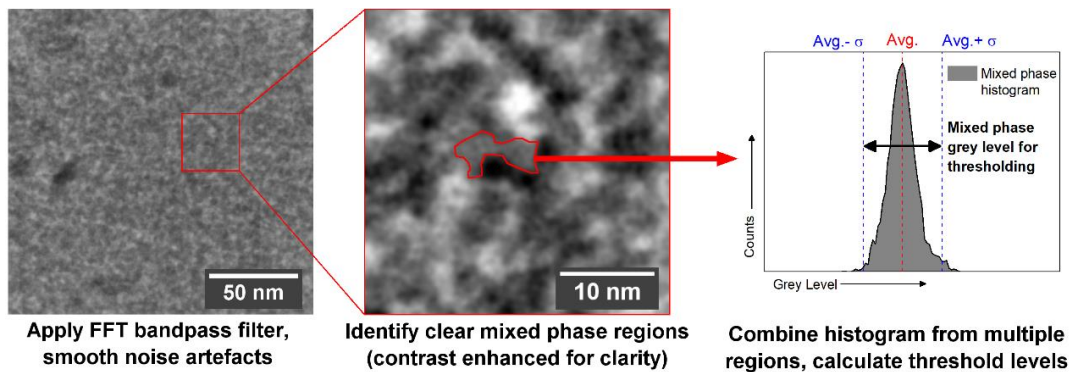


**Figure 3.2:** Image segmentation in FFT bandpass-filtered images. Easily discernible mixed phase regions are highlighted and their grey level histogram measured. The total histogram from all of these regions combined is used to calculate the grey level range equating to mixed phase. This range is taken as the mean mixed-phase grey level,  $\pm$  one standard deviation either side. Pixels with grey level above and below this range are taken as P3HT and PCBM respectively.

The correlation between the brightness of a pixel in a bandpass-filtered image and the originally-measured SE emissions from that pixel is weakened, as the filtering process alters the relative brightness of pixels across the image to reduce noise. This interferes with the contrast calculations performed on the ‘raw’ EFSEM images. As such, more conventional grey level thresholding methods were used to quantify noise-filtered images (Figure 3.2). Here, the total histogram of a number of conspicuous mixed phase regions across the image was measured. Areas of the image that fell in the range of the average grey-level of this histogram, plus or minus one standard deviation either side, were classified as mixed-phase. Regions with grey level above or below this range were classified as P3HT-rich or PCBM-rich respectively. Again, the basic particle analysis capability of ImageJ was used to calculate the total area of each phase in the image field of view.

In Chapter 6, BSE imaging of the surface P3HT:PCBM and PffBT4T-2OD:PC70BM blends produced images with clear two-phase structures. The data acquired from BSEs has a lower signal to noise ratio in comparison to EFSEM images, and topographical features were observed in the lowest- $E_0$  images of the PffBT4T-2OD:PC70BM film (at very low primary beam energies, topographical features can be visible in BSE data [8]). As such, more advanced image classification methods applying machine-learning principles were used to classify the blend film images in to polymer and fullerene regions. Specifically, using the trainable WEKA segmentation plugin in the ‘FIJI’ distribution of ImageJ [9]–[11], machine-learning algorithms are trained by the user on one or more reference images and then applied to segment other similar images. Images of two P3HT:PCBM films are presented in Chapter 6; one of an as-cast film, and one of a film annealed at a high temperature to encourage large scale phase separation. To minimise the impact of user bias on the segmentation of P3HT:PCBM images, the ‘training’ of the WEKA plugin was performed on images of an ‘intermediate’ P3HT:PCBM film that had been annealed at a lower temperature and for less time than the film discussed in Chapter 6. The ‘trained’ plugin was then used to automatically classify (with no user input) the images of as-cast and annealed P3HT:PCBM films presented in Chapter 6. The nature of the imaged PffBT4T-2OD:PC70BM

morphology was significantly different to the P3HT:PCBM films, and as such the WEKA plugin needed to be re-trained for this morphology type.

The size and distribution of the classified domains was analysed by a comprehensive methodology described at length in Section 6.7.2, and not repeated in this chapter.

WEKA segmentation can only be confidently employed in images containing features adhering to well-defined classes. In BSE images acquired with higher primary beam energies to probe morphology through the thickness of the film, the projection of contrast from different phases beneath the incidence point of the beam results in poorly defined phase contrast. For this reason, images acquired with higher primary beam energy were analysed with more conventional grey-level thresholding methods. The grey level histogram of well-defined 'bright' and 'dark' phases was measured and used to inform the selection of a threshold level for polymer and fullerene domains that demonstrated a strong degree of vertical stacking.

### **Section 3.7: UV-Visible absorption spectroscopy**

UV-visible light absorption spectroscopy was performed on P3HT films using a Perkin-Elmer Lambda 900 spectrometer. Films cast on quartz-coated glass were mounted in the spectrometer, with an uncoated substrate used as a blank to negate the absorption effects of the substrate. Absorption spectra were measured using incident light with energies in the range 700-380 nm (1.78 – 3.27 eV), with data acquired in 1 nm steps.

### **Section 3.8: References**

- [1] S. Cook, A. Furube, and R. Katoh, "Matter of minutes degradation of poly(3-hexylthiophene) under illumination in air," *J. Mater. Chem.*, vol. 22, no. 10, pp. 4282–4289, 2012.
- [2] W. Xu, L. Li, H. Tang, H. Li, X. Zhao, and X. Yang, "Solvent-Induced Crystallization of Poly ( 3-dodecylthiophene ): Morphology and Kinetics," pp. 6412–6420, 2011.
- [3] K. Kanai, T. Miyazaki, H. Suzuki, M. Inaba, Y. Ouchi, and K. Seki, "Effect of annealing on the electronic structure of poly(3-hexylthiophene) thin film.," *Phys. Chem. Chem. Phys.*, vol. 12, no. 1, pp. 273–282, 2010.
- [4] A. J. Pearson, "Correlating Structure with Optoelectronic Functionality in Polymer : Fullerene Blend Films," University of Sheffield, 2012.

- [5] T. Wang, A. J. Pearson, D. G. Lidzey, and R. A. L. Jones, “Evolution of Structure, Optoelectronic Properties, and Device Performance of Polythiophene:Fullerene Solar Cells During Thermal Annealing,” *Adv. Funct. Mater.*, vol. 21, no. 8, pp. 1383–1390, Apr. 2011.
- [6] R. Young, E. G. T. Bosch, M. Uncovsky, and L. Tuma, “Low-Energy Secondary Electron Filtering with Immersion Lens SEM,” *Microsc. Microanal.*, vol. 15, no. S2, pp. 222–223, Jul. 2009.
- [7] H. Seiler, “Secondary electron emission in the scanning electron microscope,” *J. Appl. Phys.*, vol. 54, no. 11, pp. R1–R18, 1983.
- [8] Q. Wan *et al.*, “Angle selective backscattered electron contrast in the low-voltage scanning electron microscope: Simulation and experiment for polymers,” *Ultramicroscopy*, vol. 171, pp. 126–138, 2016.
- [9] C. A. Schneider, W. S. Rasband, and K. W. Eliceiri, “NIH Image to ImageJ: 25 years of image analysis,” *Nat. Methods*, vol. 9, no. 7, pp. 671–675, 2012.
- [10] J. Schindelin *et al.*, “Fiji: an open-source platform for biological-image analysis,” *Nat. Methods*, vol. 9, no. 7, pp. 676–682, Jun. 2012.
- [11] M. Hall, E. Frank, G. Holmes, B. Pfahringer, P. Reutemann, and I. H. Witten, “The WEKA data mining software,” *ACM SIGKDD Explor. Newsl.*, vol. 11, no. 1, p. 10, Nov. 2009.

## Chapter 4: Secondary electron spectroscopy of Poly(3-hexylthiophene) in SEM conditions

### Section 4.1: Introduction

In this Chapter, the reliability, accuracy and potential of SE spectroscopy techniques applied to P3HT in SEM conditions is explored. Prior to this thesis, the SE spectrum of P3HT had never been measured, and the SEM-based SE spectrometer setups described in Section 2.7.2 had only been used to probe the SE emissions of silicon and various metal samples[1], [2]. As such, in order to accurately apply SE spectroscopy and EFSEM to probe the phase-separated morphology of a P3HT:PCBM blend, an understanding of these methods as applied to conjugated polymers must first be obtained. Further, by investigating which material properties are reflected by SE spectra, the potential of SE spectroscopy as a characterisation technique in its own right can be explored.

As discussed in Section 2.7.2, the TLD of a XL-30 design SEM has been chosen as a SE spectrometer in this thesis. This is primarily because no hardware modifications were required, and energy-selective SE detection with a TLD capable of high-resolution imaging enables high-quality energy-filtered SE imaging to be performed.

It is unsurprising however that this general-use TLD is not an ‘ideal’ SE spectrometer. Prior to this thesis, a small number of works had investigated its performance as an energy-selective SE detector, and found it capable of detecting shifts in SE energy resulting from surface doping in silicon[3] or from applying a small (1 V) bias to a copper sample[1]. It was also demonstrated that the XL-30 TLD could approximately reproduce the expected ‘cascade’ form of a copper SE spectrum in the low-energy (~0-10 eV) region[1]. The operation of the TLD as a SE spectrometer is discussed in Section 2.7.2 of this thesis.

For a TLD to act as an effective SE spectrometer, it must first be calibrated such that SE spectra can be measured in terms of SE energy rather than as a function of deflector bias  $V_{def}$ . This calibration (effectively a conversion between  $V_{def}$  in V and SE energy in eV) is related to the specific geometry of the SEM and TLD in question, and differs even between different

microscopes employing slightly different variants of the XL-30 design. For the work in this Chapter, a derivative of the FEI XL-30 microscope with an almost identical TLD design, the FEI Sirion, is primarily used. The FEI XL-30 TLD has been the subject of an in-depth calibration as a SE spectrometer by Kazemian *et al.* [1], both experimentally (by measuring the shift in detected SE spectrum between differently biased samples) and using a simulation of the detector arrangement. This work suggested that the detector demonstrates a mostly linear relationship between TLD deflector bias ( $V_{def}$ ) and SE energy ( $E_{SE}$ ) below  $D = 20$  V ( $E_{SE} \sim 8$  eV), above which nonlinearities and angular effects in the detector system make the calibration more complex and unreliable. The operation of the specific FEI Sirion TLD arrangement has also been modelled and used to calibrate this microscope's SE spectrometer capability[2] to enable SE energy filtering on the exact same microscope used in this chapter. However, the detector calibration given in Ref. [2] does not contain many details, and as such the calibration of the FEI Sirion is given a full treatment in this Chapter using the data from Refs [2], [4].

The calibration of the FEI Sirion TLD is tested and its accuracy as a SE spectrometer is discussed, following which the SE spectrum of P3HT is explored. A number of variables that can affect the shape of the measured P3HT spectrum are investigated, including the primary beam energy (Section 4.3.1), absorbed electron beam dose (Section 4.3.2), and sample history and processing (Sections 4.3.3 and 4.3.4). Energy-filtered SEM is then applied to map localised variations in a semicrystalline P3HT sample. A brief study of the SE spectra of PC<sub>60</sub>BM is also undertaken.

Finally, the shape of a P3HT SE spectrum is compared to a Monte Carlo model of SE emission in an attempt to probe the underlying material properties reflected by the shape of a spectrum. As part of this comparison, the effects of the TLD geometry on the measured SE spectrum are considered.

Whilst other materials are addressed in this thesis (most obviously PffBT4T-2OD and the PC<sub>70</sub>BM fullerene variant), focus in this chapter is placed primarily on P3HT. This is largely because it is the best-understood and most widely available conjugated polymer used for OPV[5]. As a result, its physical properties are well documented in literature[6] (crucial for building a

reliable model of SE transport through the system) and these properties can be closely controlled by altering the film processing method[5].

## Section 4.2: Calibration of FEI Sirion through-lens detector

Figure 4.1 demonstrates the calibration of the FEI Sirion TLD based on the detector modelling data published in Refs. [2], [4]. In Figure 4.1a, example detector efficiency curves for the TLD are shown. In each curve, the simulated probability of a SE emitted from the sample with energy  $E_{SE}$  being detected when applying a given bias  $V_{def}$  to the deflector electrode is shown, for the specific imaging parameters noted in Section 3.2. The detailed implications of these curves are discussed in Rodenburg *et al.* [2], [4], however some key points should be noted here.

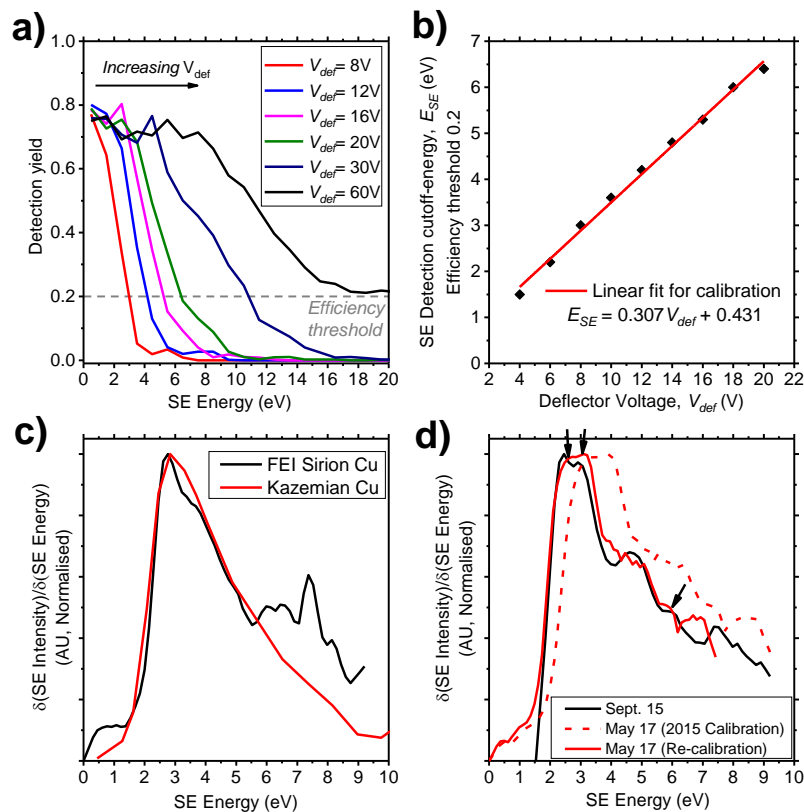


**Figure 4.1:** Calibration of FEI Sirion TLD as a SE spectrometer. a) Simulated detector efficiency plots for FEI Sirion. Each plot depicts the energy-dependent detection yield of SEs at different  $V_{def}$  values. Data extracted from [4]. b) Calibration of detector based upon part a), based upon a threshold detection efficiency of 0.2. Linear relationship between deflector voltage and SE energy at threshold yield of 0.2. c) Comparison of Copper SE spectrum measured with FEI Sirion with reference spectrum extracted from [1]; d) Change in SE spectrum measured from identical P3HT samples between Sept. 15 and May 17, and subsequent re-calibrated spectrum

The general form of the curves demonstrates a flat region of high detection efficiency at low  $E_{SE}$  followed by a sharp drop in efficiency at a certain threshold SE energy, with this threshold located at higher  $E_{SE}$  values for larger deflection biases. This effect is the origin of the SE energy-filtering functionality of the Sirion TLD. The ‘sharpness’ of this drop in efficiency towards zero reflects the energy resolution of the TLD. From Figure 4.1a, the detection efficiency drops more sharply for low  $V_{def}$  values  $< \sim 20\text{V}$  in comparison to greater  $V_{def}$  values, at which the TLD becomes a far less effective SE energy filter. This is one reason (amongst others) why, as noted by Kazemian *et al.* with regard to the FEI XL-30[1], SE spectra measured by the Sirion TLD can be considered somewhat unreliable above  $V_{def} = 20\text{ V}$ .

In order to use the detector efficiency plots to link deflector electrode bias to a SE detection cut-off energy, a threshold detection efficiency must be selected, below which SEs can be considered ‘filtered’ for the purpose of the calibration. This is a somewhat arbitrary choice, and the selection of threshold efficiency can alter the calibration that emerges from the calculation, especially at higher  $V_{def}$  where the drop in detector efficiency above the filtering threshold is less sharp. Selecting an efficiency threshold of 0.2, it is demonstrated in Figure 4.1b that the relationship between deflector voltage and the SE energy at this detector efficiency threshold is linear within the range  $V_{def} \sim 5 - 20\text{ V}$ . By fitting a straight line to this equation, the deflector bias (in V) can be converted into a related SE energy with a simple conversion factor:

$$E_{SE} = (0.307 \times V_{def}) + 0.431\text{ eV} \quad (4.1)$$

In this Thesis, a 0.2 efficiency threshold, and the resulting calibration in Equation 4.1, is used for most SE spectra measured in the FEI Sirion (a few exceptions to this are described in Section 4.2.1). This calibration is fairly consistent with that performed by Kazemian *et al.* using a FEI XL-30[1]. However, if a detection efficiency threshold of 0.3 is chosen, the calibration factor relating deflector bias and SE energy reduces to 0.273. Further, if a threshold of above 0.3 is chosen, the calculated relationship between  $V_{def}$  and  $E_{SE}$  becomes nonlinear, even in the range  $5\text{V} < V_{def} < 20\text{V}$ . As such, the calibration in Equation 4.1 must be considered an approximation with considerable error.

Further, it should be noted that the energy resolution of the detector places further error on Equation 4.1. As an example, using this Equation 4.1 it is suggested that at  $V_{def} = 12$  V, only SEs with energies of 4.12 eV and below are detected. In fact, from Figure 4.1a it is evident that at  $V_{def} = 12$  V, SEs with an energy of 5 eV are detected with a yield of 0.08, and the detection efficiency of 3.5 eV electrons is only  $\sim 0.35$ . This error is due to the limitations of the FEI Sirion TLD detector, as a non-specialised SE spectrometer.

Despite these limitations, however, it can be observed in Figure 4.1c that the FEI Sirion TLD, calibrated using Equation 4.1, accurately reproduces a literature SE spectrum in the low-energy range. Here, the SE spectrum of copper was measured and compared with a similar spectrum measured in a FEI XL-30 by Kazemian *et al.*[1] (Figure 4.1c). Especially at low SE energies, where the energy resolution is optimised, the spectrum measured in the FEI Sirion shows a similar form to the reference spectrum. The deviation in the spectrum measured in the FEI Sirion at higher energies may be a result of unexpected detector behaviour, possibly related to the calibration issues described above. However, the deviation is more likely a result of sample contamination on the surface of the copper sample measured in the FEI Sirion SEM. That the deviation appears only at higher energies is suggestive of contamination effects, as it has been previously demonstrated that a contamination layer can alter the nature of SE emission[2], [7], with low-energy SE emissions affected less by the presence of contamination layers[2].

An important observation from Figure 4.1c is that in both the experimental spectrum measured in the FEI Sirion and the reference spectrum from Kazemian *et al.*, the spectrum onset is not at 0 eV as would be expected[8], [9] (Section 2.7.1). This is almost certainly a result of the TLD demonstrating poor SE detection yield below  $V_{def} \sim 5$  V, outside of the range where the detector calibration in Equation 4.1 is valid. This effect has been observed in all samples measured to date with onset always  $>0$  eV. However, different onset shifts are observed in the experimentally measured spectrum of different materials (this effect can be seen from comparison of P3HT and PCBM spectra in Figure 5.1b, where the spectra are presented as measured). This is likely a result

of variation in the electric field at the surface of different sample materials[10], or perhaps related to contact resistance between different materials and the SEM itself.

#### ***Section 4.2.1: Long-term validity of SE spectrometer calibration***

In the course of this PhD, SE spectra were acquired from the FEI Sirion SEM over the course of ~3 years, and changes to the apparent calibration of the TLD were noted over this time. The majority of SE spectra presented in this Chapter were acquired in 2015, however further SE spectra were acquired in 2017 and it was observed that the SE spectroscopy calibration of the TLD had changed. SE spectra of identical samples (cast from chlorobenzene solvent with no anneal step), measured with the same  $E_0$  and comparable electron beam current but acquired ~20 months apart, are presented in Figure 4.1d.

It can be observed that a P3HT SE spectrum measured in September 2015 (black line) demonstrates a significantly narrower form than a P3HT SE spectrum measured after the change in May 2017 (red dashed line). For both the black and red-dashed spectra, Equation 4.1 has been used to convert deflector bias in to SE energy. It is thus assumed that the calibration of the TLD spectrometer has changed during this period. However, it appears that this change mostly equates to a reduction in the calibration factor in Equation 4.1. This reduction is on scale similar to that expected by choosing different threshold efficiencies in Figure 4.1a with which to calculate the spectrometer calibration. It has been found empirically that by replacing the calibration in Equation 4.1 with:

$$E_{SE} = 0.227 \times V_{def} + 0.431 \text{ eV} \quad (4.2)$$

The spectrum measured in May 2017 after the FEG source change (Figure 4.1d, solid red line) largely reproduces the shape and peak positions present in the spectrum measured in 2015 (as denoted by arrows in Figure 4.1d). Nonetheless, some features in the September 2015 spectrum, such as a peak around 4.5 eV and the shape of the low-energy peak, are not precisely reproduced in the 2017 spectrum even after implementing the new calibration in Equation 4.2. For this reason, most of the SE spectra chosen for inclusion in this Chapter were acquired in 2015, before any

measurable change in spectrometer calibration was observed. In instances where this was not possible and spectra measured in 2017 were required, it is stated and Equation 4.2 has been used to calibrate the spectrum.

From this effect, it is clear that the SE spectroscopy performance of the microscope must be continually assessed to ensure consistency, and the TLD re-calibrated if necessary. Insufficient information is available for the simulation data in Figure 4.1a to evaluate how the variation in calibration in Equations 4.1 and 4.2 may relate to the simulated detector yield curves. However, this variation over time is another indication that the detector energy calibration is an approximation, and the measured positions of spectral features should be treated similarly.

The specific origin of the variation in the spectrometer calibration is uncertain, as insufficient information on the detailed SEM configuration in 2015 is available for comparison with the 2017 configuration. However, a highly likely cause is changes to the relative alignments and strengths of the various electron-optical components in the electron column. Small adjustments to these alignments are regularly performed on SEMs to maintain optimal performance of the microscope[11]. Notably, between the two measurements in Figure 4.1d, a new FEG electron source (Section 2.6.1) was installed in the microscope, the process of which usually requires significant changes to the alignments of many components in the electron column. Emitted SEs must travel through the lower part of the electron column to reach the TLD during SE spectrum acquisition, and electromagnetic fields from various lenses or electrodes in the column can thus influence the path or energy of SEs prior to reaching the TLD scintillator. It is feasible, therefore, that changes to the relative alignments and strengths of these fields over time can have a significant effect on the performance and calibration of the TLD as a SE spectrometer. If this is the case, the major realignments required after maintenance events such as a FEG source replacement could have a considerable effect on the TLD calibration.

## Section 4.3: SE spectroscopy of P3HT, results

### Section 4.3.1: Effect of primary beam energy

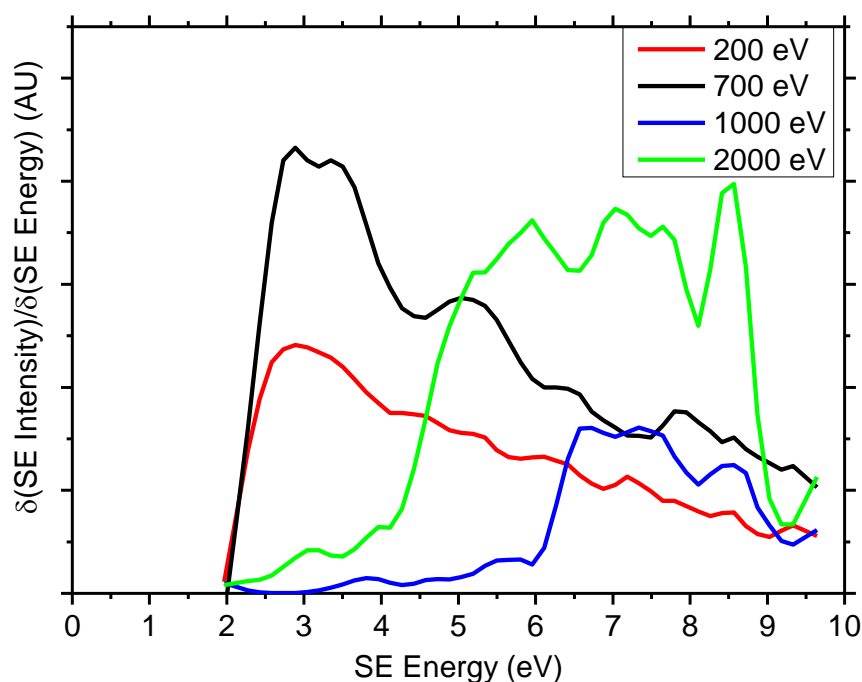


**Figure 4.2:** SE spectrum of annealed, regioregular P3HT films measured at different  $E_0$  values.

The SE spectra of an annealed regioregular P3HT sample cast from dichlorobenzene, measured at a range of primary beam energies from 200 eV to 2000 eV, is displayed in Figure 4.2. It can be seen that the  $E_0 = 200$  eV and 700 eV spectra demonstrate the same basic form, however the  $E_0 = 200$  eV spectrum shows little fine structure. This may be because exciting the P3HT film with a lower energy beam limits the modes of electron excitation. Most notably, the carbon K-edge is at 282 eV, and as such a significant excitation pathway is removed at  $E_0 = 200$  eV[12]. As a result, some spectral features that are present in higher  $E_0$  spectra may not be present at  $E_0 = 200$  eV due to having an origin in higher-energy excitations.

In the case of the  $E_0 = 1000$  eV and 2000 eV spectra, the spectrum onsets are significantly shifted with respect to the  $E_0 = 200$  eV and 700 eV spectra. This is highly indicative of negative sample charging. For the  $E_0 = 1000$  eV spectrum, the majority of the film SE emissions have been accelerated beyond the effective energy-filtering range of the TLD spectrometer, as indicated by the low intensity of the spectrum. That this charging effect was observed with the most ordered,

and as such most conductive, P3HT film studied in this chapter (Section 3.1), suggests that it is not possible to accurately measure a SE spectrum from a ‘fresh’ P3HT film using  $E_0 > 1000$  eV. The presence of charging in P3HT samples with  $E_0 > 1000$  eV but not at  $E_0 = 700$  eV is likely due to the  $E_2$  energy of the P3HT film (Section 2.6.4). This is the primary beam energy for which the total electron yield (including BSE and SE) is 1[7], where charging will not occur as every incident primary beam electron induces the emission of one electron from the sample on average.  $E_2$  is generally around 1000 eV for polymers[13], however from Figure 4.2 it appears that this energy is in fact closer to 700 eV for P3HT. Whilst  $E_0 = 700$  eV may not give a SE yield of exactly 1, the charge accumulation at this energy is clearly small enough that the localised conductivity of the film is sufficient to prevent measurable sample charging. Above  $E_0 = 1000$  eV, the SE yield is less than 1[7] and localised charge is accumulated over the course of SE spectrum acquisition, significantly affecting the energy of the emitted SE. Therefore,  $E_0 = 700$  eV was used to acquire the majority of SE spectra in this Chapter (unless stated otherwise). The  $E_0 = 700$  eV spectrum demonstrates no noticeable charging from a ‘fresh’ P3HT sample, and yet demonstrates clear spectral features not present at  $E_0 = 200$  eV.

**Section 4.3.2: Reliability of SE spectra, effects of electron beam damage**

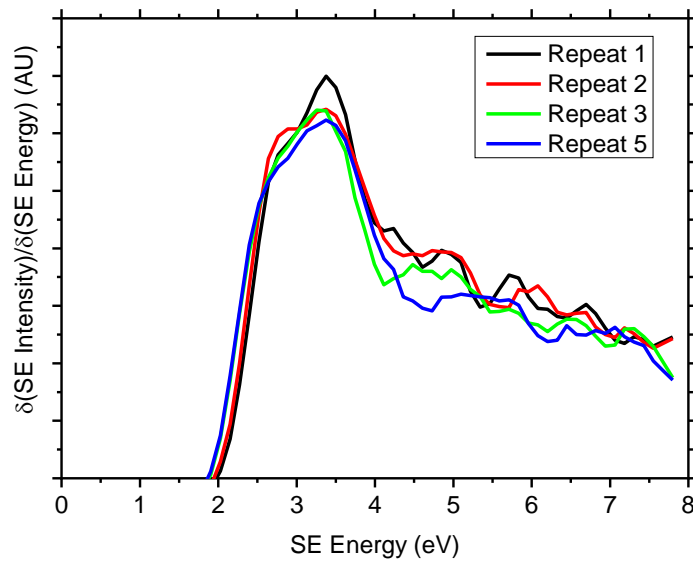


**Figure 4.3:** SE spectra of as-cast regioregular P3HT sample, repeated measurements from the same sample area,  $E_0 = 700$  eV. Spectra calibrated using Equation 4.2.

As a polymeric material, P3HT is known to be susceptible to radiation damage from the primary electron beam in a SEM[14]. A discussion of the potential effects of electron irradiation is given in Section 2.6.4 of this thesis, however it is unsurprising that the energy input by the primary beam in a SEM can break chemical bonds and change the chemical makeup of the material. This alters the localised and bulk electronic structure of a P3HT film[14], and as such will affect its SE transport and emission properties. Few steps can be taken to mitigate these damage effects for a given beam dose. As SE spectrum acquisition in a FEI Sirion SEM requires a range of SE images to be taken of the same sample area (Section 3.2), it is therefore important to establish that the effects of electron beam damage do not significantly alter the nature of the measured SE spectrum. To this end, SE spectra were repeatedly measured from an as-cast regioregular P3HT sample, cast from chlorobenzene, using similar beam and sample conditions typically used to measure SE spectra in this Chapter ( $E_0 = 700$  eV, 10-20 pA beam current, ‘fresh’ sample not exposed to air). It should be noted however that FEI Sirion SEM allows only limited (spot-size[11]) control over the beam current reaching the sample, and as such the beam current used to measure a spectrum will not be precisely constant throughout this Chapter. Efforts have been made to keep this as constant as possible however.

The effects of repeated electron beam exposure on the SE spectrum are presented in Figure 4.3, and use the new (2017) FEG-tip and related detector calibration (Equation 4.2). A (directly-measured) beam current of 15 pA was used to acquire these spectra, giving an electron dose of  $5.65 \times 10^{11}$  electrons.cm<sup>-2</sup> for one image, or  $3.39 \times 10^{13}$  electrons.cm<sup>-2</sup> for each whole spectrum using standard SE spectrum acquisition conditions (Section 3.2). It should be noted this total electron dose is many magnitudes lower than that demonstrated by Ahn *et al.* to incur significant bulk damage to a P3HT film based upon EELS experiments ( $4 \times 10^{17}$  electrons.cm<sup>-2</sup>)[14]. However, beam damage is concentrated near the top surface of the film, especially using low  $E_0$ [15], and as such would be expected to have greater influence on a SE spectrum.

In Figure 4.3, it can be observed that the electron beam dose used to acquire SE spectra in this chapter results in small but measureable changes to the sample SE spectrum. In the low-energy

range, the SE spectrum onset is shifted towards lower energy by  $\sim 0.15$  eV after 3 spectra ( $1.02 \times 10^{14}$  electrons.cm<sup>-2</sup>), with a general broadening of the low-energy peak. The peak around 3.4 eV is seen to clearly reduce in intensity with increasing electron beam exposure. A shoulder around 2.9 eV also shows lower intensity with greater electron dose, however to a lesser extent than the 3.4 eV peak. Further, a spectral region between 4.4 and 5.2 eV shows significantly reduced intensity after 5 repeated spectra ( $1.70 \times 10^{14}$  electrons.cm<sup>-2</sup>).

An interpretation of these effects requires a greater understanding of the features of the P3HT spectrum, and what physical or electronic properties each feature in the SE spectrum may represent. An important result at this point however is that after electron beam doses equivalent to those used to acquire two or more SE spectra, the locations of SE spectrum peaks remain unchanged, and the relative intensities of these peaks alters only slightly. The SE spectra presented in the following Sections can therefore be confidently taken as representative of the original sample properties.

#### ***Section 4.3.3: Crystallinity, ordering effects***

SE spectra were measured from ‘fresh’ P3HT samples that were spin-coated on to silicon substrates in a nitrogen glovebox and transferred to the microscope chamber under vacuum. In order to probe the effect of sample morphology ties on the SE emissions of chemically identical samples, spectra were measured from two different P3HT samples, having significant differences in the level of bulk crystallinity in the films (Section 2.3.2, Section 3.1). One film was processed from regioregular P3HT in a slow-drying ‘poor’ solvent (dichlorobenzene) and annealed at 170 °C to encourage high levels of crystalline formation and influence chain orientation at the surface of the film[16]. The other was processed from regiorandom P3HT, to give a largely amorphous film (although localised short-range order is known to be present even in regiorandom films[17]).

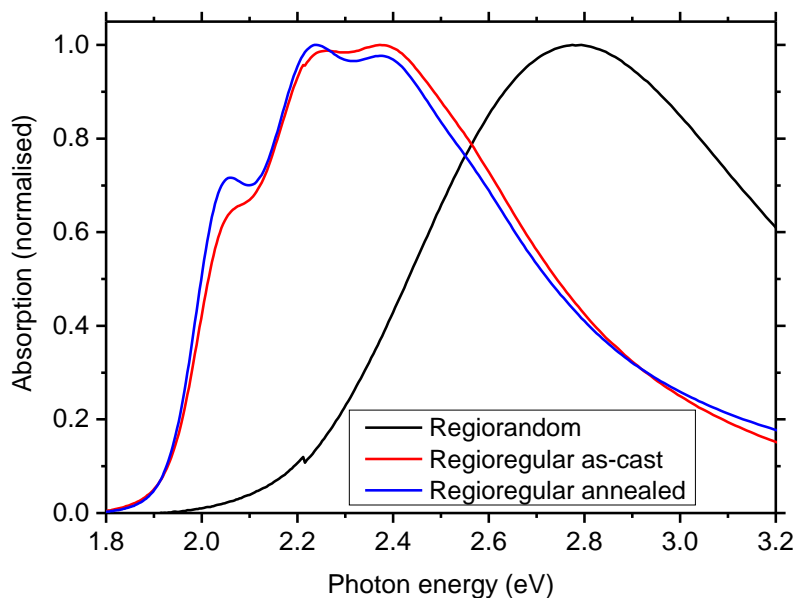


**Figure 4.4:** UV-visible absorption spectra from various P3HT films.

The variation in crystallinity between the differently processed films was probed using UV-visible light absorption spectroscopy, displayed in Figure 4.4. It can be seen that the regioregular annealed and regiorandom films demonstrate different absorption properties, which reflects the variation in electronic structure between more crystalline and amorphous P3HT films[18], [19]. Importantly, it can be observed that the regiorandom sample demonstrates the broad absorption spectrum with peak around 2.8 eV expected from a highly amorphous P3HT sample, whereas the annealed film demonstrates three well-defined peaks at energies in the range 2-2.5 eV. This is reflective of the presence of crystalline content in the film[20]. The relative height of the absorption peaks at 2.07 eV and 2.24 eV has been shown to represent the strength of the intermolecular coupling,  $J$ , indicative of the level of crystallinity within the film[5], [20]. For the annealed P3HT film, an intermolecular coupling of  $\sim 21$  meV was measured from its absorption spectrum. This reflects an increased level of crystallinity over an as-cast regioregular film processed from a faster-drying solvent (chlorobenzene,  $J \sim 34$  meV)[20]. These measurements are reflective of the level of crystalline ordering, although an accurate quantification of bulk film crystallinity[21] cannot be calculated from UV-visible spectra[17], [20]. Literature suggests that similar films demonstrate bulk crystallinity of 47-56% as measured by wide-angle x-ray diffraction[17]. The long absorption tail beyond 2.5 eV measured from the annealed and as-cast

regioregular samples reflects absorption from remaining amorphous phases in the sample, as can be observed from the overlap of this tail with the broad absorption feature measured from the regiorandom film.

To compare the SE spectra of annealed and regiorandom P3HT samples, three SE spectra were measured from widely spaced areas on the film to measure the reliability and repeatability of the measured spectra. In Figure 4.5a and b, repeat spectra are displayed from the annealed and regiorandom P3HT films, respectively. The electron beam parameters used to acquire the spectra for both samples were identical. SE Spectra in Figure 4.3 were measured with a primary beam energy of  $E_0 = 700$  eV with  $\sim 16$  pA beam current, from sample areas  $62 \times 42$   $\mu\text{m}$  in size.

From Figure 4.5, it is clear that the SE spectra of regiorandom and annealed P3HT demonstrate the same basic form, indicating the fundamental SE transport and emission properties of amorphous and crystalline phases at the film surfaces are comparable. However, upon closer inspection some notable differences in the SE spectra measured from the two P3HT films are visible.

The low-energy peak in the spectrum of both films appears around 3 eV. For both films, this peak has approximately the same width, however the annealed P3HT film shows two peaks at 2.9 eV and 3.4 eV in this region, whereas the regiorandom film shows only a single peak with an average position of 3.3 eV. However, the repeat spectra from the regiorandom sample (Figure 4.5a) show significant variation in this peak position. By comparing the annealed, regioregular P3HT film with a regioregular as-cast sample, the origin of these two peaks can be explored in Figure 4.5c. Here, it can be observed that the largest peak in the as-cast film aligns with the higher-energy, 3.4 eV peak in the spectrum of the annealed film. A shoulder is also present around 2.9 eV, aligning with the lower energy peak measured from the annealed sample. A discussion of the results in Figure 4.5 can be found in Section 4.5.

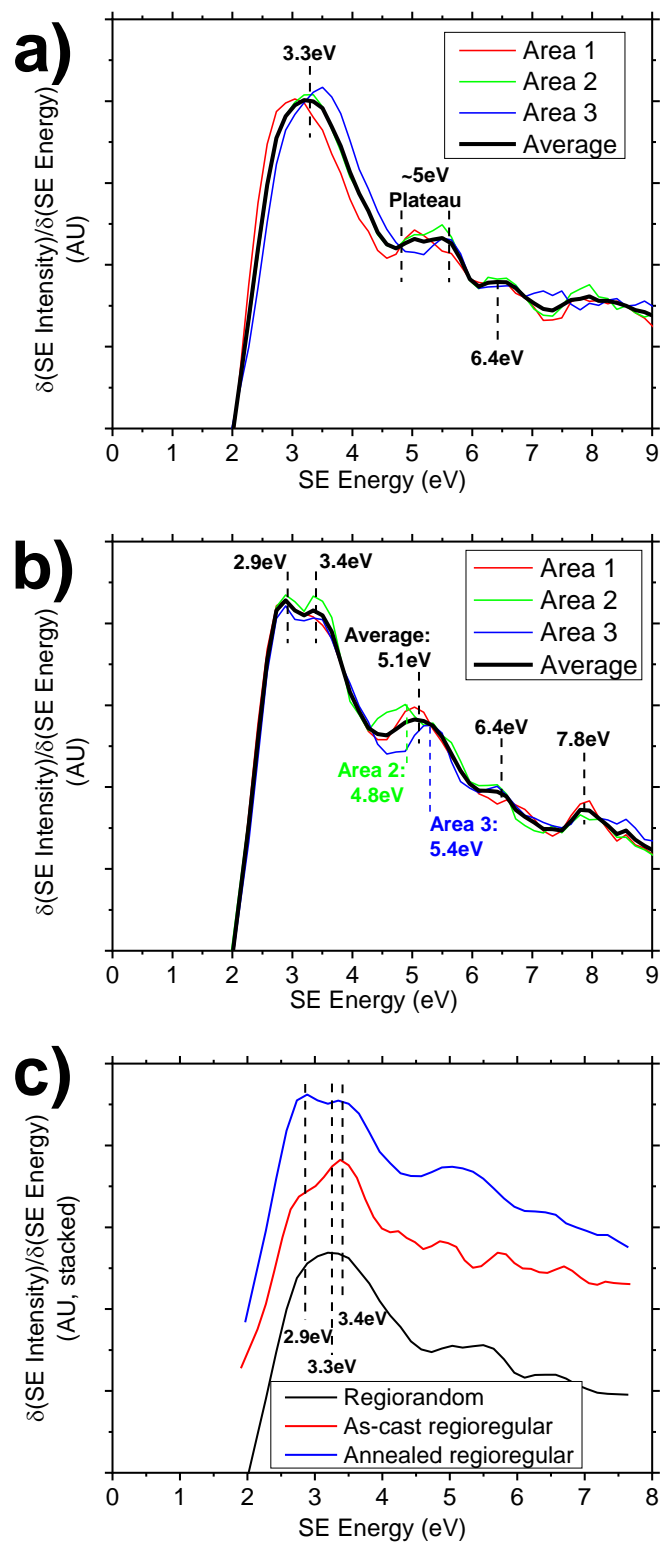


**Figure 4.5:** SE spectra of 'fresh' P3HT samples measured at  $E_0 = 700$  eV. Spectra measured from different sample areas and averages from a) Regiorandom P3HT; b) Annealed regioregular P3HT. c) Direct comparison of regiorandom, and as-cast and annealed regioregular P3HT samples. Notable peak positions marked in each chart.

The other, notable variation between the SE spectra of the thermally annealed and regiorandom samples is the clear difference in peak height measured at  $\sim 5$  eV, and, to a lesser extent, 6.4 eV.

These are again likely to relate to the higher levels of crystallinity or molecular ordering in the thermally annealed sample. By comparing Figures 4.5a and b, these peaks are much better defined in the annealed sample, especially when the non-averaged individual spectra measured from different areas are taken in to account. From comparison of the individual spectra from the annealed P3HT film, this peak varies in its location between values of 4.8 and 5.4 eV, suggesting a degree of localised variation in electronic energy levels from this film. Comparing with the as-cast regioregular sample in Figure 4.5c, it is observed that the as-cast film does not demonstrate a well-defined peak or plateau at ~5 eV. This may be related to some unique morphological aspect of the as-cast regioregular film, which affects SE emissions in relation to both the regiorandom and annealed P3HT films (both of which show features at ~5 eV). However, it should be noted that the SE spectrum of this as-cast film was measured in 2017, and is calibrated with Equation 4.2, whereas the other two spectra in this Figure (annealed and regiorandom) were measured in 2015, and use the calibration in Equation 4.1. Using Equation 4.2, the 5-6 eV detection cut-off corresponds deflector biases of 20 V and above, at which point SE energy filtering performance of the TLD is decreasing (as discussed in Section 4.2). As such, the as-cast regioregular spectrum may not have been measured with the required energy resolution in the 5-6 eV range to show this peak with much clarity.

#### ***Section 4.3.4: Effects of surface modification***

To test the effects of surface modification on the spectrum measured from a P3HT film, an annealed P3HT film was allowed to degrade under light and air exposure. As OPV devices commonly degrade *via* chemical attack by oxygen, the effects of oxygen exposure on the chemical and electronic properties of P3HT films has been well studied[22]–[24]. As such, comparing the SE spectra measured from ‘fresh’ and air-exposed samples is an ideal test of how the modification of a sample’s surface properties can alter the nature of its measured SE spectrum.

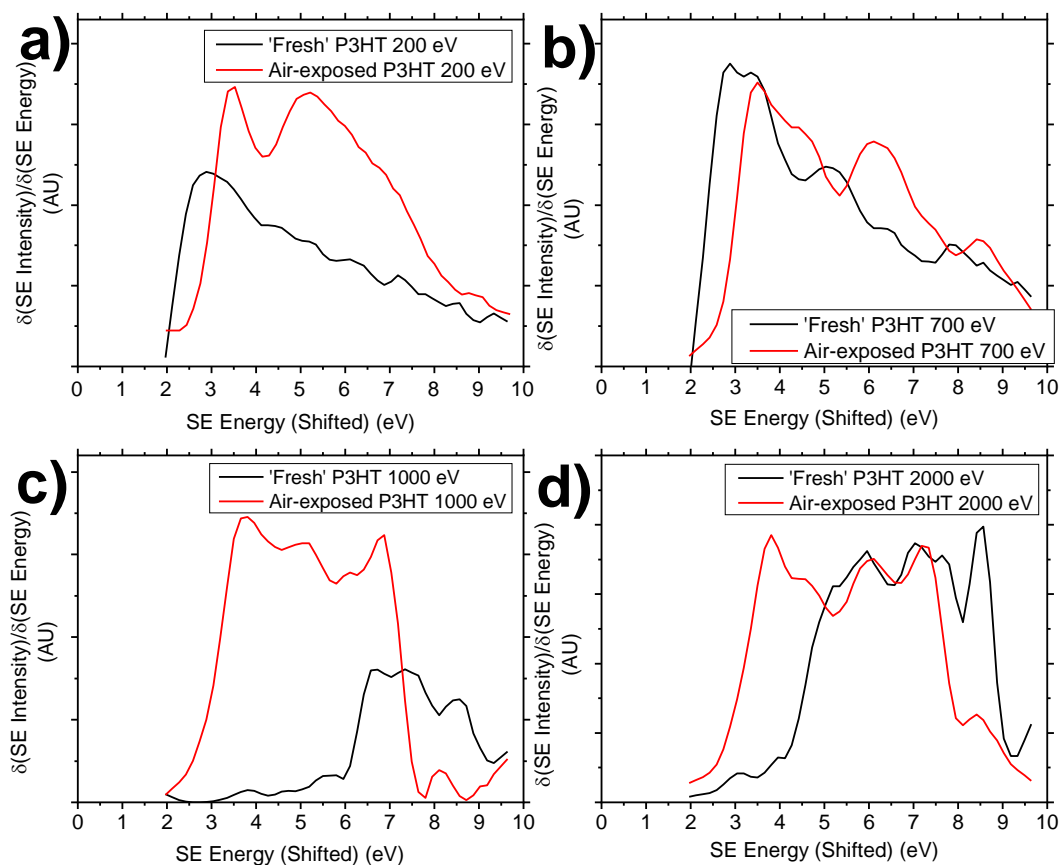


**Figure 4.6:** Comparison of SE spectra measured from 'fresh' and air-exposed annealed P3HT samples measured at  $E_0 =$  a) 200 eV; b) 700 eV; c) 1000 eV; d) 2000 eV.

In Figure 4.6, SE spectra measured at different  $E_0$  from a fresh sample (already presented in Figure 4.2) are compared with equivalent spectra measured from identical samples allowed to degrade under air and light for  $\sim 14$  days. This level of exposure is known to induce significant chemical alterations to the P3HT film[23], altering its electronic band structure[25] and molecular orientation[26], with the effects naturally most concentrated at the sample surface[22], [24]. In Figure 4.6a, the effect of air exposure measured with  $E_0 = 200$  eV is shown. Clearly, the shape and intensity of the measured spectrum change significantly. Alongside the sharp increase in the integrated intensity of the spectrum, the maximum of the first peak is shifted towards higher energies (2.8 eV to 3.4 eV), as well as demonstrating a more gradual spectrum onset. Further, a new peak is observed in the spectrum at 5.1 eV. The degradation effects at  $E_0 = 700$  eV appear less dramatic, however show a similar nature to the effects measured at  $E_0 = 200$  eV in the form of a more gradual onset, a shift in the low-energy peak to higher energies as well as a broad peak

at 6.1 eV. The  $E_0 = 700$  eV spectrum also appears to retain its ‘double’ onset peak after air exposure; however the peak ratio changes, with the lower energy peak relatively more intense after degradation.

The most notable air exposure effects are observed at  $E_0 = 1000$  and 2000 eV, where the spectrum onset is observed to shift from  $\sim 6$  eV to  $\sim 2$  eV, matching the air-exposed spectra measured at  $E_0 = 200$  and 700 eV. The  $E_0 > 1000$  eV air-exposed spectrum demonstrates a significantly different form to the lower  $E_0$  spectra however, with multiple higher-energy peaks after the low-energy peak, followed by a rapid decay to almost zero intensity at 7.5 eV. This ‘top-hat’ shape is not expected from a SE spectrum, suggesting spectrometer effects have perhaps influenced the shape of the measured spectrum. These effects, as well as the nature of the SE spectra in Figure 4.6 are discussed in Section 4.5. Despite the unexpected shape, one important observation is the general similarity in shape between the spectra measured at  $E_0 = 1000$  eV and 2000 eV. This is indicative that the shape of the SE spectrum of P3HT changes little above  $E_0 = 1000$  eV despite undergoing dramatic change between  $E_0 = 200$  and 1000 eV. This is an unsurprising observation, as the SE yield of polymers has been observed to change dramatically below  $E_0 = 1000$  eV, but stabilise as  $E_0$  increases above 1000 eV[27].

A more intense surface modification of P3HT can be effected by using a low-power plasma to etch the surface of the P3HT film (Section 3.2). Depending on the reactivity of the plasma gas, the effects can vary from sputtering[28] to chemical etching[29]. To test the effects of the different plasma gases on the nature of a SE spectrum, ‘fresh’ annealed P3HT films were placed in a low-pressure plasma cleaner and subject to a 15-minute plasma etch in air and argon. As argon is chemically unreactive the sputter rate of argon plasma is known to be low[28] and should not introduce new elements to the sample surface[30]. Contrastingly, the reactive oxygen component of air introduces new oxygen-containing species to the sample surface[31].

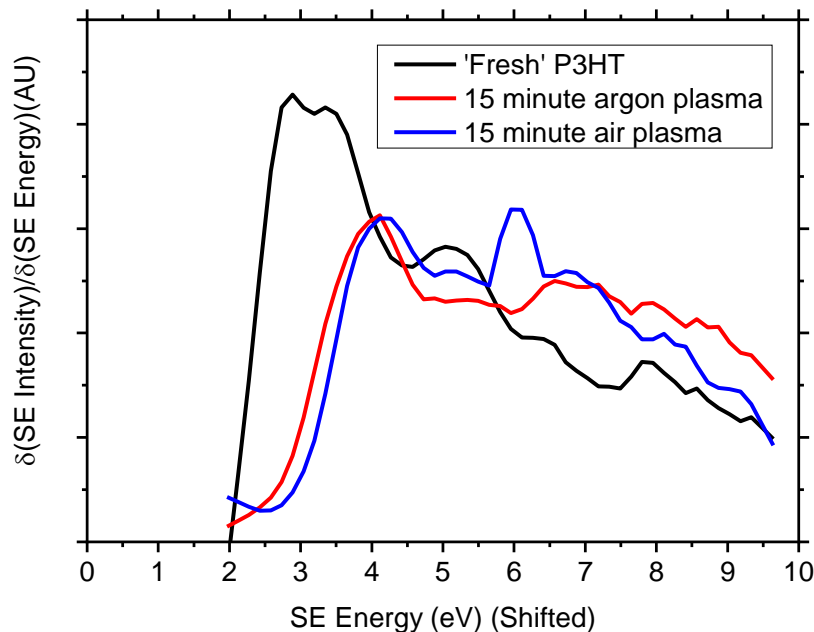


**Figure 4.7:** SE Spectra of annealed regioregular P3HT before and after plasma clean in air and argon

The effects of these different plasma etch processes on the SE spectra are demonstrated in Figure 4.7, using  $E_0 = 700$  eV. Here it can be seen that the effects of both plasma processes are broadly similar, shifting the low-energy spectrum peak towards higher energies, and giving a more gradual spectrum onset. The ‘double peak’ structure present in the ‘fresh’ sample spectrum is also no longer present after a plasma etch. Further, the spectrum shape between 5 and 9 eV is more ‘flat’ in the plasma etched samples. The only significant difference in the effects of the different plasma gases can be observed around 6 eV, where the air plasma spectrum demonstrates a well-defined peak that is not present in the argon plasma spectrum. A more detailed consideration of these effects will be given in Section 4.4.

#### Section 4.4: Energy-filtered imaging of ‘fresh’ and air-exposed P3HT films, results

Whilst its well-documented SE spectroscopy characteristics make the FEI Sirion SEM an ideal test instrument for TLD-based spectroscopy measurements, its imaging performance is relatively poor in comparison with the present state of the art[32], [33]. As such, P3HT films were imaged in a modern FEI Helios 660 SEM in order to acquire high-resolution image data. The FEI Helios SEM employs an ‘Elstar’ electron column design; this is capable of SE energy filtering via a

different mechanism to the FEI Sirion (Section 2.7.2). Images were acquired with a SE detection energy cut-off of around 8 eV, using  $E_0 = 2.8$  keV, chosen such that the interaction volume of the electron beam penetrates the thickness of the P3HT film and minimises sample charging (see Section 3.3).

The effect of energy-filtered imaging in comparison with conventional, non-filtered SE imaging is demonstrated by unfiltered and energy-filtered images of the same region of an as-cast regioregular P3HT film in Figure 4.8. All images in this section were acquired with identical SEM imaging parameters (including brightness and contrast settings), with the exception of the changes required to perform SE energy filtering (described in Section 3.3). Images are presented with no post-processing applied.

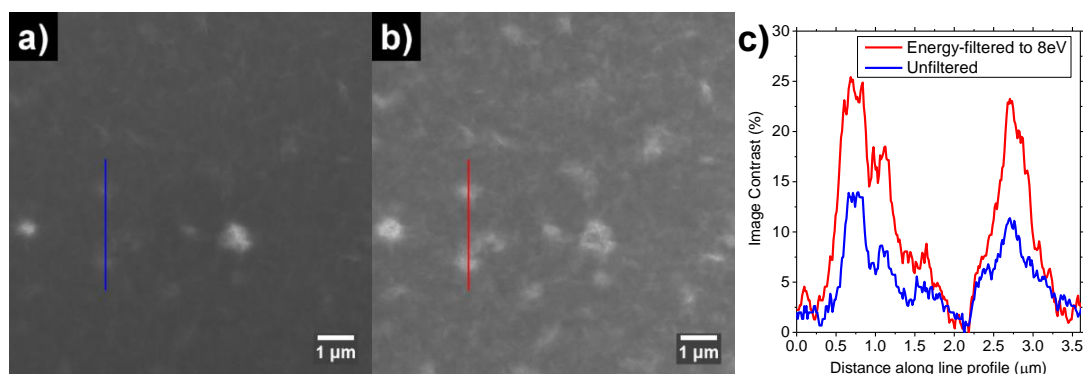


**Figure 4.8:** Demonstration of image contrast improvement using energy-filtered SE imaging on as-cast regioregular P3HT sample. a) Conventional SE image and b) energy-filtered SE imaging using only SEs of  $\sim 8$  eV and below. c) Calculated image contrast plotted along lines marked in parts a) and b)

Unsurprisingly given the semicrystalline nature of regioregular P3HT (Sections 2.3.1 and 2.3.2), localised variation in the film morphology can be observed in both the unfiltered and energy-filtered SE images. In the unfiltered image (Figure 4.8a), the image contrast is generally low with the exception of some small, bright features which are presumably large topographical features that demonstrate a significant ‘edge effect’ (Section 2.6.2). However, in the energy-filtered image, the degree of contrast across the image is far greater and allows finer aspects of the semicrystalline morphology to be visualised in more detail. The increase in total image brightness in the energy-filtered image may seem counter-intuitive given that high-energy SEs are ‘filtered out’ to generate this image. The brightness increase is almost certainly a result of the higher suction tube bias

(Figure 2.21, Section 3.3) used in an SE energy filtering condition. This increases the collection efficiency of SEs reaching the TLD scintillator. However, to demonstrate that the improvement in image quality in the energy-filtering condition is not simply a result of better signal-to-noise ratio, the imaging contrast along a line profile marked in Figures 4.8a and b was calculated. In Figure 4.8c, it is evident that the use of energy-filtered SE collection approximately doubles the available imaging contrast (as defined by Seiler[7], Equation 3.1) compared to conventional, unfiltered SE imaging.

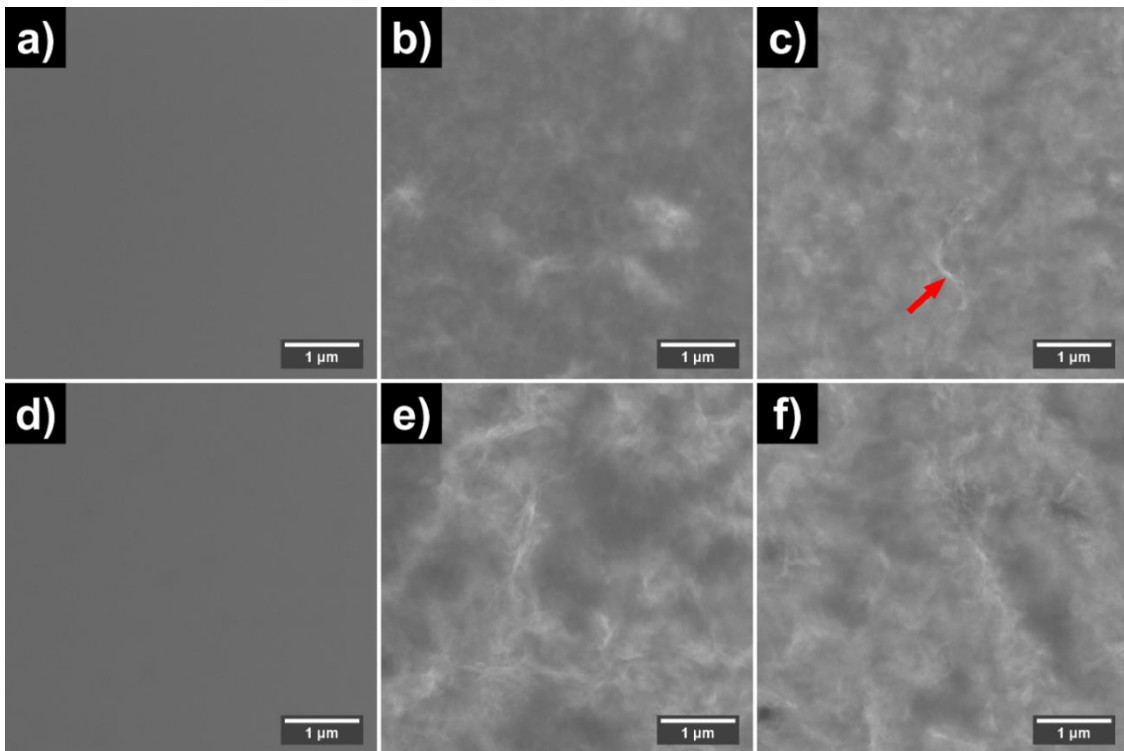


**Figure 4.9:** Energy-filtered SE images of P3HT films using SEs of energy  $<8$  eV. a)-c): 'Fresh' P3HT films: a) regiorandom; b) as-cast regioregular; c) annealed regioregular. d)-f): 24h air-exposed P3HT films: d) regiorandom; e) as-cast regioregular; f) annealed regioregular. Red arrow in part c) denotes a P3HT 'fibril' structure in a fresh film.

Energy-filtered SE images of regiorandom, and as-cast and annealed regioregular P3HT films are displayed in Figure 4.9. Clear morphological differences are visible between the different samples. In Figure 4.9a the regiorandom film demonstrates no discernible image contrast, an expected result based upon the highly amorphous nature of this film[17]. The regioregular P3HT films demonstrate localised variation, almost certainly due to the presence of molecularly ordered regions in these films[34]. After a thermal anneal, more bright sample regions are apparent,

covering the majority of the sample surface. In both regioregular films, these bright regions take the form of ‘cloud’-like regions, which contain well-defined fibril structures, with an example denoted by an arrow in Figure 4.9c.

After ~24 hours air exposure (Figure 4.9d-e), EFSEM images of the regiorandom sample remain unchanged and featureless. However, in the regioregular films significant differences in comparison to the ‘fresh’ samples can be observed. Clear image features can still be observed, including brighter and darker phases, however the nature of these phases has altered somewhat after oxygen exposure. Considering the as-cast sample (Figure 4.9e), the bright phases have become much larger and better defined, with very clear fibril structures visible. Likewise, in the EFSEM image of the annealed sample (Figure 4.9f), the level of contrast between bright and dark phases has increased. However, contrary to the as-cast sample, the size and coverage of the darker phase appears to have increased in size after air exposure. As a result, after air exposure, the as-cast and annealed P3HT films appear similar (Figures 4.9 e,f) – in stark contrast to the ‘fresh’ films where these appear very different (Figures 4.9 b,c).

#### **Section 4.5: Discussion of P3HT spectra and energy-filtered imaging**

By combining the EFSEM images of the various P3HT films with their SE spectra, deeper insights into the SE emissions of the differently processed films may be obtained.

##### ***Section 4.5.1: Secondary electron spectroscopy***

In Figure 4.5, repeat spectra measured from different areas of both a regiorandom and an annealed regioregular P3HT film are presented as measured at  $E_0 = 700$  eV. Close similarities in the basic form of the spectra measured from both samples can be observed, indicating parallels in the generation, transport and emission of SE. However, the differences present between the SE spectra are likely reflective of the obvious differences in electronic structure and morphology (Section 2.3.2), and highlighted by the EFSEM images of the samples in Figure 4.9.

In Figure 4.5a, the three repeat spectra measured from the regiorandom sample show an extremely similar form, with a broad, unstructured low-energy peak around 3.3 eV and a plateau

around 5 eV. The broad low-energy peak is likely representative of a wide range of surface energy levels in the ‘LUMO-band’ of the amorphous regiorandom sample[16], giving small and highly localised variation in the relative position of the low-energy peak. Averaging these variations over a low-magnification image ( $62 \times 42 \mu\text{m}$ ) gives a broad low-energy peak.

However, the individual repeat SE spectra measured from the regiorandom film are observed to shift relative to each other along the energy axis. Based upon the uniform, featureless EFSEM image of the ‘fresh’ regiorandom sample, as well as the close similarity in the shapes of the repeat spectra it is believed that this variation is related to charge accumulation. Amorphous P3HT is known to have poor bulk conductivity (Section 2.3.2), and serious charging of this sample during spectrum acquisition was only prevented by imaging around its apparent  $E_2$  value (Section 2.6.4) at  $E_0 = 700$  eV. However, small accumulations of charge may remain if the localised charge mobility is low. Clearly, nanoscale variation in sample ordering, even in a regiorandom sample[17], can cause variation in the localised conductivity and degree of charge accumulation in different areas the regiorandom P3HT film. This shifts the position of the onset peak in the regiorandom sample as the accumulated charge applies an electrostatic force on emitted SE[11].

From observation of Figure 4.5b, the more crystalline[16], [35] thermally annealed film demonstrates constant low-energy peak positions for all repeat spectra, indicating that this sample is not detectably charging. This is expected given the improved bulk charge transport that results from higher crystallinity[34]. In contrast to the single peak measured from the regiorandom sample, two peaks (at 2.9 and 3.4 eV) are observed in the low energy region of the annealed sample spectrum, both apparently narrower than the single low-energy peak in the regiorandom spectrum. It is postulated that the two peaks may originate from the low energy SE peak emitted from crystalline and amorphous phases. Variation in the band gap, electron affinity and ionisation energy of amorphous and molecularly ordered P3HT films has been demonstrated by Kanai *et al.*[16] as a result of greater electron delocalisation and a more uniform electronic structure (section 2.3.2) in crystalline regions. It would follow that these electronic properties result in different low-energy peak positions for amorphous and crystalline material. The narrower

distribution of electronic states measured by Kanai *et al.* after a thermal anneal[16] would also explain the comparatively narrow low-energy peaks in comparison to the regiorandom film.

Allocation of the 2.9 and 3.3 eV peaks in the annealed P3HT spectrum to amorphous or crystalline material cannot be performed confidently by simple comparison with the regiorandom spectrum. Whilst the average low-energy peak is measured at 2.2 eV from the regiorandom sample, appearing to align well with the 3.4 eV peak in the annealed sample spectrum, the variation in peak position between different sample areas means that it is difficult to be confident in this conclusion. To help with the allocation of these two peaks, a SE spectrum was also measured at  $E_0 = 700$  eV from a regioregular P3HT film, cast from a faster-drying solvent (chlorobenzene) and not annealed (Figure 4.5c). This sample demonstrates crystalline aggregation properties[34], however a lower level of ordering is observed from its UV-visible absorption spectrum (Figure 4.2) in comparison to the annealed sample[16]. The EFSEM image of the as-cast film also shows smaller, less-defined crystalline features in comparison to the annealed film, qualitatively indicating a lower level of ordering. The SE spectrum of the as-cast sample displays a large, well-defined peak at 3.4 eV, and a poorly defined shoulder at 2.9 eV. Clearly, the main difference between the as-cast and annealed samples in this low-energy region ( $< 4$  eV) is the reduction in intensity of the 2.9 eV feature relative to the 3.4 eV. This correlates with the reduction in crystalline ordering in the as-cast sample, suggesting that the 2.9 eV peak can be assigned to ordered phases of P3HT, and the 3.3 eV peak to more amorphous ones.

At energies above this low-energy peak, a further spectral feature around 5 eV can be observed in both the regiorandom and annealed P3HT samples. From the annealed sample, a peak is observed that shifts in energy between different areas of the sample, whereas the regiorandom sample shows more of a 'plateau'. As with the 'double peak' feature at lower energies it is likely that the strength of this  $\sim 5$  eV feature is in some way related to the level of ordering in the respective P3HT samples, having arisen from SE emission from electron bands or states that are concurrent with electron delocalisation or molecular ordering. The variation in peak location in the annealed sample makes this feature quite different to the 'double peak' however, as the peak

positions in the low energy ( $< 4$  eV) range (as well as at  $\sim 6.4$  and  $7.8$  eV) remain constant between the repeat spectrum measurements from this sample, whilst the  $\sim 5$  eV feature shifts relative to these. Further, it can be observed in Figure 4.5c that the as-cast regioregular sample does not demonstrate a clear peak in this region. Whilst it is possible that this reflects some unique feature of the regioregular as-cast sample, it was noted in Section 4.3.3 that this spectrum was measured in 2017 and calibrated with Equation 4.2, whereas the other two spectra in Figure 4.5c were measured in 2015 and calibrated with Equation 4.1. As a result, a lack of energy resolution in the 5 eV region of the as-cast regioregular spectrum may prevent observation of this feature.

This effect, as well as the origin of the 5 eV feature, can be investigated through observation of Figure 4.3. This shows the SE spectrum of an as-cast regioregular P3HT film as it degrades under continued electron beam exposure. In this Figure, a gradual reduction in SE emissions in the 4-5 eV range can be observed with increased electron beam exposure. It is likely that the spectral changes from repeat spectrum 1 to repeat spectrum 5 result (at least in part) to a loss of molecular ordering in the sample. This is because the electron beam doses required to measure even 5 repeat spectra are low in comparison to the doses shown to cause serious film damage, with changes to SE spectra more likely representative of the loss of conjugation and crystalline order in the film according to literature [14], [36]. As such, the reduced intensity in the 4-5 eV region with increased electron beam exposure implies that a poorly-resolved feature at this point is present in the SE spectrum detected from the ‘fresh’ as-cast regioregular film, and that this feature is likely related to molecular ordering. Without further information, it is difficult to draw any stronger conclusion regarding the origin of this feature. That the regiorandom sample also shows a (less-defined) feature in this region despite crystalline aggregation being inhibited in this sample is unsurprising, as quasi-crystalline regions can still form in regiorandom films[17].

Considering the SE spectra measured from air exposed samples (Figure 4.6), the low-energy peak of the  $E_0 = 200$  and  $700$  eV spectra is clearly shifted towards higher energies, with a more gradual onset. This change in SE spectrum is consistent with a p-type doped sample[3], [37], [38]. This is expected, as various works have described the effects of oxygen degradation of P3HT as

consistent with p-type doping[39], [40]. P-type doping is also known to increase SE yield from a sample[10], [38], explaining the generally increased spectrum intensity observed from the air-exposed  $E_0 = 200$  and  $700$  eV spectra. This ‘doping’ effect is a potentially ideal indicator of oxygen degradation in a P3HT sample.

The introduction of charge carriers *via* oxygen doping is a likely cause of the large shift in the spectrum onset energy observed after air exposure in the  $E_0 = 1000$  and  $2000$  eV spectra. As suggested in Section 4.3.1, the high-energy spectrum onsets observed in Figures 4.6c and d prior to air exposure likely result from sample charging at higher primary beam energies. The shift of the onset energy back towards low energies indicates that after air exposure, charging has been eliminated. This is likely a result of the introduction of new hole carriers by the p-type oxygen doping of the film.

Excepting this charge elimination, the effects of air exposure on spectrum shape are most clearly observed in the  $E_0 = 200$  eV spectrum, where the large increase in spectrum intensity is coupled with a significant change in the SE spectrum shape. That the  $E_0 = 200$  eV spectrum is the most affected by degradation is expected, as the interaction depth of the 200 eV electron beam within a P3HT sample is extremely low. The peak interaction depth of a 200 eV electron beam in P3HT was simulated to be  $< 5$  nm by a Monte Carlo model employed in Chapter 6 (see Figure 6.8). As such, the beam and resulting SE emissions are highly concentrated within the oxygen-attacked damage layer that forms on the surface of the film[24].

A broad new peak appears in the  $E_0 = 200$  eV spectrum around 5 eV, likely reflecting new electronic states[26], [41] that have formed in the sample LUMO as a result of oxygen exposure. A similar peak, although at 6 eV, is observed in the  $E_0 = 700$  eV spectrum (Figure 4.6b). By comparison with the plasma cleaned spectra in Figure 4.7 it is possible to investigate whether this peak is related to the  $\sim 5$  eV feature in the  $E_0 = 700$  eV spectrum measured from the ‘fresh’ annealed P3HT film, or if it is a new peak resulting from air exposure. It is clear from Figure 4.7 that a 15-minute plasma etch in both argon and air significantly alters the nature of SE emission. Etching under both gases shifts the low-energy peak towards higher energies and gives a more

gradual spectrum onset, similarly to the effects of air exposure. The spectrum measured from the argon-etched sample shows no well-defined features at higher energies above this low energy peak, with a flat spectrum form at higher energies. This indicates that the Ar plasma etch is sufficient to destroy the spectral features present in the ‘fresh’ sample spectrum. However, in the air-etched sample, a clear peak is visible at around 6 eV (measured at  $E_0 = 700$  eV). As previously discussed, the key difference between the argon and air-based etch processes is that whilst an argon plasma sputters material and breaks chemical bonds without itself chemically reacting, the oxygen component in air will react with the sample. With the 6 eV peak present only in the air-plasma spectrum, this indicates that the formation of oxygen-containing species on the surface of the film gives rise to this peak. Naturally, the air plasma etch is different and a far more intense process than the gradual degradation of P3HT under air. However, the presence of a  $\sim 6$  eV peak in SE spectra measured from P3HT films subject to both air degradation and air plasma treatment is a compelling indication that this peak is related to the oxygen-related degradation of the P3HT surface[26].

In Figure 4.6c and d, the SE spectrum of an air-exposed P3HT film, measured at  $E_0 = 1000$  and  $2000$  eV respectively, is presented. As previously noted in Section 4.3.1, the spectrum acquired from the ‘fresh’ film appears to be charging negatively, which accelerates SE emissions to higher energies as the electrons leave the sample. This makes a reliable interpretation of the ‘fresh’ spectrum extremely difficult, as the spectrum is energy-shifted beyond the limited operating range of the TLD spectrometer (Section 4.2). After air exposure, however, the spectrum is shifted back towards lower energies, such that the low-energy onset of the spectrum is aligned with the  $E_0 = 700$  eV air-exposed spectrum in Figure 4.6b. This indicates that after air exposure, the film does not accumulate charge during spectrum acquisition. It is likely that this is related to the p-type oxygen doping of the film, through the introduction of a greater number of hole carriers. These holes will readily combine and neutralise any accumulated electron charge in the film, preventing charging despite the nominally lower charge mobility of P3HT after oxygen degradation[39]. Due to the lack of charging, the P3HT SE spectrum can be measured at  $1000$  eV, demonstrating a

somewhat unexpected ‘top-hat’ form with sharp onset and low energy peak at 3.8 eV and sharp drop-off around 7.5 eV. This shape does not resemble either typical SE spectra in literature[8], [9] or the P3HT spectra measured at lower  $E_0$ .

The spectrum shape may be related to detector effects at higher deflector voltages, combined with different SE emission properties at higher  $E_0$ . Previous work on the SE yield of polymers[42] has indicated that the yield can change dramatically with increasing  $E_0$  up to around 1000 eV, indicating new pathways to SE emission are activated with increasing  $E_0$ . It is therefore unsurprising to observe a different SE spectrum shape at  $E_0 = 1000$  eV, with strong SE emissions up to  $\sim 7$  eV. Using the TLD spectrometer calibration in Equation 4.1, 7 eV corresponds to  $D \sim 21.5$  V. This is in the region of degrading spectrometer performance[1], whereby the energy filtering performance decreases and the TLD detector response becomes dependent on variables other than SE energy, such as angle of SE emission. It is therefore possible that TLD spectrometer effects have resulted in the ‘top-hat’ shape of the 1000 eV spectrum in Figure 4.6c. Of course, a similar sharp decay in the spectrum shape is not observed in related spectra measured at  $E_0 = 200$  and 700 eV (Figures 4.6 a, b) and as such this effect must be investigated further in future work. However, spectrometer effects may be easier to observe in the  $E_0 = 1000$  eV spectrum due to stronger SE emissions in the 7 eV region in comparison to the  $E_0 = 200$  and 700 eV spectra.

#### ***Section 4.5.2: Consideration of EFSEM image contrast***

From comparison of the EFSEM images acquired from ‘fresh’ P3HT films (Figure 4.9 a-c), the amorphous regiorandom sample appears featureless and darker on average than the regioregular samples. However, dark regions are present in the images of the as-cast and annealed regioregular samples that have some correlation with the grey level of the regiorandom film. As such, it is tempting to assign dark regions in these images to amorphous phases, and bright regions to crystalline phases. This suggestion is supported by the presence of fibril-like structures in the brighter phases (highlighted by an arrow in Figure 4.9c). Similar P3HT fibrils have been previously observed in EFTEM images of P3HT:PCBM blends[43]. Further, a higher SE yield and brighter grey level would perhaps be expected from ordered regions as a result of improved

SE transport to the surface [42]. However, the contrast mechanism in these images, whilst most likely related to crystallinity, is perhaps more complex. Thresholding Figures 4.6b and c to the grey level of the regiorandom sample gives crystallinity measures of ~18% for the as-cast sample, and 100% from the thermally annealed sample. In comparison to literature measures from nuclear magnetic resonance or x-ray diffraction (~50-60% crystallinity), this appears low for the as-cast sample (although surface crystallinity is expected to be low compared to the bulk film[22]), and unreasonably high for the annealed sample. Further, the UV-visible absorption spectra in Figure 4.2 suggest that only a small increase in crystallinity results from an anneal step[16].

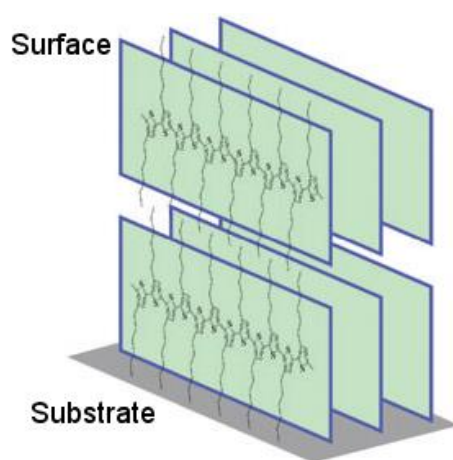


**Figure 4.10:** Schematic of 'edge-on' P3HT orientation, with hexyl side-chains oriented normally to the substrate. Adapted from [16] with permission from The Royal Society of Chemistry.

A more likely explanation of the dramatic change in image contrast resulting from a thermal anneal is the molecular orientation at the surface. It has been demonstrated that spin-casting a regioregular P3HT film from a slow-drying solvent, or subjecting it to a thermal anneal, strongly encourages the formation of 'edge-on' polymer orientation (demonstrated in Figure 4.10), whereby the hexyl side-chains on the 3HT monomers (Section 2.3.1) are oriented normally out of the sample surface[16]. As-cast P3HT films spin-cast from faster drying solvents do show a degree of edge-on orientation[16], however face-on orientation is preferred[44]. Importantly, a significant difference in the surface energy levels of differently orientated films has been observed[44]. In the edge-on orientation, the electron-donating nature of the normally-oriented hexyl group[16] results in the formation of a surface dipole that lowers the surface emission

barrier by  $\sim 0.5$  eV. This would suggest a larger SE yield in edge-on dipole-oriented regions, with the yield of low-energy SEs most affected as these are more sensitive to the height of the surface emission barrier[37]. EFSEM images are thus ideal for probing this effect, as higher energy SE emissions, which are little affected by the surface dipole effect, are filtered out, and contrast is generated only from the more sensitive low-energy signal.

From the EFSEM images in Figure 4.9, it is postulated that the brighter ‘cloud-like’ features observed in the EFSEM images of as-cast and annealed P3HT films are related to regions showing surface dipole effects due to edge-on molecular orientation. The regiorandom film shows no features of this type, as steric hindrance caused by the random side-chain position (Section 2.3.2) prevents any large-scale alignment of the 3HT monomers[16]. Any localised dipole effects are therefore too small to have any measureable effect on the EFSEM image contrast.

In the case of regioregular P3HT, molecular orientation is possible, and as such brighter regions appear where edge-on formations have caused a dipole effect. For the as-cast sample (Figure 4.9b), most of these regions are small and poorly defined, suggesting that edge-on alignment is not particularly strong, with the exception of a few regions with a particularly bright grey-level. This would be expected in an as-cast sample[16]. Many regions of a darker grey level that correlates with the regiorandom film are also present in this image, indicating regions of either no strong alignment, or face-on alignment, whereby the side-chains would be oriented parallel to the surface and have little effect on the height of the SE emission barrier. A recent study mapping P3HT order at the surface with polarised light has indicated that regions of low localised order in an as-cast regioregular sample are mostly limited to boundaries between larger regions of uniform face-on or edge-on chain orientation[45]. Given that dark regions in the as-cast EFSEM image (Figure 4.9b) are not simply restricted to boundaries between brighter regions, it is proposed that these regions of darker grey level correspond to regions of face-on orientation in the regioregular as-cast sample.

The EFSEM image of the annealed P3HT film shows large ‘clouds’ of bright grey level, much more clearly defined than the as-cast sample. Particularly bright ‘fibrils’ (denoted by an arrow)

can be observed within these ‘clouds’, which have been previously observed as highly ordered P3HT structures mostly formed after a thermal anneal[46]. The large coverage of the brightest ‘cloud-like’ features (~75% by grey-level thresholding to the average brightness of ‘cloud-like’ regions) matches the expected high level of edge-on ordering at the sample surface after an anneal step[16]. It should be noted that this does not necessarily correlate with crystallite formation at the surface, merely the localised molecular orientation of polymer chains at the surface, and the related dipole formation that lowers the emission barrier. The yield-increasing effect of the face-on dipole will act upon all SEs emitted from a dipole-affected point, regardless of the crystallinity of the region or the properties of individual SEs, such as energy or angle of emission. Regions of darker grey level are again likely to represent areas of face-on orientation.

After air exposure, the EFSEM image of the regiorandom film (Figure 4.9d) is unchanged, remaining featureless with an almost identical grey level. The appearance of the two regioregular films changes significantly after degradation in air however, with the resulting films appearing similar in Figures 4.9 e,f. As with the ‘fresh’ films, regions of bright and dark grey level can be observed, however the surface coverage of bright regions has reduced to ~88% in the annealed film, and increased to ~70% in the as-cast film. Fibril structures are still visible in the bright regions, indicating that oxygen attack has not destroyed all molecular ordering at the surface of the film. However, the significant changes observed in the EFSEM images of both films, and the fact both films appear similar after degradation, indicates that air exposure significantly alters the morphology of the film surface. Without further experiment it is difficult to speculate on the specific nature of these changes, which may also be related to the emergence of the ~6 eV peak in the  $E_0 = 700$  eV spectrum after air exposure (Figure 4.6b) and plasma etch in air (Figure 4.7). However, based upon the suggestion that image contrast is related to surface polymer orientation, it is possible that reaction of P3HT chains with oxygen generates new favourable polymer orientations for the oxidised chains. It has been shown that the reaction of oxygen with P3HT molecules can introduce characteristic chain bending or kinks[26], which may be the foundation of aligned molecules on the surface.

## Section 4.6: SE Spectrum of PCBM

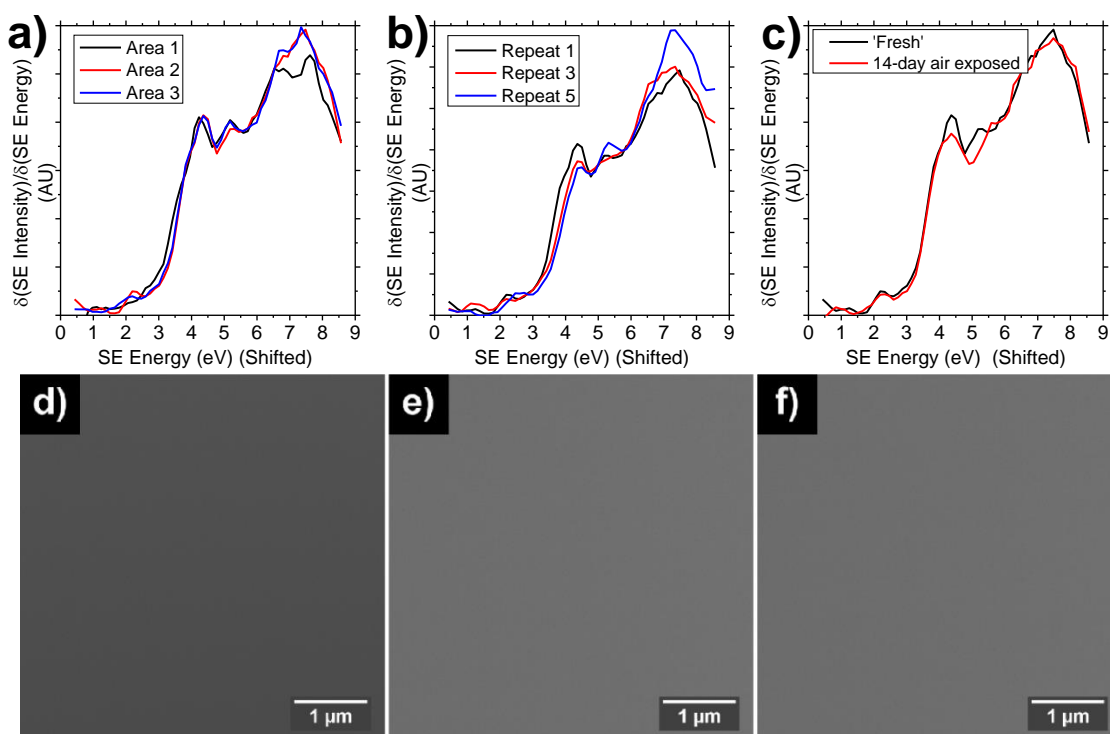


**Figure 4.11:** SE spectroscopy and energy-filtered imaging of PCBM. a) SE spectra measured from different areas of a film; b) Repeated SE spectra measured from the same film area; c) Comparison of ‘fresh’ and air-exposed film. d) Conventional (unfiltered) SE image of film. EFSEM images using SE energies  $< 8$  eV: e) ‘fresh’ film; f) air-exposed film

The SE spectra measured from PCBM demonstrate a material with SE emission properties that differ considerably in comparison to P3HT, and significantly greater electron beam and air stability. The methods used to prepare these PCBM samples can be found in Section 3.1. In Figure 4.11a, SE spectra measured at  $E_0 = 700$  eV from a PCBM film retained under vacuum are demonstrated, as calibrated using Equation 4.2. As with the P3HT films in Figure 4.5, SE spectra were measured from three different areas of the same sample and compared to test the repeatability of the measured spectrum. From this plot, it is clear that PCBM gives a very different spectrum shape to P3HT, and that the spectrum shape measured from a particular sample is again highly repeatable. A higher-energy measured onset is observed in comparison to P3HT, with a low-energy peak at  $\sim 4.4$  eV. This is followed by further peaks at 5.3, 6.7 and 7.5 eV, which are present in all three measured spectra. The repeatability of these spectra is unsurprising given the

apparent homogeneity of the film as measured by EFSEM imaging (Figure 4.11d-f), where no features are discernible with and without a SE energy-filter in place, or even after air exposure.

SE spectra were repeatedly measured from the same area of a ‘fresh’ film to probe the sensitivity of the PCBM spectrum to electron irradiation, as presented in Figure 4.11b. The SEM parameters used to measure these spectra were identical to those used to test the effects of electron irradiation on P3HT, however the actual beam current used to acquire these spectra was measured as 13.6 pA, in comparison to 15 pA for P3HT. As such, the total electron dose used to acquire each spectrum in Figure 4.11b is  $3.07 \times 10^{13}$  electrons.cm<sup>-2</sup>, with a localised dose of  $1.55 \times 10^{14}$  electrons.cm<sup>-2</sup> after acquisition of the 5<sup>th</sup> spectrum in the plot.

In Figure 4.11b it can be observed that, similarly to the P3HT SE spectra in Figure 4.3, the spectrum shape changes slightly with increasing dose, however the basic form is retained. As with the P3HT spectrum, the onset peak loses definition with increased dose, and a small shift in the onset energy is observed. Contrary to P3HT however, the shift in the PCBM spectrum is towards higher energy, with the low-energy peak shifting to 4.5 eV from 4.4 eV. The other notable change is at higher energies, where the 6.7 and 7.5 eV peaks present in the lowest dose spectrum lose their definition as a large, broader feature centred at 7.5 eV grows in intensity with increasing electron dose. This feature in Figure 4.11b bears similarity to the 7.5 eV peak in Repeat spectra 2 and 3 in Figure 4.11a. However, the highest dose spectrum in Figure 4.10b, Repeat 5 ( $1.55 \times 10^{14}$  electrons.cm<sup>-2</sup>), demonstrates no feature at 6.7 eV, and a much larger 7.5 eV peak relative to the onset peak when compared with spectra from area 2 and 3 in Figure 4.11a. This implies a degree of modification to the surface electronic properties is occurring with electron doses less than  $\sim 10^{14}$  electrons.cm<sup>-2</sup>. However, the changes are small and it appears that, similar to the P3HT SE spectra in Figure 4.3, the low-dose conditions in which the SE spectra were acquired (Section 3.2) allow for the PCBM spectrum to be accurately measured without the presence of significant beam damage artefacts.

From Figure 4.11c, it can be observed that the SE emissions of PCBM appear more air-stable than P3HT (Figure 4.6b for equal  $E_L$ ). The spectrum onset energy of PCBM appears unchanged after

14 days of air exposure, in contrast to Figure 4.6b, where a significant onset shift of  $\sim 0.5$  eV indicates oxygen doping in P3HT. Further, the low energy peak remains centred at 4.4 eV, albeit a little broader. The spectrum of the air-exposed sample appears to have less fine structure; for example, the 5.3 and 6.7 eV peaks present in the ‘fresh’ sample spectra in Figure 4.11a are not apparent in the spectrum of the air-exposed sample. This perhaps indicates some of the fine electronic structure of the sample has been damaged by air exposure. However, the broad shape of the spectrum is largely unchanged. This is in contrast to the P3HT spectrum, where although the clearest effect of air exposure is the elimination of sample charging for  $E_L > 1000$  eV (Section 4.5.1), a spectrum onset shift of  $\sim 0.5$  eV and a spectral feature around 6 eV is found after air exposure in Figure 4.6b. These changes likely reflect doping and other oxygen-related damage.

The repeatability of the PCBM spectrum shape in Figure 4.11a, and its clearly individual nature in comparison to that measured from P3HT, is a strong indication that the SE spectra measured by the FEI Sirion TLD spectrometer are strongly defined by the SE emission properties of the material, rather than detector effects. However, it must be noted that, as with the  $E_0 = 1000$  eV spectrum of air-exposed P3HT (Figure 4.6c), the shape of PCBM SE spectrum measured in the FEI Sirion does not resemble the expected SE ‘cascade’ shape (Section 2.7.1). This suggests that detector effects are nonetheless influencing the overall nature of the measured spectrum. This is discussed in depth in Section 4.7, where potential explanations are offered.

#### **Section 4.7: Comparison with modelled SE spectrum, determination of detector effects**

To probe the accuracy of the SE spectra presented above, and detector effects that may alter the nature of the measured spectrum in a FEI Sirion TLD, a model of P3HT SE emissions was built by Prof. Maurizio Dapor of the University of Trento as part of an external collaboration[47]. This Monte Carlo model simulates the generation, transport and emission of SEs from a P3HT sample by sampling the probability of the various possible electron interactions of the primary beam with the sample. The modelled interactions include elastic scattering off nuclear charge and inelastic scattering off atomic electrons, as well as electron-phonon and electron-polaron interactions. For

the purposes of the simulation, the P3HT film was treated as a homogenous film having the bulk properties of P3HT as published in literature, such as its particular band gap, electron affinity, dielectric constants and electron energy loss function (amongst others)[48]. The resulting model is undoubtedly a simplified picture of a P3HT film that does not reflect the specific nature of band-type and hopping transport in a conjugated polymer (Section 2.3), and does not consider the effects of the localised ordering and inhomogeneity evident in Figure 4.9. However, owing to the molecular-scale complexities of polymer charge transport[34], a model that accurately reproduces such effects in a simulation of SE emission was beyond the bounds of possibility for this thesis. Nonetheless, by comparing the simulated spectrum output by this model with experimental data obtained using the FEI Sirion SEM, some of the limitations of the FEI Sirion TLD as a SE spectrometer have been investigated. A full description of the model, and the inputs and methodology used to simulate the SE spectrum, have been published [6]. The following results and discussion of some detector effects that influence the measured SE spectrum shape form part of this submitted article, and are included here as work I performed as part of this PhD.

The simulated and experimental SE spectra compared in this Section both use  $E_0 = 200$  eV. This is for two reasons. Firstly, by acquiring experimental spectra from the sample below the k-shell ionisation edge (Section 4.3.1), the effects of ionisation damage are eliminated[49], ensuring the measured SE spectrum is as accurate as possible. Secondly, as demonstrated in Figure 4.2, the experimental SE spectrum of P3HT demonstrates more spectral features with increasing  $E_0$ , indicating that the physical processes that govern SE emission are more complex at greater  $E_0$ . As the Monte Carlo model employed in this section is not a wholly accurate representation of a P3HT sample, better agreement between simulation and experiment can be obtained by keeping  $E_0$  to a minimum. This allows for a better understanding of the effects of the spectrometer on the measured SE spectrum.

### Section 4.7.1: Simulated SE spectrum, initial comparison with experimental data

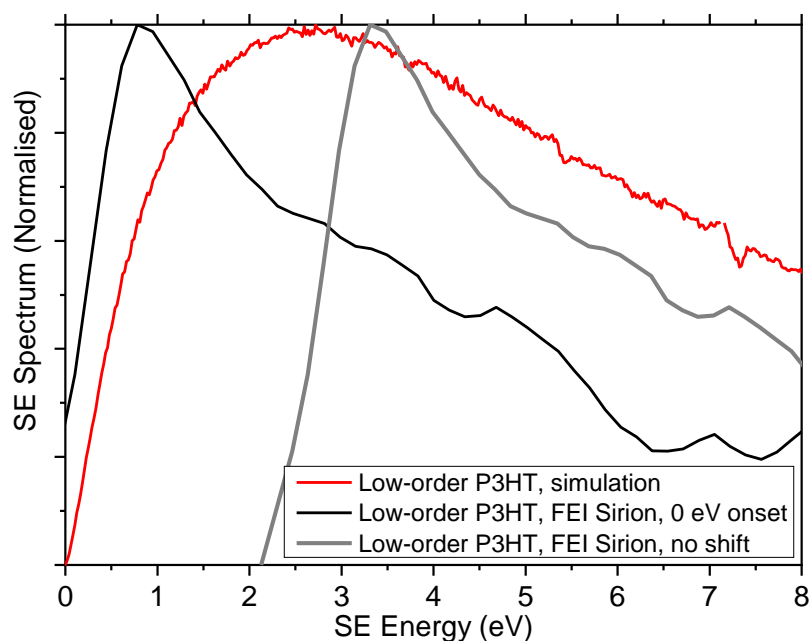


**Figure 4.12:** Comparison of simulated SE spectrum of low-order regioregular P3HT from Monte Carlo model with experimentally measured spectrum from FEI Sirion.

The simulated  $E_0 = 200$  eV SE spectrum output by the model in the range 0-8 eV is presented in Figure 4.12 (red line). The modelled system is a regioregular P3HT film that demonstrates high disorder[18], corresponding to a film cast from a fast-drying solvent (Section 2.4.4). The output spectrum is a broad, featureless peak with a typical ‘cascade’ shape. Given that the simulation treats the P3HT film effectively as a bulk, crystalline semiconductor this is unsurprising. Comparison with an experimental spectrum measured in the FEI Sirion, of a P3HT film cast from hot (70°C) chloroform to give a fast-drying highly disordered film, is not particularly favourable. The modelled SE spectrum does not take in to account any effect that may lead to the SE spectrum onset to be measured at an energy  $>0$  eV, as is the case for all experimentally measured spectra in this Chapter. As such, the experimental spectrum has been shifted to have an onset of 0 eV for direct comparison with the model. The shifted experimental spectrum demonstrates a much sharper spectrum onset, and low-energy peak, with a slow, mostly linear decay above 2 eV. The unshifted spectrum has also been included for comparison, and it can be observed that the peak energy of the unshifted spectrum better matches the peak energy of the simulated distribution, however the spectrum shape remains a poor fit. This large disparity between experimental and

simulated spectrum is a strong indicator that the Sirion TLD influences the experimentally measured SE spectrum shape.

#### ***Section 4.7.2: Effects of SE emission angle***

The SE collection efficiency of the FEI XL-30 TLD has been shown to demonstrate a dependence on the sample working distance, and, by extension, the emission angle of SEs with energy above a few eV[37]. This can be explained by the effect of the ‘suction tube’ electrode described in Section 2.6.3. The role of the suction tube electrode is to provide an ‘extraction field’ that directs SEs emitted by the sample through the pole piece and towards the TLD detector. For SE spectroscopy experiments, this bias is set to its maximum value (+250 V). When the sample is at small working distances, this extraction field has a strong effect on all SEs emitted by the sample, and gives a large collection yield for SEs independent of energy or emission angle. At greater working distances, however, the effect of this field is reduced due to the larger separation between suction electrode and sample surface. In a larger working distance condition (>3 mm[37]), whilst low-energy SEs can still be collected with high yield by the weaker extraction field[50], higher-energy emissions require a stronger field to be efficiently collected. Therefore, at a larger working distance, the detection efficiency of higher energy SEs is reduced and becomes dependent on the angle of emission[37]. If emitted with a low angle relative to the surface normal, the SE requires little deflection by the extraction field in order to be directed up the pole piece. However, higher-energy SEs emitted with larger angles will not be collected efficiently by the weaker extraction field at larger working distances.

This effect is clearly demonstrated in Figure 4.13, where  $E_0 = 700$  eV SE spectra of P3HT measured at different working distances are shown. These spectra were measured in a FEI Nova NanoSEM 450, a modern evolution of the FEI Sirion and FEI XL-30 that retains the same fundamental spectroscopy functionality of the XL-30 tube. As an evolution of this design however, the FEI Nova is a more sensitive instrument, and offers more sensitive SE signal detection than the FEI Sirion. As such, whilst the FEI Sirion demonstrated large noise levels in SE spectra measured at large working distance using  $E_0 = 200$  eV, the FEI Nova was capable of

measuring high quality spectra in this condition. However, some disparity can be observed between the FEI Nova spectrum measured at 3mm working distance in Figure 4.13 and comparable spectra measured in the FEI Sirion (Figure 4.5c). It should be noted here that the SE energy filtering performance of the FEI Nova has not been tested and verified to the same extent as the FEI Sirion[2]. Nonetheless, the basic operation and energy-filtering characteristic of the FEI Nova should remain broadly similar to the other XL-30 – based microscopes.

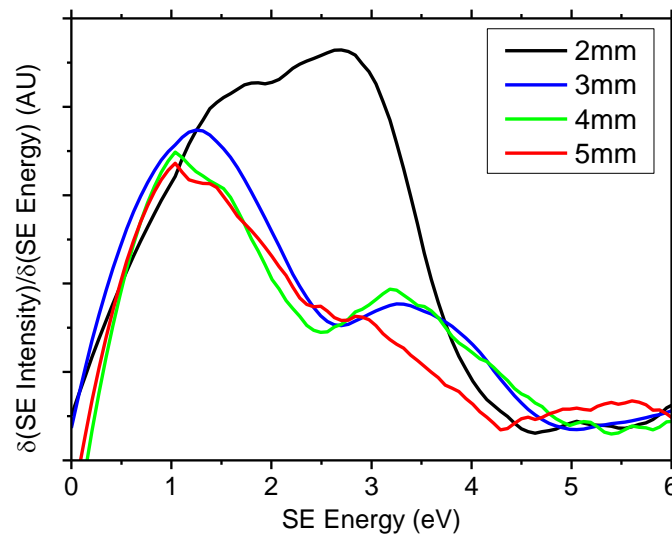


**Figure 4.13:** SE spectra of as-cast regioregular P3HT film measured at different working distances using  $E_0 = 700$  eV with FEI Nova SEM.

In Figure 4.13, it is observed that, as expected, the low-energy peak in the spectrum measured is largely preserved at all working distances. However, the intensity of the second spectrum peak around 3 eV falls significantly as the working distance is increased. This effect is most prominent between the spectra measured at 2 mm and 3 mm, where the intensity is seen to fall by more than 50% of its value at 2 mm. The spectra at 3 mm and 4 mm appear broadly similar; however, at a 5 mm working distance the collection efficiency of 3 eV SEs has fallen to the point that no second peak can be resolved.

Figure 4.13 demonstrates that low-energy SEs, and SEs with low emission angles relative to the surface normal, are preferentially detected in an XL-30 based TLD. Further, it is clear that that the magnitude of this selectivity can be controlled by altering the working distance of the sample, and as such the strength of the SE extraction field emanating from the ‘suction tube’ electrode at

the sample surface. This reflects that the characteristics of the TLD are influencing the shape of the measured SE spectrum.

This relationship between the emission angle of an individual SE (relative to the sample surface normal) and its collection efficiency is valid under the assumption of a flat sample oriented normally to the incident electron beam and SE extraction field. In the case of a sample with a high degree of roughness, the localised orientation of the surface varies considerably over the sample, altering the total angular distribution of SE emissions and disrupting the alignment between the surface and SE extraction field. In this case, SEs emitted from a surface oriented at a high angle to the SE extraction field can be emitted at a high angle relative to the local sample surface, but a low angle relative to the extraction field. As such, the relationship between SE emission angle and collection efficiency is significantly weaker on a rough sample. The effect of sample roughness has been previously demonstrated on the SE emissions from carbon samples, with implications for the experimentally measured SE spectrum[51]. The simulated SE spectrum in this Section assumes a flat sample oriented normally to the incident electron beam. Whilst experimental P3HT samples do demonstrate roughness, topographical features are small and have limited effect on SE emissions, as suggested by the low topographical contrast observed in conventional, unfiltered SEM images of P3HT (Figure 4.8a).

Assuming that a P3HT film can be considered smooth, detector characteristics can result in preferential detection of SEs generated deeper beneath the sample surface[6], [37]. An understanding of this effect can be formed by considering the simple transport and emission processes of internal SEs in the P3HT film.

#### ***Section 4.7.3: Effects of SE origin depth***

In order to be emitted from the surface of the P3HT film, a SE beneath the surface requires a momentum component normal to the surface of the film,  $p_{\perp}$ , sufficient to overcome the surface emission energy barrier of the sample. Crossing this emission barrier, taken to be the electron affinity  $\chi$  of the sample, acts only to reduce the normal component of the electron momentum. As

such, taking the example of an internal SE incident normally on film surface (internal angle  $\theta = 0$ ), the smallest momentum sufficient for escape is:

$$p_{min} = \sqrt{2m\chi} \quad (4.3)$$

If the SE has a total momentum larger than  $p_{min}$ , its momentum vector may have a component tangential to the film surface,  $p_{\parallel}$ , and still escape the sample. However, if an internal SE of a given energy,  $E_{SE(i)}$ , is to be emitted, then the magnitude of  $p_{\parallel}$ , and therefore  $\theta$ , are limited by the fact that  $p_{\perp}$  must be larger than  $p_{min}$ . Specifically, if an internal SE has energy  $E_{SE(i)}$ , it can only escape if its internal transport angle fulfils[37]:

$$\theta_{max} < \cos^{-1} \sqrt{\frac{\chi}{E_{SE(i)}}} \quad (4.4)$$

As such, higher energy SEs can be emitted with much larger angles than smaller-energy SEs. Due to the limitations of the FEI Sirion TLD, this exacerbates the preferential detection of low-energy SEs, as only high-energy SEs can be emitted with the larger angles that inhibit effective collection.

Importantly, the preferential detection of SEs emitted with low angles relative to the surface normal by the XL-30 TLD results in the preferential detection of SEs generated deeper beneath the film surface. Considering the transport of SEs through the film, the Monte Carlo simulation of SE emission from P3HT suggests the inelastic mean free path of SEs can reach ~3.5 nm at energies <10 eV[6]. If a SE must travel distances approaching 3.5 nm, its chances of undergoing an energy-loss event are therefore increased.

Consider two cases of SEs generated within the P3HT film with identical energy,  $E_{SE(i)}$ , and with  $p_{\perp}$  greater than the  $p_{min}$  required to escape the sample. In the first case, SEs are generated at a depth  $\ll 3.5$  nm, and as such are highly unlikely to undergo any energy loss event during transport to the surface. Electrons generated in this condition can be emitted from any angle allowed by its initial energy, as defined in Equation 3. In the second case, SEs are generated at a depth approaching 3.5 nm beneath the sample surface. Here, there is a far greater likelihood of a SE undergoing an inelastic collision during transport to the surface, with this probability greatly

increased if the SE is transported with a large  $\theta$  as the distance to the surface increases. Every energy loss event limits the value of  $\theta_{max}$  as defined in Equation 3.

Due to this effect, SEs that are emitted from the sample from greater depths tend to be emitted with smaller angles relative to the surface normal, and as such are highly likely to be detected using the FEI Sirion TLD arrangement. In contrast, high-angle SEs are much more likely to be emitted from close to the surface of the sample. As a result, SEs emitted from close to the sample surface are under-represented in the SE spectrum measured by the XL-30 TLD. This is the likely origin of the disparity between simulated and experimental P3HT spectra (Figure 4.12)

#### ***Section 4.7.4: Using a filtering depth in the simulated spectrum***

To account for this effect in the simulated spectrum (Figure 4.12), a filtering depth parameter,  $D$ , is introduced to the simulation, which indicates the depth above which SE emissions are not adequately represented in the experimentally measured spectrum. When applying a filtering depth in the simulation, only SEs generated at depths below  $D$  and subsequently emitted from the sample are considered part of the SE spectrum.

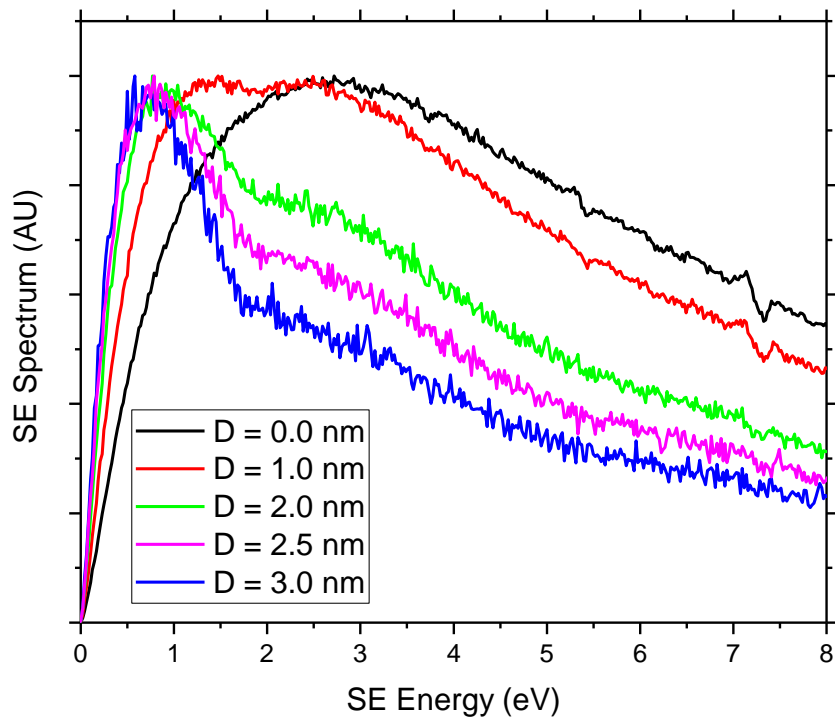


**Figure 4.14:** Effect of depth filtering parameter  $D$  on simulated SE spectrum of P3HT

Clearly, a well-defined filtering depth is not an exact representation of the influence of the FEI Sirion TLD on the shape of the measured P3HT spectrum. As an obvious example, SEs generated at the sample surface with low  $\theta$  and  $p_{\perp}$  larger than  $p_{min}$  will have a high detection yield at 3mm working distance. Rather, the concept of a filtering depth is used here as a simple method of reconciling the simulated and experimentally acquired spectra. Importantly, the effectiveness of a filtering depth at replicating the characteristics of the FEI Sirion TLD is demonstrated in Figure 4.14, where the resulting SE spectra from simulations employing a range of  $D$  values are presented. Here, using a greater  $D$  value results in a reduced contribution of high-energy SEs to the spectrum, with a sharper low-energy peak situated at a lower SE energy. It appears that the use of a greater  $D$  value equates to acquiring a SE spectrum at a greater working distance.

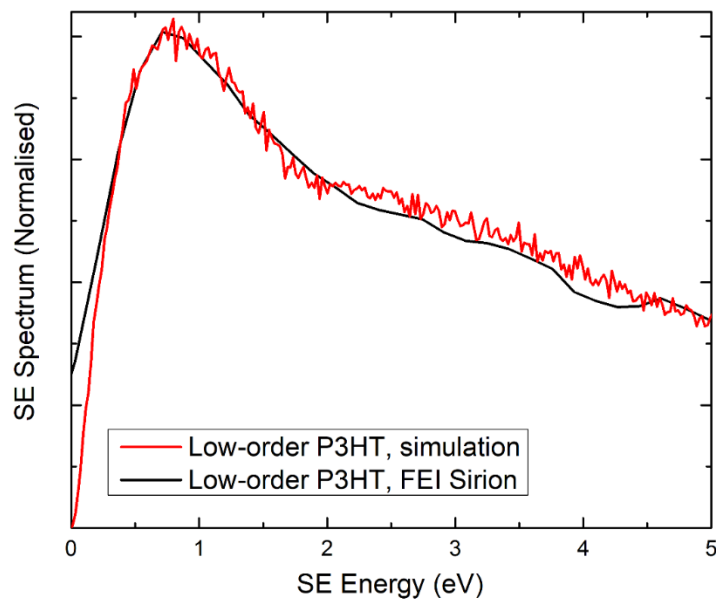


**Figure 4.15:** Comparison of low-order P3HT SE spectra: experimentally measured from FEI Sirion compared with simulated spectrum using  $D = 2.5$  nm.

In Figure 4.15, the modelled SE spectrum using a filtering depth  $D = 2.5$  nm is compared with the experimental SE spectrum previously shown in Figure 4.12 (with shift applied such that spectrum onset is at 0 eV). An excellent agreement is shown in spectrum shape in the low-energy range. This is strongly indicative that the primary influence of the FEI Sirion TLD on the measured SE spectrum shape from P3HT is to under-represent surface emissions from the sample.

## Section 4.8: Conclusions

In the course of this Chapter, the capabilities and limitations of SE spectroscopy methods in the SEM have been explored in unprecedented detail. These findings have important and wide-ranging implications that apply to any future attempt to perform SE spectroscopy or energy-filtered SE imaging using the TLD of a SEM.

As noted in the Introduction to this Chapter, the TLD of the FEI Sirion or related SEMs is not an ‘ideal’ SE spectrometer. Rather, its key strength lies in an ability to acquire high-resolution energy-filtered SE images and perform SE spectroscopy without requiring hardware modifications to a typical SEM. As such, it is extremely important to investigate the limitations of the TLD as a SE spectrometer, in order to understand better the reliability and accuracy of results acquired using the FEI Sirion TLD.

In Section 4.2, the energy-filtering characteristic of the TLD was demonstrated using previously published modelling data[4], and this data used to calibrate the TLD deflector bias to a related SE detection cut-off energy. The limitations of this calibration (Equation 4.1) were noted, specifically related to the poor energy resolution of the detector and degrading performance as a SE spectrometer at deflector biases greater than  $\sim 20$  V. Further, the calibration of the TLD was observed to change over time, with the alignments of various electron-optical components in the electron column a likely cause. Due to these mostly inherent issues, SE energies measured by the TLD should be taken as approximations. A further weakness of the TLD spectrometer performance was demonstrated in Section 4.7, where comparison of experimental and modelled P3HT spectra demonstrated that spectra measured by the TLD appear to reflect SE emissions from  $>2.5$  nm beneath the surface of the film. This is likely due to the preferential detection of SEs emitted with low angles and energies by this TLD arrangement[37].

These issues should always be considered when acquiring and analysing SE spectra acquired using the TLD of a FEI Sirion (or similar). However, by measuring the SE spectra of P3HT samples with different material properties, a characterisation tool with genuine promise was demonstrated. The SE spectra of ‘fresh’ P3HT samples were shown to be repeatable, resistant to

beam damage (at least at the electron doses used to acquire spectra for this Chapter) and apparently reflective of the level of crystalline order in the film. After degradation *via* exposure to air or plasma, the P3HT SE spectra demonstrated changes that echo the expected effects of oxidation (namely, p-type doping and destruction of the original electronic structure of the film). The analysis of P3HT SE spectra in this Chapter is largely qualitative and empirical, and it is difficult at present to link many SE spectral features to the specific electronic properties of a P3HT film. The working hypothesis is that molecular orientation at the surface[16] as well as the different band structure and transport properties of crystalline and amorphous phases influences the nature of SE emission in this energy range. A deeper understanding may be hindered by the limitations of the TLD spectrometer. However, future work can compare SE spectra with established characterisation techniques, for example x-ray photoelectron spectroscopy (XPS) or possibly surface x-ray diffraction (XRD) methods[52] to investigate in more detail how these SE spectra may relate to various aspects of electronic structure or molecular orientation[16].

The energy-filtered SEM images in Section 4.4 demonstrate that by imaging using only low-energy SEs, the material contrast visible at the surface of a P3HT film is boosted considerably. Low-energy SE emissions are more sensitive to the localised electronic properties of the material such as electron affinity[53], as small, localised variation in emission barrier height affects the yield of only the lowest energy SEs[38], [54]. Contrast resulting from emission barrier variation is therefore observed more clearly in low-energy SE images. EFSEM images of P3HT samples having demonstrably different levels of molecular order demonstrate clear variation, with brighter ‘cloud’-like features and fibrils visible in more ordered films. Whilst the fibrils are clearly indicative of crystalline order, thresholding analysis (using the region of amorphous material as a reference grey level for amorphous material) suggests that the area fraction of the bright ‘cloud’-like features in an annealed P3HT film is too large to be feasibly representative of surface crystallinity[17]. Instead, it is proposed that the origin of this contrast is molecular orientation at the surface; whereby ‘edge-on’ orientation reduces the SE surface emission barrier and gives a larger SE yield, especially at low energies. This surface barrier phenomenon affects the emission

probability of all SEs, regardless of the depth at which the SE was first generated. As such, the effect remains important despite our findings in Section 4.7 that SEs generated at the surface are suppressed by the FEI Sirion TLD.

Importantly, these results demonstrate that, despite the shortcomings of the TLD as a SE spectrometer and the need to regularly check the validity of the spectrometer calibration, the methods applied in this Chapter show promise as a reliable and useful sample characterisation tool. It has been shown that the sample processing and history of a P3HT sample is evident from its SE spectrum and from EFSEM images of the sample. Whilst the results in this Chapter were mostly acquired from an ageing, yet well-studied SEM, work is ongoing to enable and verify SE spectroscopy methods on more modern microscopes. This work includes automation of SE spectrum acquisition and data processing, which will significantly boost the wider availability and applicability of the method. Through combination of these efforts with attempts to deepen understanding of the physical origin of features in SE spectra and contrast in EFSEM images, a characterisation technique with significant potential may develop.

#### Section 4.9: References

- [1] P. Kazemian, S. A. M. Mentink, C. Rodenburg, and C. J. Humphreys, “Quantitative secondary electron energy filtering in a scanning electron microscope and its applications.,” *Ultramicroscopy*, vol. 107, no. 2–3, pp. 140–150, 2007.
- [2] C. Rodenburg, M. A. E. Jepson, E. G. T. Bosch, and M. Dapor, “Energy selective scanning electron microscopy to reduce the effect of contamination layers on scanning electron microscope dopant mapping.,” *Ultramicroscopy*, vol. 110, no. 9, pp. 1185–1191, Aug. 2010.
- [3] P. Kazemian, S. A. M. Mentink, C. Rodenburg, and C. J. Humphreys, “High resolution quantitative two-dimensional dopant mapping using energy-filtered secondary electron imaging,” *J. Appl. Phys.*, vol. 100, no. 5, p. 54901, 2006.
- [4] C. Rodenburg, M. Jepson, and E. Bosch, “Advantages of Energy Selective Secondary Electron Detection in SEM,” *Microsc. Microanal.*, vol. 16, no. S2, pp. 622–623, Jul. 2010.
- [5] K. Tremel and S. Ludwigs, “Morphology of P3HT in Thin Films in Relation to Optical and Electrical Properties,” in *P3HT Revisited - From Molecular Scale to Solar Cell Devices*, vol. 265, 2014, pp. 39–82.
- [6] M. Dapor *et al.*, “Secondary electron spectra of semi-crystalline polymers – A novel polymer characterisation tool?,” *J. Electron Spectros. Relat. Phenomena*, pp. 1–11, 2017.
- [7] H. Seiler, “Secondary electron emission in the scanning electron microscope,” *J. Appl. Phys.*, vol. 54, no. 11, pp. R1–R18, 1983.

- [8] D. C. Joy, M. S. Prasad, and H. M. Meyer, "Experimental secondary electron spectra under SEM conditions," *J. Microsc.*, vol. 215, no. Pt 1, pp. 77–85, Jul. 2004.
- [9] R. F. Willis, B. Feuerbacher, and B. Fitton, "Graphite conduction band states from secondary electron emission spectra," *Phys. Lett. A*, vol. 34, no. 4, pp. 231–233, Mar. 1971.
- [10] I. Volotsenko *et al.*, "Secondary electron doping contrast: Theory based on scanning electron microscope and Kelvin probe force microscopy measurements," *J. Appl. Phys.*, vol. 107, no. 1, 2010.
- [11] J. Goldstein *et al.*, *Scanning Electron Microscopy and X-Ray Microanalysis, 3rd Edition*. Springer, 2003.
- [12] D. Voreades, "Secondary electron emission from thin carbon films," *Surf. Sci.*, vol. 60, no. 2, pp. 325–348, Nov. 1976.
- [13] J. Butler, D. C. Joy, G. Bradley, and S. Krause, "Low-voltage scanning electron microscopy of polymers," *Polymer (Guildf.)*, vol. 36, no. 9, pp. 1781–1790, 1995.
- [14] H. Ahn, D. W. Oblas, and J. E. Whitten, "Electron Irradiation of Poly(3-hexylthiophene) Films," *Macromolecules*, vol. 37, no. 9, pp. 3381–3387, May 2004.
- [15] D. C. Joy and C. Joy, "Low voltage scanning electron microscopy," *Micron*, vol. 27, no. 3, pp. 247–263, 1996.
- [16] K. Kanai, T. Miyazaki, H. Suzuki, M. Inaba, Y. Ouchi, and K. Seki, "Effect of annealing on the electronic structure of poly(3-hexylthiophene) thin film.," *Phys. Chem. Chem. Phys.*, vol. 12, no. 1, pp. 273–282, 2010.
- [17] X. Shen, W. Hu, and T. P. Russell, "Measuring the Degree of Crystallinity in Semicrystalline Regioregular Poly(3-hexylthiophene)," *Macromolecules*, p. acs.macromol.6b00799, 2016.
- [18] S. Engmann, V. Turkovic, P. Denner, H. Hoppe, and G. Gobsch, "Optical order of the polymer phase within polymer/fullerene blend films," *J. Polym. Sci. Part B Polym. Phys.*, vol. 50, no. 19, pp. 1363–1373, 2012.
- [19] J. A. Alexander *et al.*, "Measurement of optical properties in organic photovoltaic materials using monochromated electron energy-loss spectroscopy," *J. Mater. Chem. A*, vol. 4, no. 35, pp. 13636–13645, 2016.
- [20] J. Clark, C. Silva, R. H. Friend, and F. C. Spano, "Role of intermolecular coupling in the photophysics of disordered organic semiconductors: Aggregate emission in regioregular polythiophene," *Phys. Rev. Lett.*, vol. 98, no. 20, pp. 1–4, 2007.
- [21] C. R. Snyder, R. C. Nieuwendaal, D. M. Delongchamp, C. K. Luscombe, P. Sista, and S. D. Boyd, "Quantifying crystallinity in high molar mass Poly(3-hexylthiophene)," *Macromolecules*, vol. 47, no. 12, pp. 3942–3950, 2014.
- [22] D. H. Kim *et al.*, "Visible-Light-Induced Oxidation of Poly(3-hexylthiophene-2,5-diyl) Thin Films on ZnO Surfaces under Humid Conditions: Study of Light Wavelength Dependence," *J. Phys. Chem. C*, vol. 120, no. 36, pp. 19942–19950, 2016.
- [23] M. Manceau, J. Gaume, A. Rivaton, J. L. Gardette, G. Monier, and L. Bideux, "Further insights into the photodegradation of poly(3-hexylthiophene) by means of X-ray photoelectron spectroscopy," *Thin Solid Films*, vol. 518, no. 23, pp. 7113–7118, 2010.
- [24] S. Cook, A. Furube, and R. Katoh, "Matter of minutes degradation of poly(3-hexylthiophene) under illumination in air," *J. Mater. Chem.*, vol. 22, no. 10, pp. 4282–4289, 2012.

- [25] H. O. Seo, M.-G. Jeong, K.-D. Kim, D. H. Kim, Y. D. Kim, and D. C. Lim, "Studies of degradation behaviors of poly (3-hexylthiophene) layers by X-ray photoelectron spectroscopy," *Surf. Interface Anal.*, vol. 46, no. 8, pp. 544–549, Aug. 2014.
- [26] A. Lücke, W. G. Schmidt, E. Rauls, F. Ortman, and U. Gerstmann, "Influence of structural defects and oxidation onto hole conductivity in P3HT," *J. Phys. Chem. B*, vol. 119, no. 21, pp. 6481–6491, 2015.
- [27] J. Cazaux, "A new model of dependence of secondary electron emission yield on primary electron energy for application to polymers," *J. Phys. D. Appl. Phys.*, vol. 38, no. 14, pp. 2433–2441, Jul. 2005.
- [28] B. Charlot, G. Sassine, A. Garraud, B. Sorli, A. Giani, and P. Combette, "Micropatterning PEDOT:PSS layers," *Microsyst. Technol.*, vol. 19, no. 6, pp. 895–903, Nov. 2012.
- [29] D. Baierl, B. Fabel, P. Gabos, L. Pancheri, P. Lugli, and G. Scarpa, "Solution-processable inverted organic photodetectors using oxygen plasma treatment," *Org. Electron.*, vol. 11, no. 7, pp. 1199–1206, 2010.
- [30] T. Ino, T. Hayashi, K. Ueno, and H. Shirai, "Atmospheric-pressure argon plasma etching of spin-coated 3,4-polyethylenedioxythiophene:polystyrenesulfonic acid (PEDOT:PSS) films for copper phthalocyanine (CuPc)/C60 heterojunction thin-film solar cells," *Thin Solid Films*, vol. 519, no. 20, pp. 6834–6839, Aug. 2011.
- [31] F. D. Egitto, "Plasma etching and modification of organic polymers," *Pure Appl. Chem.*, vol. 62, no. 9, pp. 1699–1708, 1990.
- [32] R. Young *et al.*, "XHR SEM: enabling extreme high resolution scanning electron microscopy," in *Proceedings of SPIE*, 2009, vol. 7378, p. 737803.
- [33] T. Ogawa, B. Cho, and S. J. Ahn, "Low-energy scanning electron microscope using a monochromator with double-offset cylindrical lenses," *J. Vac. Sci. Technol. B, Nanotechnol. Microelectron. Mater. Process. Meas. Phenom.*, vol. 33, no. 6, p. 06FJ01, 2015.
- [34] R. Noriega *et al.*, "A general relationship between disorder, aggregation and charge transport in conjugated polymers," *Nat. Mater.*, vol. 12, no. 11, pp. 1038–44, 2013.
- [35] A. Zen *et al.*, "Effect of molecular weight and annealing of poly(3-hexylthiophene)s on the performance of organic field-effect transistors," *Adv. Funct. Mater.*, vol. 14, no. 8, pp. 757–764, 2004.
- [36] Z. J. W. A. Leijten, A. D. A. Keizer, G. de With, and H. Friedrich, "Quantitative Analysis of Electron Beam Damage in Organic Thin Films," *J. Phys. Chem. C*, vol. 121, no. 19, pp. 10552–10561, May 2017.
- [37] C. Schönjahn, R. F. Broom, C. J. Humphreys, A. Howie, and S. A. M. Mentink, "Optimizing and quantifying dopant mapping using a scanning electron microscope with a through-the-lens detector," *Appl. Phys. Lett.*, vol. 83, no. 2, pp. 293–295, 2003.
- [38] C. P. Sealy, M. R. Castell, and P. R. Wilshaw, "Mechanism for secondary electron dopant contrast in the SEM," *J. Electron Microsc. (Tokyo)*, vol. 49, no. 2, pp. 311–321, 2000.
- [39] J. Schafferhans, A. Baumann, A. Wagenpfahl, C. Deibel, and V. Dyakonov, "Oxygen doping of P3HT:PCBM blends: Influence on trap states, charge carrier mobility and solar cell performance," *Org. Electron.*, vol. 11, no. 10, pp. 1693–1700, 2010.
- [40] M. S. A. Abdou, F. P. Orfino, Y. Son, and S. Holdcroft, "Interaction of Oxygen with Conjugated Polymers: Charge Transfer Complex Formation with Poly(3-alkylthiophenes)," *J. Am. Chem. Soc.*, vol. 119, no. 19, pp. 4518–4524, May 1997.

- [41] G. Volonakis, L. Tsetseris, and S. Logothetidis, "Impurity-related effects in poly(3-hexylthiophene) crystals," *Phys. Chem. Chem. Phys.*, vol. 16, no. 46, pp. 25557–25563, 2014.
- [42] J. Cazaux, "Secondary electron emission yield: graphite and some aromatic hydrocarbons," *J. Phys. D. Appl. Phys.*, vol. 38, no. 14, pp. 2442–2445, 2005.
- [43] B. G. Mendis, S. J. Bishop, C. Groves, M. Szablewski, A. Berlie, and D. P. Halliday, "Plasmon-loss imaging of polymer-methanofullerene bulk heterojunction solar cells," *Appl. Phys. Lett.*, vol. 102, no. 25, p. 253301, 2013.
- [44] Y. D. Park, J. H. Cho, D. H. Kim, W. H. Lee, and K. Cho, "Energy-Level Alignment at Interfaces between Gold and Poly(3-hexylthiophene) Films with two Different Molecular Structures," in *AIP Conference Proceedings*, 2007, vol. 879, no. 11, pp. 1623–1625.
- [45] A. Neff, F. Niefind, B. Abel, S. C. B. Mannsfeld, and K. R. Siefermann, "Imaging Nanoscale Morphology of Semiconducting Polymer Films with Photoemission Electron Microscopy," *Adv. Mater.*, vol. 1701012, p. 1701012, 2017.
- [46] N. Rujisamphan, R. E. Murray, F. Deng, C. Ni, and S. I. Shah, "Study of the nanoscale morphology of polythiophene fibrils and a fullerene derivative.," *ACS Appl. Mater. Interfaces*, vol. 6, no. 15, pp. 11965–72, 2014.
- [47] M. Dapor, *Transport of Energetic Electrons in Solids*. Berlin: Springer, 2014.
- [48] R. C. Masters *et al.*, "Novel organic photovoltaic polymer blends: A rapid, 3-dimensional morphology analysis using backscattered electron imaging in the scanning electron microscope," *Sol. Energy Mater. Sol. Cells*, vol. 160, pp. 182–192, Feb. 2017.
- [49] R. Garcia-Molina and A. Gras-Marti, "Analytical theory of electron-beam-induced damage in organic materials," *J. Appl. Phys.*, vol. 61, no. 8, pp. 3105–3107, 1987.
- [50] A. Khurshid, *Scanning Electron Microscope Optics and Spectrometers*. World Scientific, Singapore, 2011.
- [51] A. A. Schultz and M. A. Pomerantz, "Secondary Electron Emission Produced by Relativistic Primary Electrons," *Phys. Rev.*, vol. 130, no. 6, pp. 2135–2141, Jun. 1963.
- [52] I. K. Robinson and D. J. Tweet, "Surface X-ray diffraction," *Reports Prog. Phys.*, vol. 55, no. 5, pp. 599–651, May 1992.
- [53] N. E. Nickles, "The Role of Bandgap in the Secondary Electron Emission of Small Bandgap Semiconductors: Studies of Graphitic Carbon," Utah State University, 2002.
- [54] A. Howie, "Threshold energy effects in secondary electron emission," *Microsc. Microanal.*, vol. 6, no. 4, pp. 291–296, 2000.

## Chapter 5: Published paper: Sub-nanometre resolution imaging of polymer:fullerene photovoltaic blends using energy-filtered scanning electron microscopy

Nature Communications 6, 6928 (2015)

Robert C Masters<sup>1</sup>; Andrew J Pearson<sup>2</sup>; Tom S Glen<sup>2</sup>; Fabian-Cyril Sasam<sup>3</sup>; Letian Li<sup>3</sup>; Maurizio Dapor<sup>4</sup>; Athene M Donald<sup>2</sup>; David G Lidzey<sup>5</sup>; Cornelia Rodenburg<sup>1</sup>

<sup>1</sup>*Department of Materials Science and Engineering, University of Sheffield, Sir Robert Hadfield Building, Mappin Street, Sheffield, S1 3JD*

<sup>2</sup>*Department of Physics, University of Cambridge, Cavendish Laboratory, 19 J J Thomson Avenue, Cambridge, CB3 0HE*

<sup>3</sup>*FEI Co. Europe NanoPort, Achtseweg Noord 5, 5651 GG Eindhoven, The Netherlands*

<sup>4</sup>*European Centre for Theoretical Studies in Nuclear Physics and Related Areas (ECT\*-FBK) and Trento Institute for Fundamental Physics and Applications (TIFPA-INFN), via Sommarive 18, I-38123 Trento, Italy*

<sup>5</sup>*Department of Physics and Astronomy, University of Sheffield, Hicks Building, Hounsfield Road, Sheffield, S3 7RH*

This Chapter, published as an article in Nature Communications, was written by me, aided by comment from co-authors. I also performed the large majority of the work contained within, including most sample preparation, and all SE spectroscopy and data/image analysis. An exception to this is the EFSEM images of P3HT:PCBM films in Figure 5.3, for which the sample was prepared by Andrew Pearson and images were acquired by Fabian-Cyril Sasam before the start of my PhD project. All other images were acquired by me, or, in the case of Figure 5.7, by an operator (Letian Li) that I directed. The modelling data presented in Figure 5.10 is from an early form of the simulation presented in Section 4.7, with the model (described in Supplementary Note 3, Section 5.6) prepared and run by Maurizio Dapor.

The article, including all figures, is reproduced here in its entirety under a CC-BY 4.0 license, with only minor adaptations to figure and section numbering to retain continuity within the thesis. References from the supplementary information have been combined with those from the main article.

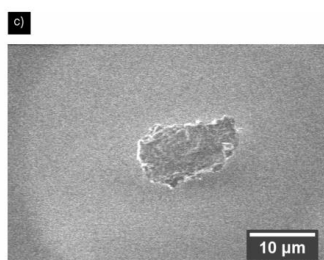
### Amendments to published work after examination.

As a result of the examinations process, a minor error was corrected by adding a scale bar to Figure 5.9 (a supplementary figure in the published version) and additional detail added. Correction in red.

### Figure 5.2 caption, page 149

Low-magnification SE images of P3HT and PCBM blend pure films. (a) and (b) show unfiltered images of P3HT and PCBM respectively, with (c) and (d) showing energy-filtered images of P3HT and PCBM pure films, using  $E_c = 8$  eV (by setting the mirror electrode bias  $M = -6$  V). Scale bars represent 5  $\mu$ m.

### Figure 5.9c, page 165 – replace image to add scale bar



***Abstract:** The resolution capability of the scanning electron microscope has increased immensely in recent years, and is now within the sub-nanometre range, at least for inorganic materials. An equivalent advance has not yet been achieved for imaging the morphologies of nanostructured organic materials, such as organic photovoltaic blends. Here we show that energy-selective secondary electron detection can be used to obtain high-contrast, material-specific images of an organic photovoltaic blend. We also find that we can differentiate mixed phases from pure material phases in our data. The lateral resolution demonstrated is twice that previously reported from secondary electron imaging. Our results suggest that our energy-filtered scanning electron microscopy approach will be able to make major inroads into the understanding of complex, nano-structured organic materials.*

### **Section 5.1: Introduction**

The scanning electron microscope (SEM) has undergone something of a minor revolution in recent years, to the point where it can now be truly considered at the cutting edge of imaging technology[1]. Sub-nanometre resolution imaging is frequently observed using secondary electron (SE) imaging. Outstanding examples include the imaging of single uranium atoms[2] and the topographical imaging of biological samples with 0.5 nm resolution[3]. However, the SEM remains uncompetitive as a tool for chemical mapping, especially with regards to nanostructured organic samples containing light elements. At present, acquiring chemical composition data in a SEM relies primarily on backscattered electron (BSE) imaging or x-ray spectroscopy. Both these techniques have low spatial resolution in comparison to SE images, and struggle to distinguish between materials with similar elemental composition.

An excellent example of an area where the SEM has failed to make a significant impact is the characterisation of nanoscale polymer blend morphology in organic photovoltaic (OPV) active layers[4]. Here, a conjugated polymer and a fullerene are cast to form a bulk-heterojunction blend film exhibiting nanoscale phase separation[5]. The morphology of this blend is known to have a

significant effect on the efficiency of an OPV device[4], and as such characterising these morphologies is hugely important to informing the development of more efficient devices. Despite its many benefits[6], conventional SE imaging in the SEM is incapable of acquiring morphology data as the contrast between blend components is too low for nanometre-scale mapping[7]. Instead, energy-filtered transmission electron microscopy (EFTEM) is currently used for best-resolution imaging[8]–[12]. Here, blend maps are acquired by exploiting the electron energy-loss spectra (EELS) of the blend components, to image in spectral windows in which the chemical contrast between the components is enhanced. Whilst lateral resolution of 1–2 nm is available from these techniques[10], there remain obvious issues with the use of EFTEM on organic blend films: 1) the high level of knock-on damage relating to the large accelerating voltages inherent to TEM[13], and 2) the loss of depth resolution, as information is averaged over the entire specimen thickness. Whilst tomography can be employed to mitigate 2), it exacerbates 1).

An alternative technique showing recent potential is energy-filtered scanning electron microscopy (EFSEM), based upon the energy spectroscopy of detected SE. Whilst such SE spectra are not widely known for exhibiting clear features related to sample chemistry, Joy *et al*[14] have shown that they can be used for fingerprint identification of inorganic materials. Nonetheless, published applications of SE spectroscopy remain rare, due to the lack (at least until recently) of commercially available SEMs that enable systematic SE spectroscopy or high resolution energy filtered SE imaging. EFSEM has however been previously employed for SE imaging of donor-acceptor junctions in silicon with improved dopant contrast[15], [16]. Given that polymer:fullerene OPV blends are in essence donor-acceptor bulk heterojunctions, it is therefore a natural step forward to implement EFSEM to similarly improve material contrast in the characterisation of organic semiconductor films.

The methodology for SE spectroscopy and EFSEM is described in detail elsewhere[17]. In brief however, the sample is imaged using a through-lens detector (TLD), whereby SEs are extracted as they travel up the pole piece of the electron column and are deflected by a series of electrodes

towards a scintillation detector mounted in the side of the column (the exact mechanism of deflection varies between SEMs). By altering the bias on one or more of these electrodes, a low-pass filter may be placed upon the detected SE. Where necessary, the electrode bias can be linked to a SE detection cut-off energy  $E_c$  by detector efficiency calculations, examples of which can be found in work published by Rodenburg *et al*[15] and Young *et al*[18].

Here, we apply energy-filtered SEM (EFSEM) as a new method for obtaining a sub-nanometre chemical characterisation of a *poly(3-hexylthiophene): [6,6]-phenyl C61 butyric acid methyl ester* (P3HT:PCBM) blend. Our technique combines the depth resolution of SE images and reduced beam damage from a low-voltage electron beam with an unprecedented level of chemical contrast in our images through the use of the first SE spectra measured for OPV materials. We measure and compare the SE spectra of the individual blend components and identify a spectral window in which one material is significantly more emissive than the other. By imaging the blend using only SEs in this window, we can boost the level of material contrast in our blend images. Sub-nanometre resolution is observed in our EFSEM images, a significant improvement over the previous best obtained by SE imaging[6] or by EFTEM[10]. Importantly, we can identify clear regions of mixed phase in our blend images, showing the potential for mapping chemical composition based upon SE image contrast. This feature of EFSEM in particular will be of interest to materials scientists and biologists alike.

## Section 5.2: Results

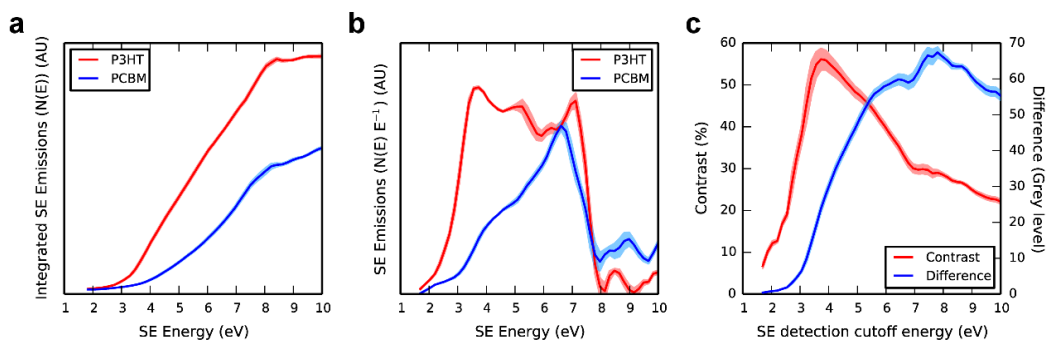


**Figure 5.1:** Measured SE spectra and contrast calculations. (a) shows the integrated SE spectra of P3HT and PCBM, averaged from multiple areas of pure samples. These plots are differentiated to give the SE spectra in (b). (c) plots both the raw brightness difference and contrast (calculated from the data in part (a) using equation (5.1)) between blend components as a function of  $E_c$ . Shaded regions represent standard error on the mean from 8 repeat measurements.

**SE spectra of pure films.** SE spectra of a sample are measured by taking a series of images whilst sweeping the bias on the TLD deflector electrode through a given range (see methods section), and measuring how the detected SE signal changes as the bias (analogous here to the SE detection cutoff  $E_c$ ) is increased or decreased. Plotting the sample image grey level as a function of  $E_c$  gives the integrated SE spectrum of a sample as demonstrated in Fig. 5.1a, which we then differentiate to obtain the SE spectra in Fig. 5.1b.

The P3HT:PCBM blend was chosen as our test system due to it being a popular and well-studied active layer for OPV purposes, thus providing an excellent sample on which to demonstrate and validate a new imaging technique. It has admittedly been long surpassed in terms of OPV performance[5], however the EFSEM technique may be easily applied to other materials systems with similar results. We measured the SE spectra of pure P3HT and PCBM films individually, as presented in Fig. 5.1. Our spectra are reproducible for freshly cast films (the shaded regions present in the spectra indicate the average level of error between different films), and were measured with sequential forward and reverse bias sweeps to ensure the spectra are unchanged in both sweep directions (the exact experimental parameters are described in the methods section). Importantly, we found that SE signal from a sample is significantly more dependent on its material composition than the material state of its components. Details of our specific findings in this

regard can be found in the supplementary information. As an example however, the spectral shape of P3HT, consisting of 3 close but distinct peaks, is retained for samples subject to a thermal anneal, used to increase the crystallinity of a sample (Fig. 5.8). Additionally, integrated SE spectra measured for P3HT:PCBM blend samples lie, as expected, between those measured for pure P3HT and pure PCBM samples, implying that the use of the two components in a blend sample does not greatly affect the nature of the SE emissions from the two individual materials (Fig. 5.9).

We believe that plasmon decay events are responsible for the characteristic shapes of the blend components' SE spectra in Fig. 5.1, or at least contribute to them. A detailed discussion of the shape of SE spectra is beyond the scope of this work, however preliminary Monte Carlo modelling results (see Fig. 5.10 and Supplementary Note 3) suggest that the shape reflects electron affinity and charge trapping. Previously it has been established that plasmons are significant contributors to SE emissions of energies 2-3 eV, based upon measurements of SE emission from amorphous carbon films using an 80 keV primary electron beam published by Pijper and Kruit[19].

**Contrast available from EFSEM.** The clear spectral differences present between the SE emissions of P3HT and PCBM (Fig. 5.1a and b) enable the use of energy-filtered SE imaging to improve chemical contrast, defined here as  $C_{P3HT/PCBM}$ . We use the integrated spectra in Fig. 5.1a, which represent the imaging grey value of the pure films as a function of  $E_c$ , to predict  $C_{P3HT/PCBM}$  between pure P3HT and PCBM as a function of spectral cut-off energy,  $E_c$ , using the SE contrast equation from Seiler[20]

$$C_{A/B} = \frac{I_A - I_B}{I_A + I_B} \times 100\% \quad (5.1)$$

where  $I_{A,B}$  represent the measured grey value for P3HT and PCBM respectively at a given value of  $E_c$ . The results of these calculations are shown in Fig. 5.1c, and predict the contrast between the blend components as a function of  $E_c$ .

In order to obtain EFSEM images with high contrast and resolution, the choice of  $E_c$  used for imaging, based upon analysis of the SE spectra in Fig. 5.1, is critical. Due to the lack of precedent

in this field, our choice is based on the appropriate optimisation of material contrast and signal-to-noise ratio (SNR). Using the contrast plotted as a function of  $E_c$  (Fig. 5.1c) (along with raw SE intensity difference), we observe a clear peak in blend contrast at  $E_c \sim 4$  eV with  $C_{P3HT/PCBM}(4 \text{ eV}) = (56 \pm 3)\%$ . However we note that imaging a blend morphology whilst filtering out all SE with  $E > 4$  eV would result in an unacceptably low signal-to-noise ratio, as data acquisition must be fast (i.e. a short dwell time must be used) to minimize sample damage. The low signal available at this detection cut-off is self-evident from the integrated SE spectra in Fig. 5.1a, and we measured a SNR of 0.06 on a fresh blend surface using  $E_c \sim 4$  eV. We are unable to identify individual blend components using these parameters. Instead we seek to improve the SNR by imaging using the cut-off point at which the numerical difference ( $I_{P3HT} - I_{PCBM}$ ) between the blend component emissions is maximized (between 7.7 eV and 8 eV, as indicated by the 'difference' plot in Fig. 5.1c). Here we still observe improved contrast of  $C_{P3HT/PCBM}(8\text{eV}) = (29 \pm 1) \%$ , and EFSEM images taken of fresh blend films with  $E_c = 8$  V give a greatly improved SNR of 0.3.

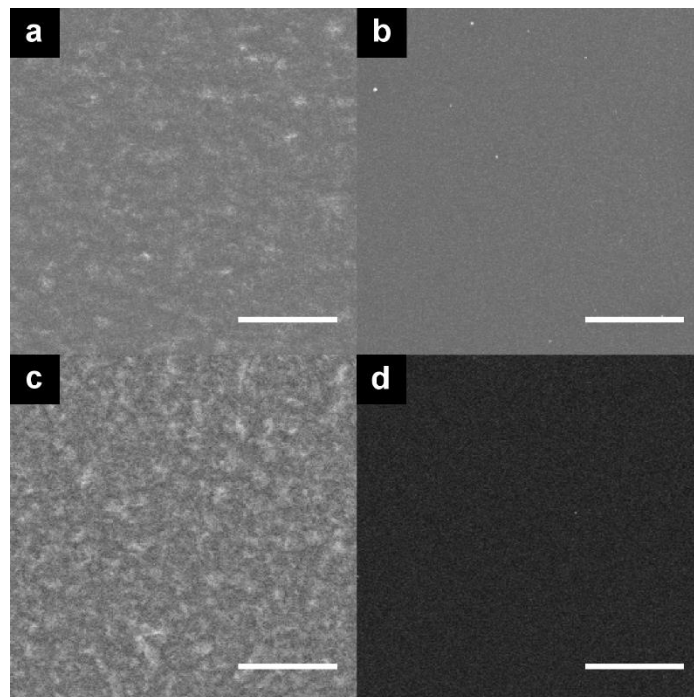


**Figure 5.2:** Low-magnification SE images of P3HT and PCBM blend pure films. (a) and (b) show unfiltered images of P3HT and PCBM respectively, with (c) and (d) showing energy-filtered images of P3HT and PCBM pure films, using  $E_c = 8$  eV. Scale bars represent  $5 \mu\text{m}$ .

An example of the contrast improvement available from energy-filtered imaging is shown in Fig. 5.2. Here we compare SE images of pure P3HT and PCBM films, all taken using a high-resolution FEI Magellan FEGSEM with identical contrast and brightness settings. Fig. 5.2a and b show the two films as imaged under standard conditions with an Everhart-Thornley detector, whereas Fig. 5.2c and d show the films imaged using the microscope's TLD with  $E_C = 8$  eV. We note that the P3HT samples show some variation within the image, which we identify as being P3HT crystallites that are positioned close to, or at the film surface; these appear with the use of high-resolution SEM equipment. Notably, the contrast appears more clearly in the energy-filtered image, possibly indicating that the contrast variations are linked to electron density changes (relating to crystallinity) at the surface rather than from topography. This effect has been alluded to previously[21]. To allow direct visual comparison of the improved material contrast available through energy-filtered imaging, the image brightness of Fig. 5.2c has been increased such that the mean grey level of Fig. 5.2c matches that of Fig. 5.2a, with the brightness of Fig. 5.2d increased by an equal amount (thus the grey level difference between Fig. 5.2c and d remains unchanged). Clearly, by comparing the contrast between Fig. 5.2c and d with that between Fig. 5.2a and b, the P3HT/PCBM imaging contrast has improved significantly using energy-filtered imaging. We find that this effect allows us to easily differentiate P3HT and PCBM in a high resolution blend image.

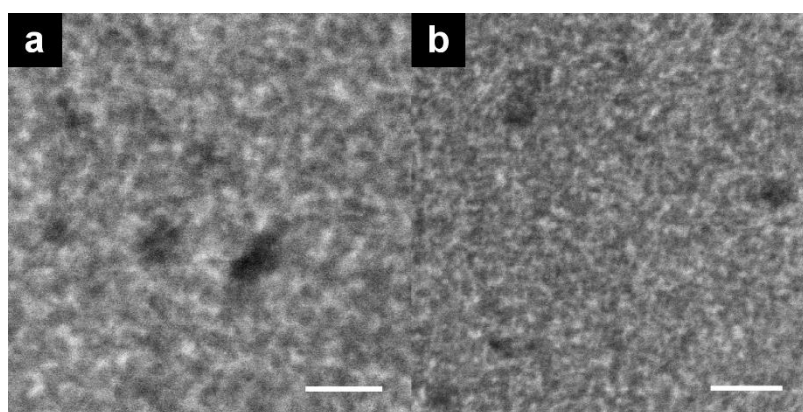


**Figure 5.3:** Overview of EFSEM results for P3HT:PCBM (1:0.8 wt%) blend. (a) Higher magnification image (scale bar 20 nm); (b) Lower-magnification image (scale bar 30 nm). Spectroscopy of blend components suggests that brighter regions are P3HT-rich, darker are PCBM-rich. Clear mixed-phase regions are also visible.

**EFSEM images of blend films.** Our blend film images (of a plasma cleaned film) are presented in Fig. 5.3a and b, covering different fields of view, hence using different electron doses (Fig. 5.3a used a dose of  $3.66 \times 10^{-2} \text{ C cm}^{-2}$ , Fig. 5.3b used  $9.36 \times 10^{-2} \text{ C cm}^{-2}$ ). Both show clear nanoscale variations in SE emission, which we attribute to the phase separation of the blend components; dark and bright areas can be identified as PCBM-rich and P3HT-rich regions respectively based on the contrast predicted in Fig. 5.1a. Directly visible in both images are areas with intermediate grey levels which we identify as molecularly mixed-phase regions.

For an as-cast blend film surface imaged at  $E_C = 8 \text{ eV}$ , we observed some extended nanostructures, however no distinct phase separation could be observed on the surface of a fresh film (see Fig. 5.11). We explain this as a result of a thin P3HT layer present at the surface of the film and obscuring the morphology beneath[22]. Similar observations were made from EFTEM analysis of P3HT:PCBM blend cross-sections published by Pfanmüller *et al*[10]. This polymer “skin” layer was removed using a plasma treatment, a technique previously shown to be effective in this regard[4], [6]. The combination of EFSEM and plasma cleaning enabled us to collect the high contrast, sub-nanometre resolution images presented in Fig. 5.3a and b.

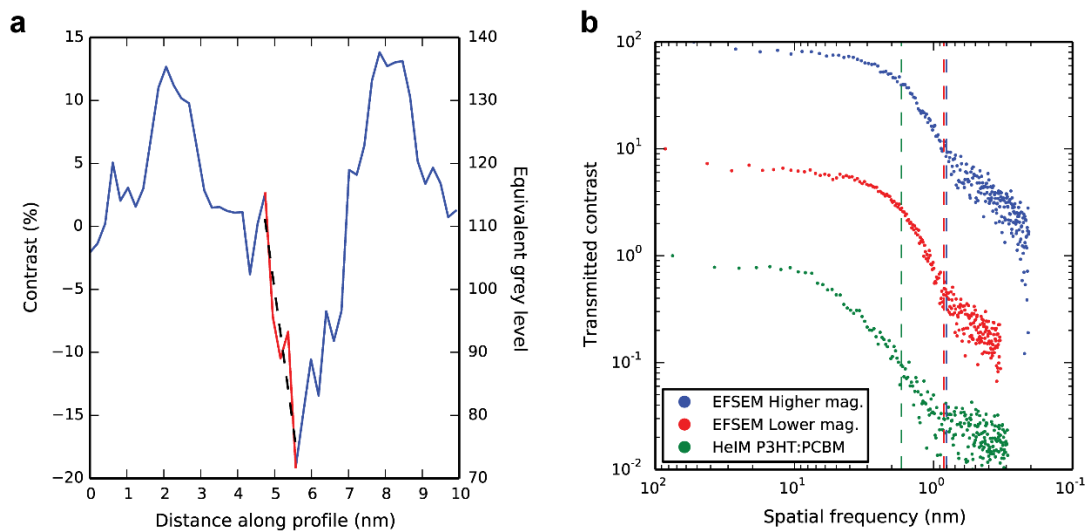


**Figure 5.4:** Analysis of EFSEM images in Fig. 5.3. (a) shows line profile (1 pixel width) extracted from Fig. 5.3a, with a mixed phase region highlighted. The red part of the line profile shows an example concentration step used to calculate resolution. (b) shows a contrast transfer function for high-resolution images of P3HT:PCBM blends using both EFSEM and HeIM. Each plot is offset by a factor of 10 for clarity. The noise-floor onset, correlating to the instrument's resolution limit, is highlighted for each plot.

We have quantified the level of contrast available in our blend images by taking 1-pixel wide line profiles from the images, spanning P3HT-rich and PCBM-rich regions (an example is presented in Fig. 5.4a). Here we have once more used a percentage contrast scale based upon equation 5.1, where for clarity, the 0-point of contrast has been set around intermediate mixed-phase regions. From ten such line profiles, we estimate the average contrast between pure P3HT and pure PCBM regions in our images to be  $(35 \pm 4) \%$ . This is almost double the material contrast seen when imaging without energy filtering (found to be  $(17 \pm 1) \%$  for low-magnification data). Highlighted in Fig. 5.4a is an example region of intermediate  $\sim 0\%$  contrast seen to extend over  $> 5$  pixels, which as such is not an artefact of limited resolution. Mixed phase regions are expected in P3HT:PCBM blends, however their nature and role in a functioning OPV device remains uncertain[23], [24], and therefore the ability to map these regions is hugely important in the context of OPV at present. To our knowledge this is the first time such mixed phase regions have been imaged directly without the need to collect supplementary data (such as statistical analysis of EELS spectra[10], [11]) or to correct for factors such as sample thickness[25].

**Spatial resolution of EFSEM images.** We can determine the lateral resolution of our data using the definition of Kump and Diebold[26], whereby resolution is defined as the distance over which the image brightness is seen to rise or fall between 16% and 84% of maximum brightness of a sharp concentration step. The line profile in Fig. 5.4a contains an example of such a concentration step (highlighted in the figure). We measure a resolution of  $(0.8 \pm 0.1)$  nm for a step between pure PCBM and mixed phase, averaged from ten such line profiles. To show that this reflects the inherent resolution seen throughout our EFSEM data, we have calculated the contrast transfer function (CTF) of our images (as defined by Joy *et al*[27], [28]). Here the onset of a noise floor sufficient to obscure the form of the CTF is defined as the resolution limit (see Fig. 5.4b). From Fig. 5.3a, we estimated the noise floor onset between spatial frequencies of 0.71-0.84 nm, and for Fig. 5.3b we estimate it to lie between 0.63 nm and 0.81 nm. We can compare this to the CTF of helium-ion microscope (HeIM) images of similar plasma-cleaned P3HT:PCBM films[6], where we observe a noise floor onset between 1.1 and 1.7 nm. Taking the upper estimates for these

resolution limits, we can thus show that the lateral resolution available from our EFSEM technique is twice the previous best shown from SE imaging in the HeIM. We also note that this suggests that the lateral resolution available from EFSEM is approaching the dimensions of a single PCBM molecule[29]. However, the overall spatial resolution of our method depends on its depth resolution which is that of the escape depth of the energy-filtered SE[20]. We believe this to be 2-2.7 nm based upon simulations of the inelastic mean free path of electrons in P3HT (see Fig. 5.10) and from studies of amorphous carbon by Inada *et al*[30], however the exact depth resolution may be dependent on the blend component and level of crystallinity[31]. The fact that we observe extended areas of intermediate contrast in perceived mixed phase regions indicates that the SE escape depth exceeds that of a PCBM molecule, and that our definition of mixed phase material will incorporate all material phases with a surface depth smaller than 2.7 nm. Nonetheless, this compares favourably to EFTEM studies of similar samples, where the lateral resolution is estimated as 1-2 nm[10] and the depth resolution is limited by the sample thickness.

**Consideration of sample damage.** Whilst one of the primary benefits of EFSEM in comparison to EFTEM is reduced sample damage, degradation resulting from primary electron beam irradiation and the plasma cleaning process remain a concern for this work. Electron beams in a TEM or SEM are known to induce sample heating and sputtering in organic films, and will destroy the electronic properties of conjugated polymers in large enough doses[32]. Additionally, surface contamination layers can quickly form as a result of chemical damage when organic samples are repeatedly scanned with electron beams[33], although it has been shown that low-energy SE emissions are affected less by such formations[15]. These effects may change the nature of SE emissions from a material and affect the level of material contrast in our data. We have found that whilst imaging a pure film, increasing the electron dose (using a greater dwell time or magnification, for example) of an image irreversibly changes the grey level of the resulting image, which we assume correlates to changes in sample chemistry resulting from electron irradiation. The exact nature of this damage requires further investigation and will be addressed in future work; however we can quantify the effect in Fig. 5.5.

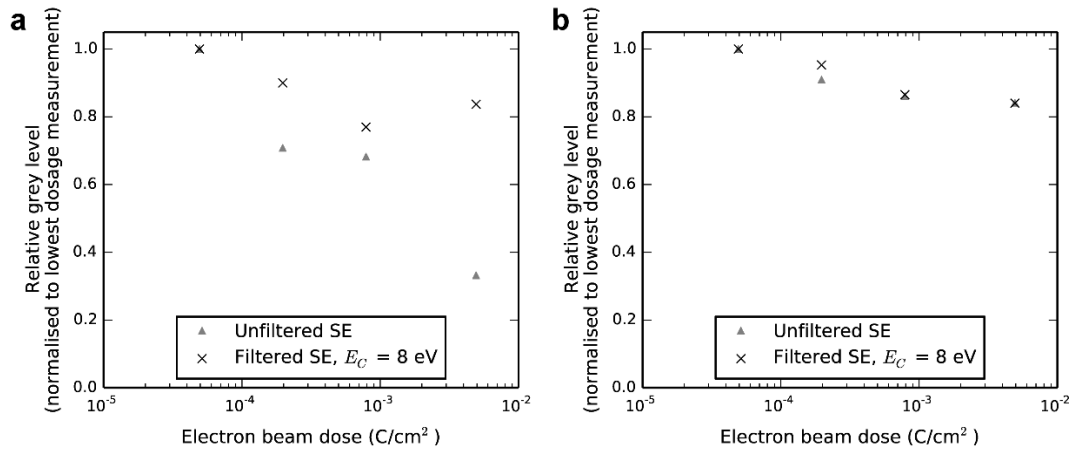


**Figure 5.5:** Relative grey level change resulting from electron beam irradiation. (a) shows data for P3HT, (b) for PCBM. Imaging grey level values are normalized to the grey level at lowest beam dose. Notably, P3HT retains its 'brightness' at higher dose far more effectively using filtered imaging. Plots here show results for plasma-cleaned films, however these results are unchanged with unprocessed films. Standard error on the mean for each data point is typically < 3 % based upon 3 repeat measurements.

Here we plot the change in imaging grey level relative to its value at 5000x magnification (a relatively small beam dose,  $\sim 5 \times 10^{-5} \text{ C.cm}^{-2}$ ) as the beam dose is increased by using larger magnifications. Most notably, the grey level of P3HT as imaged with unfiltered SE sees a significant drop in SE emission as the beam dose is increased to  $0.005 \text{ C.cm}^{-2}$ , to less than 40% of its emission at 5000x magnification. A grey level reduction at higher beam dosage is also observed with PCBM, albeit with a much smaller magnitude. However, when the films are imaged with energy filtering in place using  $E_C = 8 \text{ eV}$ , this 'darkening' effect is greatly diminished for P3HT. As images formed from low-energy SE appear to be affected less by electron beam irradiation, this may imply that the grey level change is at least partially a result of the formation of a modified surface layer. We nonetheless observe that SE emissions and material contrast are retained with energy-filtered SE (at least for  $E_C = 8 \text{ eV}$ ) (both P3HT and PCBM see similar and small relative reductions in grey level at high magnification), whereas a significant negative effect is seen when using unfiltered SE. Thus EFSEM allows for high-contrast imaging despite the apparent presence of beam damage.

We have also investigated the effect of plasma cleaning the samples by measuring the SE spectra of the pure materials after the same 6-minute plasma cleaning process that our blend film was subject to. Whilst some changes were seen in the spectra after this plasma clean, the contrast between the materials using  $E_C = 8$  eV was largely preserved. These spectra and related contrast calculations can be found in Fig. 5.12. In addition, we refer to previous work which has measured the surface topography of similar blends by AFM following plasma cleaning in air; the length scale of the topography was found to be significantly larger than that of the contrast found in Fig. 5.3[6]. We are therefore confident that topographical variation is not contributing to the contrast in our high-magnification images.

**Morphology derived from image analysis.** It is beyond the intended scope of this work to conduct an in-depth study of the relationship between blend processing parameters and morphology. However, to test the quality of our data and compare our results to similar experiments performed by other techniques, we have briefly characterized our blend images. The line profile in Fig. 5.4a demonstrates well-defined contrast levels for P3HT-rich, PCBM-rich and mixed-composition phases. Based upon ten representative line profiles, we have averaged the range of contrast levels for clear mixed-phase regions. We have subsequently calculated a contrast level for every pixel in our data; areas with contrast above the mixed-phase level have been deemed as P3HT-rich, areas with contrast below this are deemed PCBM-rich. We have found this to be an effective and reliable method, as can be seen from the results summarized in Table 1 for the two unprocessed energy-filtered images in Fig. 5.3a and b.

	% PCBM in crystalline aggregate form	% P3HT in crystalline form	% Mixed-phase
5.3a (169 nm x 169 nm), raw image	$28 \pm 3$	$35 \pm 5$	$36 \pm 8$
5.3b (105 nm x 105 nm) raw image	$29 \pm 2$	$36 \pm 4$	$36 \pm 6$
5.6a (169 nm x 169 nm) after FFT	$30 \pm 3$	$40 \pm 3$	$30 \pm 6$
5.6b (105 nm x 105 nm) after FFT	$30 \pm 2$	$42 \pm 2$	$28 \pm 5$

**Table 5.1:** Results of morphology characterisation from image thresholding. Data shows the total phase area observed in the raw images shown in Fig. 5.3 and the noise-reduced images presented in Fig. 5.6. Errors represent the variation in phase area within one standard error on the mean thresholding levels, calculated from 10-15 mixed phase areas.

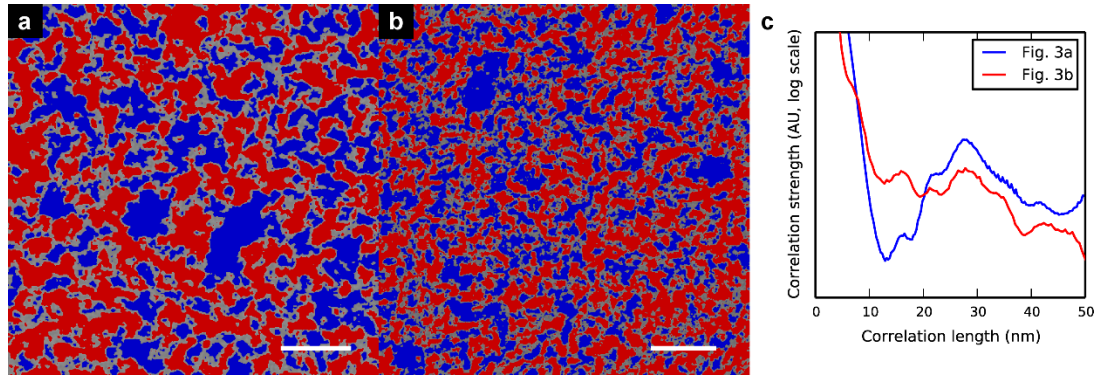


**Figure 5.6:** Summary of blend image characterization. (a) and (b) show EFSEM images subject to FFT bandpass filter and thresholded to emphasize the imaged domain structure. Red areas correlate to those deemed to be P3HT-rich, and blue to those deemed to be PCBM rich. The mixed phase is preserved in these images. (a) shows the same area as Fig. 5.3a (20 nm scale bar), and (b) the same area as Fig. 5.3b (30 nm scale bar). (c) shows radially averaged autocorrelation functions applied to Fig. 5.3a and b. Clear peaks in both functions are observed at ~16 nm and ~28 nm. Other, smaller peaks are also identified at longer correlation lengths.

While this allows us to calculate phase distributions for a quantitative image characterisation, we find a SNR of only 1.6 in our unprocessed images, whereas a SNR of 5 or better is recommended for this type of analysis[34]. Therefore we employ a FFT bandpass filter to suppress noise in each image (specifically, structures of 3 pixels in size or smaller, corresponding to the noise floor level discussed in Fig. 5.4b). Although this affects the absolute contrast values in our data, we bypass this issue by considering the brightness of intermediate mixed phase regions in the FFT images, and thresholding around this level (see methods section for more details). The threshold images

obtained in this way are shown in Fig. 5.6, with the phase area calculations included in Table 1. In spite of the fact that Fig. 5.6b was taken at a total dose of ~10x that of Fig. 5.6a, the percentage of mixed and pure phases is not changed within the uncertainty of our image analysis, and deviates by no more than 2%. This implies beam dosage is not significantly affecting the morphology data that we acquire.

We have also tested for average periodicity in our images. Radially averaged autocorrelation functions (ACFs) of the unprocessed images in Fig. 5.3a and b were calculated, with the results displayed in Fig. 5.6c. We find peaks at 16nm, 21nm and 28nm, with further, weaker correlations at greater lengths (this finds some agreement with power spectral density (PSD) calculations made on EFTEM data by Pfanmöller *et al*[10]). We find these length scales to be in the correct range for P3HT:PCBM blends[24], and tentatively note that 28nm corresponds to the separation between crystalline high  $M_w$  P3HT domains in pure samples[35]. Whilst this link may be purely coincidental, the fact that the morphology of a P3HT:PCBM blend is driven by the initial formation of P3HT crystallites[36] means that we would likely expect the characteristic length scales of a P3HT:PCBM blend to reflect the properties of crystalline P3HT to a degree..

Fig. 5.7 demonstrates that EFSEM applied to the same blend materials but with different thermal treatments reveals the morphological changes resulting from thermal annealing. Fig. 5.7a shows a sample not subject to any thermal anneal, while in Fig. 5.7b the blend has been deliberately over-annealed (for 60 minutes at 150°C). This is in comparison to Figs. 5.3 and 5.6 which reflect the morphology after a 10-minute thermal anneal at 150°. Note the lower magnification of Figs. 5.7a and b, chosen to emphasise the larger-scale phase separation in Fig. 5.7b. In Fig. 5.7a, the imaged phase separation is on a shorter length scale, with large regions of intermediate grey level, which we allocate to mixed phase, separating the pure phases, whereas the over-annealed sample displayed in Fig. 5.7b shows larger pure phases of aggregated material and a diminished amount of mixed phase. Such clear changes in imaged morphology as result of thermal treatments (with the expected trend[37]) offers further evidence that the contrast observed in our EFSEM images stems indeed from material variation .

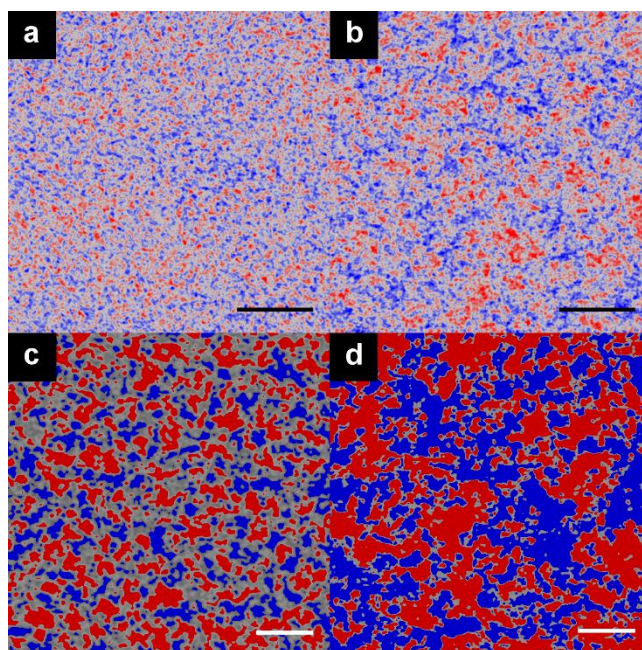


**Figure 5.7:** Blend images and characterisation for samples subject to different thermal treatments. (a) shows the image data for an as-cast sample after a 2-pixel FFT bandpass filter to reduce noise, with (b) showing a comparable image for a blend subject to a 1-hour over-anneal at 150°C. Colour has been added to emphasise the phase structure visible in the data. Parts (c) and (d) show our thresholding attempts applied to higher magnification data. Scale bars in parts (a) and (b) represent 100 nm, and in parts (c) and (d) represent 30 nm. For all parts, red areas correlate to P3HT-rich regions, blue to PCBM-rich regions

We also applied our thresholding techniques to higher-magnification data for these samples, with the resulting thresholds displayed in Figs. 5.7c and 5.7d. A visual comparison of these images is sufficient to reveal the key differences between the samples, with Fig. 5.7c showing far greater mixed phase area and smaller pure phases in comparison to Fig. 5.7d. The phase area calculations for these thresholds can however be found in Table 5.2.

### Section 5.3: Discussion

With regards to the phase area calculations in Table 1, we note that 32% mixed phase was found by Pfanmüller *et al* using EFTEM analysis of P3HT:PCBM blends[10], however due to the poor depth resolution in EFTEM (limited only by sample thickness) this value was in doubt. It is now supported by our measurements. Additionally we can compare our morphology data with results from bulk scattering studies of similar films by considering the concentration of PCBM present in the molecularly mixed phase. In the representative line profile in Fig. 5.4a, we observe that the

contrast level of mixed phase lies approximately halfway between that of the pure P3HT and pure PCBM phases. This implies that the mixed phase is composed of roughly equal parts P3HT and PCBM. Using this assumption, we find that ~14-18% of the blend volume consists of PCBM in mixed phase form. This figure finds good agreement with studies of similar films using small-angle x-ray scattering (SAXS) by Parnell *et al*[38] which suggest this figure to be 13%, and small-angle neutron scattering (SANS) by Kiel *et al*[39] which suggest it to be 16%. Whilst it is known that many parameters can affect the precise morphology of any given P3HT:PCBM blend, these values are from largely comparable blends to the one presented in this work (in that they have been processed for optimal OPV performance), and use similar P3HT  $M_w$  and regioregularity where stated. This is an important correlation; whilst our results involve some assumptions, our data agree with scattering data reliant on a completely different and unrelated set of assumptions.

Data based upon averaged periodicity data is powerful, and the results of SANS or x-ray scattering experiments on OPV blends have previously provided an excellent insight in to the nature of OPV active layers. However, we believe that over-reliance on morphology characterisation based purely on the averaging of bulk properties may lead to premature conclusions, whereby the effects of local variations in morphology or the shape of domains, for example, may be overlooked[40], [41]. Directly imaging the sample is the only way to obtain morphology information of this type, and the combination of high-resolution with clear chemical contrast is required for a morphology image to be of use in this regard. We expect high-quality morphology maps may also be beneficial for theorists, for example as an input for Monte Carlo simulations of OPV devices[42]. Here we have demonstrated a method that can fulfil this requirement, by providing high-resolution morphology data that enables reliable and meaningful thresholding techniques for blend characterisation.

Our analysis is based on upon images that have been thresholded rationally, which has been made possible by the use of SE spectra to define contrast levels between the component materials. This approach eliminates the obstacles usually encountered in attempting quantitative SEM analysis, including the variations in contrast between SEMs with different detector designs[28]. The blend

processing parameters used for the samples presented in Figs. 5.3 and 5.6 were chosen because they are known to produce good OPV performance for these specific materials. We had found indications for the presence of a mixed phase in this blend from earlier work[6], however limited resolution prevented any meaningful quantification of it. The application of EFSEM has allowed us to build upon this by directly imaging mixed-phase material. In summary, we have demonstrated sub-nanometre resolution images of a P3HT:PCBM blend morphology, using an energy-filtered SEM technique that exploits spectral differences in the SE emissions of the blend components. In addition to providing imaging resolution superior to that obtainable using competing techniques, EFSEM data is 2-dimensional with few projection issues, and can be performed on wide sample areas with short (< 1 minute) acquisition times. The resolution and chemical contrast in our data has enabled a detailed characterisation of the imaged morphology, using which we have demonstrated a powerful new technique for facilitating chemical mapping on a nanometre-scale.

We hope that the image data presented here will boost interest in coincidence spectroscopy carried out at lower  $E_0$ , in order to exploit EFSEM fully as an alternative to EFTEM. EFSEM can bypass the limitations of projection[43] because of the small escape depth of SE, and also uses significantly reduced probe energy. As EFTEM is widely used in many materials science applications[44] and is showing promise with biological samples[45], we expect that many fields beyond the OPV community could benefit from the application of EFSEM in its stead.

#### **Section 5.4: Methods**

**Sample preparation.** Polymer films were prepared by spin-coating from solution on to silicon substrates. The substrates were cleaned in isopropanol before being plasma-cleaned in air for 15 minutes. P3HT (obtained from Ossila Ltd., brand Merck SP001 with 94.2% regioregularity and  $M_w = 54200$  Da) and PCBM (purchased from Solenne BV) were dissolved separately in chlorobenzene to make  $25 \text{ mg ml}^{-1}$  solutions, and heated to  $70^\circ\text{C}$  overnight to aid dissolution. The solutions were mixed in a 1:0.8 (P3HT:PCBM) ratio by wt% to form the blend solution. All

solutions (pure and blend) were spin-coated on to the silicon substrates at 1500rpm in nitrogen atmosphere for 40s to make the films. The P3HT:PCBM film for Figs. 5.3 and 5.6 was thermally annealed at 150°C for 10 minutes in accordance with standard practice for making efficient OPV morphologies. Samples for the images in Fig. 5.7 were either not thermally annealed at all (5.7a), or annealed for 60 minutes at 150°C (5.7b). The sample substrates were attached to standard aluminium SEM stubs using conductive silver DAG paint acquired from Agar Scientific.

**Measurement of secondary electron spectra.** SE spectra were measured using a FEI Sirion FEGSEM with XL-30 tube assembly. Pure-film P3HT and PCBM samples were imaged using a 1 kV primary beam at 3 mm working distance, with SE collected using the immersion-lens through-lens detector (TLD). Energy filtering of SE was performed by changing the TLD deflector electrode bias,  $D$ , whilst using a TLD tube bias of 250 V[17].  $D$  was correlated to the cut-off energy for SE detection using detector efficiency calculations published by Rodenburg *et al* for an identical tube assembly using our imaging settings[15]. For a given value of  $D$  we took the SE detection cut-off to be the energy at which SE detection efficiency drops below 30%.  $D$  was swept from 5-25 V in 0.5 V steps with a low-magnification ( $\sim 2500\times$ ) image taken at each step. Using ImageJ, the grey level of eight 128 x 128 pixel regions across the image was averaged and plotted as a function of the SE energy, and this plot differentiated using OriginPro 9.0 software to produce the final SE spectra.

**Energy-filtered secondary electron imaging.** The P3HT:PCBM blend films for Figs. 5.3 and 5.6 were imaged using the immersion-lens TLD of a FEI Helios NanoLab 660 FEGSEM, with the images in Fig. 5.7 taken at a later date using the same detector on a FEI Helios NanoLab G3, access to both of which which was kindly provided by FEI Co. for the purposes of this experiment. For all high-resolution EFSEM images, a primary beam energy of 2.8 kV was used with a working distance of 1 mm, 3  $\mu$ s dwell time and tube bias of 140 V. The samples were plasma cleaned (with an air-plasma) inside the SEM chamber for 6 minutes to remove surface layers from the polymer film. Energy filtering of SE was performed by altering the bias on the TLD mirror electrode,  $M$ . Detector efficiency calculations for this SEM tube were again used to correlate the value of  $M$  to

a corresponding SE energy cut-off, these were provided in private communication with FEI Co. We found that a SE detection cut-off energy of  $\sim 8$  eV could be achieved by using  $M = -6$  V.

The low-magnification images of P3HT and PCBM films (Fig. 5.2) were acquired using a FEI Magellan FEGSEM, with identical electron optics to the FEI Helios used for high-resolution imaging. Parts a) and b) were imaged using an Everhart-Thornley detector, with identical beam and sample settings to those used for the high-resolution blend imaging. For the energy-filtered images (Fig. 5.2c and d), the TLD was used for imaging, using  $M = -6$  V. The same contrast and brightness settings were used for all sample images to allow their direct comparison.

**Image post-processing and analysis.** All image post-analysis was performed in ImageJ. Our resolution calculations were performed in part using SMART-J[46], a SEM image characterisation plugin for ImageJ created and distributed by David C. Joy of UTK in private communication. For the thresholding and analysis of relative phase area in raw data, pixel brightness was converted to a contrast scale using equation (5.1) with the zero-point set as the mid-point between the grey level maxima and minima averaged from ten line profiles. The contrast range equating to the mixed phase was also calculated based upon the line profiles by calculating and averaging the contrast range of conspicuous mixed phase regions. Pixel contrast values above and below this contrast range were taken to represent either pure P3HT or pure PCBM respectively. Particle analysis algorithms in ImageJ were used to calculate phase area. For quantitative analysis of Figs. 5.6a and 5.6b, we used a FFT bandpass filter to smooth structures of 3 pixels in size or smaller. Clear areas of mixed phase were identified in these images and the histograms of these areas taken. The grey level range corresponding to the mean of these histograms  $\pm 1$  standard deviation either side was taken to represent mixed phase regions. Between 10 and 15 such areas were used for each image analysed, and their properties averaged. Pixels with grey levels above and below the mixed phase range were taken to represent pure P3HT and pure PCBM domains respectively. This same technique was used to threshold the images of non-annealed and over-annealed samples displayed in Fig. 5.7. The relative lack of mixed phase material in the over-annealed sample made this difficult for thresholding Fig. 5.7d, with the

thresholds shown representing a best-attempt approximation of the phase areas present in the image.

### **Acknowledgements**

We thank Project Sunshine and the Faculty of Engineering at the University of Sheffield for funding support, and David Beamer of FEI Co. for enabling our high-resolution EFSEM imaging experiments. AJP thanks King Abdulaziz University for financial support via grant no. D-004/431. DL acknowledges financial support via grant no. EP/I028641/1 (Polymer / fullerene photovoltaic devices: new materials and innovative processes for high-volume manufacture) and EP/J017361/1 (Supersolar Solar Energy Hub). TSG was supported by EPSRC grant EP/I029257/1. MD received support from the Leverhulme Trust through the Visiting Professorship (VP1-2014-011) and from Istituto Nazionale di Fisica Nucleare (INFN) through the Supercalcolo agreement with FBK. MD also wishes to express his gratitude to Rafael Garcia-Molina, Universidad de Murcia, for his invaluable suggestions.

**Author contributions:** RCM wrote the manuscript; CR conceived the experiment; CR, DGL and AMD supervised the project. Experimental work was performed by RCM, AJP, TSG, FCS and LL. Techniques for the modelling of SE spectra were conceived and implemented by MD. Data processing and analysis was undertaken by RCM, CR and MD. Technical and conceptual advice was provided by DGL, AMD and AJP.

**Competing financial interests:** The authors declare no competing financial interests.

## Section 5.5: Supplementary Information

(Note: 'Supplementary Notes' referred to in figure captions are included in Section 5.6)

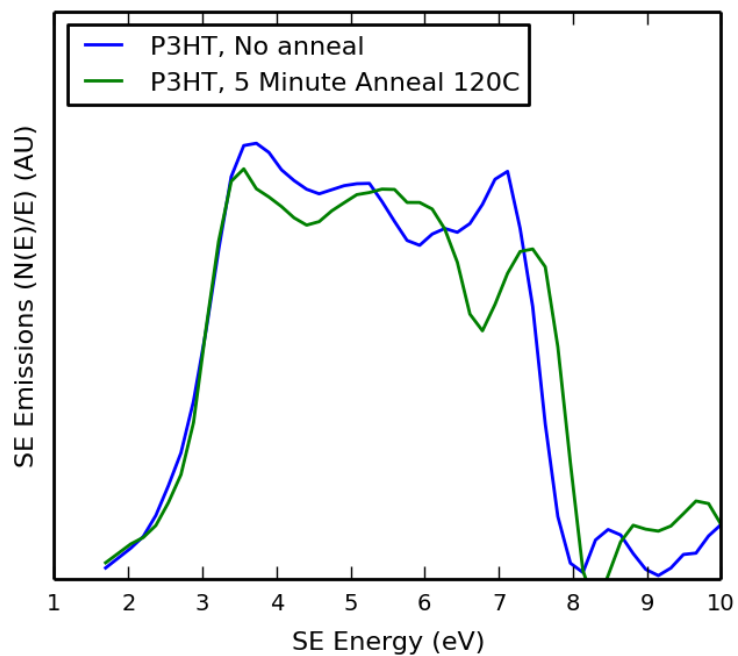


**Figure 5.8:** Comparison of SE spectra from annealed and unannealed P3HT samples. See Supplementary Note 1 for discussion.

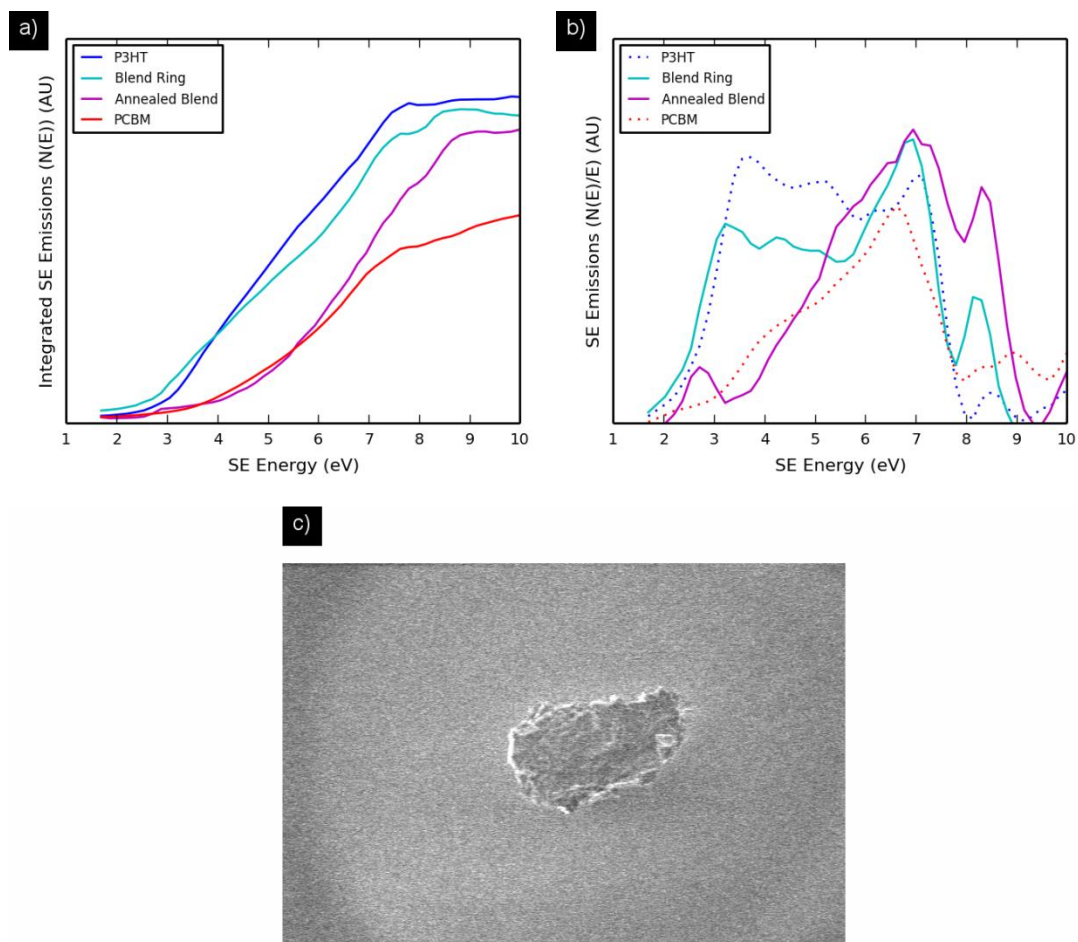


**Figure 5.9:** SE spectra from blend films. a) and b) compare SE spectra from pure and blend films, in their integrated and differentiated forms respectively. c) is an example image from our SE spectra measurements, showing a bright P3HT-rich ‘ring’ around a film defect. See Supplementary Note 2 for discussion.

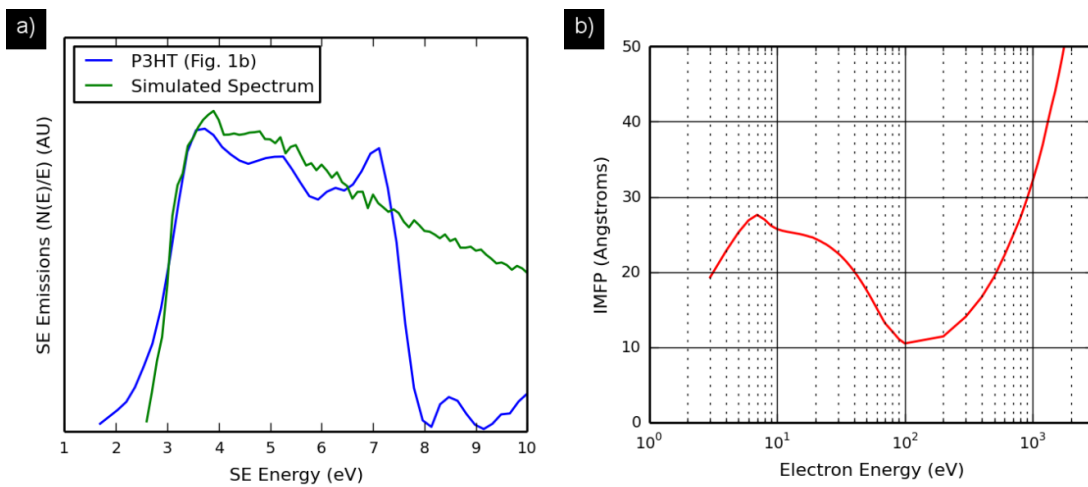


**Figure 5.10:** Summary of SE spectra simulations. a) Comparison of P3HT SE spectrum from Fig. 5.1b and initial simulation results. b) Inelastic mean free path of electrons in P3HT as a function of electron energy, calculated in the process of simulating the SE spectra. See Supplementary Note 3 for a description of the simulations performed and a discussion of the results.

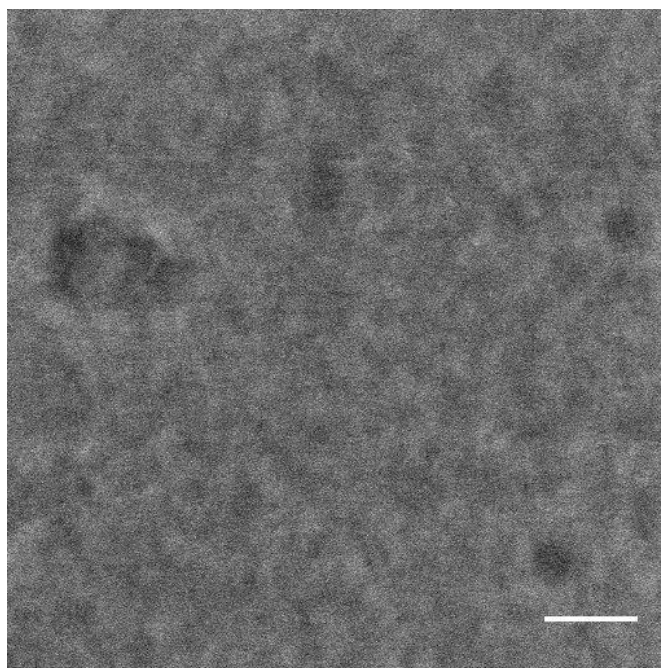


**Figure 5.11:** EFSEM image ( $E_C = 8eV$ ) of P3HT:PCBM blend prior to plasma cleaning. We observe that whilst some larger structures are visible in this image, the fine detail obtained in Fig. 5.3 is obscured by what is perceived to be a P3HT-rich 'skin' present at the surface of the film. The lack of detail available in this figure is our justification for the plasma cleaning of the blend film. The scale bar represents 30 nm.

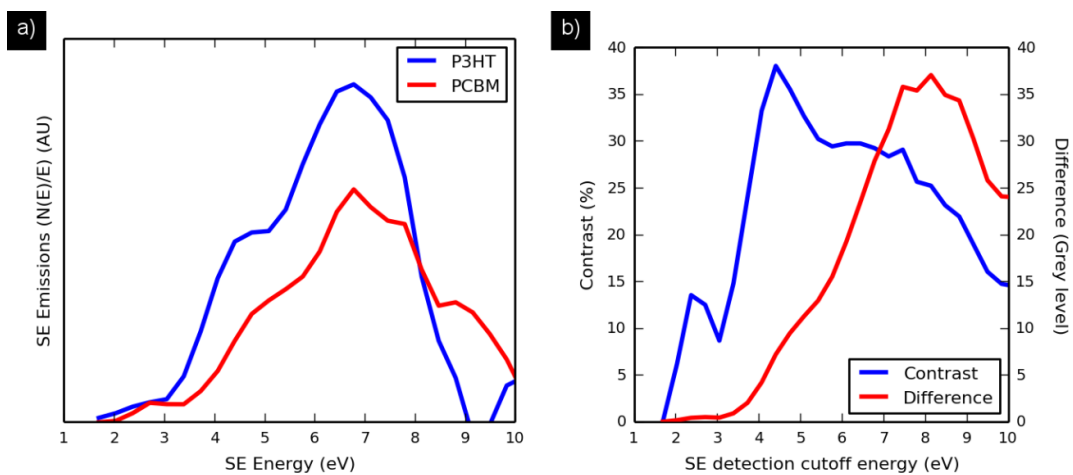


**Figure 5.12:** SE spectra of plasma cleaned pure films. a) Differentiated SE spectra, b) Contrast and grey-level difference plots calculated from the integrated spectra (not shown). Contrast improvement is still available using  $E_c = 8$  eV, see Supplementary Note 4.

<b>Sample</b>	<b>%P3HT</b>	<b>%PCBM</b>	<b>%Mixed Phase</b>
Fig. 5.7c, no thermal anneal	28.± 4	17 ± 3	54 ± 7
<i>(Fig. 5.6a, 10 mins at 150°C)</i>	<i>(40 ± 3)</i>	<i>(30 ± 3)</i>	<i>(28 ± 5)</i>
Fig. 5.7d, 60 mins at 150°C	42 ± 2	39 ± 2	18 ± 4

**Table 5.2:** Phase area calculations for films subject to different thermal anneals. See *Supplementary Note 5.*

## Section 5.6: Supplementary Notes

**Supplementary Note 1:** In Fig. 5.8, we address the notion of sample crystallinity having a potential effect on the nature of a sample's SE emissions. A pure P3HT sample was thermally annealed for 5 minutes at 120°C, in order to increase its level of crystallinity. Whilst the SE spectrum of this sample in Fig. 5.8 is slightly changed with respect to that of the unannealed sample already presented in Fig. 5.1b in the primary manuscript, we observe the same basic spectrum shape and intensity between the annealed and unannealed samples. Thus we observe contrast available between different materials is mostly preserved despite varying levels of crystallinity within a sample, especially when employing energy-filtered imaging with  $E_C = 8$  eV.

**Supplementary Note 2:** In Fig 5.9a, we plot the integrated spectra measured from P3HT:PCBM blend samples, along with the pure P3HT and PCBM samples presented in Fig. 5.1a of the main manuscript. Importantly, we find that the integrated SE spectrum for the blend sample (measured at low magnification,  $\sim 22 \mu\text{m}^2$  area) lies directly between those measured for the pure materials at the 8eV cut-off point used for energy-filtered imaging. This fits our assertion that both materials are individually emitting SE with a similar energy spectrum to that found in pure samples. A second plot is also present in Fig. 5.9a, originating from a ring around a PCBM-based defect found in the blend film. It is expected that local PCBM aggregates in to the defect, leaving a P3HT-rich area around it (see Fig. 5.9c)[47]. We measured the SE spectrum of this 'ring' and found it to appear closer to that of a pure P3HT sample than the bulk film. This effect is more exaggerated in the differentiated SE spectra shown in Fig. 5.9b. Once more, this emphasises that the SE spectrum measured from an area can be closely linked to the material composition of that area, largely independent of its material state. In the case of the P3HT-rich 'ring', its material state is undoubtedly affected by its presence in a blend film, specifically by the interspersion of remaining PCBM material within the 'ring'.

**Supplementary Note 3:** The SE spectrum for P3HT has been modelled in a preliminary form using Monte Carlo (MC) methods[48]. We consider the electron beam interaction cross-section,

$\sigma$ , to constitute the sum of all the electron scattering mechanisms experienced by the beam, such that:

$$\sigma = \sigma_{el} + \sigma_{inel} + \sigma_{ph} + \sigma_{pol} \quad (5.2)$$

Where:

$\sigma_{el}$  Is the elastic scattering cross-section due to the interaction between incident electrons and screened atomic nuclei, calculated using the relativistic partial wave expansion method (Mott cross-section)[49]–[51]

$\sigma_{inel}$  Is the inelastic scattering cross-section due to the interaction between incident electrons and atomic electrons, calculated using Ritchie theory[52], [53]

$\sigma_{ph}$  Is the scattering cross-section due to electron-phonon interaction, calculated from Fröhlich theory[54], [55]

$\sigma_{pol}$  Is the scattering cross-section of the electron-polaron interaction, based upon work by Ganachaud and Mokrani[56].

Details of the precise Monte Carlo strategy used are covered in depth elsewhere[48], however the work is based primarily on the incorporation of P3HT EELS spectra from literature in to a model of the relationship between EELS and SE spectra. The results of one such simulation for the SE spectrum of P3HT are presented in Fig. 5.10a, compared with the experimentally measured spectrum introduced in Fig. 5.1b in the main body of this work. We observe a reasonable fit of the simulated to experimental data, especially given that it relates to early work that will be greatly expanded upon in the future. Of particular note is the reproduction of the experimentally measured SE signal intensity at lower energies, as well as the presence of three peaks characteristic of the pure P3HT sample in the simulated data.

Inferring from the results of the simulation and the effects of changing various parameters in the model, we find that the lowest-energy of these three peaks can be identified as a result of the avalanche effect, and can be tuned by changing the electron affinity,  $\chi$ , input in to the simulation. We find the best-fitting value for Fig. 5.1b to be  $\chi = 2.5\text{eV}$ , which is lower than the literature

value of 3.3 eV[57]. This probably reflects that the experimental sample was briefly exposed to air, likely forming a small oxidised layer on the surface and reducing the electron affinity of the sample. The second peak around 4.5 eV corresponds to the  $\pi$ -peak in the electron energy-loss function (ELF) for P3HT, whereas a third peak around 6 eV (somewhat obscured in Fig. 5.12a) can be attributed to a joint contribution of the  $(\pi+\sigma)$  peak in the electron ELF, as well as the tail of the ‘avalanche’. These correspond to peaks found in the experimentally observed spectra. Beyond  $\sim 7$  eV our model begins to deviate, failing to reproduce a peak around 7 eV as well as the sharp drop-off observed in the experimental spectrum. This is likely a result of our preliminary data failing to take in to account some aspect of the material’s interaction with the electron beam; in Fig. 5.8 we have observed that a thermal anneal of a P3HT sample changes the intensity of the peak around  $\sim 7$ eV, therefore it is likely that the peak represents a sample property. We hope to address this in future work. However, we have established that the two highest-energy peaks represent very important aspects of the electronic properties of P3HT. We can therefore infer that SE spectra are indicative of material properties, with genuine variations in SE spectra between different materials.

In Fig. 5.10b, the inelastic mean free path of electrons in P3HT as a function of electron energy is plotted. This data was acquired in the process of simulating the SE spectrum, and provides a good estimate of the escape depth of SE from P3HT whilst using energy-filtered imaging. At energies up to 8eV, we find this to be around 20-30 Å. This will be the limiting factor on the spatial resolution of our data.

**Supplementary Note 4:** Fig. 5.11 shows the SE spectra of P3HT and PCBM films as measured after an equivalent 6-minute plasma clean process to that our P3HT:PCBM blend film was subject. We find that whilst the basic forms of both spectra change (the low-energy onset of P3HT emission is not as pronounced, and the peak emission of PCBM appears reduced), the basic contrast improvement afforded by energy-filtered imaging using  $E_C = 8$  eV is preserved. This is emphasised by the projected contrast and difference plots, presented in Fig. 5.11b, calculated from

the integrated SE spectra measured for the plasma cleaned P3HT and PCBM films (not shown).

Here we see there remains a clear contrast benefit for imaging using  $E_C = 8$  eV.

**Supplementary Note 5:** Table 5.2 displays the results of our phase area calculations for differently annealed samples. For the clearest results, the images in Fig. 5.7 were passed through a FFT bandpass filter before thresholding. The results of these phase area calculations should be directly comparable to those for Fig. 5.6b based upon the use of the same bandpass filter and magnification. Clearly, the mixed phase area present in our thresholded images decreases significantly for longer anneal times. We also observe the area fractions of pure phase material increasing with thermal annealing. These data match the expected trend for a thermally annealed sample; annealing above the glass transition temperature of the blend encourages greater phase separation of the materials, leading to larger, purer phases[37].

### Section 5.7: References

- [1] D. C. Joy, “Scanning electron microscopy: Second best no more.,” *Nat. Mater.*, vol. 8, no. 10, pp. 776–777, Oct. 2009.
- [2] Y. Zhu, H. Inada, K. Nakamura, and J. Wall, “Imaging single atoms using secondary electrons with an aberration-corrected electron microscope.,” *Nat. Mater.*, vol. 8, no. 10, pp. 808–812, Oct. 2009.
- [3] M. S. Joens *et al.*, “Helium Ion Microscopy (HIM) for the imaging of biological samples at sub-nanometer resolution.,” *Sci. Rep.*, vol. 3, p. 3514, Jan. 2013.
- [4] G. J. Hedley *et al.*, “Determining the optimum morphology in high-performance polymer-fullerene organic photovoltaic cells.,” *Nat. Commun.*, vol. 4, p. 2867, Jan. 2013.
- [5] J. Nelson, “Polymer:fullerene bulk heterojunction solar cells,” *Mater. Today*, vol. 14, no. 10, pp. 462–470, Oct. 2011.
- [6] A. J. Pearson, S. A. Boden, D. M. Bagnall, D. G. Lidzey, and C. Rodenburg, “Imaging the bulk nanoscale morphology of organic solar cell blends using helium ion microscopy.,” *Nano Lett.*, vol. 11, no. 10, pp. 4275–4281, Oct. 2011.
- [7] M. Pfannmöller, W. Kowalsky, and R. R. Schröder, “Visualizing physical, electronic, and optical properties of organic photovoltaic cells,” *Energy Environ. Sci.*, vol. 6, no. 10, pp. 2871–2891, 2013.
- [8] B. Huang, J. A. Amonoo, A. Li, X. C. Chen, and P. F. Green, “Role of Domain Size and Phase Purity on Charge Carrier Density, Mobility, and Recombination in Poly(3-hexylthiophene):Phenyl-C61-butyric Acid Methyl Ester Devices,” *J. Phys. Chem. C*, vol. 118, no. 8, pp. 3968–3975, Feb. 2014.

- [9] S. Venkatesan *et al.*, “Interplay of nanoscale domain purity and size on charge transport and recombination dynamics in polymer solar cells,” *Nanoscale*, vol. 6, no. 2, pp. 1011–1019, Jan. 2014.
- [10] M. Pfannmöller *et al.*, “Visualizing a homogeneous blend in bulk heterojunction polymer solar cells by analytical electron microscopy,” *Nano Lett.*, vol. 11, no. 8, pp. 3099–3107, Aug. 2011.
- [11] L. F. Drummy, R. J. Davis, D. L. Moore, M. Durstock, R. A. Vaia, and J. W. P. Hsu, “Molecular-Scale and Nanoscale Morphology of P3HT:PCBM Bulk Heterojunctions: Energy-Filtered TEM and Low-Dose HREM,” *Chem. Mater.*, vol. 23, no. 3, pp. 907–912, Feb. 2011.
- [12] A. A. Herzing, L. J. Richter, and I. M. Anderson, “3D Nanoscale Characterization of Thin-Film Organic Photovoltaic Device Structures via Spectroscopic Contrast in the TEM,” *J. Phys. Chem. C*, vol. 114, no. 41, pp. 17501–17508, Oct. 2010.
- [13] F. Banhart, “Irradiation effects in carbon nanostructures,” *Reports Prog. Phys.*, vol. 62, no. 8, pp. 1181–1221, Aug. 1999.
- [14] D. C. Joy, M. S. Prasad, and H. M. Meyer, “Experimental secondary electron spectra under SEM conditions,” *J. Microsc.*, vol. 215, no. Pt 1, pp. 77–85, Jul. 2004.
- [15] C. Rodenburg, M. A. E. Jepson, E. G. T. Bosch, and M. Dapor, “Energy selective scanning electron microscopy to reduce the effect of contamination layers on scanning electron microscope dopant mapping,” *Ultramicroscopy*, vol. 110, no. 9, pp. 1185–1191, Aug. 2010.
- [16] C. Schönjahn, C. J. Humphreys, and M. Glick, “Energy-filtered imaging in a field-emission scanning electron microscope for dopant mapping in semiconductors,” *J. Appl. Phys.*, vol. 92, no. 12, pp. 7667–7671, Dec. 2002.
- [17] P. Kazemian, S. A. M. Mentink, C. Rodenburg, and C. J. Humphreys, “Quantitative secondary electron energy filtering in a scanning electron microscope and its applications,” *Ultramicroscopy*, vol. 107, no. 2–3, pp. 140–150, 2007.
- [18] R. Young, E. G. T. Bosch, M. Uncovsky, and L. Tuma, “Low-Energy Secondary Electron Filtering with Immersion Lens SEM,” *Microsc. Microanal.*, vol. 15, no. S2, pp. 222–223, Jul. 2009.
- [19] F. Pijper and P. Kruit, “Detection of energy-selected secondary electrons in coincidence with energy-loss events in thin carbon foils,” *Phys. Rev. B*, vol. 44, no. 17, pp. 9192–9200, Nov. 1991.
- [20] H. Seiler, “Secondary electron emission in the scanning electron microscope,” *J. Appl. Phys.*, vol. 54, no. 11, pp. R1–R18, 1983.
- [21] C. Rodenburg, A. J. Pearson, and S. A. Boden, “Energy Selective Secondary Electron Detection in SEM for the Characterization of Polymers,” *Microsc. Microanal.*, vol. 17, no. S2, pp. 880–881, Oct. 2011.
- [22] D. M. DeLongchamp, R. J. Kline, and A. A. Herzing, “Nanoscale structure measurements for polymer-fullerene photovoltaics,” *Energy Environ. Sci.*, vol. 5, no. 3, pp. 5980–5993, 2012.

- [23] Y. Huang, E. J. Kramer, A. J. Heeger, and G. C. Bazan, "Bulk Heterojunction Solar Cells: Morphology and Performance Relationships.," *Chem. Rev.*, vol. 114, no. 14, pp. 7006–7043, May 2014.
- [24] P. E. Hopkinson *et al.*, "A Phase Diagram of the P3HT:PCBM Organic Photovoltaic System: Implications for Device Processing and Performance," *Macromolecules*, vol. 44, no. 8, pp. 2908–2917, Apr. 2011.
- [25] S. V. Kesava *et al.*, "Domain Compositions and Fullerene Aggregation Govern Charge Photogeneration in Polymer/Fullerene Solar Cells," *Adv. Energy Mater.*, vol. 4, no. 11, p. 1400116, Aug. 2014.
- [26] D. Venables, "Secondary electron imaging as a two-dimensional dopant profiling technique: Review and update," *J. Vac. Sci. Technol. B*, vol. 16, no. 1, pp. 362–366, Jan. 1998.
- [27] D. C. Joy, J. Kim, K. Jalhadi, and S. Deo, "The Contrast Transfer Function of the SEM," *Microsc. Microanal.*, vol. 13, no. S02, pp. 1682–1684, Aug. 2007.
- [28] D. C. Joy, J. Michael, and B. Griffin, "Evaluating SEM performance from the contrast transfer function," *Proc. SPIE 7638, Metrol. Insp. Process Control Microlithogr. XXIV*, vol. 7368, no. 2, p. 76383J–76383J–8, Mar. 2010.
- [29] A. Goel, J. B. Howard, and J. B. Vander Sande, "Size analysis of single fullerene molecules by electron microscopy," *Carbon N. Y.*, vol. 42, no. 10, pp. 1907–1915, 2004.
- [30] H. Inada *et al.*, "Atomic imaging using secondary electrons in a scanning transmission electron microscope: experimental observations and possible mechanisms.," *Ultramicroscopy*, vol. 111, no. 7, pp. 865–876, Jun. 2011.
- [31] S. J. Williams and A. M. Donald, "Investigation of quantitative secondary electron imaging of semiconducting polymer materials using environmental scanning electron microscopy.," *J. Microsc.*, vol. 216, no. Pt 3, pp. 241–248, Dec. 2004.
- [32] H. Ahn, D. W. Oblas, and J. E. Whitten, "Electron Irradiation of Poly(3-hexylthiophene) Films," *Macromolecules*, vol. 37, no. 9, pp. 3381–3387, May 2004.
- [33] D. C. Joy and C. Joy, "Low voltage scanning electron microscopy," *Micron*, vol. 27, no. 3, pp. 247–263, 1996.
- [34] A. Rose, "Television pickup tubes and the problem of vision," *Adv. Electron.*, vol. 1, pp. 131–166, 1948.
- [35] T. Wang *et al.*, "The development of nanoscale morphology in polymer:fullerene photovoltaic blends during solvent casting," *Soft Matter*, vol. 6, no. 17, pp. 4128–4134, 2010.
- [36] P. Kohn *et al.*, "Crystallization-Induced 10-nm Structure Formation in P3HT/PCBM Blends," *Macromolecules*, vol. 46, no. 10, pp. 4002–4013, May 2013.
- [37] T. Wang, A. J. Pearson, D. G. Lidzey, and R. A. L. Jones, "Evolution of Structure, Optoelectronic Properties, and Device Performance of Polythiophene:Fullerene Solar Cells During Thermal Annealing," *Adv. Funct. Mater.*, vol. 21, no. 8, pp. 1383–1390, Apr. 2011.

- [38] A. J. Parnell *et al.*, “Nanoscale Phase Separation of P3HT PCBM Thick Films As Measured by Small-Angle X-ray Scattering,” *Macromolecules*, vol. 44, no. 16, pp. 6503–6508, Aug. 2011.
- [39] J. W. Kiel, A. P. R. Eberle, and M. E. Mackay, “Nanoparticle Agglomeration in Polymer-Based Solar Cells,” *Phys. Rev. Lett.*, vol. 105, no. 16, p. 168701, Oct. 2010.
- [40] M. Rides, “NPL Report MAT 34: Review of Methods for the Characterisation of the Dispersion of Nanoparticles in Polymer Nanocomposites,” *National Physical Laboratory*, 2009.
- [41] C. Gutt, L. Grodd, E. Mikayelyan, U. Pietsch, R. J. Kline, and S. Grigorian, “Local Orientational Structure of a P3HT  $\pi$ - $\pi$  Conjugated Network Investigated by X-ray Nanodiffraction,” *J. Phys. Chem. Lett.*, vol. 5, no. 13, pp. 2335–2339, Jul. 2014.
- [42] M. L. Jones, B. Chakrabarti, and C. Groves, “Monte Carlo Simulation of Geminate Pair Recombination Dynamics in Organic Photovoltaic Devices: Multi-Exponential, Field-Dependent Kinetics and Its Interpretation,” *J. Phys. Chem. C*, vol. 118, no. 1, pp. 85–91, Jan. 2014.
- [43] S. Yakovlev and K. H. Downing, “Visualization of clusters in polymer electrolyte membranes by electron microscopy,” *Phys. Chem. Chem. Phys.*, vol. 15, no. 4, pp. 1052–64, Jan. 2013.
- [44] J. Verbeeck, D. Van Dyck, and G. Van Tendeloo, “Energy-filtered transmission electron microscopy: an overview,” *Spectrochim. Acta Part B At. Spectrosc.*, vol. 59, no. 10–11, pp. 1529–1534, Oct. 2004.
- [45] M. Saunders and J. A. Shaw, “Biological applications of energy-filtered TEM,” *Methods Mol. Biol.*, vol. 1117, pp. 689–706, Jan. 2014.
- [46] D. C. Joy, “SMART - a program to measure SEM resolution and imaging performance,” *J. Microsc.*, vol. 208, no. 1, pp. 24–34, Oct. 2002.
- [47] G. Berriman, B. Routley, J. Holdsworth, X. Zhou, W. Belcher, and P. Dastoor, “Mapping chemical concentration in binary thin organic films via multi-wavelength scanning absorption microscopy (MWSAM),” *Meas. Sci. Technol.*, vol. 25, p. 95901, 2014.
- [48] M. Dapor, *Transport of Energetic Electrons in Solids*. Berlin: Springer, 2014.
- [49] N. F. Mott, “The Scattering of Fast Electrons by Atomic Nuclei,” *Proc. R. Soc. A Math. Phys. Eng. Sci.*, vol. 124, no. 794, pp. 425–442, 1929.
- [50] M. Dapor, “Elastic scattering calculations for electrons and positrons in solid targets,” *J. Appl. Phys.*, vol. 79, no. 1996, pp. 8406–8411, 1996.
- [51] M. Dapor, *Electron-Beam Interactions with Solids*. Berlin: Springer, 2003.
- [52] R. H. Ritchie, “Plasma Losses by Fast Electrons in Thin Films,” *Phys. Rev.*, vol. 106, pp. 874–881, 1957.
- [53] R. H. Ritchie and A. Howie, “Electron excitation and the optical potential in electron microscopy,” *Philos. Mag.*, vol. 36, pp. 463–481, 1977.
- [54] H. Fröhlich, “Electrons in lattice fields,” *Adv. Phys.*, vol. 3, pp. 325–361, 1954.
- [55] J. Llacer and E. L. Garwin, “Electron-phonon interaction in alkali halides. I. The transport of secondary electrons with energies between 0.25 and 7.5 eV,” *J. Appl. Phys.*, vol. 40, no. 1969, pp. 2766–2775, 1969.

- [56] J. P. Ganachaud and A. Mokrani, "Theoretical study of the secondary electron emission of insulating targets," *Surf. Sci.*, vol. 334, pp. 329–341, 1995.
- [57] S. Miller *et al.*, "Investigation of nanoscale morphological changes in organic photovoltaics during solvent vapor annealing," *J. Mater. Chem.*, vol. 18, no. 3, p. 306312, 2008.

## Chapter 6: Published paper: Novel organic photovoltaic polymer blends: A rapid, 3-dimensional morphology analysis using backscattered electron imaging in the scanning electron microscope

Solar Energy Materials and Solar Cells **160**, pp. 182-192 (2017)

Robert C. Masters<sup>a\*</sup>; Quan Wan<sup>a</sup>; Yiwei Zhang<sup>b</sup>; Maurizio Dapor<sup>c</sup>; Adrian M. Sandu<sup>d</sup>; Chengge Jiao<sup>d</sup>; Yangbo Zhou<sup>e</sup>; Hongzhou Zhang<sup>e</sup>; David G. Lidzey<sup>b</sup>; Cornelia Rodenburg<sup>a\*</sup>

<sup>a</sup> *Department of Materials Science and Engineering, University of Sheffield, Sir Robert Hadfield Building, Mappin Street, Sheffield, S1 3JD, United Kingdom*

<sup>b</sup> *Department of Physics and Astronomy, University of Sheffield, Hicks Building, Hounsfield Road, Sheffield, S3 7RH, United Kingdom*

<sup>c</sup> *European Centre for Theoretical Studies in Nuclear Physics and Related Areas (ECT\*-FBK) and Trento Institute for Fundamental Physics and Applications (TIFPA-INFN), via Sommarive 18, Trento I-38123, Italy*

<sup>d</sup> *FEI Co. Europe NanoPort, Achtseweg Noord 5, Eindhoven, 5651 GG, The Netherlands*

<sup>e</sup> *School of Physics and CRANN, Trinity College Dublin, Dublin 2, Ireland*

This Chapter was published as an article in Solar Energy Materials and Solar Cells, and written entirely by me. I also performed all the imaging and data analysis within, with the exception of the helium ion microscope images, which were acquired by Yangbo Zhou as directed by me, and the STEM image in Figure 6.15, which was acquired by Chengge Jiao. Sample preparation of PffBT4T-2OD:PC70BM films was performed by Yiwei Zhang, however I made all P3HT:PCBM films for analysis. Modelling data in this chapter was acquired by Quan Wan using a model developed by Maurizio Dapor.

The article is reproduced here in its entirety under a CC BY 4.0 license, with minor adaptations to figure and section numbering for continuity within the thesis. Supporting references have been combined with those from the main article for clarity.

### **Amendments to published work after examination.**

As a result of the examinations process, issues were raised which required the following alterations in order to facilitate a clearer and fuller discussion of the results. Corrections are highlighted in red.

#### ***Abstract, page 180***

Our results also demonstrate that backscattered electron imaging offers significant advantages over conventional cross-sectional imaging techniques, and show that it enables a fast, systematic approach to ~~control~~ *investigate* 3-dimensional active layer morphology in polymer:fullerene blends.

#### ***Section 6.1, page 182***

Despite this, the detailed nature of the phase-separated blend morphology within this system was not determined. *Whilst the high performance of the blend system is related to numerous factors (most notably the low band gap of the polymer)[10], it is clear...*

**Section 6.3.2, page 193**

At  $E_L = 2-3$  keV (Figure 6.4c-d), a greater fraction of the image has a more 'intermediate' grey level, although the images retain morphology features with high contrast up to  $E_L = 3$  keV (Figure 6.4d). In the  $E_L = 4$  keV image (Figure 6.4e), features with a similar appearance to those in Figure 6.4d are observed, albeit with reduced contrast and clarity. This may result from some fraction of the image signal originating from the uniform silicon substrate beneath the film, *or from the imaging signal depth becoming significantly larger than the average penetration depth of phases in this blend. In this case, the signal depth may be large enough for the image contrast to be averaged and reduced through multiple phases of both blend components...*

**Section 6.4.1, page 198:**

By comparing the results of the Monte Carlo simulations with our experimental data, we can provide a better understanding of our BSE images. *Our simulations suggest that only the BSE signal (and not the SE signal) is emitted with the angle and energy distribution required to reach the BSE detector when the sample stage is biased at 4000 V...*

**Section 6.4.1, page 198**

Considering PffBT4T-2OD:PC70BM, we expect that electron beam interactions with this system to be largely similar to those with P3HT:PC60BM. As such the results of our Monte Carlo simulation for P3HT should be broadly applicable. ~~However, the implantation depth of the beam appears larger in the PffBT4T-2OD system.~~

~~We propose that the drop in image contrast between Figure 6.4d ( $E_L = 3$  keV) and 6.4e ( $E_L = 4$  keV) corresponds with the point at which the BSE signal begins to originate from the silicon substrate beneath the film. Given the thickness of the film is  $\sim 400$  nm (Figure 6.7a), this implies that, at  $E_L = 3$  keV, the BSE emission depth is approaching this thickness. We feel this is a feasible result, however; one would expect a slightly increased electron mean free path in the highly ordered and crystalline PffBT4T-2OD:PC70BM blend.~~

*However, in Figure 6.4e, it is observed that at  $E_L = 4$  keV, the morphological contrast from the BSE image of PffBT4T-2OD:PC70BM is significantly reduced. Here, we suggest that either 1) the Si substrate beneath the film is contributing to the image contrast in this image as the BSE signal depth increases to a size larger than the film thickness, or 2) the BSE signal depth at  $E_L = 4$  keV is larger than the average depth penetration of phases in the PffBT4T-2OD:PC70BM morphology.*

*The thickness of the PffBT4T-2OD:PC70BM film is significantly larger than that of the P3HT:PC60BM film (400 nm rather than 130 nm). As such, for the first case to be possible, the BSE emission depth from PffBT4T-2OD must be approaching 400 nm at  $E_L = 3$  keV, significantly larger than in P3HT:PC60BM (assumed to be around the thickness of the P3HT blend film, 130 nm). This would be unexpected, but perhaps possible with an increased electron mean free path in the highly ordered and crystalline PffBT4T-2OD:PC70BM blend.*

*In the second case, contrast would be lost as a result of the BSE signal averaging through multiple domains of both blend materials in the  $E_L = 4$  keV case. That contrast is retained at  $E_L = 3$  keV but not  $E_L = 4$  keV would suggest that the depthwise coherence of the film morphology is lost (i.e. single phases or domain stacks are no longer considered well aligned through the film) at a depth between the BSE emission depths at these two landing energies. This is perhaps a more likely explanation for the loss of contrast between Figures 6.4d and e, as it retains the assumption that high-energy electron transport through the different OPV films is fairly comparable. Whilst this explanation would require a concession that columnar phases do not penetrate the whole thickness of the PffBT4T-2OD:PC70BM film, this does not preclude good charge extraction properties. Whilst large, well-stacked domains facilitate extraction, continuous phase percolation with strong charge extraction properties is still possible without precisely columnar domains[5]...*

Various in **Section 6.4.5:**

Page 203

These high-contrast regions are not necessarily representative of columnar phases, which would imply single material domains that form a continuous charge extraction pathway ~~through the film thickness~~ *at least through BSE signal depth at  $EL = 3\text{ keV}$* . However, these regions are strongly indicative of a high level of phase alignment or ‘domain stacking’ of single-material phases ~~through the film~~, *at least up to the maximum depth of the BSE imaging signal. These large, aligned phases* are consistent with the impressive photovoltaic performance of the blend system....

Page 204

To further demonstrate the high level of phase alignment ~~through the depth of penetrating in to~~ the PffBT4T-2OD:PC70BM film morphology...

Page 204

We identify the dark regions in Figure 6.4d as domains of fullerene material strongly aligned ~~through the film thickness~~ *up to a high depth within the film*.

## Abstract

*Finding the optimal morphology of novel organic photovoltaic (OPV) polymer blends is a major obstacle slowing the development of more efficient OPV devices. With a focus on accelerating the systematic morphology optimisation process, we demonstrate a technique offering rapid high-resolution, 3-dimensional blend morphology analysis in the scanning electron microscope. This backscattered electron imaging technique is used to investigate the morphological features and length-scales defining the promising PffBT4T-2OD:PC70BM blend system and show how its photovoltaic performance is related to the nature of its phase separation. Low-voltage backscattered electron imaging can be used to probe for structure and domain stacking through the thickness of the film, as well as imaging surface morphology with highly competitive spatial resolution. For reference, we compare our results with equivalent images of the widely studied P3HT:PC60BM blend system. Our results also demonstrate that backscattered electron imaging offers significant advantages over conventional cross-sectional imaging techniques, and show that it enables a fast, systematic approach to control 3-dimensional active layer morphology in polymer:fullerene blends.*

## Section 6.1: Introduction

Understanding the nature of phase separation in polymer blends is of great importance for obtaining the optimal performance from various blend systems [1]. Polymer blends have found a wide range of applications in the current energy landscape, having been recently used in novel electrolyte layers in batteries [2] or dye-sensitised solar cells [3], [4], for example. However they are particularly prevalent in the field of organic photovoltaics (OPV), where control over the phase-separated morphology of the blend is a critical factor determining the photovoltaic power-conversion efficiency (PCE) [5]–[9]. One OPV material system that represents the current state-of-the-art is poly[(5,6-difluoro-2,1,3-benzothiadiazol-4,7-diyl)-alt-(3,3'-di(2-octyldodecyl)-2,2';5',2'';5'',2'''-quaterthiophen-5,5'''-diyl)]:[6,6]-phenyl C71 butyric acid methyl ester (PffBT4T-2OD:PC70BM). This material system has been reported to demonstrate a PCE of up to 10.5% [10]. In spite of its potential, this blend remains somewhat unexplored, with no detailed model of its 3-dimensional morphology yet reported.

When fabricated into a photovoltaic device, the polymer component PffBT4T-2OD absorbs incident radiation (forming an exciton), and then acts as an electron donor to the fullerene component (e.g. PC70BM). The photogenerated electrons and holes are then extracted via the fullerene and PffBT4T-2OD phases, respectively [6]. In an efficient photovoltaic blend, there is generally intimate mixing between the polymer and fullerene, as the diffusion length of excitons in many conjugated polymers is limited to < 10 nm. Thus the formation of phase-separation on a similar length scale is generally believed to be essential for efficient exciton dissociation [5]. Additionally, it is necessary to extract dissociated charges from the device without problems relating to charge recombination. In an ideal blend morphology, continuous pathways should exist comprising individual electron- or hole-transporting phases to ensure efficient electron and hole extraction [11]. It is often proposed that phase-separated morphologies composed of columnar structures passing through the film thickness are highly suited to OPV application [12], [13], as they combine optimal charge extraction characteristics with a large interface area.

Previous work with X-ray scattering has shown that optimised PffBT4T-2OD:PC70BM blend films are typically characterised by a ~300 nm thick film containing highly-crystalline polymer phases having length-scales of 30 to 40 nm [10], [14]. The phase-separated domains were also shown to be highly pure, with little intermixing between the polymer and fullerene phases. Despite this, the detailed nature of the phase-separated blend morphology within this system was not determined. It is clear that building a detailed picture of the nanoscale structure within a PffBT4T-2OD:PC70BM blend will help in the design of new systems that reach even higher efficiencies [15].

Nanoscale phase-separation in polymer blend films can be revealed using high-resolution imaging techniques such as electron microscopy. Phase-contrast in these films is often low however, and thus the generation of unambiguous electron microscope images can be challenging [16]. Various techniques have been devised to overcome such issues, including the use of energy-filtered techniques in the scanning electron microscope (SEM) [17] or transmission electron microscope (TEM) [18], [19], which employ energy-selective electron detection to boost the contrast between the component polymers. Additionally, helium ion microscopy (HeIM) replaces the incident electron beam with a helium ion beam and can produce higher quality morphology images as a result [20]. Whilst such techniques are able to generate images with impressive lateral resolution, they require specialist equipment that is not widely available or, in the case of TEM-based methods, require complex and time-consuming preparation of electron transparent samples. This lack of easily accessible information has contributed to the morphology optimisation bottleneck that is hindering the advancement of new OPV systems – a situation well addressed in ref [15]. We have implemented low-voltage backscattered electron (BSE) imaging of OPV blends to enable rapid, 3-dimensional morphology characterisation in the SEM.

Previously, BSE imaging of polymer systems has been employed by ‘staining’ one polymer phase with a heavy metal compound to improve BSE contrast [21], [22]. This technique typically uses high-energy primary beams, which can lead to poor surface sensitivity and a significant risk of sample damage. More recently, advancements in SEM technology and BSE detector performance

have allowed the development of low-energy BSE methods, which have proven effective at combining high spatial-resolution with surface-sensitive material information [23]. This has been used to demonstrate material contrast on polymer films [24], [25] using low-voltage BSE imaging without the necessity of staining. The rationale behind the technique is that contrast in BSE images mostly results from material variation, with the BSE signal strength defined by material properties such as atomic packing density or nuclear charge [26]. This is in contrast to conventional SEM imaging using secondary electrons (SE), where imaging contrast largely results from sample topography.

When using BSE to image a polymer blend sample, the interaction depth of the primary electron beam is an important factor to consider. BSE can theoretically be emitted from any depth up to the maximum interaction depth of the primary beam, although as a rough approximation they are most frequently emitted from the first half of this interaction depth [26]. The interaction depth of the primary beam is controlled by the landing energy,  $E_L$ , of the beam, with a higher  $E_L$  beam interacting up to a larger depth in the sample. As such, the emission depth of BSE can be controlled as a function of  $E_L$ . To most effectively probe a polymer film with BSE,  $E_L$  must be limited to ensure BSE are emitted from only the film and not the substrate beneath. In this work, we have limited  $E_L$  to 3 keV and below for this purpose. This is below energies used in previous polymer BSE imaging experiments [21], [22].

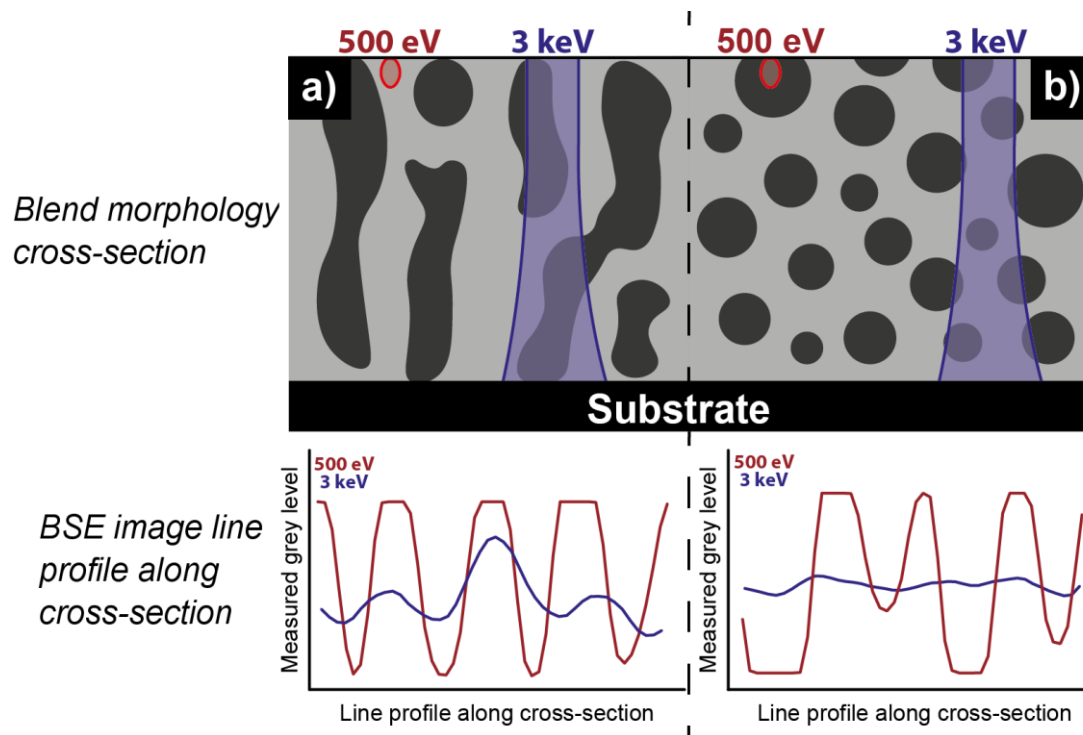


**Figure 6.1:** Schematic of BSE imaging contrast when imaging different morphology types with  $E_L = 500 \text{ eV}$  and  $3 \text{ keV}$ . a) represents an ordered morphology, with phases highly aligned through the thickness of the film. b) represents a more disordered morphology, with a small, randomly dispersed phase distribution. Red and blue shaded regions represent approximate BSE emission volumes at  $E_L = 500 \text{ eV}$  and  $3 \text{ keV}$ , respectively.

For an OPV blend, BSE imaging can be used to probe the nature of the blend morphology over different depths through the film by changing  $E_L$ . By imaging with a very low energy,  $E_L = 500 \text{ eV}$ , BSE emissions are restricted to the top few nm of the sample, allowing the surface morphology to be probed. Likewise, by tuning  $E_L$  such that the BSE emission depth is roughly equal to the thickness of the film, we can probe for structures passing through the whole thickness of the film. When imaging morphology in this case, contrast in a BSE image is highly dependent on whether the BSE emission volume can be largely contained within domains of a single blend component (Figure 6.1). If a given blend morphology is comprised of phase-separated structures that are highly aligned through the thickness of the film, it is possible to increase  $E_L$  whilst largely containing the BSE emission volume within domains of a single blend component. This results in an image that retains high contrast as a function of beam energy (Figure 6.1a). However if BSEs are used to study morphologies with small length scales relative to the dimensions of the BSE emission volume, or disordered blend systems that are heterogeneous through the film

thickness, at higher  $E_L$  the BSE emission volume at any given point will contain significant amounts of both blend components. In this case, BSE images will show very low phase contrast in the higher beam energy condition, as the BSE signal is averaged over both blend components (Figure 6.1b). We can thus easily probe for morphologies showing columnar features or domain stacking ideal for OPV, based upon a BSE image at optimised  $E_L$ . We note that similar principles are used as the basis for multi-energy confocal microscopy, typically used to image biological samples deemed too fragile for TEM or focused ion-beam milling techniques [27], [28]. However, to date these techniques have only been used at relatively low resolutions, or on stained samples. Imaging a film using BSE at low  $E_L$  brings benefits in the form of reduced knock-on damage from the incident primary beam [29], however additional challenges occur as our BSE detector has inherently poor detection efficiency for low-energy electrons [23]. To overcome this issue, a large negative bias (-4 kV) can be applied to the sample stage in order to improve image quality. This has a three-fold effect [23]: (i) the primary electron beam is generated at higher energy and then decelerated to be incident on the sample with the desired ‘landing energy’  $E_L$ , (ii) electrons emitted from the sample are accelerated and incident on the detector (mounted directly above the sample) with a larger energy, increasing the electron detection efficiency, and (iii) electrons emitted over a larger range of angles are ‘focused’ on to the detector by the applied-field. This significantly improves the signal-to-noise ratio in BSE images recorded at low primary beam energies. We note however that care must be taken to understand the effect the stage bias has on emitted electrons, and ensure that our images are formed from BSE in this condition. Details of such considerations can be found in the Supporting Information for this work.

In this work we explore the surface and sub-surface morphology of a PffBT4T-2OD:PC70BM blend using low-energy BSE imaging. By acquiring the first 3-dimensional image data from this blend, we offer a fresh insight in to the morphological features and length-scales that define the performance of an exciting OPV system. The effectiveness of our imaging technique is verified on reference P3HT:PC60BM samples as well as by comparison with cross-sectional helium-ion microscopy and theoretical considerations from Monte Carlo modelling. Our results suggest that

low-energy BSE imaging is an excellent high-throughput technique for 3-dimensional morphological study.

## **Section 6.2: Experimental Methods**

### ***Section 6.2.1: Sample formation***

The PffBT4T-2OD:PC70BM blend films were cast from solution in chlorobenzene and *o*-dichlorobenzene (1:1 volume ratio) with 3% diiodooctane by volume used as a solvent additive. The polymer and PC70BM solution concentrations were 9 mg·mL<sup>-1</sup> and 10.8 mg·mL<sup>-1</sup> respectively. The solutions were heated on a hot plate at 110 °C and spin-coated on to pre-heated silicon substrates (110 °C) at 1000 rpm in a nitrogen glove box. The substrates were then moved to a hot plate at 100 °C immediately after spin casting for drying.

P3HT:PC60BM samples were formed by spin-coating from chlorobenzene solution. P3HT (purchased from Ossila, brand Merck SP001 with 94.2% regioregularity and  $M_w = 54,200$ ) and PC60BM (purchased from Solenne BV) were separately dissolved in chlorobenzene with concentration 25 mg·mL<sup>-1</sup>, and the solutions left on a hotplate overnight at 70 °C to ensure complete dissolution. Solutions of 1:0.8 (P3HT:PC60BM) ratio by weight were spin-cast on to silicon substrates at 1500 rpm for 40 s. Two P3HT:PC60BM samples were imaged; one in its as-cast state and one that had been thermally annealed at 190 °C for 60 minutes.

### ***Section 6.2.2: Imaging of polymer blends***

All samples were imaged using a FEI Nova NanoSEM 450 scanning electron microscope equipped with a segmented concentric backscatter (CBS) electron detector acquired from FEI Co. The detector is mounted to the pole piece of the electron column and consists of 4 solid-state components arranged in concentric rings of increasing radius, with a hole in the middle. The CBS detector was optimised for BSE imaging by the enabling only the detector segments (or combination of segments) giving the strongest signal-to-noise ratio. Imaging was performed at 4 mm working distance with immersion lens active, and a -4 kV bias applied to the sample stage.

We note that at the surface of a P3HT:PC60BM blend, a wetting layer of P3HT obscures the film morphology beneath. This layer has been previously shown to impair efforts at imaging surface morphology [17], [20], and a similar effect was found for PffBT4T-2OD:PC70BM blend films. When acquiring sub-surface data however the effect of this surface layer on the BSE images is negligible. Therefore, we first imaged pristine films to acquire sub-surface morphology data. Then, to remove the capping layer and obtain clearer surface morphology images, we subjected fresh films to a brief, gentle plasma etch in air (following the procedure of previous works [17], [20]). We etched the films for 8 min at low power before immediately placing them in the SEM sample chamber.

Reference images of polymer blend cross-sections were taken with a Zeiss Orion Plus HeIM located at the CRANN facility, Trinity College Dublin. The samples were submersed in liquid nitrogen and cleaved with a diamond knife, then immediately transferred to the microscope chamber. To remove cleaving artefacts the samples were then subject to a plasma clean in air for 24 min. The cross-sections were imaged at a 70° tilt, using a 30 kV primary beam at a working distance of 10 mm.

### ***Section 6.2.3: Image Analysis***

In order to perform quantified analysis of the surface morphologies, the images were classified in to binary polymer and fullerene domains using trainable WEKA segmentation in the ‘FIJI’ distribution of ImageJ [30]–[32]. This employs machine-learning algorithms that are trained by the user on one or more reference images and then applied to segment other similar images. WEKA segmentation can only be confidently employed in images containing features adhering to well-defined classes. For this reason we only segmented surface-sensitive ( $E_L = 500$  eV) images in this work. Images taken at higher  $E_L$  are complicated by the varying overlap of phases in the BSE imaging signal, making WEKA segmentation difficult. Domain size in higher  $E_L$  data was estimated by user-controlled grey level thresholding techniques (as demonstrated in [17]). It should also be noted that WEKA segmentation was used to classify the morphology of P3HT:PC60BM blends, despite the well-documented [17] presence of intermixing between

polymer and fullerene phases in this blend type. This was justified as the spatial resolution of our BSE imaging technique is not sufficient to resolve mixed phase material, which tends to form in 2-3 nm wide regions around phase boundaries [17]. Therefore our imaging data shows effectively a 2-phase system at this resolution level.

To measure the important length-scales inherent to the surface morphology, the ‘distance maps’ [33] of the binary-classified surface morphology images were first calculated using ImageJ. From the distance map image, the morphological features were ‘skeletonised’ [34], again in ImageJ [35]. The product of the distance map and skeletonised image was taken, such that the distance map was reduced to only display the distance to the nearest phase boundary from the medial axis of any phase. The histogram of this image was taken to demonstrate the distribution of phase radius across the whole image. A more detailed consideration of this process can be found in the Supporting information.

#### ***Section 6.2.4: Monte Carlo modelling of backscattered electron emission***

A stepwise Monte Carlo simulation of the interactions of primary electrons with a pure P3HT sample was performed. At each step, the likelihood of the primary electron interacting with the sample via numerous interaction pathways was calculated. In particular, elastic scattering from atomic nuclei, inelastic scattering from atomic electrons, electron-phonon interactions, and electron-polaron interactions were considered and sampled according to common Monte Carlo protocols using random numbers and event probabilities. For each step in the simulation, the nature of the scattering event and the resulting energy loss and scattering angle were calculated. Details of the specific modelling strategy can be found in previous work by Dapor [36]. As inputs to the simulation, the following constants previously determined from P3HT samples were used; electron affinity was taken from Kanai *et al.* [37], electron energy loss spectra from Engmann *et al.* [38], band gap data from Nolasco *et al.* [39], dominant electron trap-depth from Schafferhans *et al.* [40], and dielectric constants (both static and high-frequency) from Singh *et al.* [41]. Similar calculations could not be performed for PffBT4T-2OD, as the material properties required as

inputs to the simulation are not yet available for this material. It is nonetheless expected that the results of the calculations for P3HT should be largely applicable to PffBT4T-2OD.

The output from this simulation was used to calculate the interaction depth of primary electrons in a P3HT sample for a given primary beam landing energy, to indicate the maximum depth of origin in a sample for BSE at different values of  $E_L$ . The predicted distribution of emission angles (correcting for the effect of the stage bias) for emitted SE and BSE at all values of  $E_L$  used in this work was then calculated. This allows a clear differentiation between signals that originate from BSE and from SE (see Supporting Information).

### Section 6.3: Results

#### Section 6.3.1: Imaging polymer blend surfaces

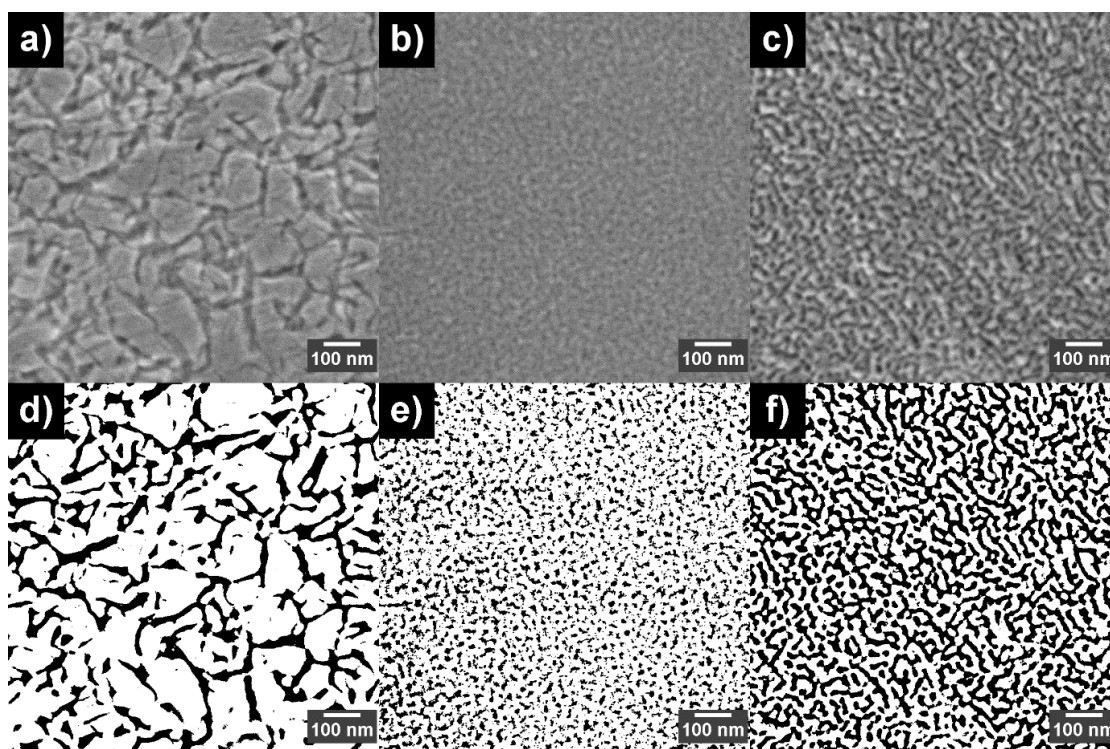


**Figure 6.2:** Surface morphology images of OPV polymer blends imaged using BSE technique at  $E_L = 500$  eV. Part a) shows a PffBT4T-2OD:PC70BM film, b) as-cast P3HT:PC60BM, and c) P3HT:PC60BM annealed for 60 min at 190 °C. All samples were subject to an 8-min plasma clean in air prior to imaging. Parts d), e) and f) show parts a), b), and c), respectively, after having been classified in to polymer and fullerene domains by WEKA segmentation. Black regions represent fullerene, white represents polymer.

Surface morphology images taken from the polymer blend films using  $E_L = 500$  V are displayed in Figure 6.2. In Figure 6.2, parts a, b and c were recorded with identical contrast settings and are presented with no post-processing applied. Features are visible in all images that resemble phase separation in a polymer blend morphology. We have measured the image contrast between pure film samples of PffBT4T-2OD, P3HT, PC70BM and PC60BM, and use this to assign the brighter regions in the images to polymeric phases, with the darker regions being assigned to the fullerene (see Supporting Information). The surface morphology of PffBT4T-2OD:PC70BM (see Figure 6.2a) has the appearance of highly crystalline PffBT4T-2OD phases with a wide range of lateral diameters (~40-200 nm), separated by narrow regions of different composition (PC70BM).

The PffBT4T-2OD:PC70BM morphology is strikingly different to that observed in a P3HT:PC60BM sample, which shows phase separation on a significantly smaller length scale. In the P3HT blends we observe round, dark fullerene phases interspersing a brighter P3HT matrix, with phase contrast in the thermally annealed sample (see Figure 6.2c) appearing coarser and better defined than the as-cast sample (see Figure 6.2b). The smallest resolvable features in our surface morphology images (analogous to the lateral imaging resolution) have been measured by the SMART-J plugin for ImageJ [42] as approximately 6 nm.

Figure 6.2d, e and f show binary images produced by trainable segmentation in Image J (see Section 6.2.3), in which the locations of polymer and fullerene phases are defined. Immediately apparent is the area fraction of each blend component at the surface for the three blends. For the P3HT:PC60BM samples, we observe that the measured surface area of PC60BM increases from 22% for the as-cast sample to 43% for the thermally annealed sample. The area fraction of PC70BM at the surface of the PffBT4T-2OD:PC70BM was measured as 25%, which is significantly smaller than the PC70BM weight fraction in this blend (55%). This suggests that the distribution of blend components through the film is not constant – an effect discussed in more detail later in this work.

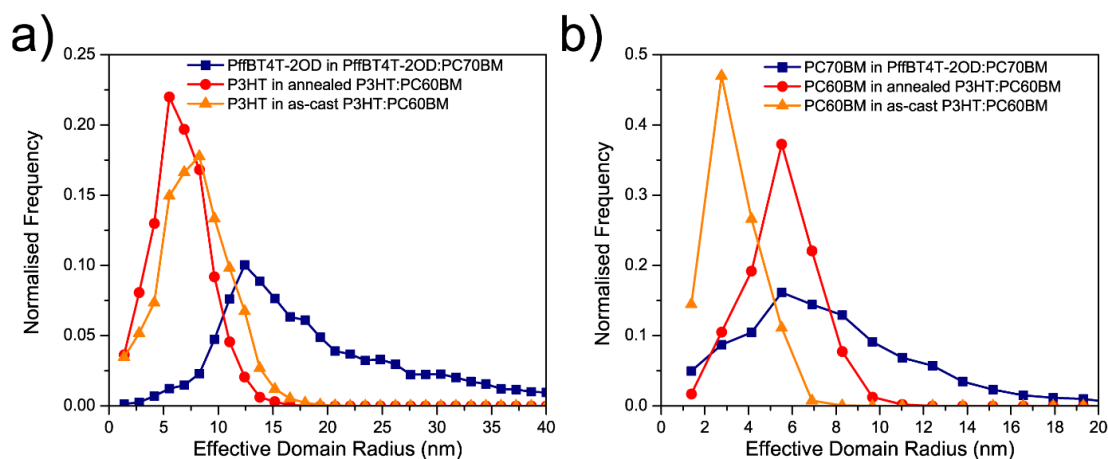


**Figure 6.3:** Domain size histograms for a) polymer phases and b) fullerene phases. The morphological differences between PffBT4T-2OD:PC70BM and different P3HT:PC60BM blend samples can be observed.

Figure 6.3 shows the distribution of effective domain radius measured from the binary morphology images. The image analysis techniques used to obtain these results can be found in Section 6.2.3, with a more detailed consideration in the Supporting Information. Additionally, the data required to reproduce these plots (and all others in this work) are available at ref [43]. These histograms show the distribution of localised domain radius, and can be used to probe the blend morphology length-scales at the surface. Part a) shows the radius distribution for polymer domains, and b) for fullerene domains. For polymer domains, we find that the PffBT4T-2OD:PC70BM film is characterised by a broad size distribution, which peaks in the 10-20 nm range but indicates some phases having a radius that reaches 50 nm. These larger phases are somewhat unexpected given the literature values of ~20-40 nm domain size [10], however we believe they are a result of the increased polymer composition at the surface. For the as-cast and thermally annealed P3HT:PC60BM films however, we determine comparatively narrower size distributions, that indicate P3HT phases have a peak radius in the 5-10 nm range. Considering the fullerene domain size distributions (see Figure 6.3b), we find a similarity between the histograms for PffBT4T-2OD:PC70BM and annealed P3HT:PC60BM. Both systems show a domain size distribution that peaks at ~5 nm, although in the PffBT4T-2OD:PC70BM blend the fullerene phases can reach a radius of up to ~20 nm. The as-cast P3HT:PC60BM film however appears to

have a significantly smaller average PC60BM domain size, with its domain size distribution peaking at  $\sim 3$  nm and no domains found with radius larger than 8 nm.

**Section 6.3.2: Probing sub-surface morphology with higher primary beam landing energy**

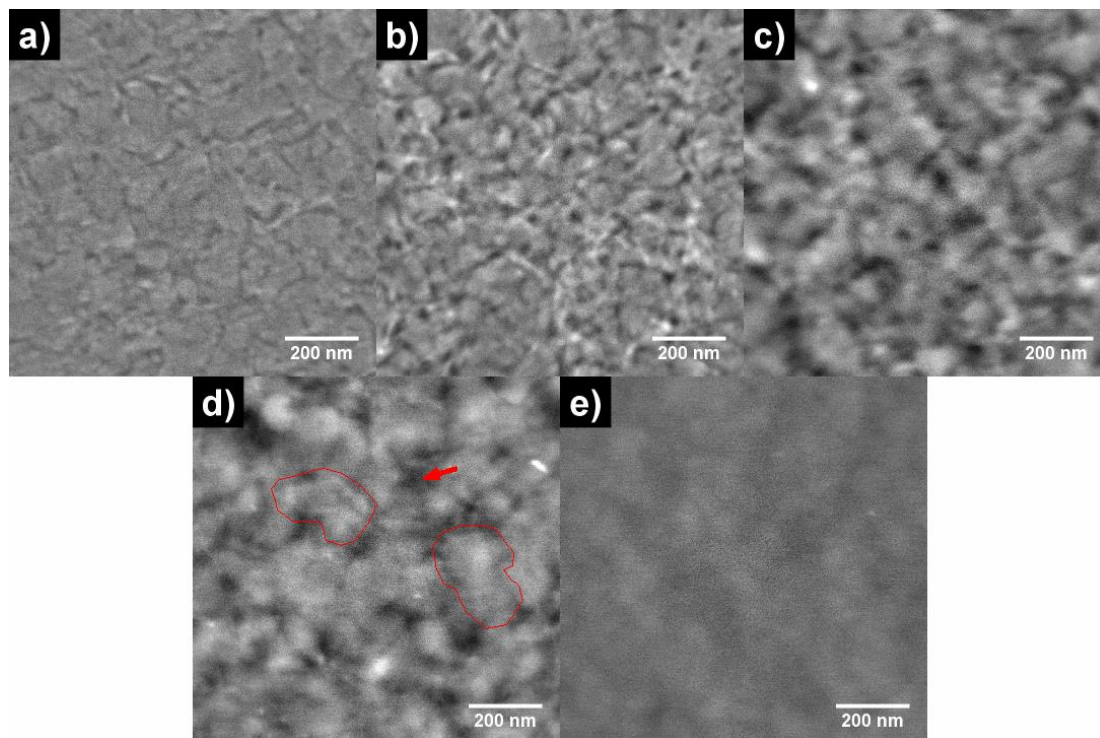


**Figure 6.4:** Images of a PffBT4T-2OD:PC70BM blend imaged with increasing  $E_L$ . The film was imaged using  $E_L =$  a) 500 eV, (b) 1 keV, (c) 2 keV, (d) 3 keV, and (e) 4 keV. In part d), the arrow highlights a typical highly-aligned PC70BM area, and circled regions highlight typical highly-aligned PffBT4T-2OD areas.

Figure 6.4 displays electron micrographs of the PffBT4T-2OD:PC70BM samples as imaged at  $E_L = 500$  eV, 1 keV, 2 keV, 3 keV, and 4 keV, respectively. All images are taken from different areas of the sample; taking multiple high-quality images of the same sample area was not possible due to damage caused by a single exposure. The samples in Figure 6.4 were not plasma cleaned; whilst probing for sub-surface morphology, a few-nm thick wetting layer has a negligible effect on results. We note that the contrast in the  $E_L = 500$  eV image (Figure 6.4a) is less clear in comparison to images taken at higher landing energies as well as the  $E_L = 500$  eV image taken from a plasma-cleaned PffBT4T-2OD:PC70BM sample (see Figure 6.2a).

We find that morphological features can be observed at all  $E_L$  used in Figure 6.4. In Figure 6.4b to d), we observe bright features with the appearance of crystallite grains that are separated by

narrow, darker regions. Typical features are highlighted in Figure 6.4d. Although there are fewer bright crystallite features in images recorded at  $E_L = 2-3$  keV (Figure 6.4c and d), they appear to be roughly similar in size (lateral diameter of 40-200nm) to those observed in the surface morphology image in Figure 6.2a. Notably, the size distribution of such features is narrower in Figure 6.4c and d, suggesting a greater uniformity in the structure of the phase-separation through the thickness of the film in comparison to the surface.

At  $E_L = 2-3$  keV (Figure 6.4c-d), a greater fraction of the image has a more 'intermediate' grey level, although the images retain morphology features with high contrast up to  $E_L = 3$  keV (Figure 6.4d). In the  $E_L = 4$  keV image (Figure 6.4e), features with a similar appearance to those in Figure 6.4d are observed, albeit with reduced contrast and clarity. This may result from some fraction of the image signal originating from the uniform silicon substrate beneath the film. We note that the sharpness and definition of the observed features generally reduces with increasing  $E_L$ , indicating a progressive reduction in lateral resolution. We also observed that as  $E_L$  was increased, the angular distribution of electrons incident our BSE detector increased in width. This is important evidence suggesting that our images are predominately formed from BSE emission and not SE (see Supporting Information).

To aid the interpretation of the SEM images, we performed similar imaging experiments on P3HT:PC60BM blends. Images of as-cast, unannealed P3HT:PC60BM blends recorded at  $E_L = 500$  eV, 1 keV, 2 keV and 3 keV are displayed in Figure 6.5, parts a-d respectively. Parts e to h show images recorded from films that had been thermally annealed at 190 °C for 60 min, imaged using the same range of  $E_L$ . It can immediately be seen that the films subject to a thermal anneal are characterised by significantly greater image contrast. Once again, we observe that, at  $E_L = 500$  eV, only low contrast is visible in images of either sample. At  $E_L = 1$  keV, some morphological contrast is visible in both samples, although phase separation is more pronounced in the annealed sample. At higher  $E_L$  (2-3 keV) however, the samples appear rather different. Image contrast in the as-cast sample has largely disappeared apart from a few larger length-scale features that have the appearance of large aggregates, whereas the annealed sample displays numerous regions with

a high degree of contrast. Using  $E_L = 3$  keV (see Figure 6.5h) we observe a 'background' of intermediate brightness interspersed with small, round features that are either bright or dark. Based upon pure-film contrast (see Supporting Information), we interpret these to represent P3HT (bright) or PC60BM (dark) structures that penetrate through a large fraction of the film's thickness at that point.

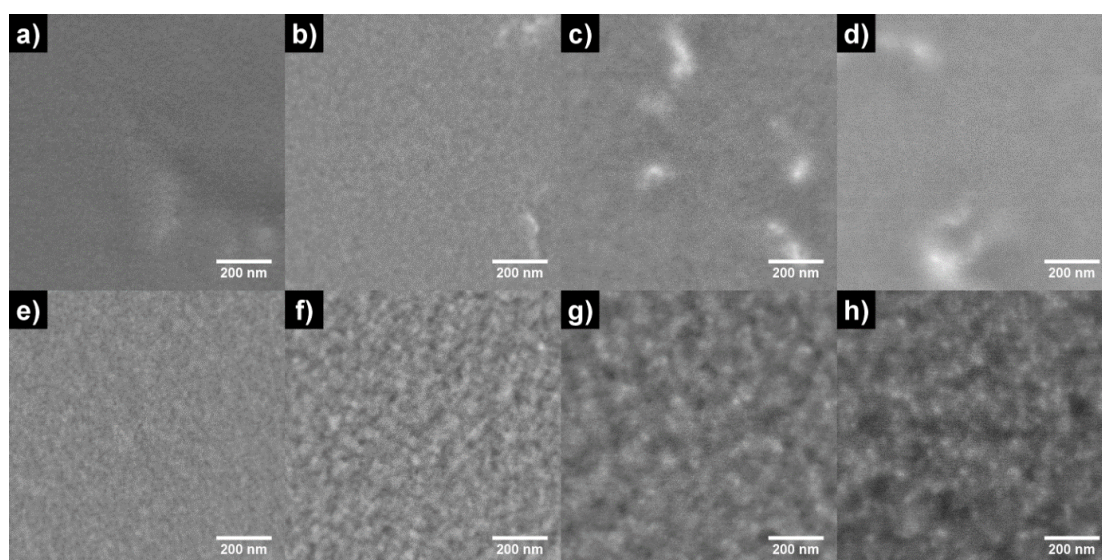


**Figure 6.5:** Images of P3HT:PC60BM blends using with increasing  $E_L$ . Parts (a)-(d) show an as-cast blend film imaged using primary beam energies (a) 500 eV, (b) 1 keV, (c) 2 keV and (d) 3 keV. Parts (e)-(h) show a thermally annealed (190 °C for 60 min) blend film imaged at (e) 500 eV, (f) 1 keV, (g) 2 keV and (h) 3 keV. Identical contrast and brightness settings were used for all images.

To perform size analysis on these highly-aligned features, the same image analysis techniques as applied to the surface morphology could not be used. In the  $E_L = 3$  keV images, the large and frequent regions of 'intermediate brightness' present made it difficult to confidently classify the image in to regions of polymer and fullerene material showing strong alignment through the film. Instead, user-controlled thresholding techniques as demonstrated in [17] were combined with more conventional particle-size analysis techniques to define the size of high-contrast features in the higher  $E_L$  images.

The well-defined dark features in Figure 6.5h (assumed to be highly-aligned fullerene domains) have a similar size (15 - 25 nm radius) and shape to that observed in the PffBT4T-2OD:PC70BM blend (Figure 6.4d) recorded under equivalent conditions. In both cases, the fullerene features

occupy ~ 3% of the imaged blend area. Example images from our analysis are shown in the Supporting Information to emphasise this finding.

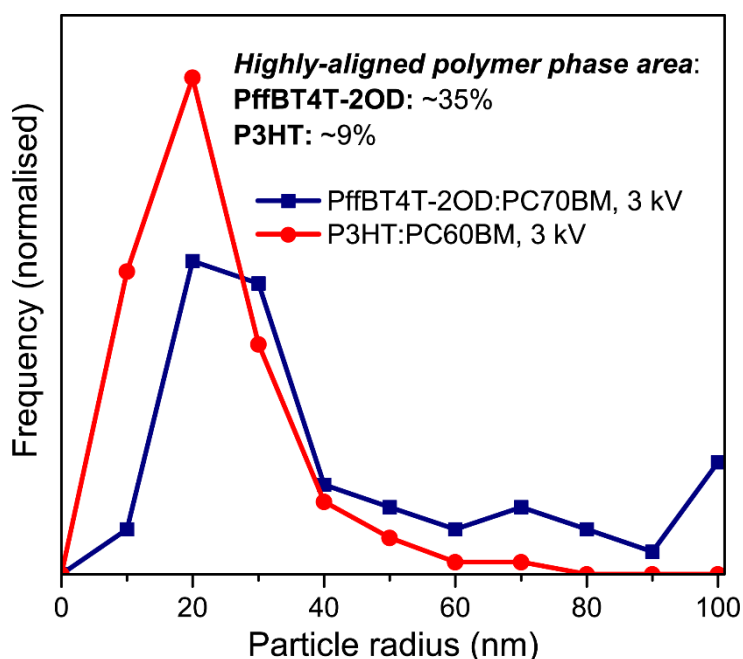


**Figure 6.6:** Sub-surface phase size histogram from  $E_L = 3$  keV images of PffBT4T-2OD:PC70BM (Figure 6.4d) and annealed P3HT:PC60BM sample (Figure 6.5h).

In Figure 6.6, we compare the regions of strong polymer phase alignment as determined from thresholded images recorded at  $E_L = 3$  keV. We calculate that in the PffBT4T-2OD system, regions of highly aligned polymer account for ~35% of the image area, compared to ~9% in the P3HT:PC60BM system. In both systems a majority of highly-aligned polymer phase domains have a radius between 10 and 30 nm. However this size distribution is narrower in P3HT:PC60BM where the aligned polymer domains are more concentrated in this size range (~90% have <30 nm radius) and show a significant fraction having a radius <10 nm. In contrast, the 3 keV images of the PffBT4T-2OD blend system indicate a large fraction (~45%) of aligned polymer regions having a diameter > 30 nm in diameter, with domains having a diameter greater than 100 nm also observed.

### Section 6.3.3: Reference images of polymer blend cross-sections

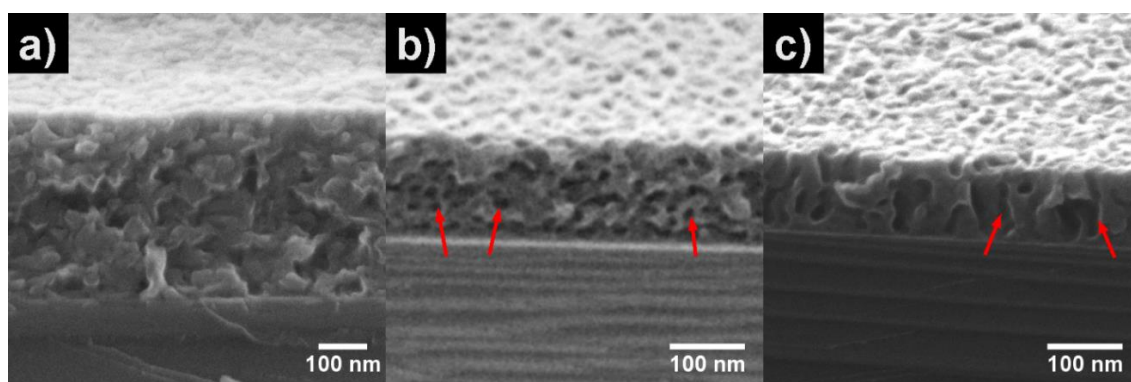


**Figure 6.7:** Cross-sectional images of cleaved polymer blend films, imaged in a helium ion microscope. a) shows a PffBT4T-2OD:PC70BM film, b) an as-cast P3HT:PC60BM blend, and c) P3HT:PC60BM after a 60 minute anneal at 190 °C. Arrows show typical phases observed in the P3HT:PC60BM cross-sectional morphology. Note the different size scale bar in part a).

To see if morphology mapping using higher  $E_L$  provides a correct interpretation of 3-dimensional morphology, data from Figure 6.4 and 6.5 were compared with cross-sectional images of cleaved blend films taken with a HeIM, presented in Figure 6.7. Specifically, part a) shows a PffBT4T-2OD:PC70BM film, with P3HT:PC60BM films before and after annealing shown in 7b and 7c, respectively. It can be seen that the PffBT4T-2OD:PC70BM film is significantly thicker than the P3HT:PC60BM films (~400 nm compared to 130 nm). Cleaving artefacts can be observed in all images, which make the definition of the exact size, shape and distribution of the phase domains difficult. This is especially the case for the PffBT4T-2OD:PC70BM film. A plasma etch was required to remove some artefacts and reveal morphological features in all samples. For the P3HT:PC60BM samples these features appear as voids likely as a result of the preferential etching of one blend component. For the PffBT4T-2OD:PC70BM film in Figure 6.7a we observe small features having a highly crystalline appearance, and a variety of narrow, dark features resembling the fullerene domains identified at the surface (Figure 6.2a). Some larger dark regions are also observed, however it is difficult to determine whether these are fullerene domains or simply voids in the cross-section. The cross-sectional morphology of the P3HT:PC60BM films is clearer, with small and highly circular domains seen in the as-cast film (Figure 6.7b), and a coarser, more column-like morphology seen in the thermally annealed sample (Figure 6.7c). Morphological features have been highlighted by arrows in images of the P3HT:PC60BM cross-sections.

### Section 6.3.4: Validation of 3-dimensional morphology data with Monte Carlo simulation

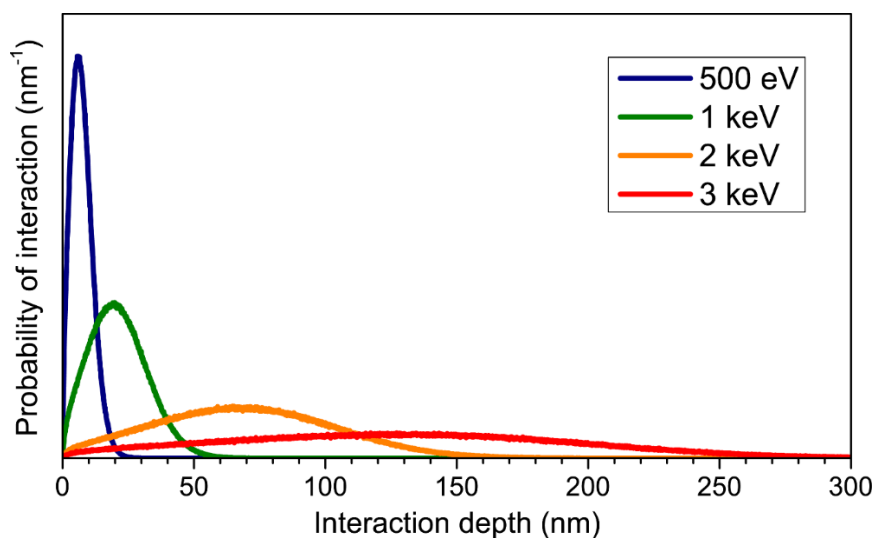


**Figure 6.8:** Depth distribution of primary electron interactions in P3HT as simulated by Monte Carlo model for different values of  $E_L$ .

To understand the generation of BSE image data recorded at different  $E_L$ , we have simulated the interaction depth of an electron beam in P3HT at different  $E_L$ . Figure 6.8 shows this depth distribution for  $E_L = 500 - 3000$  eV and can be used to estimate the depth through the film probed by imaging at each  $E_L$  value. As previously noted, BSE are typically emitted from around the first half of the primary beam's interaction volume. As such, we can estimate from our simulations that at  $E_L = 500$  eV, BSE are emitted from the first  $\sim 10$  nm of the beam's 20 nm interaction depth. As  $E_L$  increases, the interaction depth increases considerably, with the BSE images probing the strength of domain alignment over increasing depths. At  $E_L = 3$  keV the BSE signal is generated from the top  $\sim 150$  nm of the sample, and as such probes for structure over this depth range in a P3HT sample.

By considering the angular distribution of emitted electrons when the SEM stage is subject to biasing, we can understand the origin of contrast in our images. Our simulations show that as  $E_L$  increases, BSE are emitted over a wider distribution of angles. The angle of peak emission (relative to the incidence angle of the beam) also increases at greater  $E_L$ . In contrast, the angular distribution of emitted SEs was found to be largely independent of  $E_L$ , with SE emissions concentrated at significantly lower angles than BSE, even at  $E_L = 500$  eV. This results from a

focussing effect of the stage bias field, which has a stronger effect on low-energy SE emissions than on BSE. Our simulations suggest that the majority of SEs are in fact not detected in our experimental setup (a detailed consideration can be found in the Supporting Information).

## **Section 6.4: Discussion**

### ***Section 6.4.1: Consideration of Monte Carlo modelling, correlation with experimental BSE data***

By comparing the results of the Monte Carlo simulations with our experimental data, we can provide a better understanding of our BSE images. Our simulations suggest that only BSEs (carrying information relating to material composition) are emitted at the correct angle and energy necessary to be incident on our BSE detector when the sample stage is biased at 4000 V. We note that our simulations found both the angle of peak emission and spread of the angular distribution for BSE emission to increase with greater  $E_L$ . Importantly, this correlates with our imaging experiments (see Supporting Information). We are confident therefore that the major constituents of our imaging signal are BSEs, and that material variation is the dominant origin of contrast in the SEM images presented in Figure 6.2, 6.4 and 6.5.

Figure 6.8 shows the change in the implantation depth of incident primary electrons as  $E_L$  increases. We have observed that the BSE signal is averaged over a greater fraction of the film's depth as  $E_L$  increases. At  $E_L = 3$  keV the beam penetrates up to  $\sim 300$  nm into a P3HT film, with BSE emissions coming from the top  $\sim 150$  nm of the sample as a result. This indicates that at  $E_L = 3$  keV, we are in fact probing for domain structure passing through the whole of a P3HT:PC60BM film. By reducing  $E_L$  the BSE signal is emitted from a smaller fraction of the film volume, and probes for structure closer to the film surface (we estimate that BSE emissions occur from the top 10, 25 and 75 nm of the film for a beam energy of  $E_L = 500$  eV, 1 keV and 2 keV, respectively). Considering PffBT4T-2OD:PC70BM, we expect that electron beam interactions with this system to be largely similar to those with P3HT:PC60BM. As such the results of our Monte Carlo simulation for P3HT should be broadly applicable. However, the implantation depth

of the beam appears larger in the PffBT4T-2OD system. We propose that the drop in image contrast between Figure 6.4d ( $E_L = 3$  keV) and 6.4e ( $E_L = 4$  keV) corresponds with the point at which the BSE signal begins to originate from the silicon substrate beneath the film. Given the thickness of the film is  $\sim 400$  nm (Figure 6.7a), this implies that, at  $E_L = 3$  keV, the BSE emission depth is approaching this thickness. We feel this is a feasible result, however; one would expect a slightly increased electron mean free path in the highly ordered and crystalline PffBT4T-2OD:PC70BM blend. Nonetheless, at  $E_L = 500$  eV, the BSE emission depth is smaller than the size of a typical phase in either a P3HT:PC60BM or PffBT4T-2OD:PC70BM system. Imaging at  $E_L = 500$  eV, BSE emissions will be isolated in a single material phase at the surface with minimal contribution from the morphology beneath, allowing accurate mapping of surface morphology.

#### ***Section 6.4.2: Experimental validation of BSE technique – 1) Surface morphology***

The blend surface images presented in Figure 6.2 demonstrate the ability of our BSE technique to map surface morphological changes resulting from different film processing conditions. From our images of P3HT:PC60BM films (Figure 6.2b-c), we note fullerene phases that are  $\sim 3$  nm in radius and become larger and better defined in the thermally annealed film. We interpret the improved image contrast seen in the annealed sample as resulting from an increased level of phase purity. This observation is consistent with previous work on P3HT:PC60BM blends in which thermal annealing is seen to improve phase purity and increase the size of PC60BM domains [44]–[46].

The WEKA segmented images indicate (Table 1) a significantly smaller area fraction of PC60BM (22%) in the surface morphology of the as-cast sample in comparison to the thermally annealed sample. Previous works using neutron reflectivity measurements [47] have identified the presence of a  $\sim 20$  nm thick PC60BM-depleted layer (separate to the 1-2 nm wetting layer previously discussed [20]) at the top of a comparable P3HT:PC60BM sample. It was also demonstrated that subjecting a sample to a thermal anneal acts to homogenise the PC60BM concentration throughout the sample, eliminating this PC60BM depleted layer. We observe such effects in our images of the thermally-annealed P3HT:PC60BM sample, where the PC60BM content (as

defined by WEKA segmentation) increases to 43%. We note that PC60BM has a relative concentration of 44% (by weight) in our films; as such our results also suggest that PC60BM becomes distributed evenly throughout the film after thermal annealing. In addition to this, the domain size histograms in Figure 6.3 show PC60BM domain sizes that peak at ~6 nm in radius for the annealed sample. This result is in agreement with previous studies [20]. We thus conclude that the results from our BSE imaging technique are consistent with other methods used to study polymer:fullerene blends at the surface.

### ***Section 6.4.3: Experimental validation of BSE technique – 2) Through-thickness morphology***

When we increased the  $E_L$  used for imaging, we observed significant differences between BSE images recorded from as-cast and thermally annealed P3HT:PC60BM blend samples (see Figure 6.5). These appear to correspond with differences in the cross-sectional morphology of the blends as imaged by HeIM (Figure 6.7b-c). We note that as-cast samples were characterised by low image contrast (see Figure 6.5a-d), with phase-separation largely invisible for  $E_L > 2$  keV. This finding is consistent with cross-section HeIM imaging shown in Figure 6.7b where small, circular domains with little depth penetration were observed. We believe that the BSE emission volume at higher  $E_L$  will contain multiple phases of both blend components in this case, resulting in a loss of contrast as the BSE signal is averaged over all phases in this volume. It is also clear that low phase-contrast will also result from the low phase purity present in as-cast P3HT:PC60BM blends [45]. We note the larger bright features present in Figure 6.5c-d, which we suspect are larger P3HT aggregates formed in solution.

In the BSE images of thermally annealed samples (Figure 6.5e-h), morphological features are clearly observed at all  $E_L$ . This is a result of the large surface depth of phases in the more ‘columnlike’ [48] morphology formed by a thermal anneal. Again, we refer to the HeIM reference image of the annealed sample cross-section in Figure 6.7c, where we observe phases that penetrate through a large fraction of the film. For material domains with a large degree of depth penetration, the BSE emission volume up to  $E_L = 3$  keV can be mostly contained within that domain, with a high-contrast region observed in BSE images as a result. We therefore interpret the small, high-

contrast features seen at  $E_L = 2\text{-}3$  keV (see Figure 6.5g-h) to be P3HT and PC60BM structures highly aligned through the thickness of the film. Our BSE imaging method thus replicates morphology information from cross-sectional HeIM imaging from P3HT:PC60BM blends, without the need for sample cross-sectioning. This demonstrates the effectiveness of low-energy BSE imaging for probing the sub-surface morphology of polymer blends.

#### ***Section 6.4.4: Analysis of PffBT4T-2OD:PC70BM morphology – 1) Surface Morphology***

From the surface image presented in Figure 6.2a we conclude that the PffBT4T-2OD:PC70BM surface morphology is highly crystalline in nature, with large crystallites separated by narrow regions of another phase. We believe the bright crystallites to be the polymer phase; a conclusion supported by both the contrast between PffBT4T-2OD and PC70BM in pure-film images (see Supporting Information) as well as previous findings that reported that the morphology of a PffBT4T-2OD:fullerene blend is dominated by the initial crystalline aggregation of the polymer phase [10]. The surface data in Figure 6.2a closely resembles surface maps of similar blends from atomic force microscopy published previously [10].

The surface morphology of PffBT4T-2OD:PC70BM is in stark contrast to the morphology of a P3HT:PC60BM blend. The difference in length-scale and ordering between the different blends is exemplified by the segmented binary images and their related domain size histograms. These histograms, derived from our BSE images and calculated from the shortest path to a domain boundary in a given phase (see Supporting Information), are a useful morphology analysis tool in the context of OPV blends. They reflect an important aspect of OPV active layer morphology – i.e., the maximum distance an exciton has to diffuse in order to be dissociated in to free charges at a phase boundary.

In the domain size histograms, we observe some notable differences and similarities between the blends. From the polymer histograms shown in Figure 6.3a, we note that the PffBT4T-2OD blend has a large peak polymer domain size for an OPV system (~13 nm radius), with the majority of the radius measurements lying in the range 10-20 nm. This matches literature values from both resonant soft x-ray scattering and small-angle neutron scattering experiments well [10], [14], [49].

The large polymer domain size in the PffBT4T-2OD blend system suggests that the exciton diffusion lengths in PffBT4T-2OD must be larger than in P3HT in order to retain good photovoltaic performance. We suspect that such enhanced diffusion lengths are possible due to the high level of crystallinity in the PffBT4T-2OD phases, as high ordering has been previously shown to improve exciton diffusion in a photovoltaic blend system [50].

The histogram also demonstrates some larger domain sizes, with some polymer phases showing a radius of 40 nm and above, significantly larger than would be expected from this system based upon literature [10]. The presence of these larger phases is likely linked to the large fraction of PffBT4T-2OD material at the surface, where we measure 75% of the surface area to be PffBT4T-2OD despite the blend consisting of only 45% PffBT4T-2OD by weight. This indicates some variation of the relative polymer and fullerene concentrations through the thickness of the film, with the surface morphology showing different relative concentrations with respect to the bulk.

The fullerene domain size histograms (Figure 6.3b) indicate similar peak domain radius (~6 nm) for both the annealed P3HT:PC60BM sample and the PffBT4T-2OD:PC70BM sample. This suggests that the fullerene phase is self-ordered in to domains having similar dimensions in two different polymer systems optimised for photovoltaic performance – an intriguing correlation, although the PffBT4T-2OD:PC70BM blend shows a much larger fullerene domain size distribution.

#### ***Section 6.4.5: Analysis of PffBT4T-2OD:PC70BM morphology – 2) Through-thickness morphology***

The HeIM images of cleaved PffBT4T-2OD blend films (Figure 6.7a) are not particularly revealing, as the features and voids present may simply be artefacts remaining from the cleaving process. It should be noted that scanning TEM (STEM) analysis of a focused ion beam-prepared PffBT4T-2OD:PC70BM sample can be used to image the cross-sectional morphology without such cleaving artefacts (see Supporting Information for an example). Preparation and imaging of a single cross-section in this way takes several hours to perform however, with sample damage

from the invasive preparation and imaging processes a certainty. We can gain some insight into the film structure from our non-destructive BSE imaging method in minutes.

It can be seen that the morphology of a PffBT4T-2OD:PC70BM film as recorded using  $E_L = 500$  eV (Figure 6.4a) appears less clear than that of an otherwise identical sample that had been plasma cleaned (compare Figure 6.4a before plasma cleaning with Figure 6.2a after plasma cleaning). This perhaps indicates the presence of a similar surface wetting layer to that previously observed in P3HT:PC60BM blends [17]. The surface morphology is seen more clearly in Figure 6.4b ( $E_L = 1$  keV), which shows similar features to Figure 6.4a ( $E_L = 500$  eV) but with greater clarity.

It is apparent however that the appearance of the film changes as  $E_L$  is increased, with Figure 6.4c ( $E_L = 2$  keV) and Figure 6.4d ( $E_L = 3$  keV) displaying morphological features with reduced sharpness in comparison to Figure 6.4a and b. At greater  $E_L$  there are more regions of 'intermediate' contrast surrounding and separating the high-contrast domains of polymer and fullerene material highly aligned normal to the substrate. The intermediate contrast regions represent either areas containing a heterogeneous arrangement of phases through the film or simply boundaries between phases, where the larger interaction volume at  $E_L = 3$  keV intersects two or more material domains. Nonetheless it is clear that in both Figure 6.4c and d we observe high contrast, with both bright and dark areas clearly visible. These high-contrast regions are not necessarily representative of columnar phases, which would imply single material domains that form a continuous charge extraction pathway through the film thickness. However, these regions are strongly indicative of a high level of phase alignment or 'domain stacking' of single-material phases through the film. This is consistent with the impressive photovoltaic performance of the blend system. We define the bright and dark domains in the  $E_L = 3$  keV images as highly-aligned polymer and fullerene domains respectively, again based upon the pure film contrast displayed in the Supporting Information.

By thresholding the  $E_L = 3$  keV images we were able to approximately quantify the size and frequency of the high-contrast features in Figure 6.4d. We estimate that such high-contrast regions of polymer material cover ~35% of the imaged area for the PffBT4T-2OD blend (where PffBT4T-

2OD constitutes ~45% of the blend by weight). These high-contrast regions show a size distribution (Figure 6.6) that peaks at 10-30 nm (in radius), but also includes a large fraction of domains (45%) having a radius > 30 nm. The size of the smallest features identified in Figure 6.4d is approaching the apparent resolution limit of our imaging technique at  $E_L = 3$  keV. We therefore note that smaller domain-stacked features may also be present in the film.

To further demonstrate the high level of phase alignment through the depth of the PffBT4T-2OD:PC70BM film morphology, we can compare Figure 6.4d with the high- $E_L$  BSE image of the annealed P3HT:PC60BM film (Figure 6.5h). Clearly, the bright regions indicating highly-aligned P3HT regions are comparatively smaller and less frequent than the equivalent PffBT4T-2OD phases. This observation is emphasised by comparison of the particle radius histograms in Figure 6.6. These give the approximate size distribution of highly-aligned polymer domains in both blend systems. We see that the P3HT blend shows very few highly-aligned regions (~9%) that are larger than 30 nm in radius. Therefore we can conclude that the degree of polymer domain alignment through the film thickness is a key differentiator between the PffBT4T-2OD and P3HT blend morphologies. The PffBT4T-2OD:PC70BM system is comprised by a significantly greater proportion of domains having large surface depth in comparison to P3HT:PC60BM, with the size of these aligned regions also being significantly larger on average.

We identify the dark regions in Figure 6.4d as domains of fullerene material strongly aligned through the film thickness. As with the surface morphology, there is a similarity in the size and frequency of aligned fullerene regions in both PffBT4T-2OD and the annealed P3HT blend. From our image analysis, demonstrated in the Supporting Information, the highly-aligned fullerene domains appear in both blend systems with similar size (~15-25 nm radius) and spatial frequency. Once again, the size of the smallest features in our  $E_L = 3$  keV images may be resolution-limited here. For the PffBT4T-2OD:PC70BM blend however we note that our analysis suggests that highly-aligned fullerene structures represent only ~3% of the imaged morphology area. This is surprisingly small, as the fullerene comprises approximately 55% of the blend by weight. PffBT4T-2OD blends are known to display extremely high phase purity [10], and as such it is

unlikely that much of the remaining fullerene material is dispersed in mixed phase domains. We believe therefore that PC70BM is dispersed in regions that are not well aligned normal to the substrate, in the large portions of the higher  $E_L$  images are of ‘intermediate’ brightness and cannot be easily identified as either highly-aligned PffBT4T-2OD or PC70BM domains. In Figure 6.4d ( $E_L = 3$  keV), we estimate that over 60% of the image can be defined as heterogeneous in this regard, indicating that in terms of morphology there remains significant room for improvement even in this highly-evolved system.

### **Section 6.5: Conclusion**

We have investigated the surface and sub-surface morphology of a state-of-the-art PffBT4T-2OD:PC70BM blend using a novel BSE imaging method. We found direct evidence of a phase structure with a high degree of domain stacking and formation of material structures that penetrate through a large fraction of the film thickness. The defining length-scales of the surface morphology is in agreement with published work, and the size and distribution of domain-stacked polymer and fullerene regions were also measured. Our combined image data reveals a phase-separated morphology that is expected to be highly beneficial for charge extraction. The BSE imaging technique has been shown to be capable of quickly and easily determining the morphological suitability of a polymer blend for photovoltaic application. As verification we have also applied our BSE imaging method to P3HT:PC60BM blends and successfully compared our data with previous studies, as well as reference images taken using established HeIM techniques.

The ability to probe for structure through the film with no cross-sectioning or complex sample preparation reflects a very powerful sample analysis tool, especially in the context of OPV where morphology plays a significant role in defining the performance of a given system [15]. We believe that this BSE imaging technique should be particularly attractive as a tool to aid the development of new, advanced OPV systems, complimenting already established high-speed techniques [51]. By providing scope for high-resolution, 3-dimensional morphology analysis with

unprecedented throughput, the technique enables swift analysis and subsequent optimisation of morphology in novel OPV material systems.

### **Acknowledgements**

We thank the Faculty of Engineering at the University of Sheffield and the Grantham Centre for Sustainable Futures for funding support. We also thank the UK EPSRC for supporting this research through grants EP/J017361/1 “Supergen Supersolar Hub” and EP/M025020/1 “High resolution mapping of performance and degradation mechanisms in printable photovoltaic devices”. MD was supported by a visiting professorship from the Leverhulme Trust (VP1-2014-011), and Istituto Nazionale di Fisica Nucleare (INFN) through the Supercalcolo agreement with FBK. Y.Z. thanks the University of Sheffield for providing a PhD scholarship. The Royal Society funded a collaboration with YZ and HZ of Trinity College Dublin (IE140211). C. R. is supported by EPSRC grant EP/N008065/1. We would also like to extend thanks to the Sorby Centre for Electron Microscopy at the University of Sheffield for the technical support provided.

## Section 6.6: Supporting Information

### *Section 6.6.1: Using detection angle to separate BSE signal from SE*

Using a large stage bias for BSE imaging in the SEM brings a potential drawback in that all electrons emitted from the sample are accelerated towards the detector without discrimination. As such the difference in energy of emission (often the primary feature used to distinguish SE from BSE in an SEM environment [52]) is somewhat diminished and it can prove difficult to selectively detect BSE over SE. This issue is exacerbated at low  $E_L$ , as in this case the elastically scattered BSE emissions already have energies much closer to SE than in conventional BSE imaging applications. To deconvolute the BSE from SE signal, we can consider the landing point of the emitted electrons on our BSE detector, a ‘Concentric Backscatter’ (CBS) detector, mounted to the end of the electron column (see Figure 6.9).

In the presence of a stage bias, the path of an emitted electron will be affected by the electric field, altering its final landing point on the CBS detector. The strength of this effect will depend on the initial electron velocity perpendicular to the field, with lower-energy electrons being focused more strongly by the biasing field towards the centre of the CBS detector (where a hole is present). The low energy of SE means that these are more strongly focused on to the centre of the detector, and the higher-energy BSE signal is located at a larger radius on the CBS detector. As such, the use of the correct CBS detector segments, either alone or in combination, can be used to ensure the BSE signal is the primary contributor to our imaging signal (this is the fundamental rationale behind the segmented detector design of the CBS detector). This effect can be simulated and confirmed by Monte Carlo modelling of the interaction of the primary electron beam with the sample. We have implemented an in-depth version of such a model in this work, in order to provide theoretical verification of the underlying principles behind our technique.

As mentioned in the main body of this work, the results of our Monte Carlo simulation show that the width of the BSE angular distribution increases with  $E_L$ , while the angle of peak emission relative to the incidence angle of the primary beam also increases (see Figure 6.10). This effect is not seen to occur for SE, with the angular distribution and peak emission angle remaining

independent over the range of  $E_L$  sampled here. Importantly, the stage bias has a much stronger effect on the trajectory of comparatively low-energy SE emissions than on BSE. The result of this is that the large majority of SE are focused in to the hole present in to the middle of the CBS detector (Figure 6.9), and do not contribute to the image signal in any way. Only BSEs are emitted with the correct combination of emission angle and energy to be detected by the CBS detector in our experimental setup.

Further evidence that BSE are the primary constituents of our imaging signal can be found by comparing our experimental results with those from the Monte Carlo simulations. Specifically, we monitored the CBS detector segments on which our imaging signal could be found (see Figure 6.9) and observed how this changed with  $E_L$ . At  $E_L = 500$  eV, all of the image contrast originated from the innermost detector segment A with nothing observed in the other segments (see Figure 6.11). As  $E_L$  increased however, the imaging signal spread over the larger-radius detector segments, with the segment containing peak contrast also shifting radially outwards from A to B. At  $E_L = 3$  keV, the image signal was mostly spread over A and B segments with B being the strongest contributor. This spreading of the imaging signal matches the effect seen in Figure 6.10, and is reminiscent of BSEs. It also indicates that SEs (for which the angular distribution of emission was found to be independent of  $E_L$ ) are not responsible for the contrast making up the images in Figure 6.2, 6.4 and 6.5 in the main work.

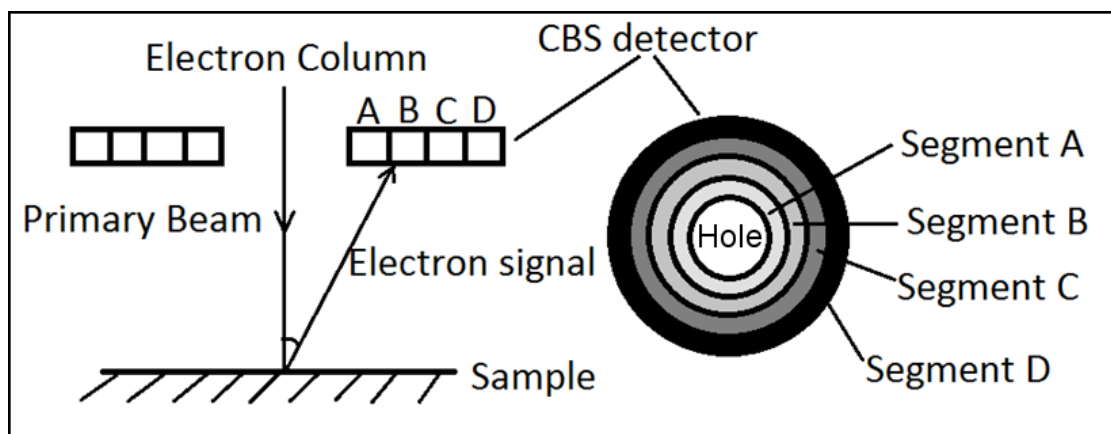


**Figure 6.9:** Schematic of CBS detector, located on the end of the SEM electron column. The segmented, concentric design of the detector is described in cross-section and in planar view.

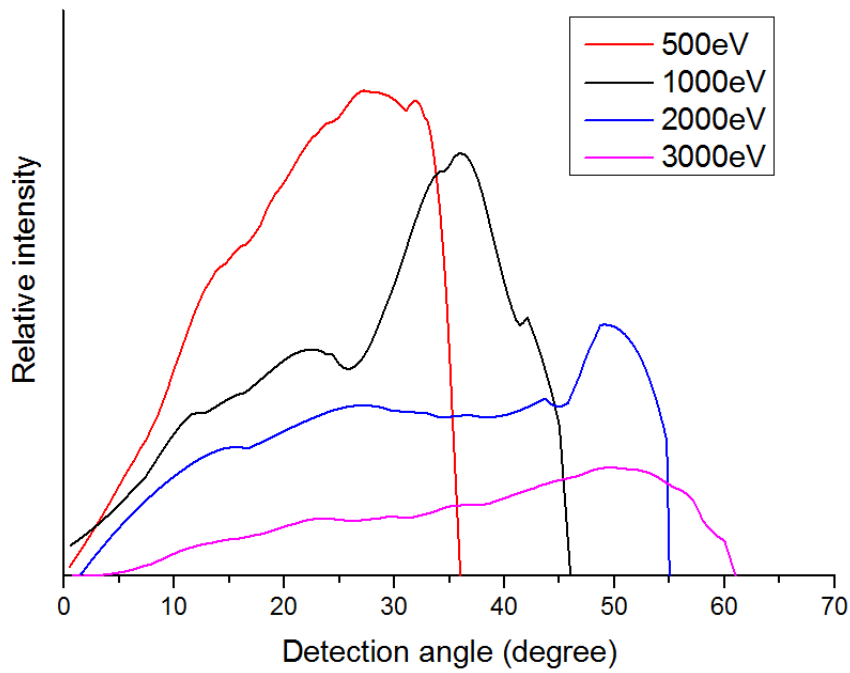


**Figure 6.10:** Angular distribution of BSE emitted from a pure P3HT sample at a range of primary beam landing energies as simulated by Monte Carlo model.

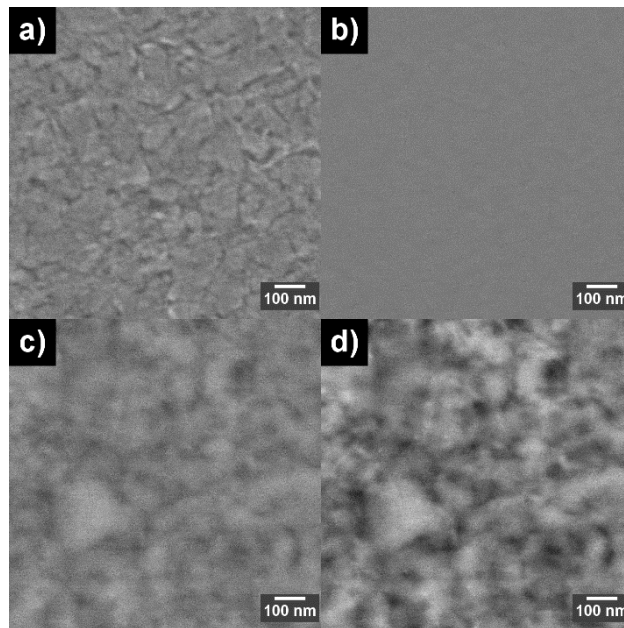


**Figure 6.11:** Image contrast on different CBS detector segments at  $E_L = 500 \text{ eV}$  and  $E_L = 3 \text{ keV}$ . Parts a) and b) show images taken at  $E_L = 500 \text{ eV}$  on detector segments A and B respectively, and parts c) and d) show images taken at  $E_L = 3 \text{ keV}$  on detector segments A and B, respectively. Images taken at the same  $E_L$  were taken simultaneously of the same sample area.

Section 6.6.2: Image Analysis with WEKA segmentation, distance maps and skeletonization

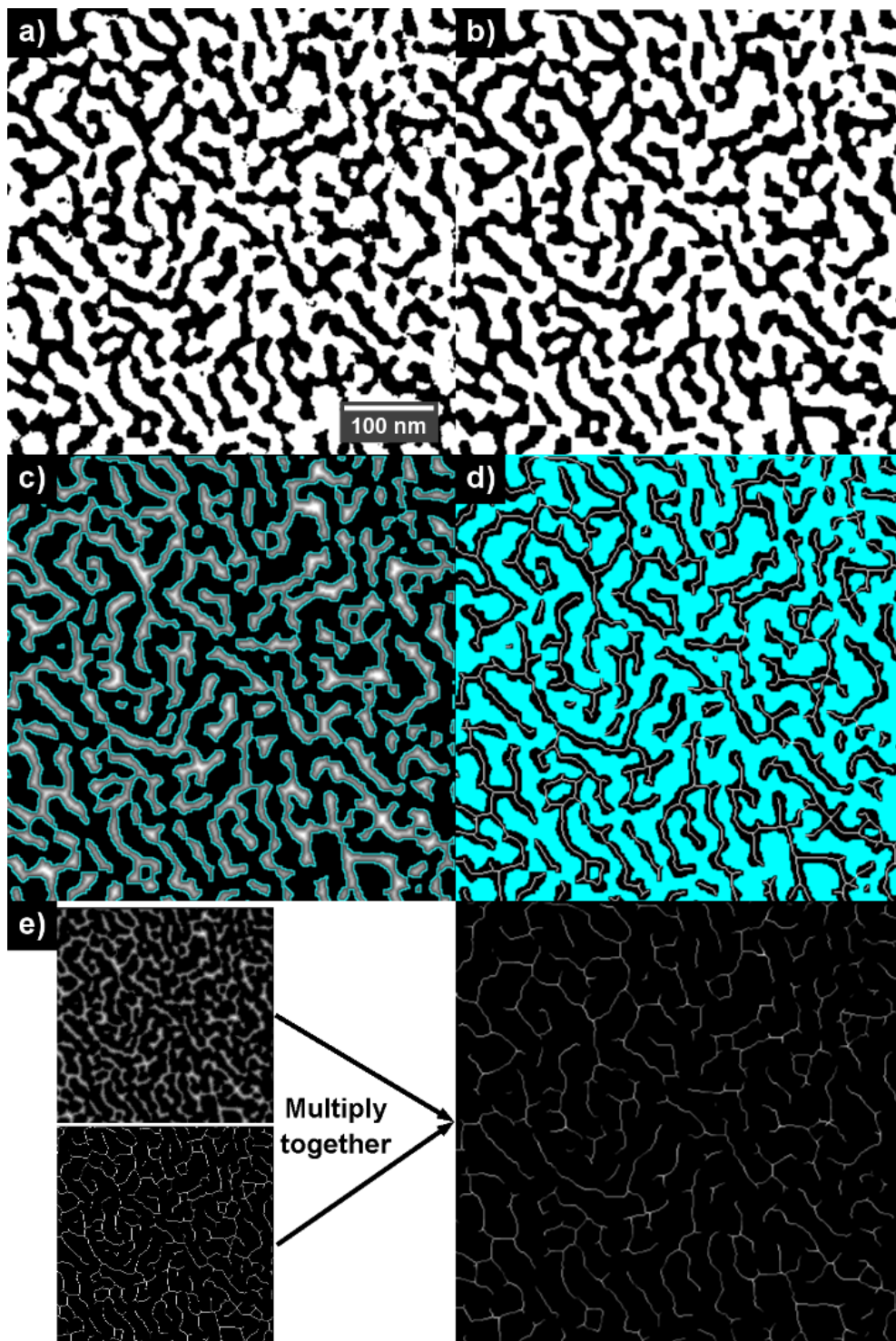


**Figure 6.12:** Summary of surface image analysis process. *a)* shows the initial binary image, with *b)* the same image after coarsening to simplify the image analysis process. Part *c)* shows the distance map of *b)*, with the outline of the domains from *b)* included in cyan for clarity. Part *d)* shows the skeletonization of *b)*, with the white lines showing the medial axis reduction of the domains from *b)*. Part *e)* demonstrates the combination of the skeletonised image and distance map to give the final domain radius estimation, with the histogram of the resulting image being displayed in Figure 6.3 in the main work.

Using images of OPV blend films to characterise the length-scales of a given phase-separated blend can be challenging, with a common issue being that phases often have complex shapes that make it difficult to quantify their actual size with a single number. In this work we implemented an image analysis technique not used before in OPV morphology analysis, in an attempt to tackle this issue. The rationale behind the technique is to define the phase size by the maximum distance to a phase boundary from any point along the axis of a given phase – this defines the maximum required exciton diffusion length in that phase and so is particularly relevant to OPV.

WEKA trainable segmentation was used to classify our surface morphology images in to regions of polymer and fullerene as discussed in the main manuscript, generating a binary image where every pixel has been defined as either belonging to the polymer or fullerene class (Figure 6.12a) [30]–[32]. This image was subsequently processed in ImageJ in order to produce a detailed analysis of the domain size. Firstly, the image was coarsened using a series of dilation and erosion processes in order to remove finer features in the image which would otherwise complicate the image analysis. This generated the simplified image in Figure 6.12b, which retains the basic appearance of Figure 6.12a but with some smaller features removed or smoothed out.

We subsequently took the distance map of Figure 6.12b [33]. Here, the polymer or fullerene class is selected, and then for every pixel the distance to the nearest phase boundary is determined, with the results visualised in a distance map image (Figure 6.12c). In these images, the brightness of a given pixel corresponds to the shortest distance between that pixel and the nearest phase boundary, with brighter pixels representing a greater distance. Therefore, at the location of brighter pixels, a greater exciton diffusion length is required to reach a phase boundary.

The information in the distance map can be used to calculate the ‘skeleton’ of the binary morphology data (Figure 6.12d) [34]. In the process of skeletonisation, the morphological features are reduced down to a set of lines and arcs, which represent the ‘backbone’ of the morphology. Specifically, these lines are the series of points that have a closest domain boundary in two or more places (effectively localised maxima in the distance map), and represent the centre line or ‘medial axis’ [34] of a phase.

By taking the distance map value at any point on the medial axis of a phase, we measure the effective minimum radius of the phase at that point. Naturally, for complex-shaped phases, this will vary along the medial axis of any given phase. We take the product of the skeletonised image and the distance map (Figure 6.12e). The resulting image is of a skeletonised morphology, with each non-zero pixel representing the medial axis of a phase, and the absolute brightness of the non-zero pixels representing the effective minimum radius of the phase at that point. By taking the histogram of our resulting image, we can measure the distribution of domain radius across our binary images, and give a far better estimation of domain size (or required exciton diffusion length in the context of OPV) than is possible using conventional particle analysis techniques.

**Section 6.6.3: Further Supporting Figures:**

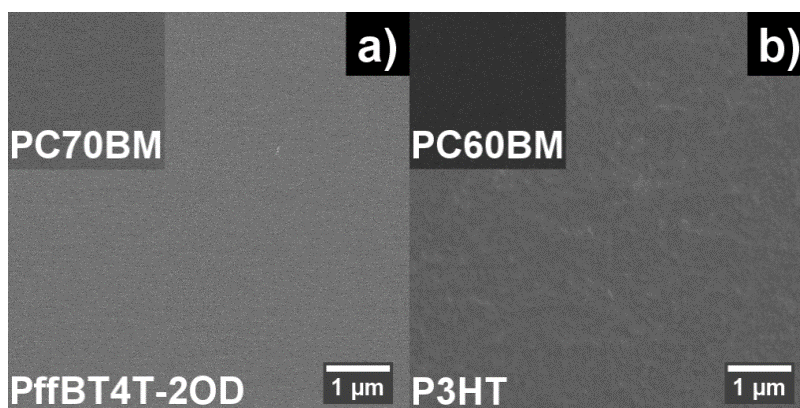


**Figure 6.13:** Images of pure film samples. a) shows PffBT4T-2OD and PC70BM, b) shows P3HT and PC60BM. The polymer-fullerene pairs were imaged using identical conditions in a 4 kV stage bias condition, with all other settings including working distance and contrast/brightness settings identical.

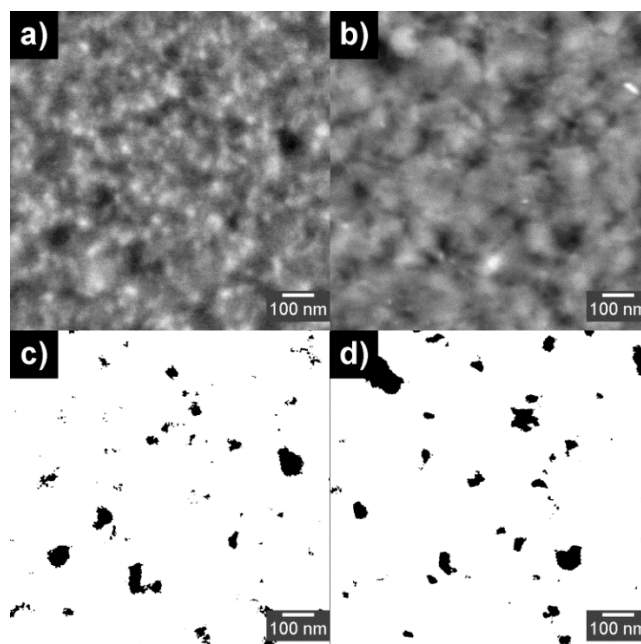


**Figure 6.14:** Particle analysis indicating similar columnar fullerene structures in both P3HT- and PffBT4T-2OD-based blends. a) and b) show Figure 6.5h and 6.4d, respectively, after noise reduction and contrast enhancement. c) and d) show parts a) and b), respectively, after being thresholded to highlight the darkest features in the images, which we perceive to originate from columnar fullerene structures. These images have been post-processed, contrast enhanced and thresholded to an identical brightness level in order to highlight the dark fullerene domains.

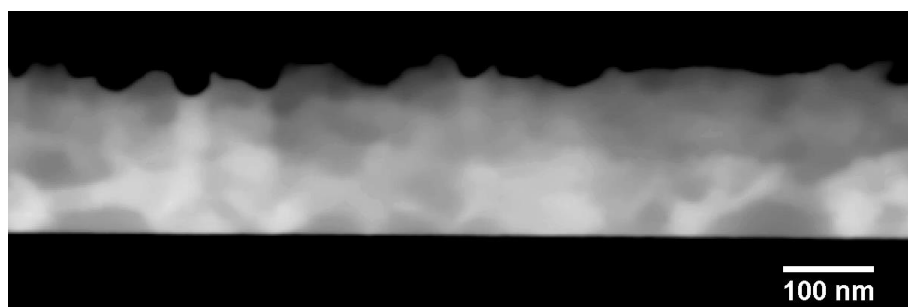


**Figure 6.15:** Example STEM image of PffBT4T-2OD:PC70BM cross-section, as prepared by FIB. The cross-section is of a different PffBT4T-2OD:PC70BM sample to that addressed in the main part of this work (this sample has been thermally annealed, whereas the one in the main work has not). Prior to FIB preparation this blend film was already subject to an intense plasma cleaning process, explaining the high surface roughness. The cross-section is ~100 nm thick, and prepared and imaged in a FEI Helios Nanolab G3 FIBSEM.

## Section 6.7: References

- [1] E. Moons, “Conjugated polymer blends: linking film morphology to performance of light emitting diodes and photodiodes,” *J. Phys. Condens. Matter*, vol. 14, no. 47, pp. 12235–12260, Dec. 2002.
- [2] J. R. Nair, M. Destro, F. Bella, G. B. Appetecchi, and C. Gerbaldi, “Thermally cured semi-interpenetrating electrolyte networks (s-IPN) for safe and aging-resistant secondary lithium polymer batteries,” *J. Power Sources*, vol. 306, pp. 258–267, 2016.
- [3] M. Gerosa *et al.*, “Toward Totally Flexible Dye-Sensitized Solar Cells Based on Titanium Grids and Polymeric Electrolyte,” *IEEE J. Photovoltaics*, vol. 6, no. 2, pp. 498–505, Mar. 2016.
- [4] R. Shanti, F. Bella, Y. S. Salim, S. Y. Chee, S. Ramesh, and K. Ramesh, “Poly(methyl methacrylate-co-butyl acrylate-co-acrylic acid): Physico-chemical characterization and targeted dye sensitized solar cell application,” *Mater. Des.*, vol. 108, pp. 560–569, Oct. 2016.
- [5] J. Nelson, “Polymer:fullerene bulk heterojunction solar cells,” *Mater. Today*, vol. 14, no. 10, pp. 462–470, Oct. 2011.
- [6] H. Hoppe and N. S. Sariciftci, “Organic solar cells: An overview,” *J. Mater. Res.*, vol. 19, no. 7, pp. 1924–1945, Mar. 2011.
- [7] N. D. Treat and M. L. Chabynyc, “Phase separation in bulk heterojunctions of semiconducting polymers and fullerenes for photovoltaics,” *Annu. Rev. Phys. Chem.*, vol. 65, pp. 59–81, Jan. 2014.
- [8] C. Gao *et al.*, “Hexa-peri-hexabenzocoronene and diketopyrrolopyrrole based D-A conjugated copolymers for organic field effect transistor and polymer solar cells,” *Org. Electron.*, vol. 38, pp. 245–255, Nov. 2016.
- [9] Y.-C. Huang, H.-C. Cha, C.-Y. Chen, and C.-S. Tsao, “Morphological control and performance improvement of organic photovoltaic layer of roll-to-roll coated polymer solar cells,” *Sol. Energy Mater. Sol. Cells*, vol. 150, pp. 10–18, 2016.
- [10] Y. Liu *et al.*, “Multiple Cases of High-Efficiency Polymer Solar Cells,” *Nat. Commun.*, vol. 5, no. 9, pp. 1–8, 2014.
- [11] A. J. Heeger, “25th Anniversary Article: Bulk Heterojunction Solar Cells: Understanding the Mechanism of Operation,” *Adv. Mater.*, pp. 10–28, Dec. 2013.
- [12] Y.-C. C. Tseng and S. B. Darling, “Block Copolymer Nanostructures for Technology,” *Polymers (Basel)*, vol. 2, no. 4, pp. 470–489, Oct. 2010.
- [13] W. Cai, X. Gong, and Y. Cao, “Polymer solar cells: Recent development and possible routes for improvement in the performance,” *Sol. Energy Mater. Sol. Cells*, vol. 94, no. 2, pp. 114–127, 2010.
- [14] W. Ma *et al.*, “Influence of Processing Parameters and Molecular Weight on the Morphology and Properties of High-Performance PffBT4T-2OD:PC71BM Organic Solar Cells,” *Adv. Energy Mater.*, vol. 5, no. 23, 2015.
- [15] N. E. Jackson, B. M. Savoie, T. J. Marks, L. X. Chen, and M. A. Ratner, “The Next Breakthrough for Organic Photovoltaics?,” *J. Phys. Chem. Lett.*, vol. 6, pp. 77–84, 2015.

- [16] M. Pfannmöller, W. Kowalsky, and R. R. Schröder, “Visualizing physical, electronic, and optical properties of organic photovoltaic cells,” *Energy Environ. Sci.*, vol. 6, no. 10, pp. 2871–2891, 2013.
- [17] R. C. Masters *et al.*, “Sub-nanometre resolution imaging of polymer–fullerene photovoltaic blends using energy-filtered scanning electron microscopy,” *Nat. Commun.*, vol. 6, p. 6928, 2015.
- [18] M. Pfannmöller *et al.*, “Visualizing a homogeneous blend in bulk heterojunction polymer solar cells by analytical electron microscopy,” *Nano Lett.*, vol. 11, no. 8, pp. 3099–3107, Aug. 2011.
- [19] R. Murray, N. Rujisamphan, and S. I. Shah, “Predicting current from cross section images of organic photovoltaic devices,” *Sol. Energy Mater. Sol. Cells*, vol. 134, pp. 231–235, 2015.
- [20] A. J. Pearson, S. A. Boden, D. M. Bagnall, D. G. Lidzey, and C. Rodenburg, “Imaging the bulk nanoscale morphology of organic solar cell blends using helium ion microscopy,” *Nano Lett.*, vol. 11, no. 10, pp. 4275–4281, Oct. 2011.
- [21] G. Goizueta, T. Chiba, and T. Inoue, “Phase morphology of polymer blends: scanning electron microscope observation by backscattering from a microtomed and stained surface,” *Polymer (Guildf.)*, vol. 33, pp. 886–888, 1992.
- [22] G. Bar, E. Tocha, E. Garcia-Meitin, C. Todd, and J. Blackson, “New Routes to High Resolution and Automated Polymer Morphology Microscopy via Scanning Electron Microscopy,” *Macromol. Symp.*, vol. 282, no. 1, pp. 128–135, Aug. 2009.
- [23] D. Phifer, L. Tuma, T. Vystavel, P. Wandrol, and R. J. Young, “Improving SEM Imaging Performance Using Beam Deceleration,” *Microsc. Today*, vol. 17, no. 4, pp. 40–49, Jun. 2009.
- [24] R. C. Masters *et al.*, “Application of low-voltage backscattered electron imaging to the mapping of organic photovoltaic blend morphologies,” *J. Phys. Conf. Ser.*, vol. 644, p. 12017, 2015.
- [25] Q. Wan, R. A. Plenderleith, M. Dapor, S. Rimmer, F. Claeysens, and C. Rodenburg, “Separating topographical and chemical analysis of nanostructure of polymer composite in low voltage SEM,” *J. Phys. Conf. Ser.*, vol. 644, no. JUNE, p. 12018, 2015.
- [26] W. Zhou, R. P. Apkarian, Z. L. Wang, and D. C. Joy, “Fundamentals of Scanning Electron Microscopy,” in *Scanning Microscopy for Nanotechnology*, W. Zhou and Z. L. Wang, Eds. New York, NY: Springer New York, 2006, pp. 1–40.
- [27] F. Boughorbel, X. Zhuge, P. Potocek, and B. Lich, “SEM 3D Reconstruction of Stained Bulk Samples using Landing Energy Variation and Deconvolution,” *Microsc. Microanal.*, vol. 18, no. S2, pp. 560–561, Jul. 2012.
- [28] V. Marx, “Neurobiology: Brain mapping in high resolution,” *Nature*, vol. 503, no. 7474, pp. 147–152, 2013.
- [29] J. Butler, D. C. Joy, G. Bradley, and S. Krause, “Low-voltage scanning electron microscopy of polymers,” *Polymer (Guildf.)*, vol. 36, no. 9, pp. 1781–1790, 1995.
- [30] C. a Schneider, W. S. Rasband, and K. W. Eliceiri, “NIH Image to ImageJ: 25 years of image analysis,” *Nat. Methods*, vol. 9, no. 7, pp. 671–675, 2012.

- [31] J. Schindelin *et al.*, “Fiji: an open-source platform for biological-image analysis,” *Nat. Methods*, vol. 9, no. 7, pp. 676–682, Jun. 2012.
- [32] M. Hall, E. Frank, G. Holmes, B. Pfahringer, P. Reutemann, and I. H. Witten, “The WEKA data mining software,” *ACM SIGKDD Explor. Newsl.*, vol. 11, no. 1, p. 10, Nov. 2009.
- [33] P. E. Danielsson, “Euclidean distance mapping,” *Comput. Graph. Image Process.*, vol. 14, no. 3, pp. 227–248, 1980.
- [34] A. K. Jain, *Fundamentals of digital image processing*. Englewood Cliffs, NJ: Prentice Hall, 1989.
- [35] T. C. Lee, R. L. Kashyap, and C. N. Chu, “Building Skeleton Models via 3-D Medial Surface Axis Thinning Algorithms,” *CVGIP Graph. Model. Image Process.*, vol. 56, no. 6, pp. 462–478, Nov. 1994.
- [36] M. Dapor, *Transport of Energetic Electrons in Solids*. Berlin: Springer, 2014.
- [37] K. Kanai, T. Miyazaki, H. Suzuki, M. Inaba, Y. Ouchi, and K. Seki, “Effect of annealing on the electronic structure of poly(3-hexylthiophene) thin film.,” *Phys. Chem. Chem. Phys.*, vol. 12, no. 1, pp. 273–282, 2010.
- [38] S. Engmann, V. Turkovic, P. Denner, H. Hoppe, and G. Gobsch, “Optical order of the polymer phase within polymer/fullerene blend films,” *J. Polym. Sci. Part B Polym. Phys.*, vol. 50, no. 19, pp. 1363–1373, 2012.
- [39] J. C. Nolasco, R. Cabré, J. Ferré-Borrull, L. F. Marsal, M. Estrada, and J. Pallarès, “Extraction of poly (3-hexylthiophene) (P3HT) properties from dark current voltage characteristics in a P3HT/n-crystalline-silicon solar cell,” *J. Appl. Phys.*, vol. 107, no. 4, p. 44505, 2010.
- [40] J. Schafferhans, A. Baumann, A. Wagenpfahl, C. Deibel, and V. Dyakonov, “Oxygen doping of P3HT:PCBM blends: Influence on trap states, charge carrier mobility and solar cell performance,” *Org. Electron.*, vol. 11, no. 10, pp. 1693–1700, 2010.
- [41] R. Singh, R. K. Singh, J. Kumar, R. Kant, and V. Kumar, “The origin of DC electrical conduction and dielectric relaxation in pristine and doped poly(3-hexylthiophene) films,” *J. Polym. Sci. Part B Polym. Phys.*, vol. 48, no. 10, pp. 1047–1053, May 2010.
- [42] D. C. Joy, “SMART - a program to measure SEM resolution and imaging performance,” *J. Microsc.*, vol. 208, no. 1, pp. 24–34, Oct. 2002.
- [43] R. C. Masters *et al.*, “Novel organic photovoltaic polymer blends: A rapid, 3-dimensional morphology analysis using backscattered electron imaging in the scanning electron microscope,” *Sol. Energy Mater. Sol. Cells*, vol. 160, pp. 182–192, Feb. 2017.
- [44] A. J. Pearson *et al.*, “Rationalizing Phase Transitions with Thermal Annealing Temperatures for P3HT:PCBM Organic Photovoltaic Devices,” *Macromolecules*, vol. 45, no. 3, pp. 1499–1508, Feb. 2012.
- [45] D. E. Motaung, G. F. Malgas, C. J. Arendse, S. E. Mavundla, C. J. Oliphant, and D. Knoesen, “The influence of thermal annealing on the morphology and structural properties of a conjugated polymer in blends with an organic acceptor material,” *J. Mater. Sci.*, vol. 44, no. 12, pp. 3192–3197, Mar. 2009.

- [46] Y.-C. Huang, Y.-C. Liao, S.-S. Li, M.-C. Wu, C.-W. Chen, and W.-F. Su, "Study of the effect of annealing process on the performance of P3HT/PCBM photovoltaic devices using scanning-probe microscopy," *Sol. Energy Mater. Sol. Cells*, vol. 93, no. 6–7, pp. 888–892, 2009.
- [47] A. J. Parnell *et al.*, "Depletion of PCBM at the cathode interface in P3HT/PCBM thin films as quantified via neutron reflectivity measurements.," *Adv. Mater.*, vol. 22, no. 22, pp. 2444–7, Jun. 2010.
- [48] J. S. Moon, J. K. Lee, S. Cho, J. Byun, and A. J. Heeger, "'Columnlike' structure of the cross-sectional morphology of bulk heterojunction materials.," *Nano Lett.*, vol. 9, no. 1, pp. 230–4, Jan. 2009.
- [49] Y. Zhang *et al.*, "1,8-diiodooctane enables domain coarsening upon thermal annealing to increase power conversion efficiency in PffBT4T-2OD/PC71BM devices," *Submitted*.
- [50] M. Sim *et al.*, "Dependence of Exciton Diffusion Length on Crystalline Order in Conjugated Polymers," *J. Phys. Chem. C*, vol. 118, no. 2, pp. 760–766, 2014.
- [51] F. C. Krebs and M. Jørgensen, "2D Characterization of OPV from Single and Tandem Cells to Fully Roll-to-Roll Processed Modules with and without Electrical Contact," *Adv. Opt. Mater.*, vol. 2, no. 5, pp. 465–477, 2014.
- [52] H. Seiler, "Secondary electron emission in the scanning electron microscope," *J. Appl. Phys.*, vol. 54, no. 11, pp. R1–R18, 1983.

## Chapter 7: Conclusions

In this thesis, a range of novel and advanced characterisation techniques for OPV materials and blends have been developed and demonstrated in the SEM. These have been designed to develop a deeper understanding of OPV materials, and crucially, to have the potential for wide-scale uptake by researchers and industry in the OPV field whilst reducing the requirements for specialised equipment. Interpreting image data reliably and quantitatively remains a challenge with no obvious solution (as demonstrated by the variety of different methodologies used within this thesis). However, the data analysis process will considerably easier if the methods described in this thesis reach a wider uptake and a greater level of refinement. In Chapter 4, the first applications of SE spectroscopy to organic electronic materials were detailed, and a deeper understanding of the characteristics of a TLD applied for SE spectroscopy and energy-filtered SE imaging developed. These findings were built upon in Chapter 5, where energy-filtered SEM images exploited the variation in SE spectrum between P3HT and PCBM to acquire images of the phase-separated blend morphology with unprecedented lateral resolution. Finally, in Chapter 6, a novel method using state-of-the-art backscattered electron imaging techniques was used to probe the 3-dimensional morphology of both the P3HT:PC60BM and PffBT4T-2OD:PC70BM blends. Although none of these methods were applied to OPV materials prior to this PhD, no hardware modifications to commercially available SEM equipment was required to enable any of the techniques. Further, in practice, both SE spectroscopy-based and low-voltage BSE imaging techniques are fast and simple to perform in comparison to established and competitive methods such as energy-filtered TEM.

In Chapter 4, the limitations and potential of an unmodified FEI Sirion TLD used as a SE spectrometer were explored. Unsurprisingly for a non-specialised spectrometer, this TLD was found to demonstrate relatively poor energy resolution, and its mechanism of SE collection and detection results in SEs emitted from deeper beneath the sample surface being favourably detected. Despite these drawbacks, however, the TLD was found to be capable of detecting variation in the SE spectra emitted by a range of P3HT samples having different sample history

or processing variables. Microscope variables that affect the nature of a measured P3HT SE spectrum were investigated, including primary beam energy  $E_0$ , electron beam damage and sample working distance, in order to deduce optimised conditions for studying this spectral variation. By increasing the level of crystalline order in a P3HT sample, new peaks appeared in the SE spectra measured in the FEI Sirion, which are likely related to the different electron transport properties of amorphous and crystalline P3HT[1]. Further, the SE spectra measured from a P3HT film demonstrated changes reflective of expected effects after surface modification *via* air exposure and plasma etching. As a result, SE spectroscopy using the FEI Sirion TLD has been proven capable of identifying aspects of sample history and morphology, underlining that despite the drawbacks of the TLD's spectroscopy characteristics, it remains a characterisation tool with significant potential. High-resolution EFSEM images of pure P3HT films formed using only  $<8$  eV SEs were shown to demonstrate improved material contrast, with molecular alignment at the surface postulated as the origin of the new features revealed by energy-selective SE detection. The findings in Chapter 4 demonstrate that SE spectroscopy and EFSEM as performed on OPV materials is a viable and promising technique, which generates reproducible results that qualitatively match expectations. With further work to obtain a deeper theoretical understanding of the results acquired in Chapter 4 (see Section 7.1) may prove to be a powerful characterisation technique in its own right, capable of identifying and probing in detail the electronic properties of organic electronic materials.

In Chapter 5, the capability of EFSEM as an OPV characterisation tool is demonstrated. By imaging using only SE in a spectral window in which the contrast between P3HT and PCBM is increased, the phase-separated morphology of a P3HT:PCBM film was imaged with unprecedented lateral resolution. By imaging only the top surface of the sample with heightened material contrast, this work constituted the first example of mixed-phase regions being imaged directly within the blend morphology. This was not previously possible using established TEM techniques, as the projection of contrast through a TEM sample hinders the identification of such mixed regions. The images acquired from the P3HT:PCBM blend system show the phase-

separated morphology in impressive detail, and the effects of a thermal anneal on the morphology can be clearly observed on a nanometre scale. Domain size and coverage results from rationalised thresholding of the EFSEM images agree with literature studies from different techniques, indicating that the images accurately represent the blend morphology. Alongside the high-quality morphology characterisation offered, the key benefit of EFSEM lies in its accessibility. In stark contrast to competing techniques such as energy-filtered TEM, EFSEM methods can be used to probe the morphology of an OPV blend film with sub-nanometre resolution in minutes with no complex sample preparation required. Whilst the 2-dimensional picture of the morphology from EFSEM gives little insight in to the crucial cross-sectional morphology of the film, the lack of projection artefacts as seen from TEM methods means that image contrast is simpler to interpret. As a result, this work has already been cited as a leading reference study in to the nanoscale morphology of P3HT:PCBM blends[2], [3]. Future applications of the technique may focus on building a more 3-dimensional picture of the blend film however, for example by imaging blend film cross-sections (Section 7.1).

In Chapter 6, a novel solution was sought to the challenge of imaging polymer blend morphology in 3 dimensions, by imaging using low-energy backscattered electrons. By probing for domain stacking through the full thickness of an OPV blend film, SE images acquired with an optimised primary beam energy were able to detect high levels of domain stacking in films that give superior solar cell performance. Whilst the high performance of OPV films is dependent on a range of factors, of which morphology is only one (the performance of PffBT4T-2OD:PC70BM films is largely attributed to its low band gap[4], for example), morphology is nonetheless an important aspect of device efficiency, as outlined in Section 2.4. Importantly, the modern high-performance PffBT4T-2OD:PC70BM film was demonstrated to show improved levels of domain stacking in comparison to the now-ageing P3HT:PC60BM blend. Whilst the lateral resolution available from low-energy BSE imaging is not competitive with that available from EFSEM, the ability to probe for domain stacking promises to be a powerful morphology analysis tool in the context of OPV. Again here, the key benefit lies in the accessibility and speed of the technique. The methods

presented in Chapter 6 offer an insight into the level of domain stacking within a particular blend film without first needing to cross-section the film or prepare an electron transparent sample for TEM analysis. Further, whilst reliant on a modern SEM with recent technology (this work was performed on a FEI Nova NanoSEM 450 from 2009 using a commercially available CBS detector), the methods can, similarly to EFSEM, be performed without requiring any hardware modifications or advanced expertise.

In this thesis, corrections were made to an already published work in Chapter 6, based upon suggestions resulting from the examination process. One such change was made clarify that the PffBT4T-2OD system's OPV characteristics are not wholly reliant on its optimised morphology, rather that its morphology is one of a multitude of factors (most notably its low bandgap) that define its excellent OPV performance. This is an important point not directly addressed (albeit not contradicted) by the published work.

The majority of the changes to Chapter 6, however, addressed an alternative interpretation of some results presented in the published work. Specifically, the published work suggested that at  $E_L = 3$  keV, high-contrast regions in the through-thickness images of PffBT4T-2OD:PC70BM represented phases penetrating the majority of the film, as at  $E_L = 4$  keV, the BSE signal starts to originate from the Si substrate beneath. This interpretation showed inconsistencies with the results obtained from the P3HT:PC60BM system, however. Through the examination process, an alternative interpretation arose; that the loss of contrast at  $E_L = 4$  keV in images of the PffBT4T-2OD system reflected the point at which the BSE imaging depth is larger than the average depth penetration of phases in to the film. With this interpretation, the loss of contrast at  $E_L = 4$  keV is a result of the BSE signal being averaged through multiple phases of different blend components. The changes noted in the introduction to Chapter 6 aim to include this additional interpretation alongside the original, in order to allow a fuller discussion of the results presented. As the corrections to the published manuscript mainly constitute an additional interpretation to some of the work's findings, without making any significant impact on the work's conclusions, it was decided not to attempt formal amendment to the published manuscript with these changes.

<b>Characterisation technique</b>	<b>Strengths</b>	<b>Weaknesses</b>
Phase-contrast AFM	<ul style="list-style-type: none"> <li>• Polymer-fullerene contrast from different energy dissipation properties</li> <li>• Widely available equipment</li> </ul>	<ul style="list-style-type: none"> <li>• Slow, low-throughput</li> <li>• Difficult to interpret data without deep understanding of mechanical properties of materials</li> <li>• 2-dimensional information</li> </ul>
Advanced scanning probe methods	<ul style="list-style-type: none"> <li>• Directly measure electronic properties</li> <li>• Can infer aspects of 3-dimensional morphology</li> </ul>	<ul style="list-style-type: none"> <li>• Very low throughput</li> <li>• Complex to set up</li> <li>• Difficult to interpret data</li> </ul>
Bright field TEM	<ul style="list-style-type: none"> <li>• Infer aspects of 3-dimensional morphology</li> <li>• Excellent lateral resolution</li> </ul>	<ul style="list-style-type: none"> <li>• Difficult to interpret – contrast projection, defocus methods produce contrast of questionable origin</li> <li>• Time consuming sample preparation</li> <li>• Limited field of view</li> </ul>
Analytical TEM	<ul style="list-style-type: none"> <li>• Tomography allows full 3-dimensional reconstruction of morphology</li> <li>• Material identification from EELS – removes ambiguity in data interpretation</li> <li>• Excellent resolution</li> </ul>	<ul style="list-style-type: none"> <li>• Data interpretation requires specialist expertise</li> <li>• Preparation of samples for tomography is time consuming, challenging</li> <li>• Tomography + EELS collection risks electron beam damage</li> </ul>
Helium-ion microscope	<ul style="list-style-type: none"> <li>• High SE yield of He<sup>+</sup> ions gives high quality morphology image</li> <li>• Good resolution</li> <li>• High throughput, little/no sample preparation</li> </ul>	<ul style="list-style-type: none"> <li>• Data is 2-dimensional</li> <li>• HIM equipment is rare, potential uptake of techniques is limited at present</li> </ul>

*Table 7.1: Continued overleaf*

Reciprocal space techniques	<ul style="list-style-type: none"> <li>• Range of complimentary techniques available to probe different aspects of morphology</li> <li>• Excellent resolution – probe crystallinity, intermixing</li> <li>• Bulk averaging gives whole-sample overview of sample properties</li> </ul>	<ul style="list-style-type: none"> <li>• Highest-quality data requires specialised facilities such as synchrotrons</li> <li>• Reliable interpretation of scattering data is difficult</li> </ul>
Conventional SEM	<ul style="list-style-type: none"> <li>• Modern SEM has lateral resolution competitive with TEM</li> <li>• High throughput, little/no sample preparation</li> <li>• SEMs widely available</li> </ul>	<ul style="list-style-type: none"> <li>• Low contrast between polymer and fullerene</li> <li>• SE imaging methods only give 2-dimensional data</li> <li>• Data can be difficult to reliably analyse, open to interpretation</li> </ul>
Energy-filtered SEM	<ul style="list-style-type: none"> <li>• Commercially available on many modern SEMs</li> <li>• High throughput, little/no sample preparation</li> <li>• Unprecedented lateral imaging resolution</li> <li>• Energy-filtering boosts material contrast and aids interpretation, mixed phase visible</li> </ul>	<ul style="list-style-type: none"> <li>• Information is only 2-dimensional, method for layer-by-layer imaging required</li> <li>• Quantification of image data still challenging (difficult to segment three intimately mixed phases based only on images)</li> </ul>
Low-voltage BSE imaging	<ul style="list-style-type: none"> <li>• Commercially available on many modern SEMs</li> <li>• High throughput, little/no sample preparation</li> <li>• Low-voltage BSEs give clear material contrast</li> <li>• Can infer aspects of 3-dimensional morphology</li> </ul>	<ul style="list-style-type: none"> <li>• No complete 3-dimensional picture</li> <li>• Contrast in higher <math>E_L</math> images open to interpretation</li> <li>• Lateral resolution not as high as TEM/EFSEM (though competitive with eg. AFM)</li> </ul>

**Table 7.1:** An extension to Table 2.1 – strengths and weaknesses of newly developed techniques in an OPV characterisation context

The primary goal of this thesis has been to develop the SEM as a viable, competitive characterisation tool for use by the OPV community. By developing the SEM as a tool to provide a detailed morphology characterisation in a high-throughput, accessible manner, the work aimed to provide new understanding of OPV materials and help relieve the morphology characterisation bottleneck that has hindered the development of new OPV solutions. The progress towards this

goal is summarised in Table 7.1, an extended version of the overview in Table 2.1 that includes EFSEM and low-voltage BSE imaging in comparison to the existing state-of-the-art.

In the case of EFSEM and low-voltage BSE imaging, methods have been developed and verified that are capable of probing nanoscale OPV morphology in high resolution, both offering a powerful and unique insight in to the nature of polymer blend morphology. Whilst these methods have been successful in enabling effective morphology analysis in the SEM, it should be noted here that despite the progress made EFSEM and low-voltage BSE imaging cannot be seen as inherently superior to the existing state-of-the-art. Most obviously, acquiring full 3-dimensional information on OPV morphology still requires a technique such as tomographic TEM or scattering methods, and accurate layer-by-layer imaging or some advancement on the BSE technique is required for the SEM to be competitive in this regard. Attempts at performing cross-sectional SE imaging are described in the next section in an attempt to remedy this situation. Further, unambiguous phase identification and quantification from the SEM techniques demonstrated in this work is challenging, as identification is based solely upon image contrast. The use of hyperspectral methods such as analytical TEM, whereby an EELS spectrum is measured for each pixel to enable clear phase identification, makes sample analysis more precise, if also a more specialised task.

Importantly however, despite some drawbacks in comparison to established methods, all of the techniques developed presented in this work meet a central goal of rapid sample analysis, alongside accessibility to OPV researchers without specialised electron microscopy expertise. Whilst the TEM and other characterisation methods may be capable of a more complete morphology picture, the poor throughput and accessibility of the most advanced techniques mean that, for the day-to-day operations of an OPV laboratory, the practical applicability is limited. The SEM based techniques in this project succeed in offering a competitive, detailed morphology characterisation in an approachable, practical package.

Additionally, SE spectroscopy of P3HT films has been demonstrated, and it has been believed that various electronic properties of the films are reflected in spectral features. With further efforts to

understand the origin of these spectral features, SE spectroscopy of OPV films may prove to be a highly promising analysis tool in its own right. It is hoped that through the works published during this PhD and future collaboration with OPV researchers, these methods will offer researchers a more detailed insight into new and developing materials systems, helping to direct and accelerate new advancements in the field.

### **Section 7.1: Future work**

As noted above, further work is required to help develop the techniques addressed in this thesis in to more complete and reliable material characterisation tools. As it is believed that SE spectra reflect the electronic properties of the sample[5], an obvious starting point for future investigations in to SE spectroscopy is comparison with conventional methods for probing electronic structure, such as ultraviolet and x-ray photoelectron spectroscopy (UPS and XPS). Whilst these methods have already been applied to study conjugated polymers in depth, variation in the specific material and processing parameters for the material studied in each work can make direct comparison with SE spectroscopy data difficult. An experiment to compare the SE spectrum and XPS/UPS data from identically processed samples may help to elucidate the specific aspects of electronic structure reflected in a SE spectrum. Initial studies of this nature are already underway. Likewise, with regard to the EFSEM images in Chapter 4, where image contrast is believed to reflect molecular orientation at the surface, x-ray diffraction (XRD) combined with EFSEM images of identical P3HT films may be used to investigate the origin of contrast. XPS data has also already been shown to reflect molecular orientation at the surface of P3HT[6].

Regarding SE spectroscopy, the accessibility of this emerging technique will be improved significantly through the development of faster, automated methods for SE spectrum acquisition and analysis. The FEI Sirion used to acquire the large majority of SE spectra presented in this thesis is ~15 years old and is controlled by outdated software in comparison to modern standards. As mentioned in Chapter 4 however, work is presently ongoing, in collaboration with FEI Co., to enable and verify SE spectroscopy methods on more modern SEMs, including a FEI Nova from

~2009 and a FEI Helios installed in 2016. These tools use modern software that allows computer algorithms to control the operation of the microscope for repetitive tasks. This is ideal for automating SE spectrum acquisition. Significant progress has been made to date, with simple algorithms running on both the FEI Nova and FEI Helios SEMs that automate the spectrum acquisition process and significantly reduce acquisition times. MATLAB scripts have also been written to process the raw image data acquired by the microscope in to SE spectra. Future work will focus on combining the acquisition and processing of SE spectra in to an accessible yet robust software package that enables rapid SE spectrum acquisition and analysis. The greatly reduced sample analysis times facilitated by such a package will accelerate attempts to develop a deeper understanding of the SE spectra acquired by a TLD.

As previously discussed, a major weakness of the EFSEM data presented in Chapter 5 is that the images only reflect morphology at the surface of the film, and offer no insight in to the nature of cross-sectional morphology. It is therefore proposed that future efforts can focus on obtaining EFSEM data from a sample cross-section. In Chapter 6, it was already demonstrated that it is possible to image the morphology a cryo-fractured P3HT:PCBM film using a HeIM in combination with a plasma etch to remove cleaving artefacts and selectively remove one material phase. However, in this same Chapter it was observed that such a technique method did not allow the cross-sectional morphology of PffBT4T-2OD:PC70BM films to be imaged with much clarity. EFSEM may be used to improve phase contrast whilst imaging blend film cross-sections and improve on this situation; however, the presence of cleaving artefacts in the cross-section makes contrast interpretation difficult when imaging a cross-section surface.

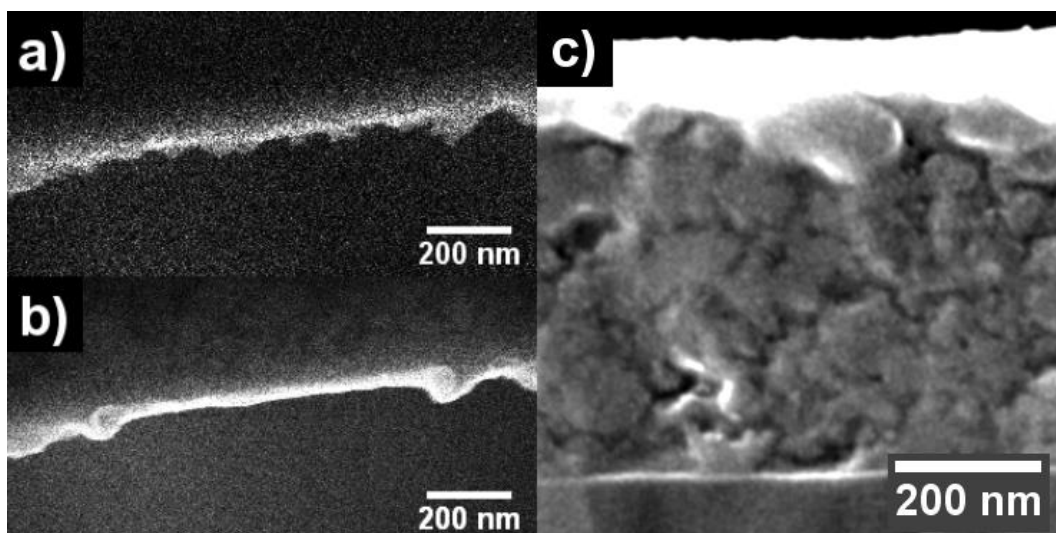


**Figure 7.1:** Polishing and imaging a PffBT4T-2OD:PC<sub>70</sub>BM blend in a helium ion microscope. Part a) shows a top-down view of a cryo-cleaved edge immediately after cleaving, and b) after polishing the cleaved edge with helium ions. The sample was then plasma etched to remove a damage layer from the ion polish step, and imaged using the helium ion beam, revealing the cross-sectional morphology in part c).

Over the course of this PhD, the cross-sectional HeIM imaging technique demonstrated in Figure 6.7 was developed further, by using the helium ion beam to ‘polish’ a cryo-cleaved cross-section and remove cleaving artefacts[7]. The polishing method was optimised for a PffBT4T-2OD:PC70BM sample, in order to ensure that the cross-section surface was effectively milled with no redeposition of material and without incurring significant beam damage in the bulk of the film. An example of the resulting polished cross-section is presented in Figure 7.1, showing the removal of cleaving artefacts in a top-down view (Figure 7.1a) and the subsequent polished cross-section (Figure 7.1b). Morphological features can be observed in the polished cross-section albeit with limited clarity. The HeIM used to acquire this data (a Zeiss Orion NanoFab based in Trinity College Dublin) is equipped with a SE energy filter that has to date been used for rudimentary SE spectroscopy studies. Future work will therefore combine energy-filtered SE detection principles with the polishing method presented in Figure 7.1 in order to boost the material contrast available from the film cross-section. It is hoped the resulting method will offer a robust alternative to cross-sectional TEM methods (Section 2.5.1) that can probe cross-sectional morphology in detail without issues related to contrast projection.

## Section 7.2: References

- [1] R. Noriega *et al.*, “A general relationship between disorder, aggregation and charge transport in conjugated polymers.,” *Nat. Mater.*, vol. 12, no. 11, pp. 1038–44, 2013.
- [2] G. J. Hedley, A. Ruseckas, and I. D. W. Samuel, “Light Harvesting for Organic Photovoltaics,” *Chem. Rev.*, vol. 117, no. 2, pp. 796–837, Jan. 2017.
- [3] R. Alessandri, J. J. Uusitalo, A. H. de Vries, R. W. A. Havenith, and S. J. Marrink, “Bulk Heterojunction Morphologies with Atomistic Resolution from Coarse-Grain Solvent Evaporation Simulations,” *J. Am. Chem. Soc.*, vol. 139, no. 10, pp. 3697–3705, Mar. 2017.
- [4] Y. Liu *et al.*, “Multiple Cases of High-Efficiency Polymer Solar Cells,” *Nat. Commun.*, vol. 5, p. 5923, 2014.
- [5] R. F. Willis, B. Feuerbacher, and B. Fitton, “Graphite conduction band states from secondary electron emission spectra,” *Phys. Lett. A*, vol. 34, no. 4, pp. 231–233, Mar. 1971.
- [6] K. Kanai, T. Miyazaki, H. Suzuki, M. Inaba, Y. Ouchi, and K. Seki, “Effect of annealing on the electronic structure of poly(3-hexylthiophene) thin film.,” *Phys. Chem. Chem. Phys.*, vol. 12, no. 1, pp. 273–282, 2010.
- [7] D. Fox, Y. Chen, C. C. Faulkner, and H. Zhang, “Nano-structuring, surface and bulk modification with a focused helium ion beam.,” *Beilstein J. Nanotechnol.*, vol. 3, pp. 579–85, Jan. 2012.